Abstract

High Tc superconductors and the contact properties

A thesis submitted for the degree of Doctor of Philosophy in the University of Oxford.

Hua Huang, St. Anne's College, Oxford, Michaelmas term 1992.

Methods of processing large grained textured superconductor have been successfully developed, based on a melt texturing process. Large grained textured superconductor with grain size over 10mm along the growth direction and Jc over 3600A/cm^2 (77K, 0.5 Tesla) has been produced in both one - zone and two - zone furnaces with good reproducibility.

Two kinds of design of reactive metal contacts have been proposed and investigated, aiming to make low resistivity contacts with strong mechanical strength. Three possible reactive contact metals have been tested for contact making, and the microstructures at the interfaces have been studied to find the relations between contact resistivity and contact processing conditions. Titanium/noble metal multilayer contacts is a promising type of contact technique for low resistivity and strong mechanical bonds.

Gold and silver contacts give resistivities among the best reported results in the literature, and they turned out to be extremely stable in time, could withstand repeated thermal cycling from room temperature to 10K and yield very reproducible R-T curves.

The electrochemical titration method has been used to increase the oxygen stoichiometry of bulk textured $YBa_2Cu_3O_{7-x}$ samples. The electrochemical titration method can further oxidize melt textured thick film $YBa_2Cu_3O_{7-x}$ samples in which it may be difficult to further improve oxygen content by conventional annealing. The solid state electrochemical cell has been used to study the thermodynamic properties of the Y-Ba-Cu-O system at high oxygen pressure by measuring the oxygen activity versus time continuously immediately after the electrochemical titration.

A series of computer models have been set up according to the microstructure of the contact interface to simulate the complicated contact resistivity behaviours. The nature of, and geometry of, the reaction products at the contact interfaces may be revealed by the temperature dependence of the contact resistance. This information combined with direct observations on the structure and chemistry of the contacts provided a fuller understanding of conduction mechanism at the contact interface.

High Tc superconductors and the contact properties

Hua Huang

St. Anne's College, Oxford

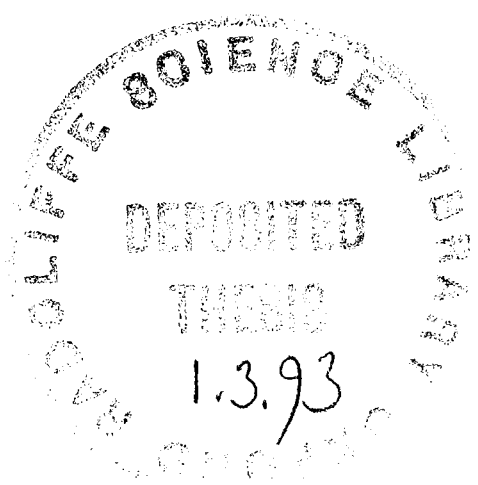

A thesis submitted for the degree of Doctor of Philosophy in the University of Oxford.

Michaelmas term 1992

ACKNOWLEDGEMENTS

I would like to thank professor Sir Peter Hirsch for the provision of laboratory facilities, and I'd like to express my sincere gratitude to Dr. C.R.M. Grovenor for his constant supervision, help and encouragement throughout the past four years.

To the others who have provided support and assistance during this work, I would like to extend my sincere thanks. I am especially grateful to:

Mr. C.J. Salter for his expert operation of the electron microprobe.

Dr. S.G. Roberts for helping me solving the problems during my thesis writing using the computer network, and Mr. B. Williams for the provision of key to the computer room.

All the members of the high Tc group, especially Dr. O.F.C. Schilling and Mr. H.C. Lai for the useful discussions.

Mr. J. Short for his cheerfulness and help in the students's workshop, Mr. I.R. Lloyd for helpful discussions in building furnaces, Mr. A.Mcknight, Mr. M. Taheri for photographic work.

Finally, I should like to thank my wife and my parents, to whom this thesis is dedicated, for their unfailing love, support and encouragement.

INDEX

Chapter 1 Introduction to High T_c Superconductors 1

1.1 Introduction 1

1.2 Phases and Phase diagrams 3

1.3 Structure, oxygen nonstoichiometry and superconductivity 6

1.4 Microstructure 11

1.5 Practical application of high Tc superconductors 12

1.5.1 Critical current density 13

1.5.2 Environmental protection 14

1.5.3 Cryostabilization 14

1.5.4 Reliable, low - resistance contacts 15

Chapter 2 Interaction of superconducting $YBa_2Cu_3O_{7-x}$ and oxygen 16

2.1 $YBa_2Cu_3O_{7-x}$ under low oxygen pressure 16

2.2 $YBa_2Cu_3O_{7-x}$ under high oxygen pressure. 21

2.3 Kinetics of oxygenation in the superconductor oxide 26

Chapter 3 Electrical Contacts to Superconductors 28

Chapter outline 28

3.1. Introduction 28

3.2 Silver paint and gold paste direct bonding 30

3.3 Contacts made with reactive metals 31

3.4 Contacts made with noble metals 32

3.5 The cleanness of the superconductor surface and contact properties 35

3.6. The problems associated with poor contacts 35

3.6.1 Long term mechanical problems 36

3.6.2 The critical current problem in contacts 37

3.6.3. The oxygen stoichiometry problem 37

Chapter 4 Interactions between $YBa_2Cu_3O_{7-x}$ and other materials 38

Chapter outline 38

4.1 Interactions between $YBa_2Cu_3O_{7-x}$ and reactive metals 38

4.1.1 Superconductor-Indium 38

4.1.2 Superconductor-Iron 38

4.1.3 Superconductor-Nickel 38

4.1.4 Superconductor-Aluminium 39

4.1.5 Superconductor-Copper 39

4.1.6 Superconductor-Lead 39

4.1.7 Superconductor-Niobium 40

4.1.8 Superconductor-Bismuth 40

4.1.9 Superconductor-Titanium 41

4.1.10 Superconductor-Molybdenum 41

4.2 Interaction between superconductor and noble metals 41

4.2.1 Superconductor-Platinum (group) 41

4.2.2 Superconductor-gold 42

4.2.3 Superconductor-silver 43

4.3 Summary 44

Chapter 5 Preparation of high Tc superconductor samples 46

5.1 Introduction 46

5.2 Sample preparation 47

5.2.1 Samples prepared by the ordinary sintering method 47

5.2.2 Samples prepared by melt growth technique 47

5.2.2.1. Melt growth in the one-zone furnace. 48

5.2.2.2 Melt growth in the two-zone furnace 50

5.3 Results and discussion 54

5.3.1 Crystal growth 54

5.3.2 The microstructure of melt grown $YBa_2Cu_3O_{7-x}$ sample 59

5.3.3 Texture and properties of the melt grown $YBa_2Cu_3O_{7-x}$ 61
5.4 Conclusions 62

Chapter 6 Electrical contacts to high temperature superconductor 63
6.1 Introduction 63
6.2 Experimental methods 63
6.2.1 Superconductor sample preparation 64
6.2.2 Superconducting property measurement 64
6.2.3 Contact sample preparation 65
6.2.4 Electrical measurement: 66
6.2.5 Microstructural examination of the contact interface 69
6.3 Silver thin film contacts 70
6.3.1 Experiment 70
6.3.2 Experimental results 71
6.3.3 Discussion 72
6.4 Silver epoxy 72
6.4.1 Experiment 73
6.4.2 Experimental results 73
6.4.3 Discussion 73
6.5 Titanium contacts 74
6.5.1 Titanium metal contact 75
6.5.1.1 Background 75
6.5.1.2 Thermodynamic and kinetic analysis 75
6.5.2 Thermal evaporated Ti contacts 77
6.5.2.1 Experiment and results 77
6.5.2.2 Discussion 78
6.5.3 Diffusion bonded titanium metal contact: 79
6.5.3.1 Experiment and results 79
6.5.3.2 Discussion 80

6.5.4 Titanium contacts made in a vacuum furnace..... 80
6.5.4.1 Experiment and results 80
6.5.4.2 Discussion 81
6.5.5 Titanium contacts on melt-textured superconductor 81
6.5.5.1 Experiment and results 82
6.5.5.2 Discussion 83
6.5.6 Conclusion 84
6.6 Molybdenum contact 84
6.6.1 Experiment and results..... 85
6.6.2 Discussion..... 86
6.7 Multilayer contacts..... 86
6.7.1 Experiment design 86
6.7.2 Experiments on Ti/Ag and Ti/Au contacts..... 87
6.7.3 Results..... 87
6.7.4 Discussion..... 87
6.8 'Semi-noble' metal-palladium contacts..... 88
6.8.1 Experiment..... 88
6.8.2 Results and discussion..... 89
6.9 Solderable gold contacts..... 90
6.9.1 Introduction..... 90
6.9.2 Background 90
6.9.3 Experiment and results..... 91
6.9.4 Discussion..... 93
6.10 Conclusions..... 96

Chapter 7 Solid state electrochemical studies on $YBa_2Cu_3O_{7-x}$ 97
7.1 Introduction 97
7.2 Background 97
7.2.1 Theory of electrolytes 97

7.2.2 Experimental principles 99
7.2.3 Selection of solid state ion conductor 100
7.3 Experimental equipment 101
7.3.1 Apparatus for electrochemical titration 101
7.3.2 Furnace 102
7.3.3. Electronic equipment for electrochemical titration 102
7.4 Sample preparation 103
7.4.1 $YBa_2Cu_3O_{7-x}$ samples 103
7.4.2 Zirconia electrolytes 103
7.4.3. Platinum and silver paste electrodes 104
7.4.4 Gold buffer layers 104
7.5 Coulometric titration 104
7.5.1 Experiment 104
7.5.2 Experimental results 106
7.5.2.1 Bulk textured crystal $YBa_2Cu_3O_{7-x}$ samples 106
7.5.2.2 $YBa_2Cu_3O_{7-x}$ thick film sample 107
7.5.3 Discussion 107
7.6 Thermodynamic properties of $YBa_2Cu_3O_{7-x}$ and the formation of $YBa_2Cu_4O_8$ 108
7.6.1 Electrical circuit 108
7.6.2 Experiments 109
7.6.3 Discussion 113
7.7 Resistance measurements during titration 120
7.7.1 Experiment and results 120
7.7.2 Discussion: 121
7.8 Contact making during electrochemical titration 122
7.8.1 Background 122
7.8.2 Experiment 123
7.8.3 Discussion 124

7.9 Conclusions: 125

Chapter 8 Modelling of $YBa_2Cu_3O_{7-x}$ contacts 126

8.1 Introduction 126

8.2 A possible explanation for the contact resistance drop near T_c 126

8.3 Contact interface models 127

8.3.1 Model for contacts with poor resistivities 127

8.3.2. Model for noble metal contacts 128

8.3.3 Model for contacts with resistivities (10^{-5}-$10^{-6}\Omega cm^2$) 130

8.3.4. Model for contacts with resistivities (10^{-2}-$10^{-3}\Omega cm^2$) 131

8.3.5. Model for contacts with resistivity (10^{-3}-$10^{-4}\Omega cm^2$) 133

8.3.6 Model for Pd contact with strange behaviour 134

8.4. Discussion: 135

Chapter 9 Conclusions and suggestions for further work 138

9.1 Conclusions 138

9.2 Suggestions for further work 140

References

Chapter 1

Introduction to High Tc Superconductors

1.1 Introduction

The phenomenon of superconductivity was first discovered in mercury by H.K. Onnes and his assistant G.Holst in 1911. Further study revealed that many of the elements exhibit superconductivity, niobium having the highest Tc of 9.3K.

Superconductivity can be recognised by the following characteristic signs:

- No measurable electrical resistance to a small d.c. current below a certain temperature, the critical temperature T_c.

- The type I superconductors expel magnetic flux from themselves when cooled below T_c in a magnetic flux density less than H_c (the Meissner effect) (Fig.1.1a). Type II superconductors have a similar behaviour at low field strength ($H < H_{c1} < H_c$), but then allow a gradual penetration of magnetic field and return to the normal state when the penetration of the field is complete at $H > H_{c2} > H_c$ (Fig. 1.1b).

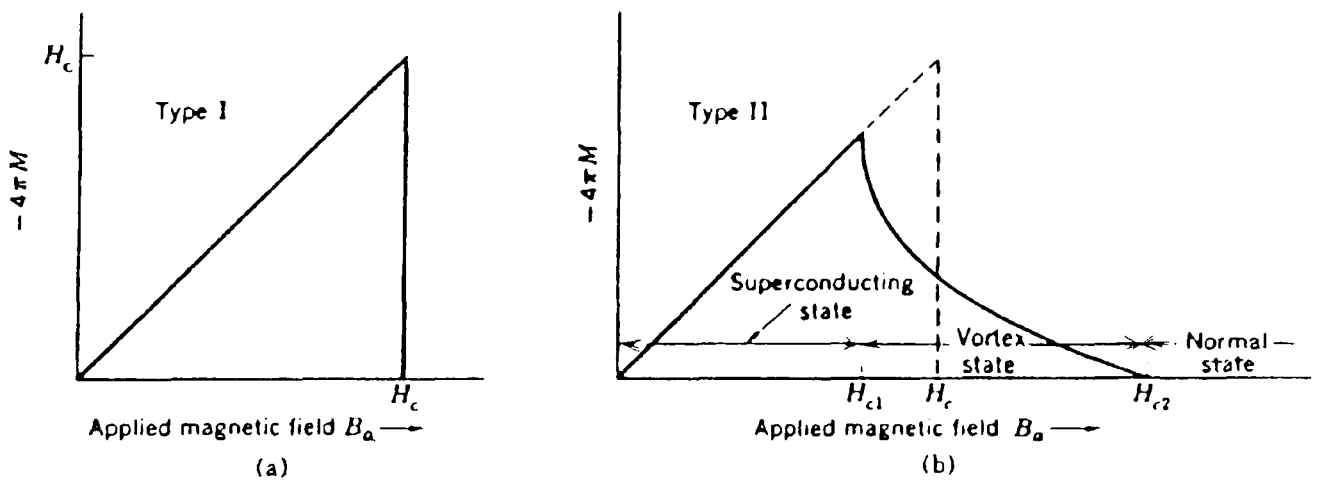

Figure 1.1: Schematic diagram illustrating type I and type II superconductivity (after [Kittel 1976])

- The zero resistance is destroyed by the application of magnetic fields when the flux density exceeds a critical value H_c for type I superconductors or H_{c2} for type II superconductors.

Except for the obvious advantage of zero electrical resistance below Tc over other materials, superconductors can provide devices and circuits with performance not obtainable from any other known technology due to their unique properties. [Nisenoff 1988].

Studies in the 1920's and 1930's found that metallic alloys and compounds could exhibit higher T_c than elements. For many years the record for the highest superconducting transition temperature remained 23.2K, which was achieved in 1973 for niobium-germanium thin films near the stoichiometric composition Nb_3Ge [Gavaler 1973]. Then suddenly the discovery of superconductivity above 30K by

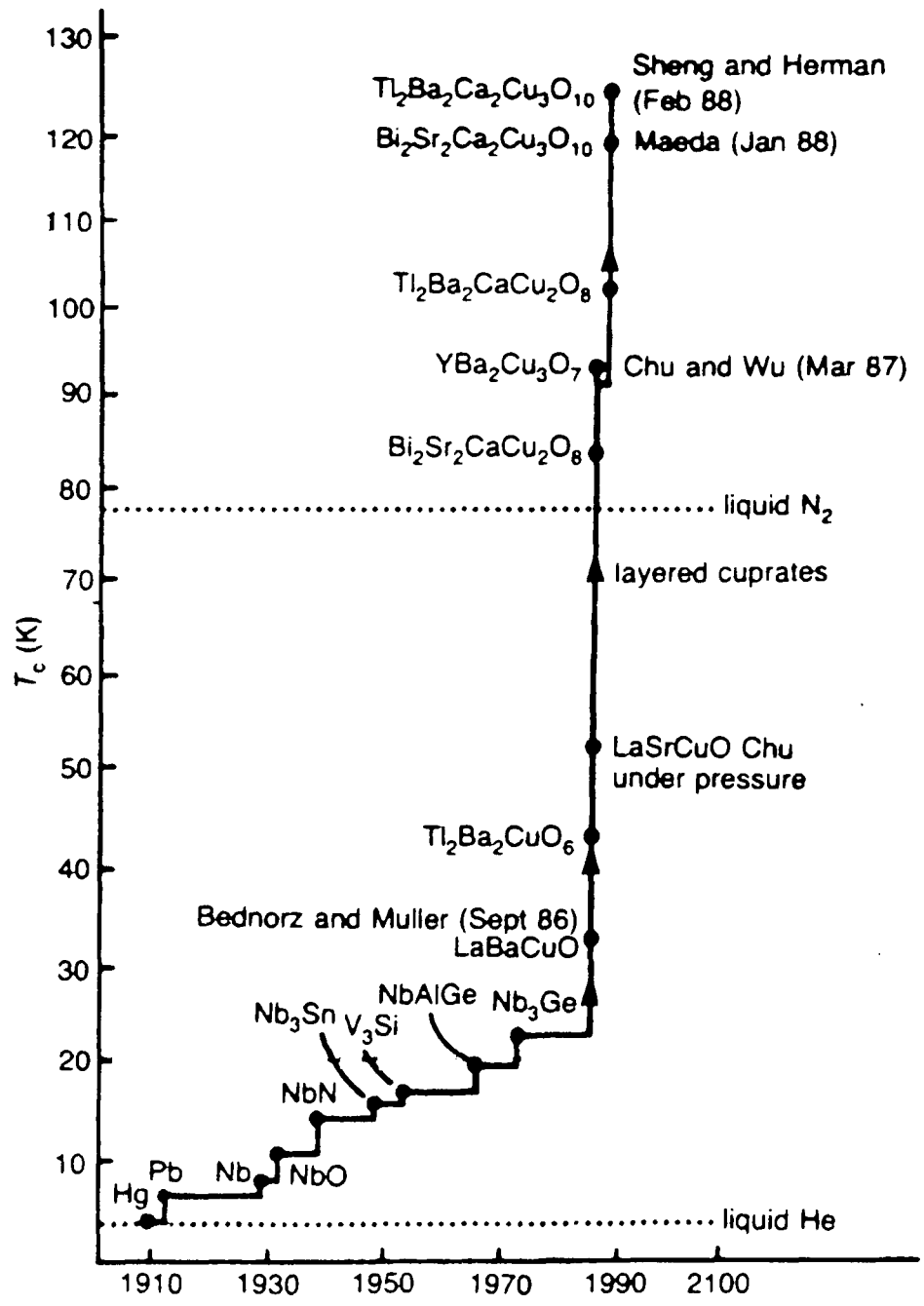

Figure 1.2: A brief T_c development history of the superconductors (after [Gough 1991])

Bednorz and Muller in the lathanum copper oxide system in 1986 [Bedorz 1986] launched an exciting race to increase the transition temperature of the high Tc superconductors. Since then the critical temperature has been raised to 90K in $Y_1Ba_2Cu_3O_7$, 110K in Bi-based copper oxides and 125K in Tl-based copper oxides (Fig. 1.2) [Gough 1991].

The discovery of new classes of ceramic superconductors with transition temperatures above the boiling point of liquid nitrogen (77K) has opened the doors for many applications. Reaching liquid nitrogen temperatures is quite cheap compared with cooling to 4K and is an affordable temperature in current technology. Energy storage, magnetic shielding, and sensitive detection of electromagnetic radiation are some of the possible applications.

It is not surprising that another race has been on to produce the materials, improve the properties and exploit the practical applications for the high Tc superconductors. The application of high Tc superconductors is highly dependent on the existing processing techniques, and one of the most important things needed is understanding and engineering the interfaces of high Tc superconductors with other materials: metals, semiconductors, or insulators.

The aim of the work reported in this thesis was to design, fabricate and test novel contact technologies for high T_c superconducting ceramics, with especial interest in determining the conduction mechanisms at metal/superconductor interfaces.

1.2 Phases and Phase diagrams

Compared with the Bi-based and Tl-based superconducting oxides for which we know little more than the structure and compositions of the compounds (Table 1.1), phase relations in the $YBa_2Cu_3O_X$ system have been studied more closely. Many papers have been published concerning these phase relations [Roth 1987, Frase 1987, de Leeuw 1988 and Lee 1991]

$Bi_2Sr_2Ca_{n-1}Cu_nO_{2n+4}$

Bi	Sr	Ca	Cu	Tc(K)
2	0	1	1	20
2	2	0	1	70
2	2	1	2	90
2	2	2	3	110

$TlBa_2Ca_{n-1}Cu_nO_{2n+3}$

Tl	Ba	Ca	Cu	Tc(K)
1	2	0	1	<17
1	2	1	2	91
1	2	2	3	116
1	2	3	4	122
1	2	4	5	<120

$Tl_2Ba_2Ca_{n-1}Cu_nO_{2n+4}$

Tl	Ba	Ca	Cu	Tc(K)
2	2	0	1	80
2	2	1	2	110
2	2	2	3	128
2	2	3	4	102

Table 1.1: Superconducting phases in the Bi- and Tl- based superconducting oxides [Dew-Hughes 1988]

The thermodynamic or subsolidus phase diagram of the ternary Y-Ba-Cu oxide system is illustrated in Fig.1.3 [de Leeuw 1988]. The phases which have been observed in the system at 1223K are: the end point oxides - Y_2O_3, BaO, and CuO; the binary oxides - Ba_3CuO_4, Ba_2CuO_3, $BaCuO_2$, $Y_2Cu_2O_5$, $Y_4Ba_3O_9$, Y_2BaO_4 and $Y_2Ba_4O_7$; the ternary oxides - $Y_1Ba_4Cu_3O_{8.5+d}$, $Y_3Ba_8Cu_5O_{17.5+d}$, $Y_1Ba_5Cu_2O_{8.5+d}$, $Y_1Ba_2Cu_3O_{6.5+d}$ and $Y_2Ba_1Cu_1O_5$. Those ternary oxides are marked as 143, 385, 152, 211 and 123.

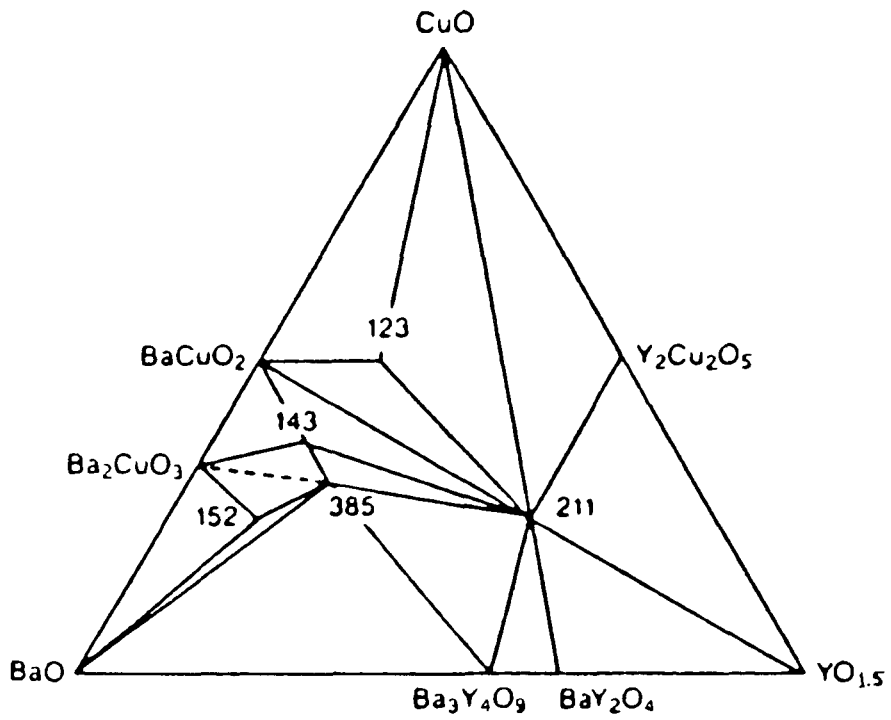

Figure1.3: Ternary phase diagram of the Y_2O_3-BaO-CuO system at 1223K

Two sections of the thermodynamic calculated phase diagram of the system are illustrated in Fig1.4 and 1.5 [Lee 1991].

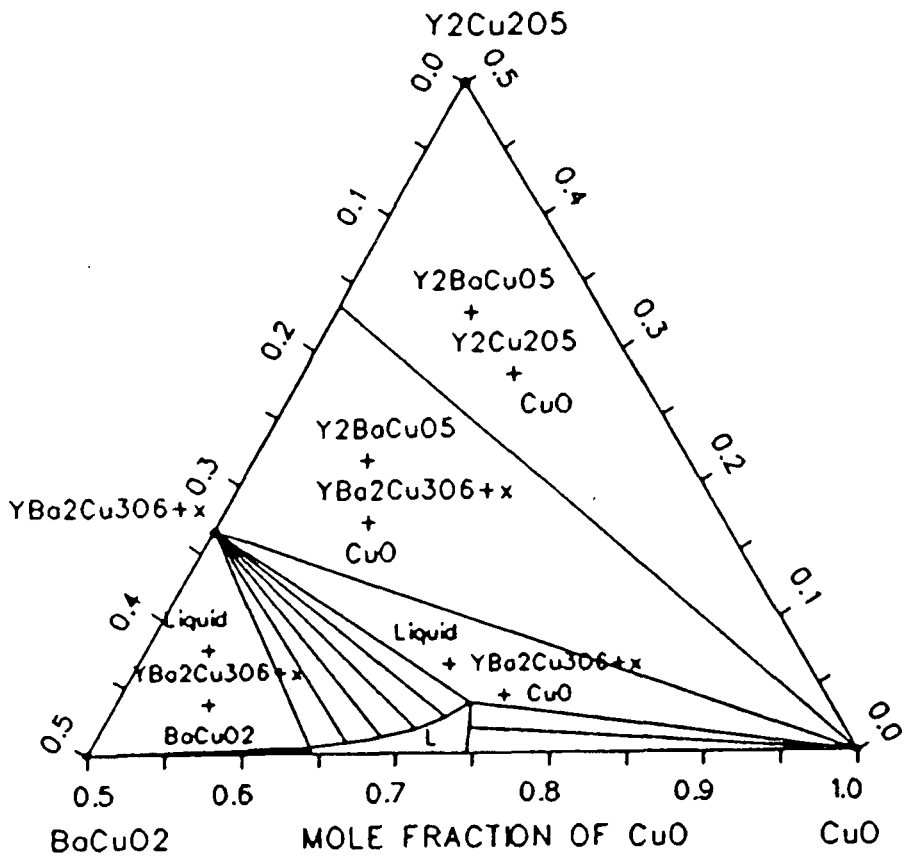

Figure 1.4: Calculated isothermal section of the Y_2O_3-BaO-CuO system at 1223K.

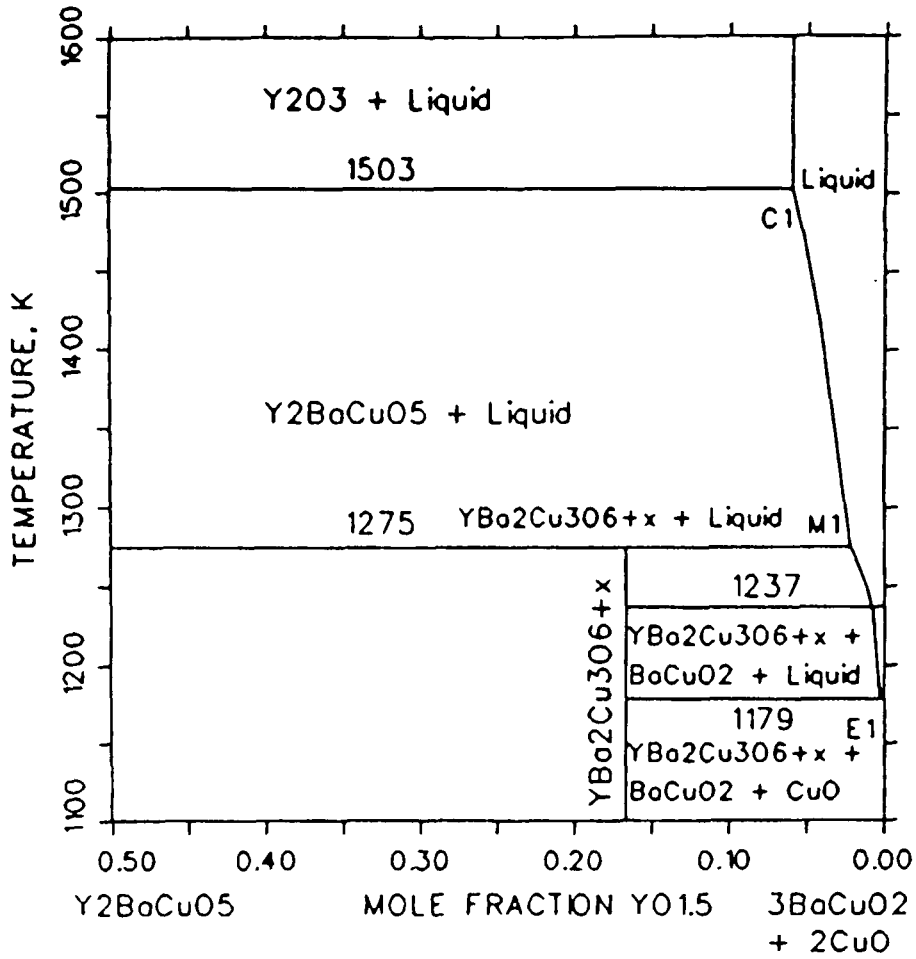

Figure 1.5: Calculated vertical section of the Y_2O_3-BaO-CuO system at 0.21atm oxygen.

These phase diagrams provide a useful tool to understand the existence range of the 123 superconducting phase and its relation with other phases, and to design the heat treatment, crystal growth and other material processing procedures to prepare pure phase superconducting materials.

1.3 Structure, oxygen nonstoichiometry and superconductivity

The cuprate high T_c superconductors all contain stacked perovskite blocks with CuO planes, and there is some relation between the number of CuO planes and the superconducting transition temperature. In general, T_c increases as the number of CuO planes in the unit cell increases from 1 to 3, however further increasing the number of CuO planes causes the decrease of Tc [Hervieu 1989].

The $YBa_2Cu_3O_{7-x}$ superconductor has the formula $YBa_2Cu_3O_7$ (x=0) in its fully oxidized form, and $YBa_2Cu_3O_6$ (x=1) in its oxygen reduced form. The structure of the $YBa_2Cu_3O_{7-x}$ system has been comprehensively studied [Jorgensen 1987] and is very well understood. The $Y_1Ba_2Cu_3O_{7-x}$ structure is a layer structure

accommodated in a triple perovskite unit cell.

The ideal perovskite structure is shown in Fig.1.6. The diagrammatic representation of the general lattice of $Y_1Ba_2Cu_3O_{7-x}$ is shown in Fig. 1.7.

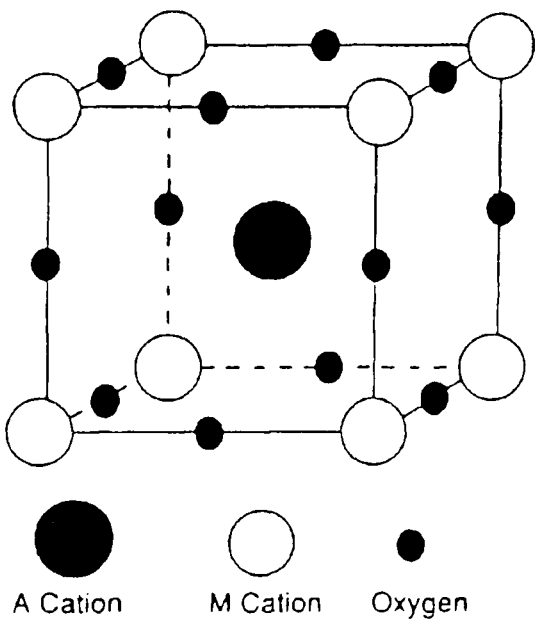

Figure 1.6: Ideal perovskite structure unit cell

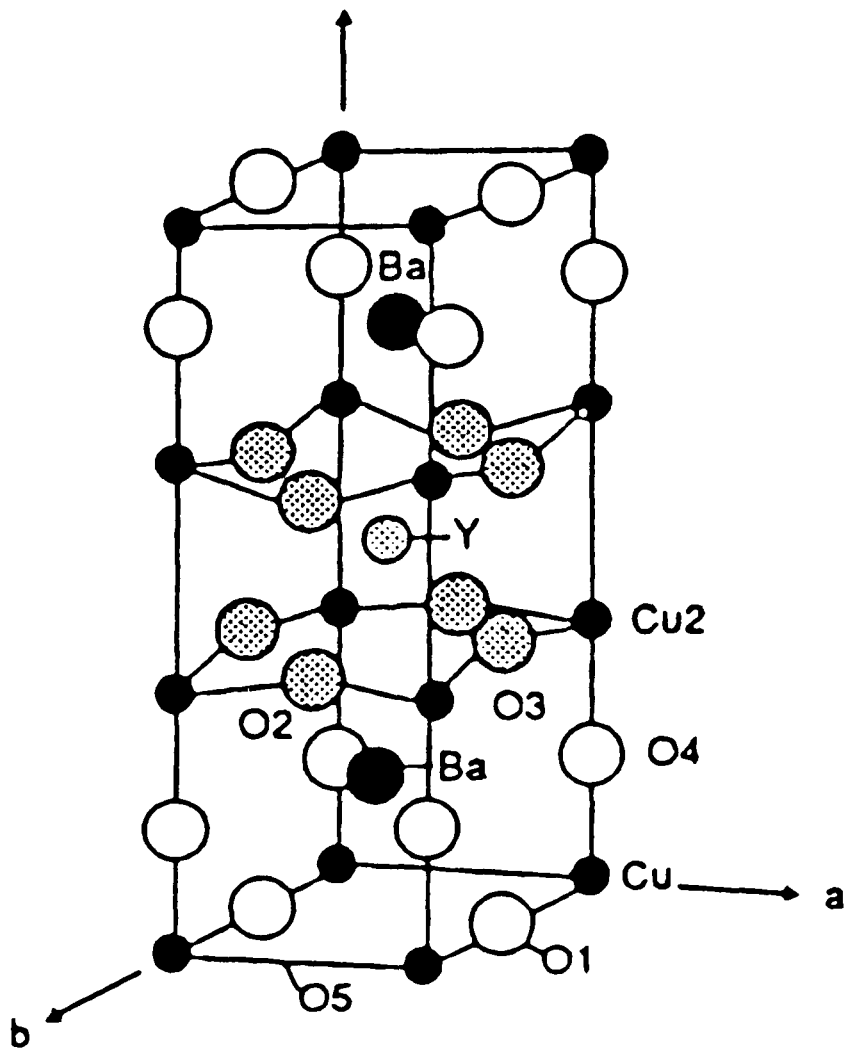

Figure 1.7: The structure of $Y_1Ba_2Cu_3O_{7-x}$

The structure of the $Y_1Ba_2Cu_3O_{7-x}$ superconductor deviates from the ideal triple perovskite cell, the oxygen vacancies always occur on the vertical edges of the yttrium cube, leaving the (Cu_2) atoms five-fold co-ordinated (Fig.1.6 & 1.7). At low oxygen content (high values of 'x'), the tetragonal structure is adopted, in which the basal plane oxygen sites, (O_1) and (O_5), are vacant; At high oxygen content (low values of 'x'), orthorhombic structure is adopted, in which the basal plane oxygen sites (O_1) are partially filled to different extents. At 'x'=0, the (O_1) sites have become completely occupied along the 'b' axis, and the (O_5) sites are vacant along the 'a' axis.

Tetragonal oxygen deficient $YBa_2Cu_3O_{7-x}$, typically at x=1, has a structure with unit cell a=b=3.862Å, c=11.793Å, and is a semi-conductor (Fig.1.8a). Orthorhombic oxygen rich $YBa_2Cu_3O_{7-x}$, typically at x=0, has a structure with unit cell a=3.825Å, b=3.883Å and c=11.680Å (Fig.1.8b). This orthorhombic structure is metallic down to its T_c in the region of 93K.

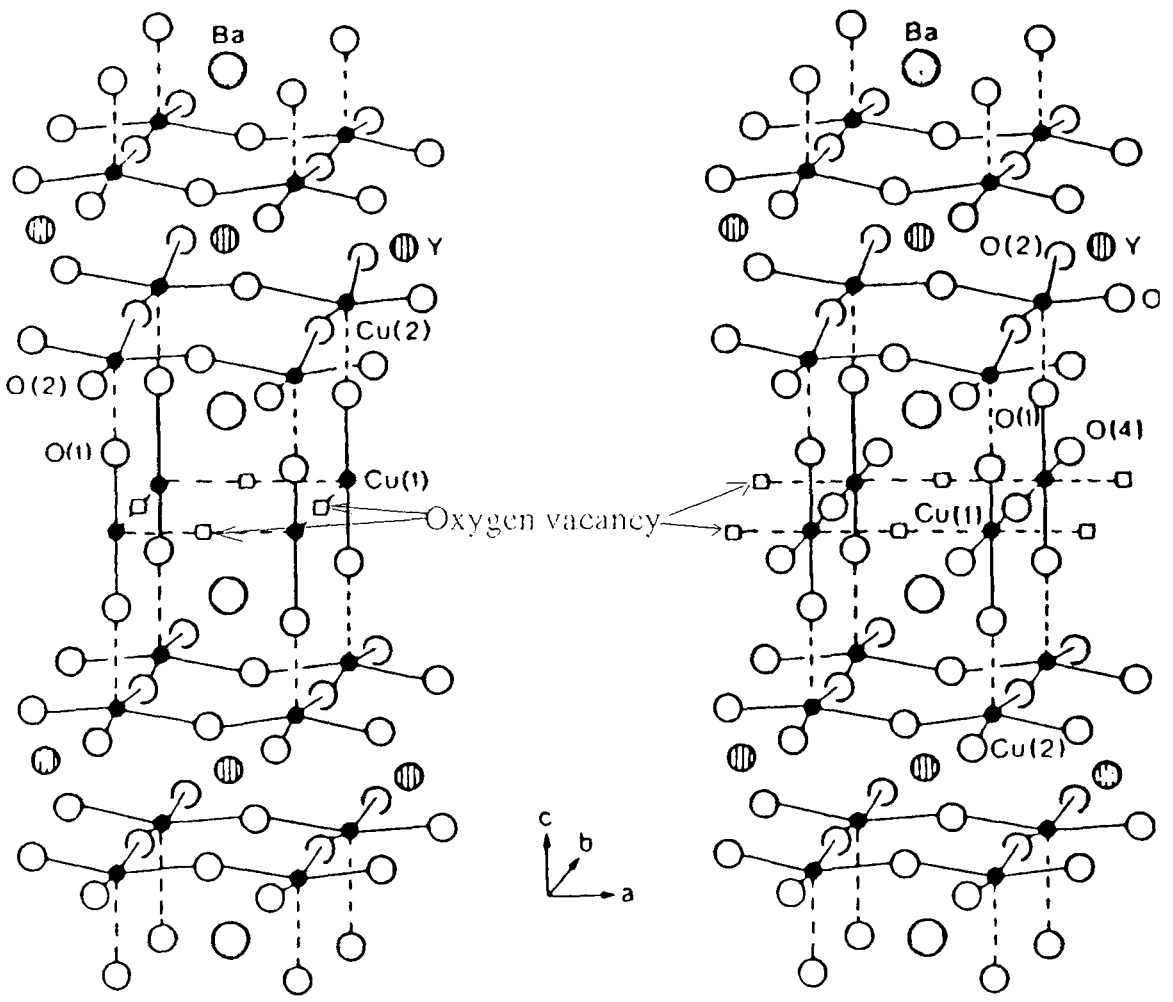

(a) (b)

Fig.1.8: Structure of (a) tetragonal $YBa_2cu_3O_6$ and (b) orthorhombic , ideal $Y_1Ba_2Cu_3O_7$. (after [Swinnea 1987 and David 1987])

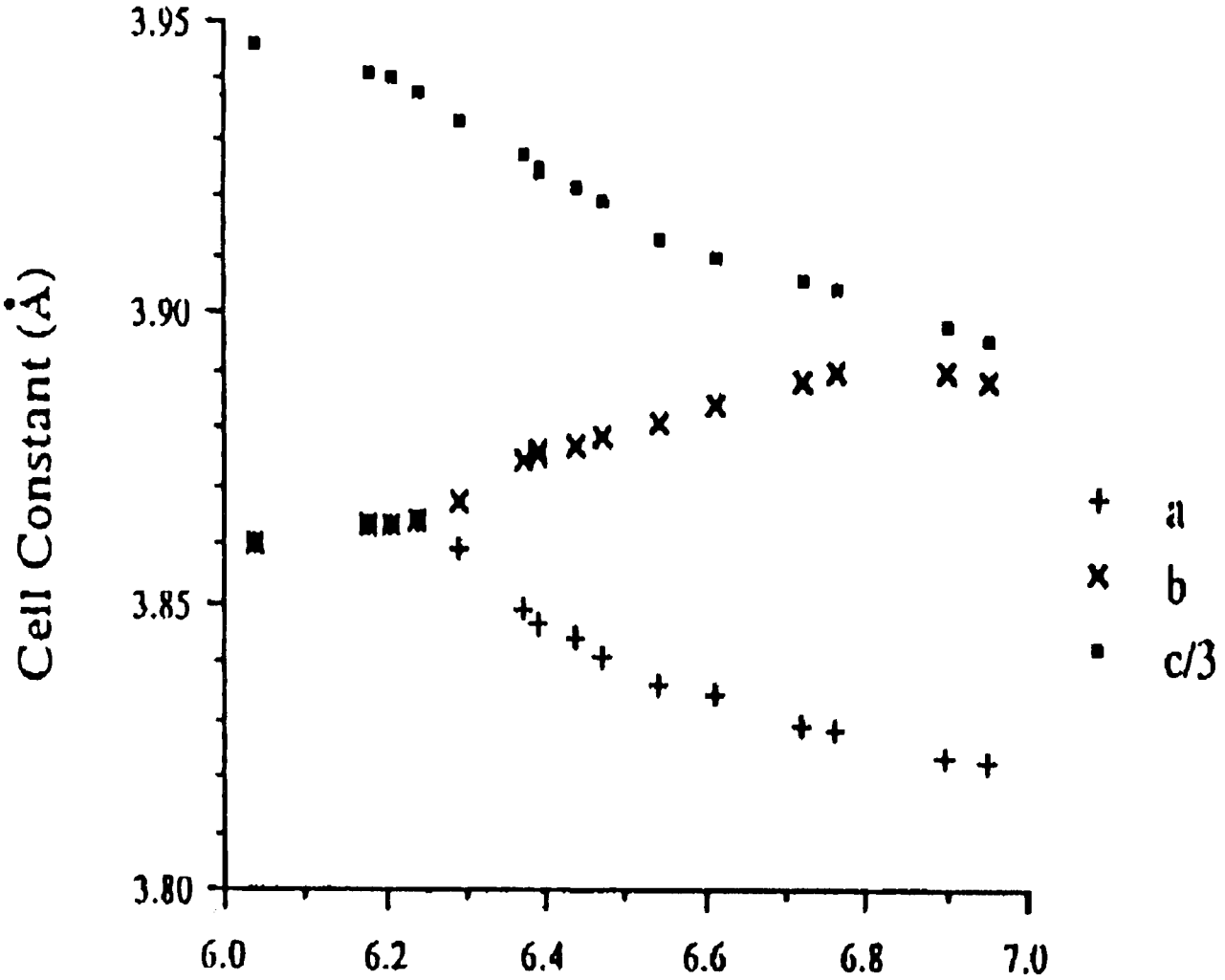

[7-x]

Figure 1.9: Various of lattice parameters with oxygen concentration in the system $Y_1Ba_2Cu_3O_{7-x}$ (after [Manthiram 1987])

The transition from orthorhombic structure to tetragonal structure happens at about x=6.4 by an expansion in the c axis and the disappearance of the difference between the a and b lattice parameter (Fig.1.9) [Manthiram 1987].

The temperature at which the tetragonal - orthorhombic transition occurs is reported to vary considerably in the literature, 873K [O'Bryan 1987], 949K [Specht 1988]. The tetragonal - orthorhombic transition depends on both temperature and the oxygen pressure. This will be further discussed in chapter 2.

The changes in the oxygen stoichiometry affect both the electronic properties of the normal state superconductor and the superconducting properties (T_C) (Fig.1.10 & 1.11).

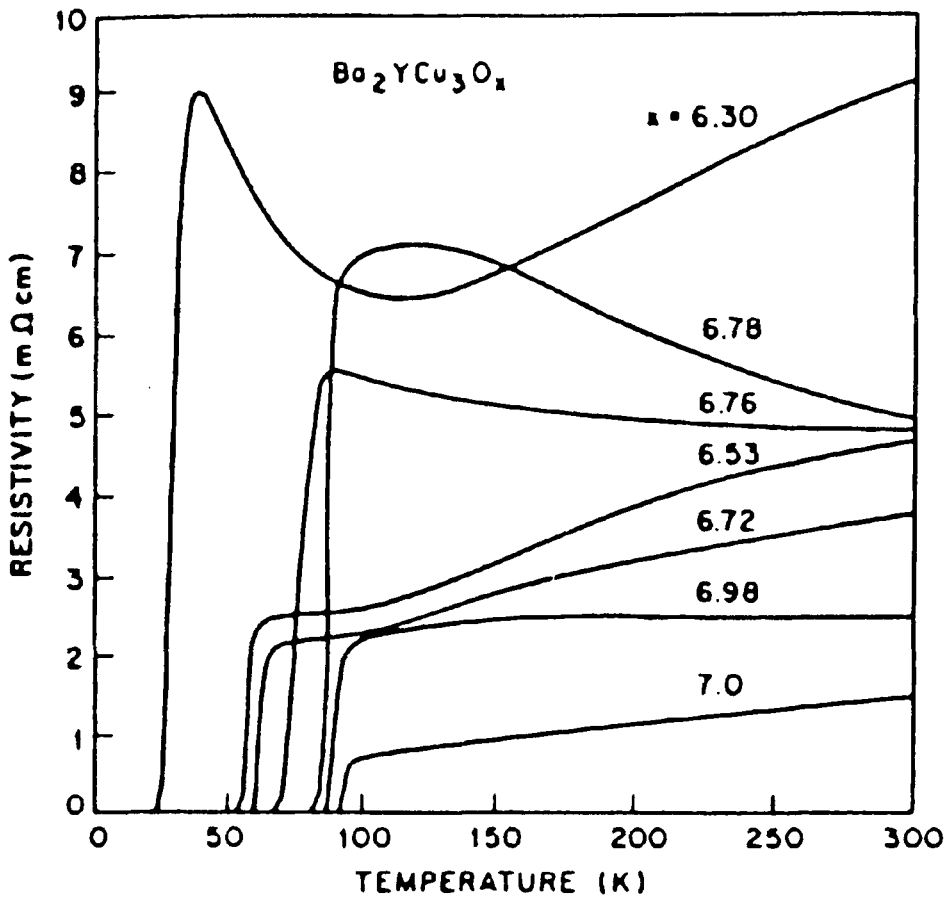

Figure 1.10: Resistivities of sintered $YBa_2Cu_3O_x$ Samples [Phillips 1989].

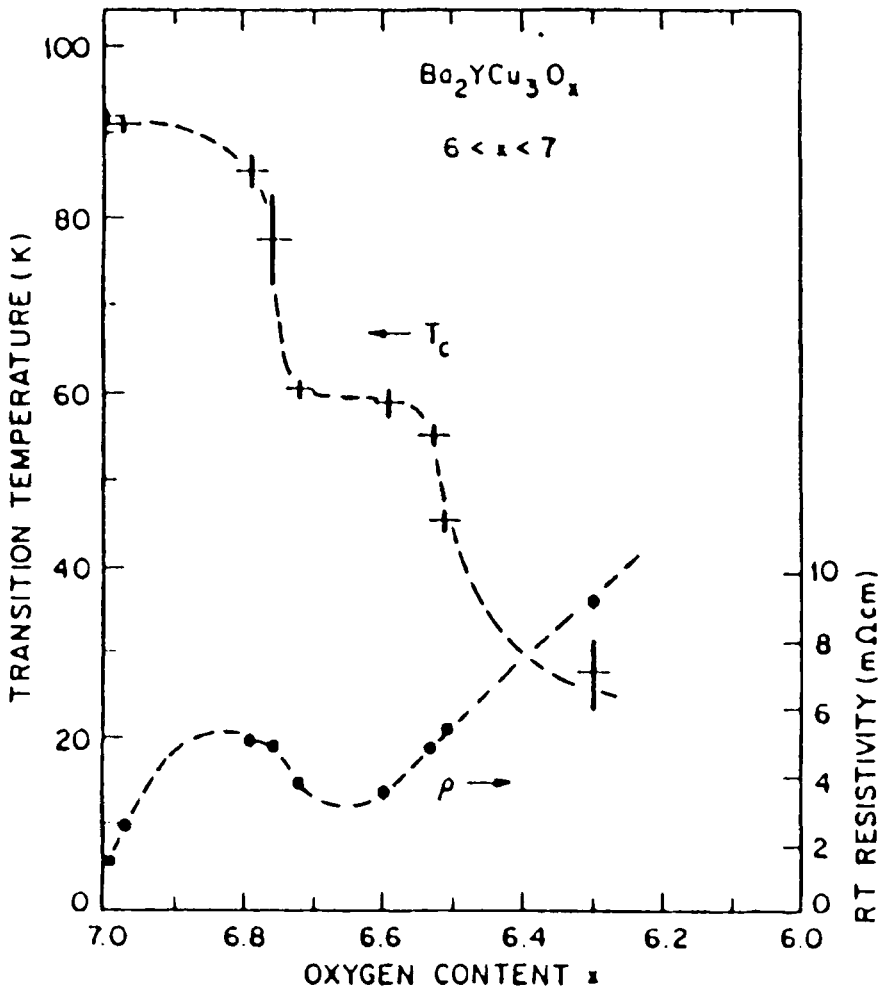

Figure 1.11: Variation of T_c and normal state resistivity ρ with oxygen concentration [Cava 1987].

In Fig.1.10 and 1.11, as the oxygen content changes from 7 to 6.3, the normal state electrical resistivity increases dramatically from 10^{-3} to 10^{-2} Ohm·cm, and the superconducting transition temperature of $YBa_2Cu_3O_{7-x}$ changes from about 90K to 0K. This sensitivity of the superconducting properties to the oxygen nonstoichiometry state induces lots of problems for applications.

There is no evidence that the $YBa_2Cu_3O_{7-x}$ phase exists at $x<0$ or $x>1$ [Sleight 1988]. If the sample is subjected to high oxygen activity, the $YBa_2Cu_3O_x$ superconducting phase is not stable, and the system will decompose into other phases involving $YBa_2Cu_{3.5}O_{7-x}$ (123.5) or $YBa_2Cu_4O_8$ (124) superconducting compounds. If the sample is subjected to low oxygen pressure, the $YBa_2Cu_3O_x$ superconducting phase is not stable either, and the system will decompose into various compounds including the Y_2BaCuO_5 (211) phase. The detailed interaction of superconductor and oxygen will be discussed in chapter 2.

At present, little is known about the concentration of oxygen vacancies in the bismuth and thallium compounds although there have been reported that Tc and Jc may be enhanced by annealing samples in oxygen [Wada 1988, Cava 1988, Deluca 1991]. In general, they show relatively weak oxygen stoichiometry variation with little effect on Tc, compared with the $YBa_2Cu_3O_{7-x}$ phase, but the oxygen activity is a common key factor during synthesis and heat treatment.

1.4 Microstructure

Twinning occurs in the $YBa_2Cu_3O_{7-x}$ superconductor during the transition from a tetragonal structure (high temperature/low oxygen content) to an orthorhombic structure (low temperature/high oxygen content). In the orthorhombic structure, a and b axes are no longer the same length, as shown in Fig1.8. This loss of symmetry will always result in some areas of the crystal having a and b directions reversed in relation to other areas. Twinning is prolific in the $YBa_2Cu_3O_{7-x}$ superconductor to accommodate the transformation strains produced by the tetragonal to orthorhombic

transition when the basal plane accommodates extra oxygen. The twins provide an easy way to identify the superconducting orthorhombic structure in $YBa_2Cu_3O_{7-x}$, and indicate when a sample contains the optimum oxygen content.

Another common feature of the bulk high Tc superconductors is that the porosity of the ordinary sintered bulk samples is often high. The density of conventionally processed material is only 75% of the theoretical density, and pores and impurity phases at grain boundaries are the major factor limited the critical current density of the bulk samples. This porosity is also a problem for contact resistivity studies. It has been found that the contact metals diffuse into the superconductor and fill pores [Hollin 1990]. A similar effect with different contact materials has also been observed [Caton 1990]. The actual contact areas are then much larger than the apparent contact area at the surface, and it is difficult to measure the exact contact area even by destroying the sample to observe a cross section of the interface. The error in contact area measurement will result in errors in the value of the contact resistivity. The details of this error will be discussed in chapters 3 and 9.

1.5 Practical application of high Tc superconductors

The high degree of excitement over high Tc superconductors is certainly because of the potential scientific and commercial importance. However, there are several problems with applying these materials in practical devices, the most important one being the poor critical currents in sintered ceramic samples. There are other technologies which will have to be developed once the critical current densities have been improved.

Most superconductor devices require a normal metal electrical contact to superconductor. The metal overlayers on top of the superconductors are also required to combine a parallel current path for the normal-state superconductor when the critical currents are exceeded locally with environmental protection of the reactive superconductor, and to provide mechanical and thermal support.

1.5.1 Critical current density

One of the obstacles to develop applications of the high Tc superconductors is the low critical current density (Jc) of the bulk polycrystalline materials, with a typical figure 10^2 A/cm^2 (Fig.1.12). This is due to the presence of very weakly coupled superconducting regions at grain boundaries. Since the intragranular current density is large even at 77K, it is natural to think of using a melt texturing method to align the grains and improve the connection between grains. It has been reported that the critical current density (Jc) can be greatly improved by developing a melt texturing technique for bulk $YBa_2Cu_3O_{7-x}$ samples [Jin 1987, Jin 1988, Murakami 1989 and Murakami 1990].

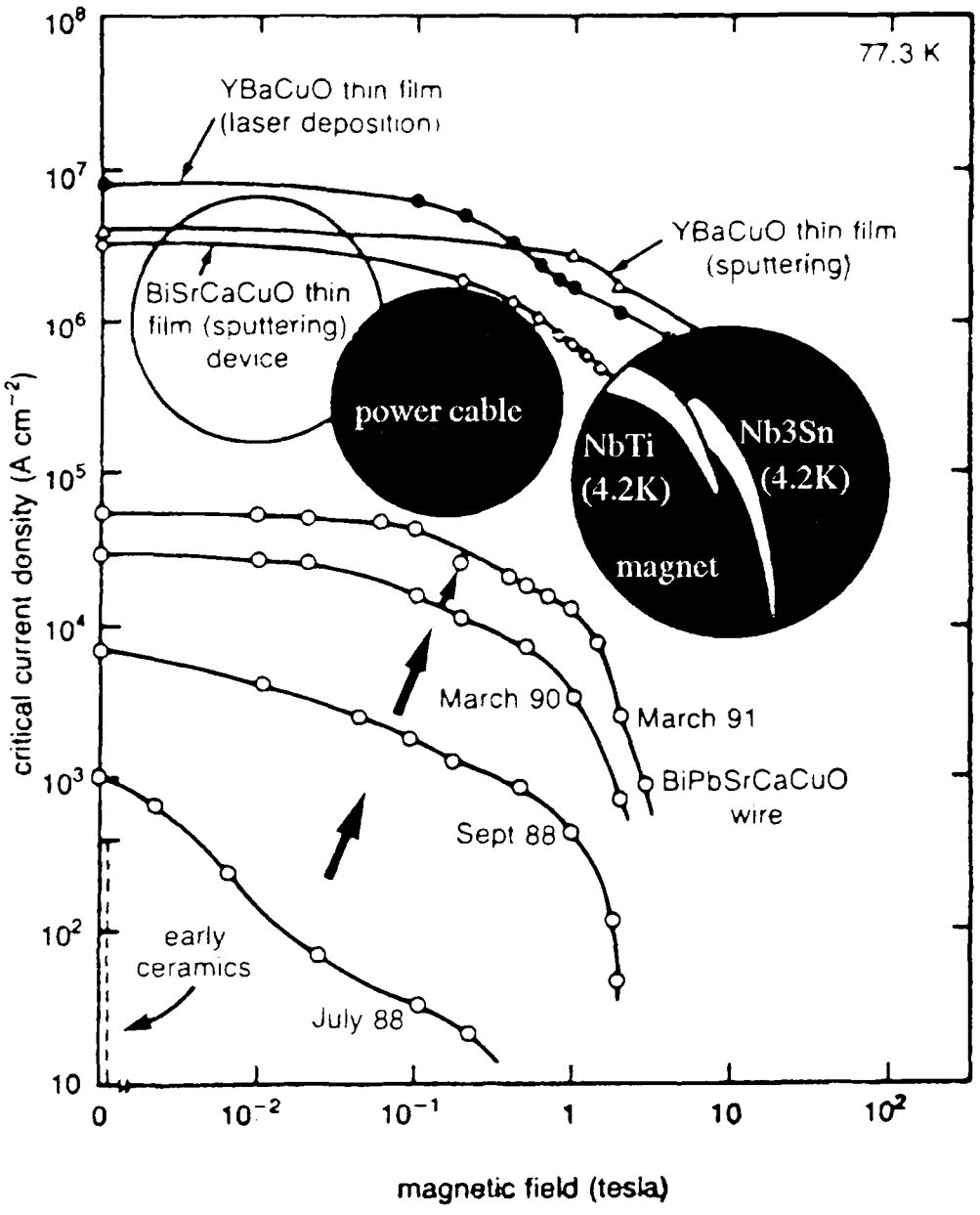

Figure1.12: Jc development in superconductors.(after[Gough 1991])

1.5.2 Environmental protection

The existing high Tc superconductors are especially famous for their instability in the ordinary laboratory environment. The $YBa_2Cu_3O_{7-x}$ phase decomposes to CuO, $Ba(OH)_2$, Y_2BaCuO_5 and oxygen in the presence of water [Yan 1987]. In the presence of CO_2 during sintering or heat treatment, the $YBa_2Cu_3O_{7-x}$ phase decomposes into various compounds: $BaCO_3$, CuO, $Y_2Cu_2O_5$ and Y_2BaCuO_5 [Gao 1990].

For unsheathed $YBa_2Cu_3O_x$ wires, the superconducting phase in the presence of both water and carbon dioxide in the atmosphere will decompose into hydroxides and carbonates of Ba and Y [Holland 1987], and deplete the surface concentration of Cu [Zandbergen 1988], so destroying the superconductivity.

Therefore, it is essential for the application of high Tc superconductors to have a metal overlayer to provide environmental protection.

1.5.3 Cryostabilization

The cryostabilization of a superconductor is a very severe test of superconductor to normal metal contacts. If a normal zone is produced in a current carrying superconductor, the current must be carried by a parallel and low resistivity normal metal. The contact resistivity between superconductor and metal must be very low to minimize the heat generated by high currents.

In commercial Nb-Ti and Nb_3Sn superconducting cables, the superconducting filaments are only few microns in cross section, and are in close electrical contact with parallel conducting paths of Cu or Al. Thus, any current flow which drives the superconductor normal during a temporary instability is shorted.

For the composites of high Tc superconducting oxide and a metal stabilizer with high electrical conductivity, the contact making has been proved to be difficult. The contact resistivity values may be now good enough for the material with critical current density achieved in Y-Ba-Cu-O bulk samples, but when the current density in the oxide superconductor corresponds to that in the practical metallic one, the

electrical contact must be improved for cryogenic stability [Funaki 1991].

1.5.4 Reliable, low - resistance contacts

As having been discussed above, the cryostabilization of a practical superconductor wire requires low contact resistance metal overlayers. In addition, contact resistances are often so poor that contact heating often limits the measurement of critical current in bulk samples at low temperature and low fields [Cava 1987].

Low-resistivity and stable electrical contacts to superconductors are required in many cases for the large-scale low-power applications such as bulk and thin film superconductor devices, and also for high power applications like power transport. Practical use of the high temperature superconducting material will require a substantial improvement of the contacts between superconducting and normal conducting material to connect the superconductors to the normal-conducting world.

The contact resistance for a superconducting Nb_3Sn power cable at 4.2K has already been improved to 10^{-8}-10^{-11} Ohm·cm^2 [Forsyth 1973, Luderer 1974 Leupold 1976, Blaugher 1982, and Waldram 1989], which is close to the experimental sensitivity limit. However, in the field of high Tc superconductors the development of high-quality contacts has been proved to be much more difficult. Because of the chemical instability of the surface of $YBa_2Cu_3O_{7-x}$, the superconductor surface is often degraded during the contact making procedure, and it is difficult to obtain good electrical contacts. This fact has serious implications when considering possible applications of the superconductors, especially in electronics.

We shall see from chapter 3 that the choice for the contact metals is quite limited due to the sensitivity of the high Tc superconducting properties to its oxygen nonstoichiometry.

Chapter 2

Interaction of superconducting $YBa_2Cu_3O_{7-x}$ and oxygen

The properties of the $YBa_2Cu_3O_{7-x}$ superconducting ceramic are determined by the crystal structure and oxygen content. The oxygen content in the high Tc superconductor is extremely unstable, both temperature and oxygen pressure have strong influences on it. This sensitivity of the superconducting properties to the oxygen nonstoichiometry induces many problems for applications. For a good superconducting ceramic it is necessary to have an orthorhombic structure with the oxygen stoichiometry as close to 7 as possible. Even though the importance of the oxygen stoichiometry has been recognized, control and measurement of the oxygen content are difficult. In order to obtain the correct oxygen content and crystal structure, it is normally necessary to subject the material to a high temperature annealing in which the temperature and oxygen pressure must be controlled in order to avoid oxygen loss and prevent the formation of second phase material. Knowledge of the $YBa_2Cu_3O_{7-x}$ phase stabilization conditions and its phase relation with other compounds in the system under different oxygen pressure is of great importance to develop a reliable sample processing technology. A lot of work has been done on the kinetics of oxidation which involves the determination of the P-T-X diagram. These kinds of diagrams contain straight lines or curves which represent different oxygen stoichiometries at different temperatures and pressures.

2.1 $YBa_2Cu_3O_{7-x}$ under low oxygen pressure

Krebs et al [1988] found that annealing the sample in vacuum leads to an irreversible, diffusion controlled phase transformation from the orthorhombic superconducting phase to a semiconducting tetragonal structure. Chen et al [1991] found that lowering the oxygen pressure, followed by repeated temperature cycling even at very low temperature (20-180K), produced a continuous reduction in Tc to an value of 60K at 1mTorr. Reintroduction of air or O_2 immediately increased Tc.

Although any oxygen loss must be occurring at or near the surface (including internal surfaces such as grain boundaries), the surface modification must be occurring to a depth great enough to influence a four-point probe measurement of the bulk properties of the sample.

The interrelationship of X-P-T for the $YBa_2Cu_3O_{7-x}$ system at low oxygen pressure is shown in Fig.2.1 [Specht 1988], where X is the oxygen stoichiometry parameter, P is oxygen pressure and T is absolute temperature.

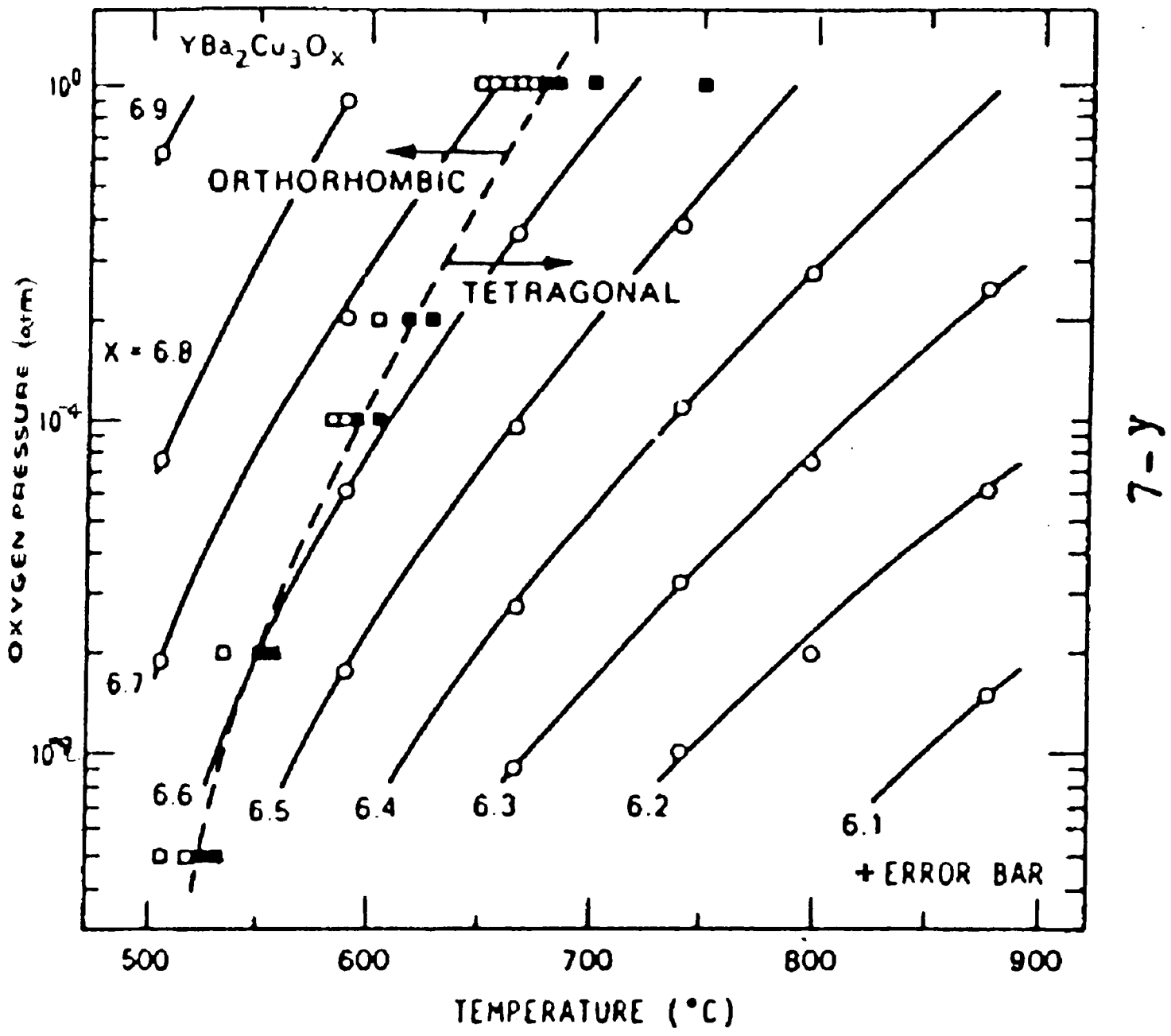

Fig.2.1: Relation of oxygen stoichiometry, oxygen partial pressure and temperature. (after [Specht 1988])

It shows that the equilibrium oxygen pressure must increase as the temperature increases in order to maitain the same oxygen stoichiometry. Kishio et al have

obtained similar results but presented them in another way (Fig.2.2) [Kishio 1987].

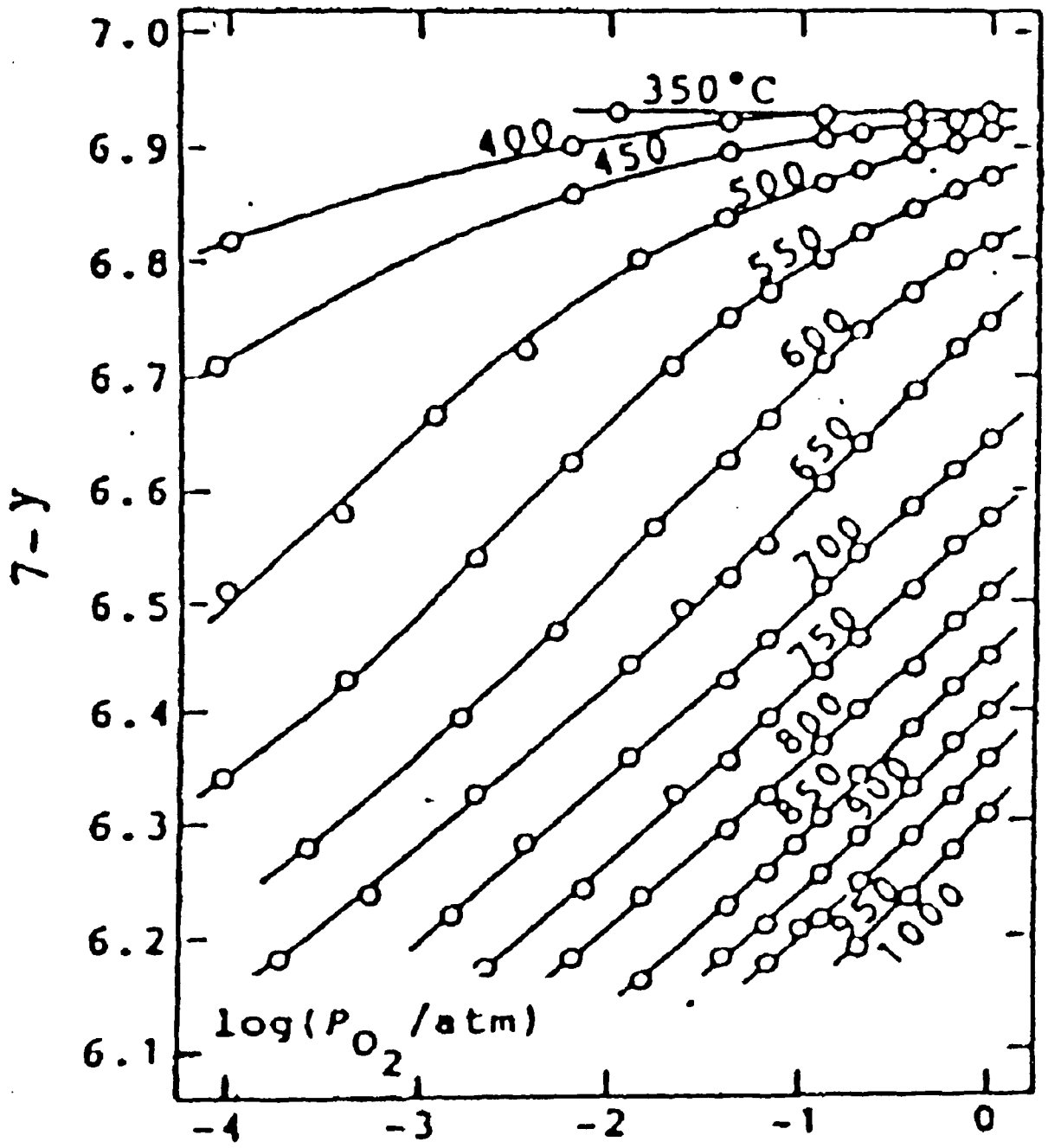

Fig.2.2: Relation of oxygen stoichiometry, oxygen partial pressure and temperature (after [Kishio et al 1987])

It is generally agreed that the oxygen stoichiometry of the superconductor ceramic will be low if the sample is treated at high temperature under low oxygen pressure, and the experimentally determined X-T-P diagrams are all in good agreement.

Further reducing the oxygen pressure, the phase relations in the YBCO system begin to change. Finally the $YBa_2Cu_3O_{7-x}$ phase becomes unstable and decomposes into other phases at about 10^{-4}atm oxygen pressure [Ahn, 1990]. Fig.2.3 shows how the phase relations change as the oxygen pressure decreases from 0.2 atm to 10^{-4}atm

at 850°C:

Fig. 2.3a represents the system's original state at 0.2 atm oxygen pressure (in air). The system starts its changes at $5.5*10^{-3}$ atm oxygen pressure: $YBa_2Cu_3O_{7-x}$ + $BaCuO_2$ +CuO=Liquid +O_2 (Fig.2.3b), then at $4*10^{-3}$ atm oxygen pressure cupric oxide is reduced to cuprous oxide, and the $YBa_2Cu_3O_{7-x}$-CuO tie line is replaced by the $YBa_2Cu_3O_{7-x}$-Cu_2O tie line (Fig.2.3c); At $3.0*10^{-3}$ atm oxygen pressure $BaCu_2O_2$ forms from $BaCuO_2$ and the liquid (Fig.2.3d); At $3.0*10^{-3}$ atm oxygen pressure the L-$BaCuO_2$ tie line is replaced by $YBa_2Cu_3O_{7-x}$-$BaCu_2O_2$ tie line (Fig. 2.3e); At $2.7*10^{-3}$ atm oxygen pressure, the Y_2BaCuO_5-$BaCuO_2$ tie line is replaced by the $YBa_2Cu_3O_{6+x}$-$YBa_3Cu_2O_{6+y}$ tie line(Fig.2.3f); At $1.5*10^{-3}$ atm oxygen pressure the liquid phase is no longer present on the phase diagram (Fig.(2.3g); At $1.0*10^{-3}$ atm oxygen pressure the $YBa_2Cu_3O_{6+x}$-Cu_2O tie line is replaced by the Y_2BaCuO_5 -$BaCu_2O_2$ tie line (Fig2.3h). At $7.0*10^{-4}$ atm oxygen pressure $YBa_2Cu_3O_{6+x}$-$BaCuO_2$ tie line is replaced by the $YBa_3Cu_2O_{6+x}$-$BaCu_2O_2$ tie line (Fig2.3i); Finally at $4.0*10^{-4}$ atm oxygen pressure, $YBa_2Cu_3O_{6+x}$ phase is not a thermodynamically stable phase and decomposes into Y_2BaCuO_5, $YBa_3Cu_2O_{6+x}$ and $BaCu_2O_2$ (Fig.2.3j).

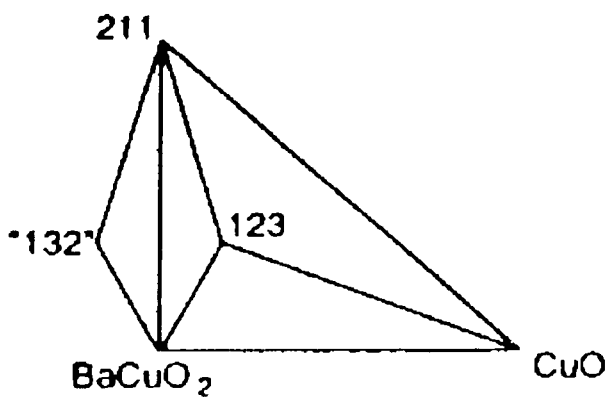

(a) Po_2=0.2 atm

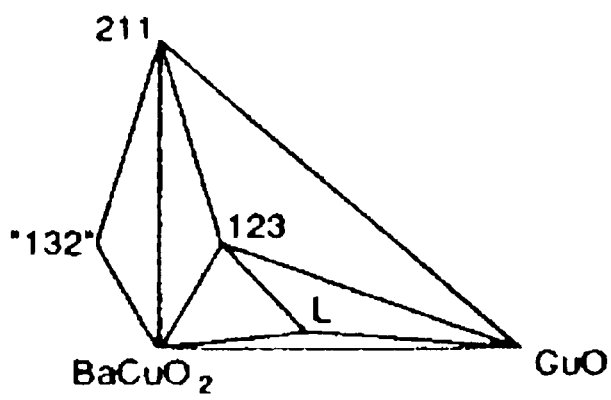

(b) $Po_2=5.5*10^{-3}$ atm

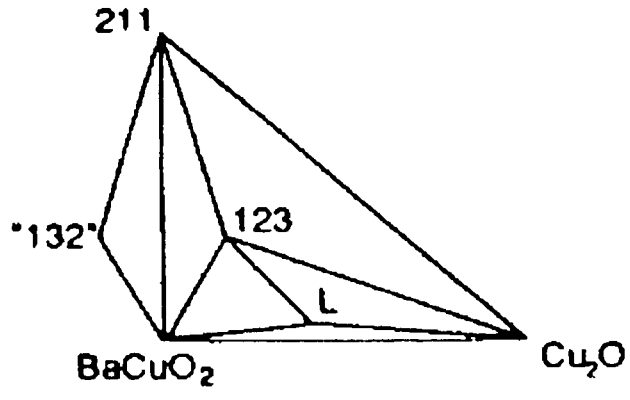

(c) $Po_2 = 4.0*10^{-3}$ atm

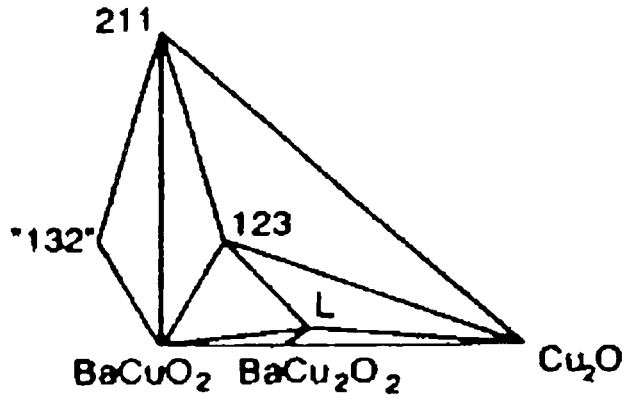

(d) $Po_2 = 3.0*10^{-3}$ atm

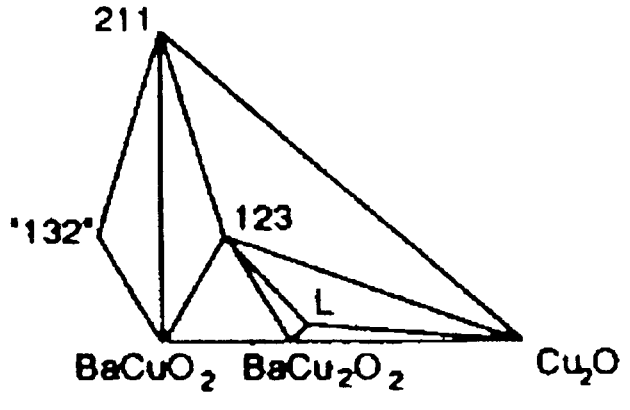

(e) $Po_2 = 3.0*10^{-3}$ atm

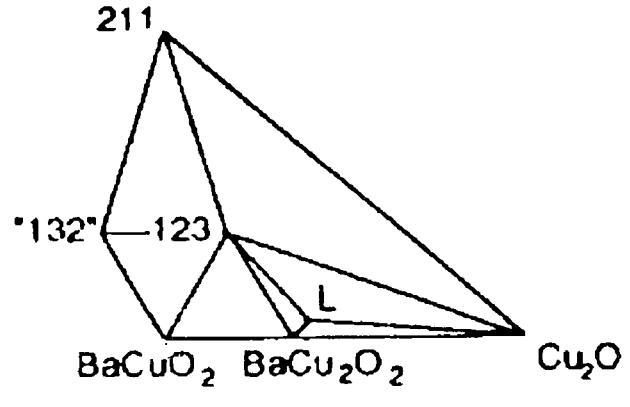

(f) $Po_2 = 2.7*10^{-3}$ atm

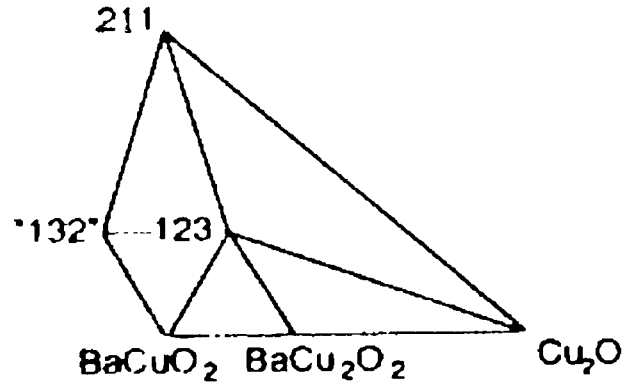

(g) $Po_2 = 1.5*10^{-3}$ atm

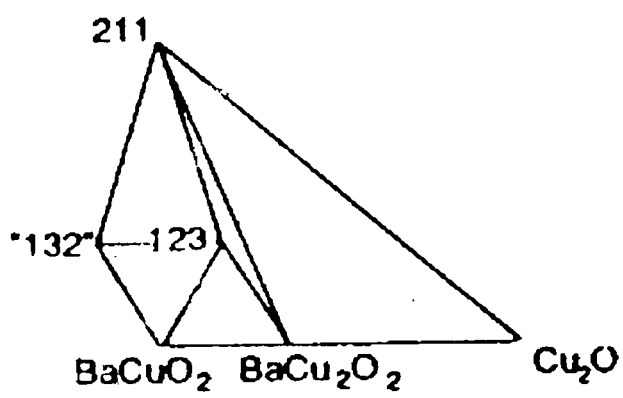

(h) $Po_2 = 1.0*10^{-3}$ atm

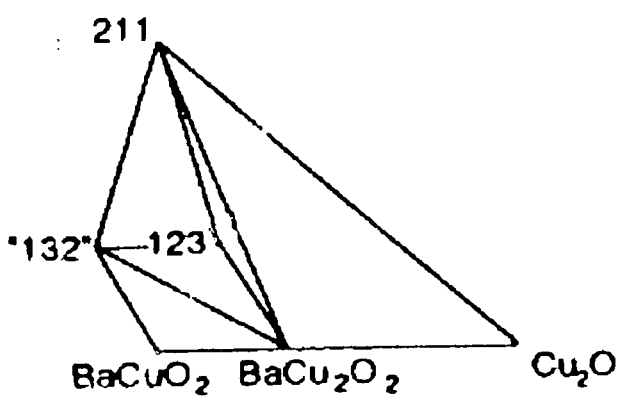

(i) $Po_2 = 7.0*10^{-4}$ atm

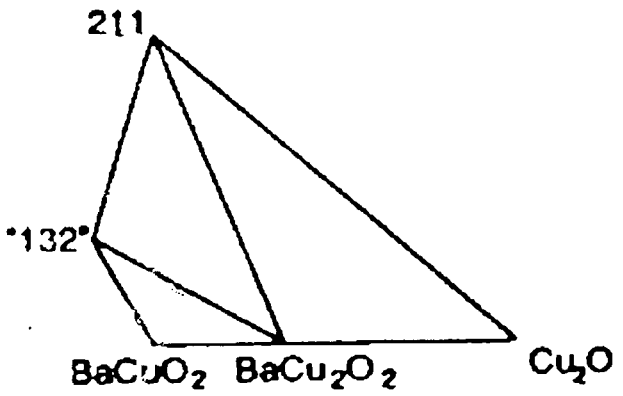

(j) $Po_2 = 4.0*10^{-4}$ atm

Fig. 2.3 Phase relation of $YBa_2Cu_3O_{7-X}$ at reduced oxygen pressure at 850°C (after [Ahn 1990])

2.2 $Y_1Ba_2Cu_3O_{7-d}$ under high oxygen pressure.

Karpinski et al [1988] found that there are two so-called decompositions in the $YBa_2Cu_3O_{7-x}$ superconductor under high oxygen pressure (Fig. 2.4). One is the strong decomposition - the transition from orthorhombic to tetragonal structure, represented by line DD'; The other is the slight decomposition - probably the transition from orthorhombic2 ($0.4 < x < 0.7$) to orthorhombic1 ($0 < x < 0.4$), represented by line EE'.

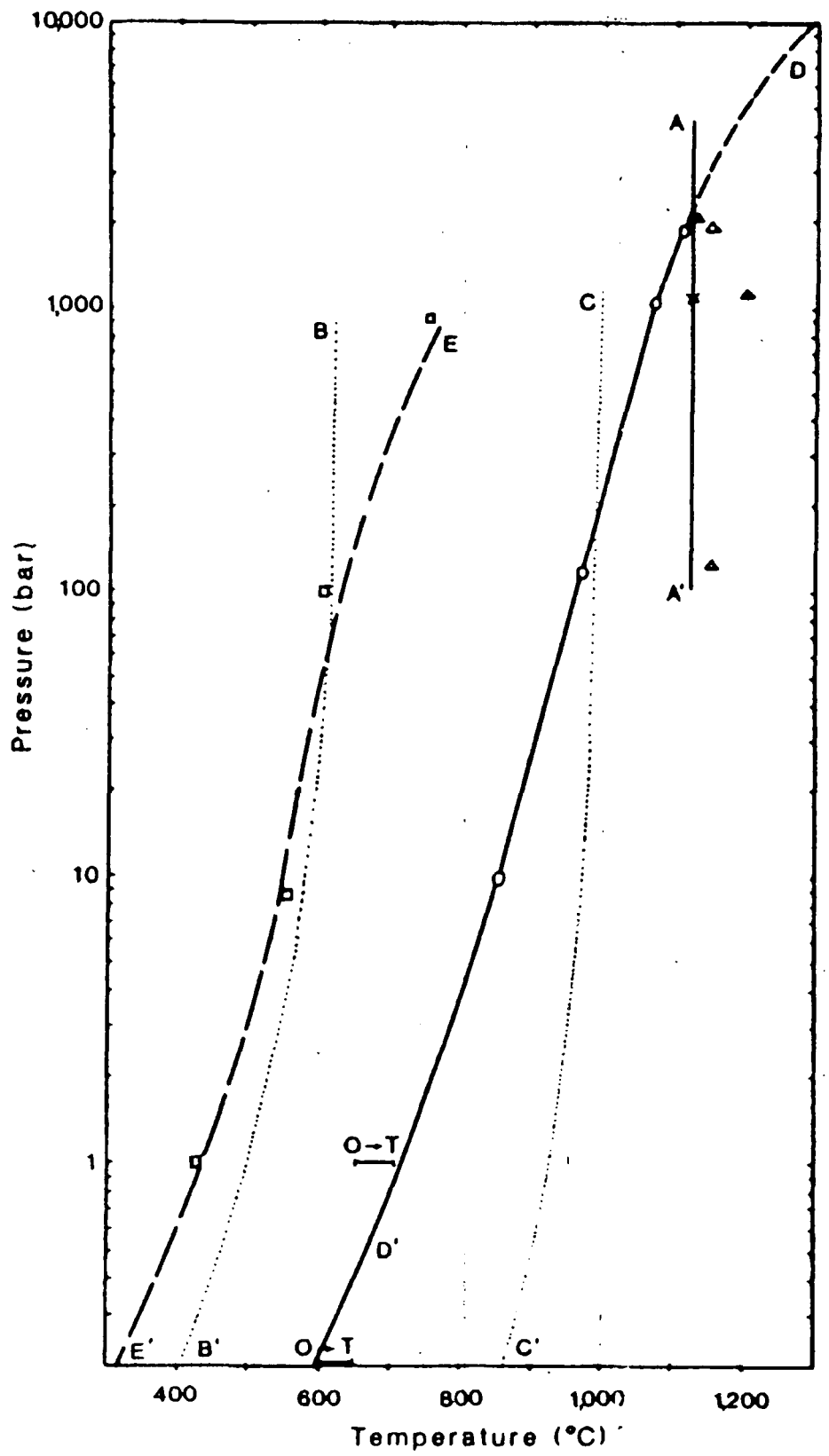

Figure 2.4: $Y_1Ba_2Cu_3O_{7-x}$ under high oxygen pressure (after [Karpinski et al 1988])

Gallagher et al [Gallagher 1987 and O'Bryan 1988] observed a similar result (Fig.2.5). The position of the orthorohmbic - tetragonal transition is clearly defined in this diagram. Although the oxygen stoichiometry of the sample may change with the temperature, the composition for the O-T transition is almost unchanged.

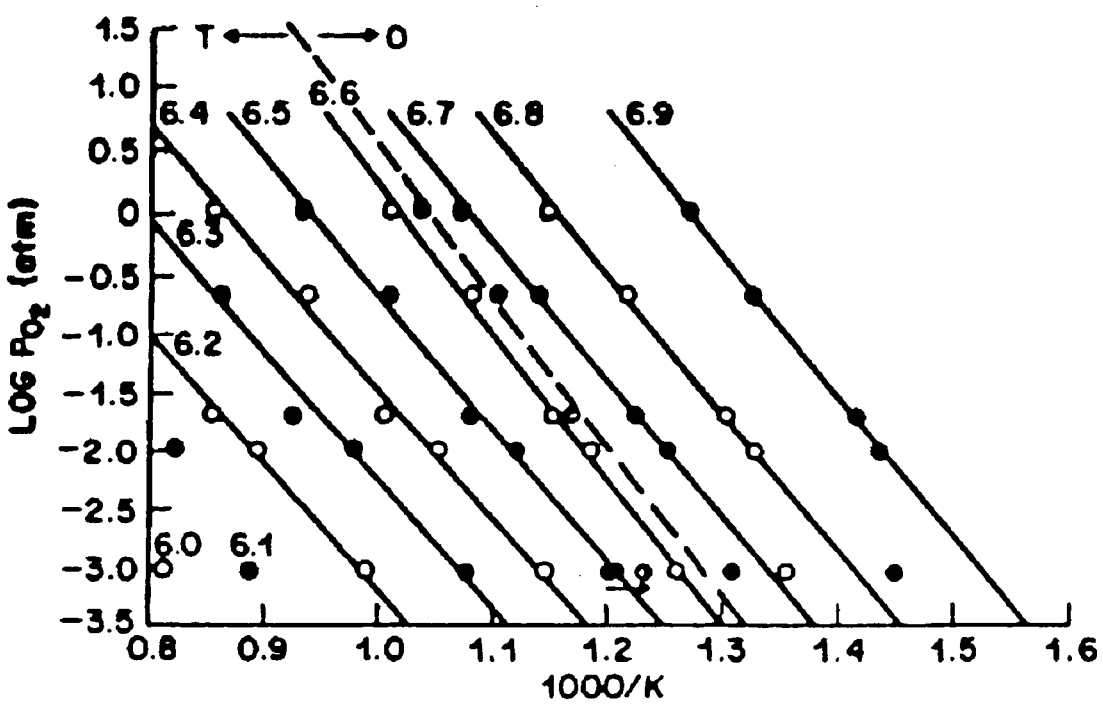

Figure 2.5: Relation of oxygen stoichiometry, oxygen partial pressure and temperature (after [Gallagher 1987])

In short, the oxygen stoichiometry can remain unchanged at high temperature only under high oxygen pressure. The higher the temperature, the higher the oxygen pressure is required to fully oxygenate a sample of $YBa_2Cu_3O_{7-x}$. However, if the oxygen pressure is too high (over 200 bar.), the 123 phase ($YBa_2Cu_3O_{7-x}$) may decompose into the 124 ($YBa_2Cu_4O_8$) or 123.5 ($YBa_2Cu_{3.5}O_{7+x}$) phases. The phase relations of the Y-Ba-Cu-O system under high oxygen pressure (200 Bar) at 980^{o}C have been experimentally determined (Fig. 2.6a) [Chandrachood, 1990]. Compared with Fig.2.6b [Frase 1987), it shows that highly oxidized phases are stabilized at high oxygen pressure: BaO_2 instead of BaO and $Y_1Ba_2Cu_4O_8$ instead of $Y_1Ba_2Cu_3O_{7-x}$.

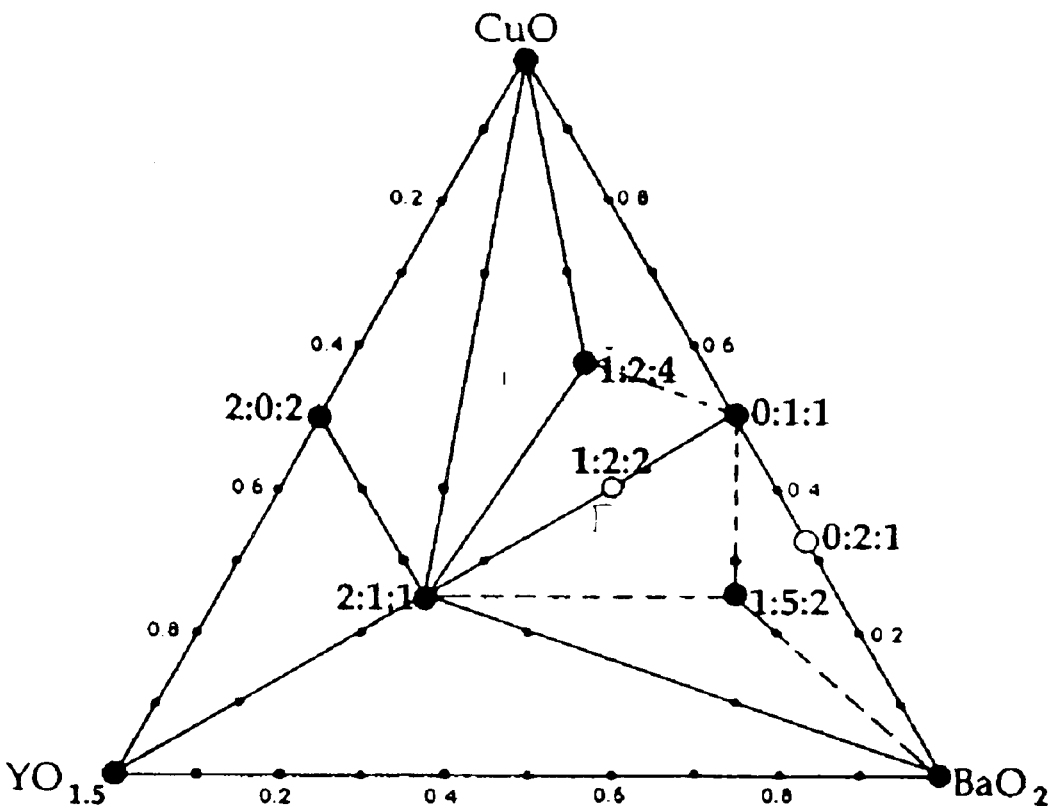

Figure 2.6a: Phase diagram of Y-Ba-Cu-O system at 200 bar oxygen pressure, 980^{o}C (after [Chandrachood 1990])

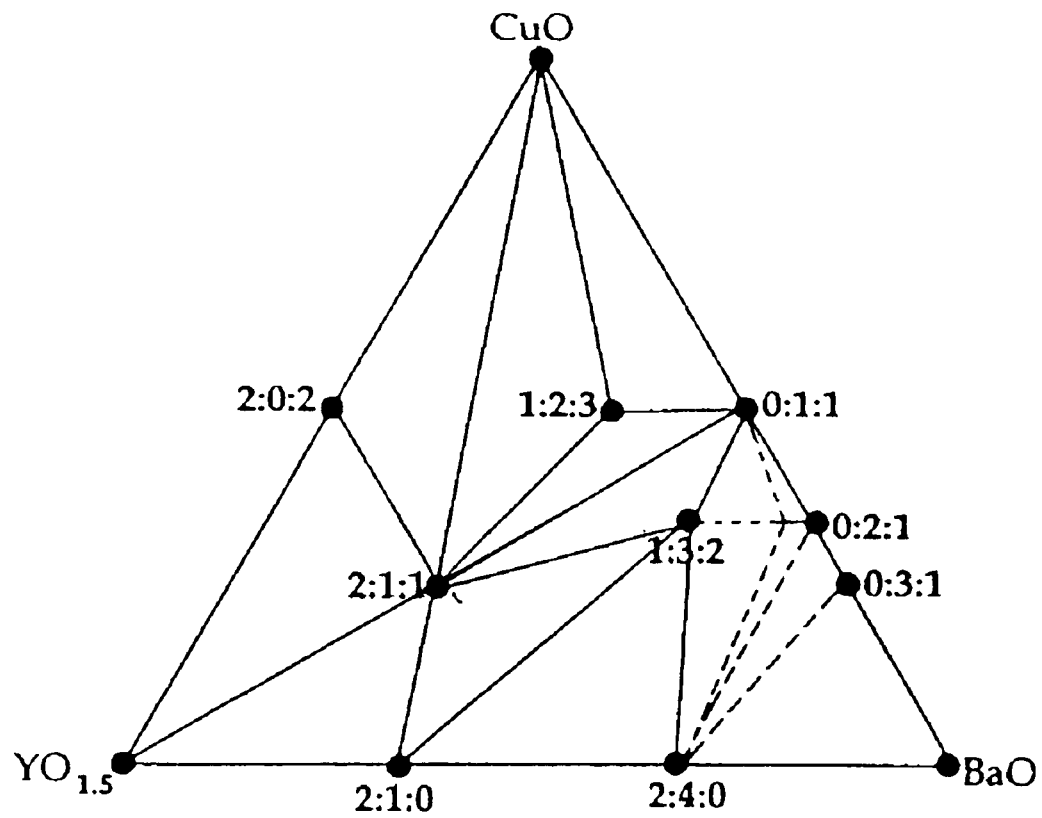

Figure 2.6b: Phase diagram of Y-Ba-Cu-O system at 1 bar oxygen pressure, 980^{o}C (after [Frase 1987])

The 123.5 and 124 superconducting phases are related to 123 by insertion of additional CuO planes between two 123 cells (Fig.2.7). 124 has T_c of 80K, but with proper doping of Ca, the T_c is near 100K. Unlike the 123 superconductor, 124 has a fixed oxygen content, and an orthorhombic structure with unit cell a=3.84Å, b=3.87Å and c=27.26Å,

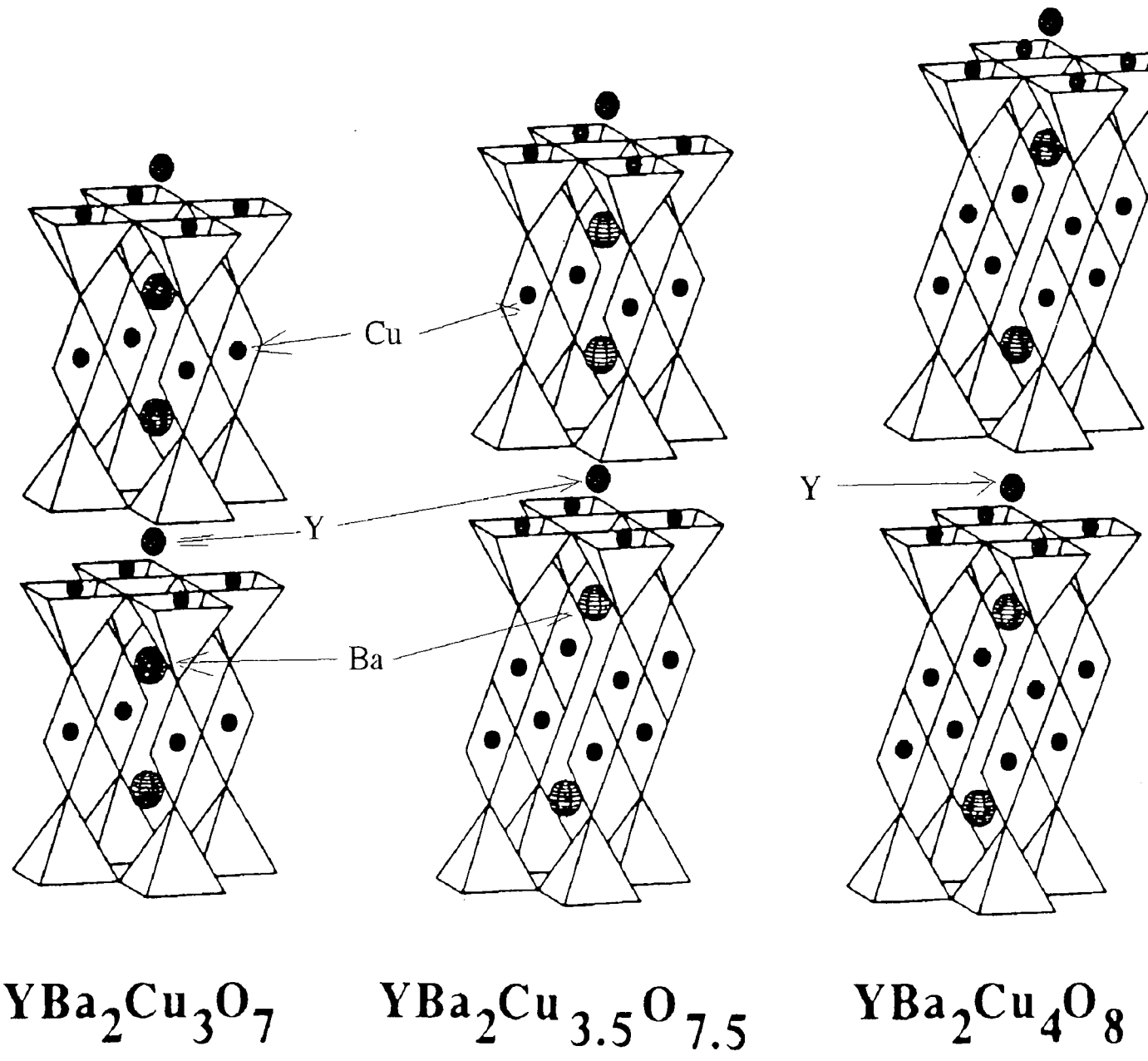

Figure 2.7: Schematic diagram of structures of 124 ($YBa_2Cu_4O_8$), 123.5 ($YBa_2Cu_{3.5}O_{7+x}$) and 123 ($YBa_2Cu_3O_{7-x}$) (after [Karpinski 1989])

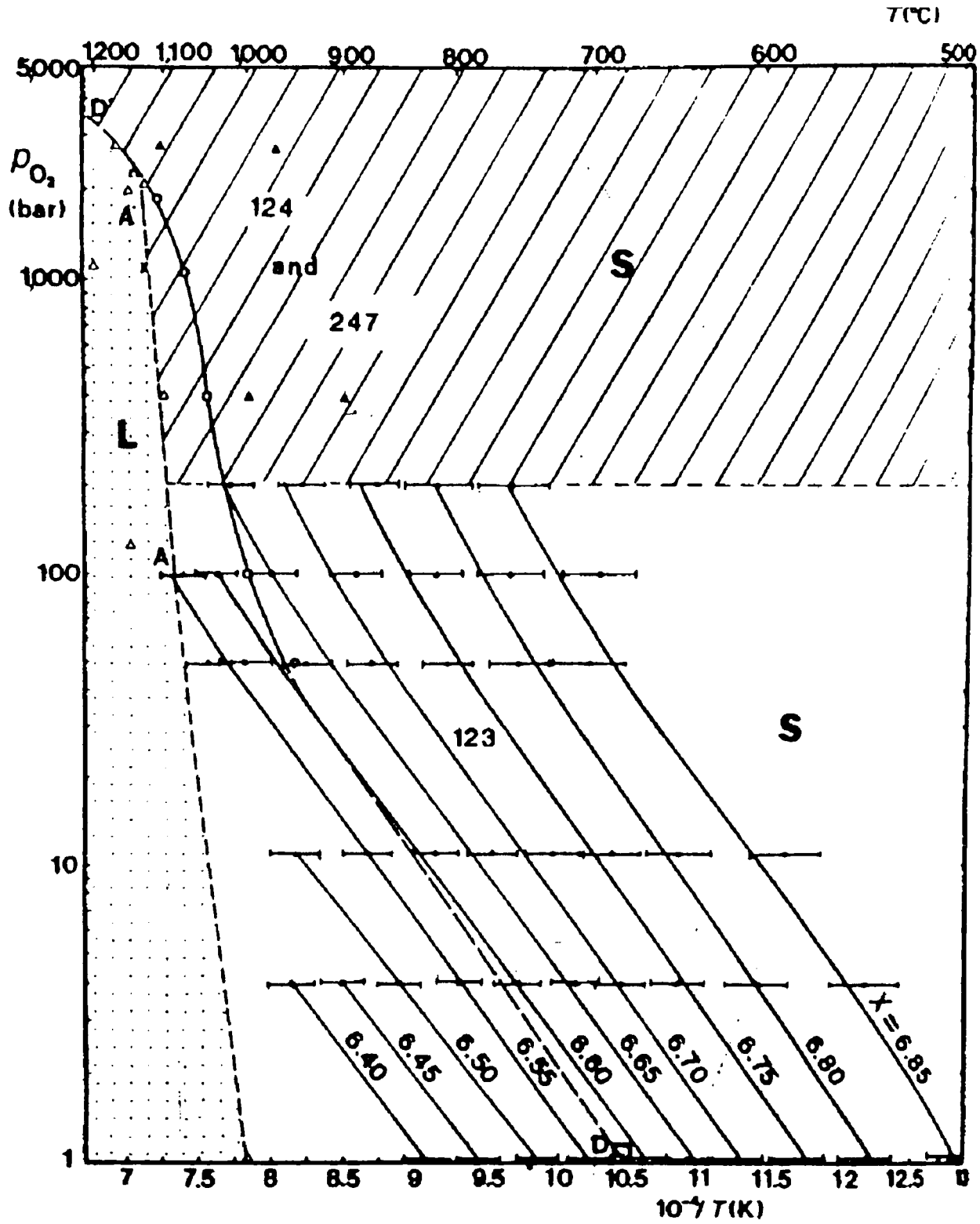

Figure 2.8 $Y_1Ba_2Cu_3O_{7-x}$ under high oxygen pressure (after [Karpinski 1988b]

The P-T-X diagram published by Karpinski et al with the stabilizing regions of the new phases 123.5 and 124 is the most complete diagram for high temperature and high oxygen pressure conditions (Fig.2.8) [Karpinski 1988b]. It provides useful guidance for oxygenation treatment of $YBa_2Cu_3O_{7-x}$ superconductor at high oxygen pressures.

2.3 Kinetics of oxygenation in the superconductor oxide

At the proper temperature and oxygen pressure, the sample oxidation process is controlled by the diffusion of oxygen atoms in the superconductor. This oxidation process is difficult in densified samples.

Town et al [1990] made high density YBCO samples by hot pressing techniques, and found that samples required very long oxygenation annealing to become largely homogeneous with $T_c > 90K$. Even after 19 days oxygen annealing, they still showed the weak link behaviour.

O'Bryan et al [1988] found that the oxidation anneal is completely effective in achieving high x only for the porous samples, the dense samples do not recover the equilibrium oxygen content after long annealling at 450°C (Fig. 2.9). The oxygen content x was measured as a function of annealing time at different temperatures (Fig.2.10). Under one atmosphere oxygen pressure at 600 and 700°C the oxygenation rates are initially fast, but slow down at long times. At 400°C the oxidation kinetics are slow but much more linear, while at 500°C the rate is nearly linear and fast.

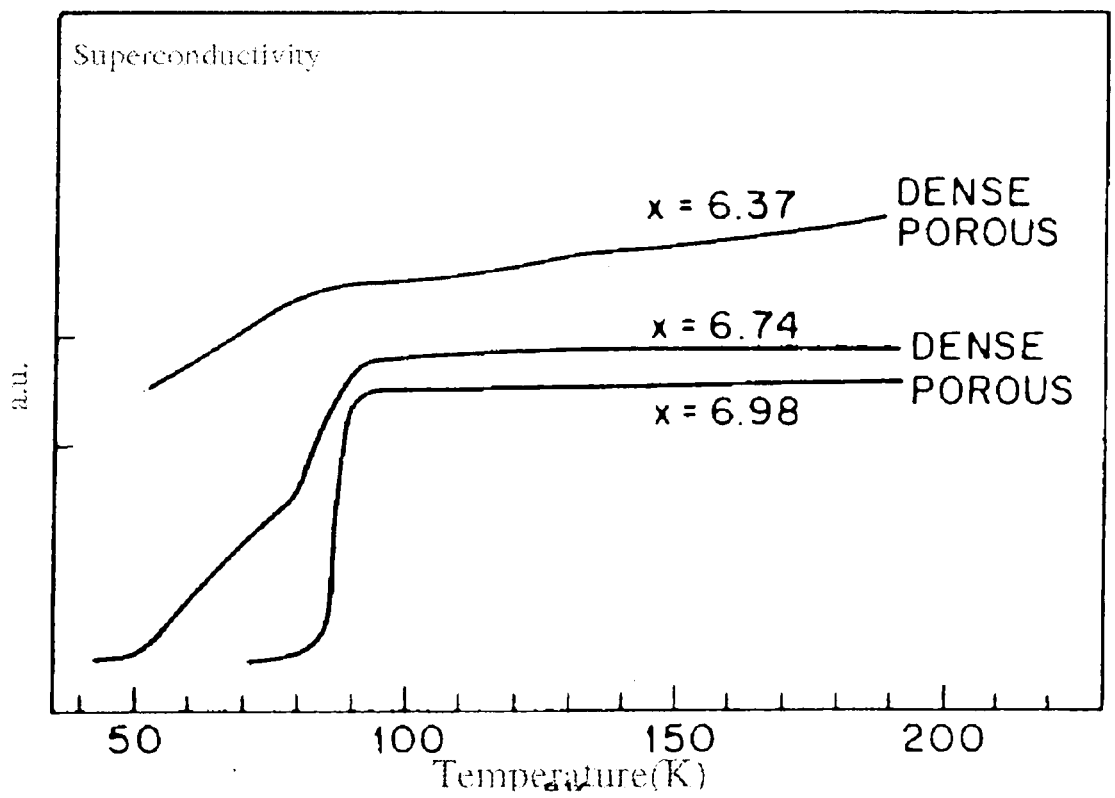

Figure 2.9 : Oxygen stoichiometry and superconductivity of samples with different densities after oxygenation treatment (after [O'Bryan 1988])

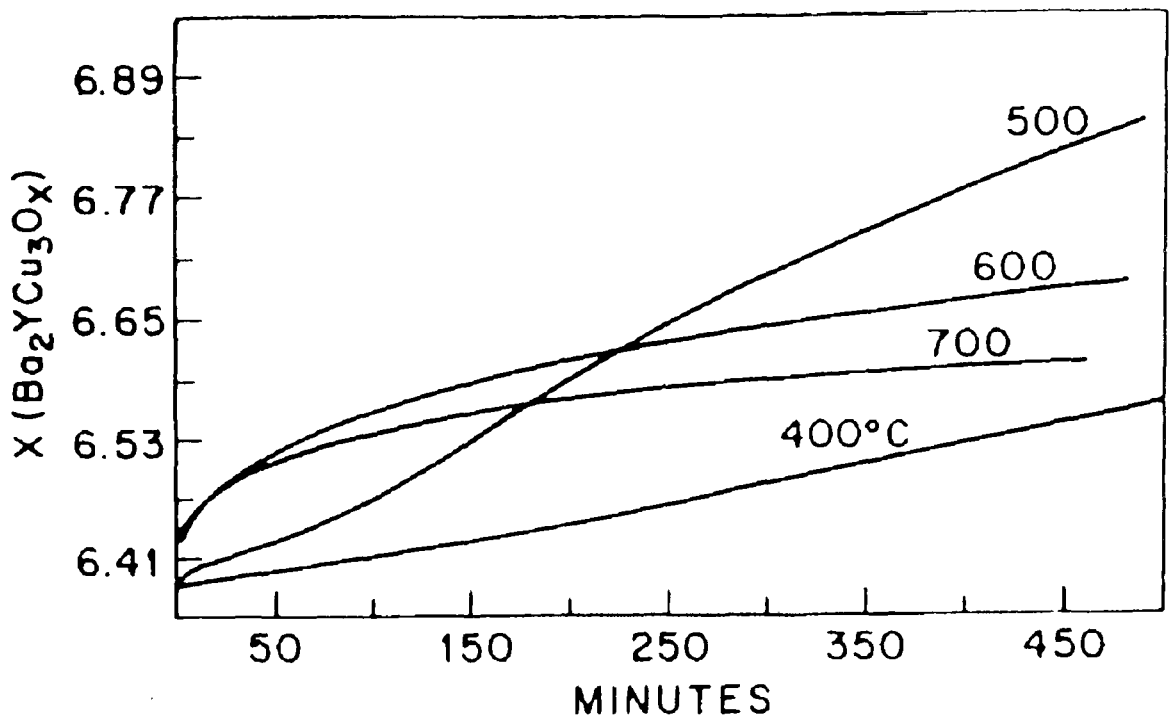

Figure 2.10: Oxidation speed and stoichiometry of densified sample (after [O'Bryan 1988])

So we can see that this oxidation process is limited by the fixed oxygen pressure. High temperatures certainly can increase the speed of the oxidation process, but then levels off at a relatively low oxygen stoichiometry compared with the low temperature annealing which starts slowly but can reach a much higher oxygen stoichiometry. Therefore there has to be a compromise between the oxidation speed and the final oxygen stoichiometry of the sample.

Chapter 3

Electrical Contacts to Superconductors

Chapter outline

Practical application of the high temperature superconducting materials will require a substantial improvement of the contacts between superconducting and normal conducting material to connect the superconductors to the normal-conducting world. Most superconductor devices require a normal metal electrical contact to the superconductor. That is why so many contact materials and methods have been tested to improve contacts to superconductors. In this chapter, the concept of contact resistance and the methods of contact resistivity measurement are summarised; various contact materials and methods are discussed and the problems of contacts to superconductors are presented at the end of the chapter.

3.1. Introduction

The contact resistivity r (Ohm cm^2) is defined by the following equation (3.1):

$$r_C = V_C / J_C \qquad (3.1)$$

where V_C refers to the voltage across the interface layer and J_C refers to the current density there.

There are two basic types of planar contacts, the horizontal and the vertical types, according to how the direction of the current flow in the superconductor relates to the planar contacts (Fig. 3.1 and Fig. 3.2.)

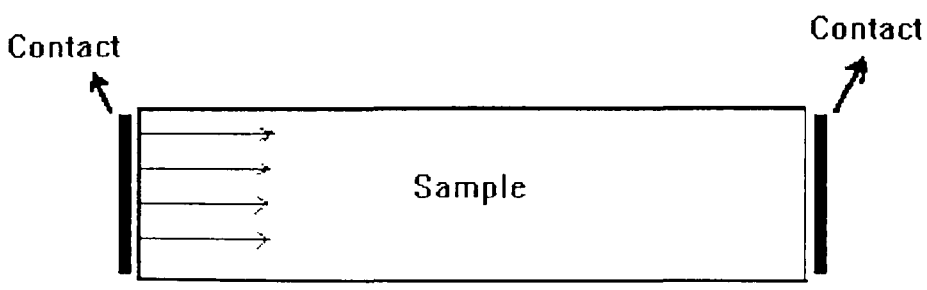

Figure 3.1: Vertical contact

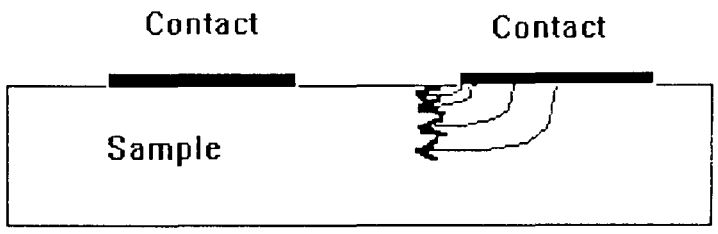

Figure 3.2: Horizontal contact

The Rc value for pure vertical type contact resistance can easily be calculated from equation 3.2 because of the simplicity of its current distribution:

$$R_C = r_C / A_C \qquad (3.2)$$

Where r_C is the contact resistivity and A_C is the contact area.

For the horizontal contact, the main current in the superconductor region flows horizontally, which leads to current crowding at the contact edge (Fig.3.2). Since there are no sufficiently accurate quantitative descriptions of the current density at the contact interface, the interface resistivity has to be described by the lump sum 'contact resistivity', which is to be measured experimentally from equation 3.3

$$r_C = R_C A_C \qquad (3.3)$$

The value of the contact resistivity r_C is expressed in terms of a surface resistivity, where R_C is the contact resistance and the A_C is the contact area.

Two conventional methods for the measurement of contact resistance are shown in Fig. 3.3 and Fig. 3.4. Fig.3.3 shows the three-point measurement configuration, from which the single contact resistance (centre contact) is continuously monitored throughout all the temperature range from room temperature to a temperature below the superconducting transition.

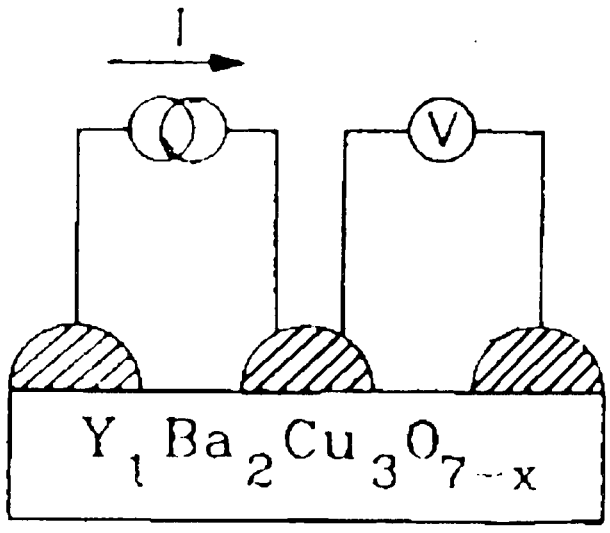

Figure 3.3: Three terminal measurement (after [Hui 1989])

Fig. 3.4 shows the two-point measurement configuration which can only measure approximately the two contact resistances as a sum at a temperature below the superconducting transition temperature.

$$U_{2P} = I \times R_{2P}$$

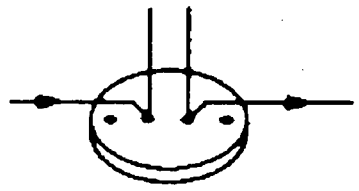

Figure 3.4: Two terminal measurement (after [Wieck 1988])

Results from these two contact measurement methods are summarized in Chapter 6 to compare the different results obtained with each method.

3.2 Silver paint and gold paste direct bonding

At a very early stage of research on high temperature superconductors, gold paste and silver paint were used to bond metal wires directly to the superconductors. The contact resistances of the contacts made from these materials were very poor [Torrance 1987, Chu 1987, Cava 1987 and Holtzberg 1987], typically about 4k Ohm at room temperature. These values increased monotonously with the decrease of temperature, up to 10^9 Ohm at 77K. In general, silver paint contacts were found to

burn out at relatively low currents (0.1A) and had poor mechanical properties [Ekin 1988].

3.3 Contacts made with reactive metals

Indium is one of the most conventional contact materials. But the contact resistivity of the best indium contact to $Y_1Ba_2Cu_3O_{7-x}$ is only 10^{-2}Ohm cm^2, and has a semiconducting character [Hui 1989 and Ekin 1988]. The contact resistance increases about 3 to 7 times as the temperature decreases from 295 to 76K, and also decreases as the current increases [Suzuki 1988]. The resistivity of the contacts typically increases more than 50% several days after the contact is made. These results show that indium is not a good candidate material for making contacts to high Tc superconductors where low contact resistivity is required.

Many other reactive metals have been tested as contact materials to $Y_1Ba_2Cu_3O_{7-x}$. They are summarized in Table 3.1, and we can see that reactive materials have very poor contact resistivities, especially after oxygenation annealing which is vital for $YBa_2Cu_3O_{7-x}$ to obtain the right oxygen stoichiometry in order to maintain superconducting properties. The only exceptional results are nickel and tungsten contacts reported by Bessergenev et al [Bessergenev 1991]. The nickel and tungsten contact resistivities were improved by 1 to 2 orders of magnitude after annealing at 700^{o}C. But this report is contrary to the earlier nickel contact result reported by Ashworth et al [Ashworth 1989], and we can see from chapter 4 that a continuous layer of NiO forms at the interface between Ni and superconductor after high temperature treatment, which makes it quite unlikely that the contact resistivity can be improved by high temperature annealing.

It should be pointed out that my experiment started before the Bessergenev's paper which is concerned with Mo and Pd contacts was published. Part of my work on Mo and Pd contacts has thus overlapped with Bessergenev's work, although my study of the contact interfacial structure and reactions is much more thorough.

Table 3.1

Contact materials	Processing method	Annealing temperature	Contact resistivity Ohm cm^2	Contact properties	Reference
Copper	Electro-deposition	without annealing	1-10	Semi-conducting	Robin 1989
Aluminium	Thermal evaporation	without annealing	10	Semi-conducting	Lakshmikumar 1989, Siegrist 1987
Bismuth	Thermal evaporation	without annealing	1-8	Semi-conducting	Lakshmikumar 1989
Zinc & Tin	Thermal evaporation	without annealing	10^{-2}	Semi-conducting	Suzuki 1988
Zinc & Tin	Flame spray method	-----	10^{-2}	Semi-conducting	Ashworth 1989
Nickel	Flame spray method	-----	$>10^{-2}$	Semi-conducting	Ashworth 1989
Nickel	Thermal evaporation	700°C	$7*10^{-5}$	metallic	Bessergenev 1991
Molybdenum	Thermal evaporation	700°C	$6.5*10^{-2}$	Semi-conducting	Bessergenev 1991
Tungsten	Thermal evaporation	700°C	$3.5*10^{-2}$	Semi-conducting	Bessergenev 1991
Niobium	Thermal evaporation	-----	10^{-3}	Semi-conducting	Ma 1991
Lead	Thermal evaporation	without annealing	10^{-4}	metallic	Vasquez 1988

Table 3.1: Properties and processing conditions for reactive metal contacts

3.4 Contacts made with noble metals

Noble metal materials have been extensively studied for the purpose of forming contacts to $YBa_2Cu_3O_{7-x}$. The results of previous work are briefly summarized in table 3.2.

Table 3.2

Processing method	Contact	Processing and annealing condition	Resistivity Ohm cm^2	Reference
Diffusion Bonding	Au	Press and diffusion bond Au beads on superconductor at 950°C	10^{-7}	Wieck 1988
Sputter deposition	Ag & Au	Sputter deposit silver or gold film on clean surface of $YBa_2Cu_3O_{7-x}$ superconductor followed by annealing at 500-600°C for an hour	10^{-9}-10^{-10}	Ekin 1987, 1988 a & b
Embedded contacts	Ag	Mix Ag metal pieces with superconductor powder, then sinter the mixture over 950°C	10^{-12}	Jin 1989
Direct wire bonding	Au	Electric discharge spot weld Au wires on superconductor, then anneal it at temperatures over 800°C.	10^{-7}	Suzuki 1989
	Au	Ultrasonic bond Au wires on superconductor, then anneal it at temperatures over 800°C.	10^{-8}	Suzuki 1989
Contact made with incorporated wires	Ag	Connect gold wires to silver dag contact or silver foil contact, followed by 900-950°C annealing.	10^{-8}	Hollin 1990
Ionized atom cluster beam and laser beam evaporation	Ag	Make contacts by ionized clusters beam and laser-beam evaporation deposition, followed by 673K annealing	10^{-7}-10^{-8}	Barlamov 1990
Noble metal alloy contact	Ag-Cu	Make Ag-Cu alloy contacts by dipping superconductor into 925-950°C Ag-Cu melt, followed by 500°C annealing for 24 hours	10^{-5}	Schmitz 1990
Silver epoxy contact	Ag	Make contact on superconductor by silver epoxy, then anneal it at 900°C in oxygen	10^{-5}-10^{-7}	Maas 1987
Melting silver & gold bead	Au	Make gold contact by melting gold bead on superconductor surface (1065°C), followed by annealing at 900°C for 48 hour.	10^{-6}-10^{-7}	Caton 1988 &1990
	Ag	Make silver contact by melted Ag bead (970°C) on superconductor.	$< 10^{-8}$	Tzeng 1988b

Mechanical procedure	Ag	Make silver contact by mechanical abrasion of silver on superconductor, and then anneal it.	10^{-6}	Lorenz 1989
Plasma spraying method	Ag	Make silver contact by plasma spraying method, followed by heat treatment.	10^{-8}	Katz 1988
Chemical vapour deposition	Pd	Deposit palladium contact by metal-organic chemical vapour method, and annealing at 300°C	10^{-1}	Bessergenev 1991
	Ir	Deposit iridium contact by metal-organic chemical vapour method, and annealing at 930°C	10^{-6}	Bessergenev 1991
Thermal-evaporation	Au	Anneal the contact at 850°C for an hour and 500°C for 8 hours	10^{-8}	Mizushima 1988
	Ag	Anneal the contact at 100°C	10^{-6}	Tzeng 1988a
		Anneal the contact at 500°C	10^{-8}	Tzeng 1988a
		Anneal the contact at 900°C	10^{-10}	Liu 1989
	Au, Ag, & Pt	deposit Au, Ag and Pt on cleaved $YBa_2Cu_3O_{7-x}$ crystal without heat treatment	10^{-7}-10^{-9}	Jing 1989, Takeuchi 1991
Thermal-evaporation	Pt	Make platinum contact at low temperature (~100 °C)	10^{-4}	Kusaka 1988
	Au	*ex situ* evaporate Au contact on $YBa_2Cu_3O_{7-x}$ film, without heat treatment	$2*10^{-4}$	Gavaler 1988
		in situ evaporate Au contact on $YBa_2Cu_3O_{7-x}$ film, without heat treatment	$4*10^{-10}$	Gavaler 1988

Table 3.2: Properties and processing conditions of noble metal contacts

From table 3.2 we can see that palladium has a poor contact resistivity (10^{-1} Ohm cm^2), while iridium can have a contact resistivity about 10^{-6} Ohm cm^2 after extensive annealing over 930°C. Platinum contacts made on newly cleaved crystals without heat treatment have contact resistivities about 10^{-7}-10^{-9} Ohm cm^2.

Noble metal contacts, or more precisely only gold and silver contacts, can have contact resistivity below 10^{-8} Ohm cm^2 after heat treatment, although platinum contacts can also have contact resistivity down to 10^{-9} Ohm cm^2 in an impractical ultra-clean surface condition. The typical heat treatment is at 500°C - 600°C for 5

hours. Without such treatment, the contact resistivity is only below 10^{-6} Ohm cm^2.

For some methods like direct bonding and melting gold beads which induce degradation of the superconductor surface, a typical annealing procedure at 950°C for over 24 hours is required to bring down the contact resistivity to 10^{-7}-10^{-8} Ohm cm^2.

3.5 The cleanness of the superconductor surface and contact properties

It is found that the rapid deterioration of the $YBa_2Cu_3O_{7-x}$ surfaces from exposure to air plays a significant role in degrading the contact resistivity [Ekin 1988].

Noble metal contacts (Au, Ag, Pt) on newly cleaved $YBa_2Cu_3O_7$ crystals can have contact resistivities of 10^{-9} Ohm cm^2 without further heat treatment [Jing 1989 and Takeuchi 1991], and the contact resistivities of *in situ* made contacts (10^{-10} Ohm cm^2) are six orders of magnitude lower than the contact made by *ex situ* methods (10^{-4} Ohm cm^2) [Gavaler 1988]

Acid etching and mechanical prepolishing of the superconductor surface immediately before making the electrical contacts has been reported to be effective in improving the contact resistivity [Vasquez 1988, Kussmaul 1991, and Ekin 1988]. Mechanical polishing only a few seconds before contact making can change the electrical contact character from semiconducting to ohmic. Noble metal contacts made on *in situ* sputter etched clean surface of $YBa_2Cu_3O_{7-x}$ can reach a contact resistivity of 10^{-10} Ohm cm^2 below T_c. Gold, silver, and platinum contacts on oxygen plasma cleaned superconductor surfaces can also have a contact resistivity in the range of 10^{-9} Ohm cm^2 without heat treatment [Tsai, 1990].

In general, all kinds of contact making methods will benefit from the precleaning of $YBa_2Cu_3O_{7-x}$ superconductor surfaces, and this is particularly important when the contact is made without heat treatment.

3.6. The problems associated with poor contacts

There are several ways in which problems can arise both during formation of

the contact itself and in service.

3.6.1 Long term mechanical problems

Though there are some reports of contacts made of reactive metals such as copper, bismuth, indium and indium alloys [Robbin 1989, Lakshmikumar 1989, and Ekin 1988], the contact properties are poor because chemical reactions cause disruption of the superconductor surface to form oxide insulators.

The most successful contacts are made with noble metals, more precisely only gold and silver. After low temperature annealing, these contacts can give very low contact resistance and have no harmful effect on the superconductivity.

It has been shown that when metals make contact with oxide ceramics, for instance metals which form stable oxides such as copper, nickel and cobalt, the adhesion is very good. While for the metals that do not form stable oxides such as gold and silver, strong chemical bonding does not occur at the interface, and adhesion is weak [Donald 1985]. In many cases, even after heat treatment, contacts made with deposited Ag or silver paint on high T_c superconductors still have a very poor adherence, the contact can come off the superconductor without leaving a trace [Kussmaul 1991 and Ekin 1988]. Even worse, the deposited silver contact on the high T_c superconductor could be so inadherent that it won't even stand cycling between the soldering temperature and 77K [Rubin 1989].

This casts a doubt on the long term mechanical stability of noble metal contacts on the high T_c superconductors, especially for those noble metal contacts made without further annealing procedure on the less porous, high J_c, superconductors such as single crystals or melt textured $YBa_2Cu_3O_{7-x}$ superconductors.

In addition to these problems, most methods described above require wires to be attached subsequently. It has been proved that soldering methods are not suitable for attaching wire to the thin film metal contacts [Ekin 1988], which leaves silver paste or some kind of mechanical clamping as the only choices for attaching electrical leads to the as-made thin film contact. This limits the current carrying ability and the

mechanical strength of metal contacts to the superconductor.

3.6.2 The critical current problem in contacts

Although many contact making techniques can give sufficiently low contact resistance for low current (mA) applications, there is still a lack of satisfactory high current contact methods.

Noble metal thin film contacts are only satisfactory for carrying the small currents involved in the resistive determination of T_c, it is inadequate for the much higher current used to measure J_c. A reliable method for injecting high currents is ultrasonic indium contacts [Jones 1989].

3.6.3. The oxygen stoichiometry problem

From previous chapters we know that the superconducting properties of $YBa_2Cu_3O_{7-x}$ are very sensitive to the oxygen content. $YBa_2Cu_3O_{7-x}$ is also very unstable and reacts with other materials easily, losing oxygen and its superconductivity. This sensitivity and instability induce a lot of problems for contact making, since the metal contacts will inevitably absorb oxygen from the $YBa_2Cu_3O_{7-x}$ during the contact making procedure.

The loss of oxygen content could be recovered by low temperature oxygen annealing (500-600^oC), however this still excludes the possibilities of most reactive metals as contact materials to $YBa_2Cu_3O_{7-x}$. This is because the reactive metals will further react with $YBa_2Cu_3O_{7-x}$ during the annealing. In the worst cases, the reactive metal contacts decompose the $YBa_2Cu_3O_{7-x}$ in the near surface regions and form insulating oxides.

Even for noble metal contacts, except for those made on ultra-clean $YBa_2Cu_3O_{7-x}$ surfaces, low temperature oxygen annealing is an essential step to the recovery of the oxygen losses at the interface between $YBa_2Cu_3O_{7-x}$ and contact material. This is why this low temperature anneal is usually essential to bring down the contact resistivity by several orders of magnitude.

Chapter 4

Interactions between $YBa_2Cu_3O_{7-x}$ and other materials.

Chapter outline

To understand the factors which influence contact properties, the investigation of interactions between $YBa_2Cu_3O_{7-x}$ and other materials is of great interest. In this chapter the previous work on interactions between $YBa_2Cu_3O_{7-x}$ and reactive metals, and $YBa_2Cu_3O_{7-x}$ and noble metals are summarized and discussed; a summary containing the information which can be used in searching for new contact materials is presented at the end of chapter.

4.1 Interactions between $YBa_2Cu_3O_{7-x}$ and reactive metals

4.1.1 Superconductor-Indium

Indium was found to absorb large amount of oxygen from the $YBa_2Cu_3O_{7-x}$ at the indium/superconductor interface [Ekin 1988]. This indicates that indium has reacted with $YBa_2Cu_3O_{7-x}$ and formed an indium oxide layer, probably In_2O_3, at the superconductor/indium interface. This is believed to be responsible for the poor contact resistivities and the semiconducting character of indium contacts. Photoelectron spectroscopy study has also confirmed that indium reacts with high T_c superconductors even at room temperature [Kulkarni 1989].

4.1.2 Superconductor-Iron

Iron was found to react severely with $YBa_2Cu_3O_{7-x}$ [Gao, 1987]. The reaction induced substantial disruption of the $YBa_2Cu_3O_{7-x}$, and formed an insulating phase of FeO compound at the interface by withdrawing oxygen from the superconductor. The disruption of the superconductor surface promoted the loss of barium and its persistent segregation at the surface even after 50 Å of coating.

4.1.3 Superconductor-Nickel

The diffusion of nickel into $YBa_2Cu_3O_x$ as well as the diffusion of barium,

copper and yttrium into nickel are very limited [Champagne 1989]. However, a thin interaction zone consisting of NiO and a nickel-rich oxide compound was formed at the Ni/$YBa_2Cu_3O_X$ interface. T_c measurements of Ni/$YBa_2Cu_3O_{7-X}$ composites also showed that there is limited interaction between nickel and the superconductor [Kammlott 1990]. The presence of such an interaction zone could have a detrimental affect on the thermal stabilisation of Ni-$YBa_2Cu_3O_X$ composite wires or on electrical properties of the nickel contacts.

4.1.4 Superconductor-Aluminium

Aluminium was found to have a reaction with $YBa_2Cu_3O_{7-X}$ thin films to form an oxidized aluminium layer (Al_2O_3) [Asano 1989]. In some cases [Chen 1988, Siegrist 1987 and Kakabatake, 1988], the reactions between aluminium and $YBa_2Cu_3O_{7-X}$ are so strong in Al/$YBa_2Cu_3O_{7-X}$ composites that the superconductivity of the $YBa_2Cu_3O_{7-X}$ superconductor was lost.

4.1.5 Superconductor-Copper

From chapter 3 we have seen that copper contacts to $YBa_2Cu_3O_{7-X}$ have high contact resistivity (1-10 ohm cm^2) and non-ohmic behaviour. This indicates that degradation occurs at the interface between copper and the superconductor.

In the Cu/$YBa_2Cu_3O_{7-X}$ composite system copper was found to react vigorously with the superconductor, and withdraw oxygen atoms from the $YBa_2Cu_3O_{7-X}$ to form copper oxides [Hill, 1987, 1988]. The reaction of the $YBa_2Cu_3O_{7-X}$ phase and copper resulted in the reaction product CuO at temperatures above 800°C, and a mixture of CuO and Cu_2O at 600°C [Cheung 1989]. It is believed that the bonding in the Cu-O sheet structure in the superconductor is less stable than the copper oxide that is formed at the surface after metal deposition.

4.1.6 Superconductor-Lead

Lead was found to have strong interaction with $YBa_2Cu_3O_{7-X}$, and formed

PbO_y oxide at the interface [Plecenik 1991].

Complex chemical interactions were found to occur in the system $YBa_2Cu_3O_{7-}$ PbO at 600-800 ^oC, the reaction products contain the $BaPbO_3$ non-superconducting compound [Kamarzin, 1990].

So lead cannot used as contact material although it forms conducting oxides like PbO_2. The lead will leach oxygen from superconductor during deposition which will resulted in a oxygen deficient semiconductor layer at the surface. This oxygen deficient layer can not be recovered by oxygenation treatment, since further heat treatment will encourage the PbO to react further with $YBa_2Cu_3O_{7-x}$ and form $BaPbO_3$.

4.1.7 Superconductor-Niobium

Niobium was found to be highly reactive with $YBa_2Cu_3O_{7-x}$. The niobium layer on the superconductor surface interacted with the oxygen chemically bound in the $YBa_2Cu_3O_{7-x}$ and formed niobium oxides [Plecenik 1991 and Ma 1991].

Niobium reacts vigorously with $YBa_2Cu_3O_{7-x}$ even at 600^oC, the reaction decomposed the superconductor and forms Ba_2YNbO_6, CuO, Cu_2O, Y_2BaCuO_5, $Ba_5Nb_4O_{15}$ and other Ba-Nb and Ba-Y binary oxides [Cheung 1989].

In the case of superconductor/Nb composite material, the composite system was found to be not superconducting which confirms the detrimental effect of Nb doping [Kammlott, 1990].

So Nb metal can not use as contact material due to its highly reactivity with the superconductor oxide.

4.1.8 Superconductor-Bismuth

Bismuth metal has very limited reaction with $YBa_2Cu_3O_{7-x}$. The cross section of the Bi/$YBa_2Cu_3O_7$ interface shows the superconductor substrate has a very thin disrupted region, a very thin but continuous region of Bi_2O_3 [Meyer 1988]. This can be explained by the nonequilibrium kinetically limited interface formation.

This Bi_2O_3 layer and the very thin disrupted region in the superconductor will induce a large resistance at the interface, so it may be a good passivation material but not a good contact material.

4.1.9 Superconductor-Titanium

The cross section of the Ti/$YBa_2Cu_3O_{7-x}$ interface revealed that Ti metal reacted with the superconductor. The interface structure contains a disrupted layer of $YBa_2Cu_3O_{7-x}$ of unknown stoichiometry which is deficient in oxygen, a TiO_2 layer, Ti suboxides, and metallic Ti [Meyer 1990]. This reaction is limited by the diffusion of oxygen to the surface, and when the amount of Ti exceeds the amount needed to form TiO_2, a lower binding energy Ti-O species forms.

4.1.10 Superconductor-Molybdenum

Mo was found to have very bad effect on the superconductor. A Mo/$YBa_2Cu_3O_{7-x}$ composite did not show superconductivity, but after high temperature treatment (over 1000^oC), the superconductivity of the composite recovered to a certain extent with Tc just over 60K [Kammlott 1990].

4.2 Interaction between superconductor and noble metals

4.2.1 Superconductor-Platinum (group)

It has been found that the platinum-group metals (Pt, Pd, Re, Rh, Ru) react vigorously with the superconductor to eliminate not only the superconductivity but also the metallic behaviour (giving semiconductor-like behaviour) [Gazit 1989 and Jin 1988].

Further study of the system [Kammlott 1990 and Tiefel 1990] revealed that although every member in the Pt group (Pt, Pd, Re, Rh and Ru) has a detrimental effect on the superconductor, for some of them (Pt, Ph and Re) the superconductivity can be partially recovered after high temperature treatment (over 1200^oC). SEM studies show these noble metals reacted with the superconductor and formed (Pt, Ph

and Re)-rich phases in the superconductor, but they are scattered and isolated in the material.

The reactions of Pt and Pd-Ag alloys with $YBa_2Cu_3O_{7-x}$ at 930°C form various non-superconducting compounds: $Ba_2Y(Cu_{1-x}Pt_x)_3O_{6+x}$, CuO, BaO-CuO mixtures for Pt reaction with $YBa_2Cu_3O_{7-x}$, and $Ba(Cu_{1-x}Pd_x)O_2$, CuO, and BaO-CuO-Ag mixtures for Pd-Ag reaction with $YBa_2Cu_3O_{7-x}$ [Jennifer 1989].

Although platinum reacts with superconductor and forms various compounds after annealing, it seems that platinum metal is quite harmless to the superconductor if the composite is not subject to high temperature heat treatment. We have seen in chapter 3 that platinum contacts on a clean surface of $YBa_2Cu_3O_{7-x}$ without heat treatment can achieve a contact resistivity of the same magnitude as silver or gold contacts (10^{-9}-10^{-8} Ohm cm^2).

4.2.2 Superconductor-gold

The gold - $YBa_2Cu_3O_{7-x}$ system has been intensively studied. At a very early stage of work, gold was thought to have no reaction with $YBa_2Cu_3O_{7-x}$. However, later research showed that gold/superconductor interactions seem to fall into two categories:

Gold inside samples of $YBa_2Cu_3O_{7-x}$ was found to be quite harmless to the superconductivity. Microstructural studies showed that gold and $YBa_2Cu_3O_{7-x}$ form separated phases in the composite material [Meyer 1987]. Further study showed that composites of gold and $YBa_2Cu_3O_{7-x}$ could be doped with up to 10% of gold per formula unit [Marta 1990], and the superconducting transition temperature (T_c) was slightly enhanced upon Au doping. Further increase in the amount of gold inside $YBa_2Cu_3O_{7-x}$ will form separate gold phases in the $YBa_2Cu_3O_{7-x}$, and there is no further improvement of Tc above the maximum gold doping level (10% per formula unit).

However, if gold plate instead of gold powder is in contact with the $YBa_2Cu_3O_{7-x}$ surface, strong interaction with the superconductor was found [Plecenik

1991]. Gold plate was found to react with $YBa_2Cu_3O_{7-x}$ at 800-878°C in 1 atm O_2 [Ray 1989]. Cu and small amounts of Ba were removed from the $YBa_2Cu_3O_{7-x}$ by gold, leaving 211 and presumably $BaCuO_2$ and CuO crystals at the interface. The exact reaction mechanism is not clear and needs further investigation.

4.2.3 Superconductor-silver

Silver, like gold, was thought to be completely inert to $YBa_2Cu_3O_{7-x}$, and early research also showed that silver does not degrade the T_c of $YBa_2Cu_3O_{7-x}$. It was also observed to promote the formation of a densified material with the silver filling voids and perhaps coating grain boundaries as well. This second effect reduces contamination of internal surfaces with hydrocarbons, and should produce improved superconducting critical current in samples limited by intergranular weak links [Peterson 1988, Weinberger 1989 and Chang 1988].

However, further study revealed that silver does have some detrimental effect on $YBa_2Cu_3O_{7-x}$. At temperatures above 931°C, Ag-O eutectic liquid is formed at the interface between silver and which penetrates into the $YBa_2Cu_3O_{7-x}$. The silver gains oxygen by reduction of $YBa_2Cu_3O_{7-x}$. Y_2BaCuO_5 forms as a reaction product when the Ag-O eutectic liquid dissolves Cu from the $YBa_2Cu_3O_{7-x}$ and forms Ag-Cu alloys or Ag-Cu-O eutectic. The ceramic at the interface exhibits a variable composition, the grains surrounded silver are Y_2BaCuO_5 phase, the rest of the material is a complex mixture of silver, $YBa_2Cu_3O_{7-x}$, and Y-containing phases that may be partially overlapping, and the reaction was interpreted as $YBa_2Cu_3O_{7-x} + AgO = Y_2BaCuO_5 +$ Liquid [Loehman 1990, Ganapathy 1989 and Aselage 1988].

The most recent result also shows that silver can be doped into the $YBa_2Cu_3O_{7-x}$ structure. The superconductor $YBa_2Cu_{3-x}Ag_xO_{6+y}$ solid solution can be doped up to about $x=0.035$. The superconducting transition temperature T_c is enhanced about 1.1K over that of the undoped material. However, on further increase in the silver amount in $YBa_2Cu_3O_{7-x}$ (at $x>0.035$), the superconducting properties are considerably degraded. The Ag-O eutectic liquid forms above 931°C and

dissolves copper from 123 leading to the decomposition of 123 into 211 phase [Gangopadhyay 1991].

Silver addition to the superconductor were found to be very effective in reducing the normal state electrical resistivity of composite samples at $T > T_c$ [Plechacek 1988, Dwir 1989, Varma 1990 and Wilber 1990]. This can be understood by the short circuit effect of silver at grain boundaries and the pores, since silver has considerably lower resistivity than the superconductor in its normal state. In addition, the silver additions were found to have an effect to reduce the silver contact resistivity to the superconductor [Sun 1991]. This is probably caused by an error in the value of the actual contact area of metal to superconductor used in the contact resistance measurement. This kind of problem will be discussed later in chapter 5 and chapter 6.

4.3 Summary

All reactive metals studied have strong interactions with $YBa_2Cu_3O_{7-x}$. Some metals have limited reaction, such as indium, titanium, bismuth and copper, the reaction products only contain the metal oxides, the surface of the $YBa_2Cu_3O_{7-x}$ is still stable and has only suffered loss of oxygen. However, some of the metals have very detrimental reactions which involve the decomposition of $YBa_2Cu_3O_{7-x}$, for example iron, nickel and aluminium.

The studies of the reactions between reactive metals and $YBa_2Cu_3O_{7-x}$ explain the electrical properties of reactive metal contacts in chapter 3. It also suggests that in the choice of reactive metals as possible contact materials, at least the possible contact materials should not cause the decomposition of $YBa_2Cu_3O_{7-x}$. The loss of oxygen content at the $YBa_2Cu_3O_{7-x}$ surface may be recovered later by low temperature oxygen annealing.

Noble metals except gold and silver, all have detrimental effect on the superconductivity of $YBa_2Cu_3O_{7-x}$ after heat treatment. Although the superconductivity can be recovered by extensive annealing (over 1200^{o}C), the complex reaction products are still observable from SEM.

Gold and silver are not as inert on YBCO as people once thought. A small amount of doping of gold and silver into the $YBa_2Cu_3O_{7-x}$ can slightly increase the superconducting transition temperature. However the differences in the effect of gold and silver arises over doped samples. Gold simply forms separate phases if present in concentration over 10% at, and shows there is no harmful effect to the superconductivity of $YBa_2Cu_3O_{7-x}$; silver on the other hand will react with $YBa_2Cu_3O_{7-x}$ and form a series of insulating compounds. This reaction considerably degrades the superconducting transition temperature, T_c.

These results of the interactions between silver/gold and $YBa_2Cu_3O_{7-x}$ seem in conflict with the contact resistivity results in chapter 3. This does not necessarily mean that the interaction and the reaction products have little effect on contact resistivity. One of the possible explanations lies in the contact making procedure. Small amounts of the noble metals may diffuse into the superconductor during low temperature annealing and is then in contact with clean $YBa_2Cu_3O_{7-x}$ especially in the case of sintered low density $YBa_2Cu_3O_{7-x}$ [Hollin 1990 and Caton 1990]. This could explain why the contact resistivities are considerably improved by the annealing procedure.

Chapter 5

Preparation of high Tc superconductor samples

5.1 Introduction

One of the important features of high T_c superconductors is the very short superconducting coherence length. For the $YBa_2Cu_3O_{7-x}$ superconductor the coherence length is 20-30 Å in the CuO_2 planes and only 1.5-3 Å in the perpendicular c-direction [Gough 1991]. Such a short coherence length results in many problems in the application of these materials, and 'weak links' is one of the major ones. The weak links in $YBa_2Cu_3O_{7-x}$ are the localised regions where the superconducting properties are degraded by incorrect chemical stoichiometry (mainly oxygen deficiency), microcracks, pores, lattice defects and grain boundaries, which lead to low critical current density in sintered $YBa_2Cu_3O_{7-x}$ superconductor. A typical value is only 10^2 A/cm^2. However, single crystal $YBa_2Cu_3O_{7-x}$ samples exhibit critical current densities several orders of the magnitude higher than those measured in polycrystalline material with randomly oriented grains [Ekin 1987]. This shows that the intrinsic critical current density of the material is much larger than the value measured in sintered materials.

Several melt growth techniques have been tested to overcome the problem of weak links, such as melt textured growth [Jin 1987, Jin 1988, Salama 1989 and Selvamanikham 1990], the quench/melt growth [Morita 1989, Murakami 1989], and melt/powder melt growth [Murakami 1990]. The samples made with melt growth techniques have much larger critical current densities (Jc) than the sintered materials. However, it is difficult to control the direction of the grain alignment throughout the sample length and further improve the size of the large textured grains, which may be the obstacle to the further improvement of the critical current density.

The work reported in this chapter was to investigate the melt-growth technique for the processing of $YBa_2Cu_3O_{7-x}$, optimize the crystal growth conditions, and produce large textured $YBa_2Cu_3O_{7-x}$ crystal samples with high sample density and

high critical current density.

The samples needed for contact research and the electrochemical titration research introduced in later chapters are all processed by the methods described below.

5.2 Sample preparation

5.2.1 Samples prepared by the ordinary sintering method OS

Most of the $YBa_2Cu_3O_{7-x}$ single phase precursor powder used in my experiment was bought from Cooksons, although some of it was made by myself. The solid state reaction route was used to prepare the ordinary sintered high T_c superconductor. The procedures are:

1. Preparing the $YBa_2Cu_3O_{7-x}$ precursor powder

Mix starting powders of $Y_1O_{1.5}$, BaO, and CuO at the ratio of 1:2:3, all of them > 99.99% purity; Finely grind the mixture in an Al_2O_3 mortar; Uniaxially press into a pellet shape and sinter at 950 ^oC for 24 hours in air; Then regrind the superconductor powder in order to make a homogeneous mixture, and the precursor powder is ready for the further processing.

2. Preparing the sintered $YBa_2Cu_3O_{7-x}$ samples

Isostatically press the $YBa_2Cu_3O_{7-x}$ precursor powder at 100 MPa to form a pellet with the dimension of 20 mm diameter and 2-4 mm thickness; Sinter the pellet at 950 ^oC for 12 hours; Slowly cool down to 500 ^oC in air and anneal for about 2 hours at this temperature; Then cool down to room temperature.

5.2.2 Samples prepared by melt growth technique MG

The precursor pellets for making large textured crystal superconductor samples were prepared in the same way as described above. The method applied in my experiment is the partial melt growth technique based on the peritectic growth mechanism. The peritectic reaction is:

$$Y_2BaCuO_5 + (3BaCuO_2+2CuO)_{liquid} \text{---} > 2(YBa_2Cu_3O_{7-x})$$

First, the precursor pellet is melted into the single phase liquid region or to the two-phase region (Y_2BaCuO_5 + $(3BaCuO_2+2CuO)_{liquid}$) in the phase diagram, Fig.5.1, then the sample is slowly cooled down to let the $YBa_2Cu_3O_{7-x}$ superconductor crystallize from the melt by the peritectic reaction.

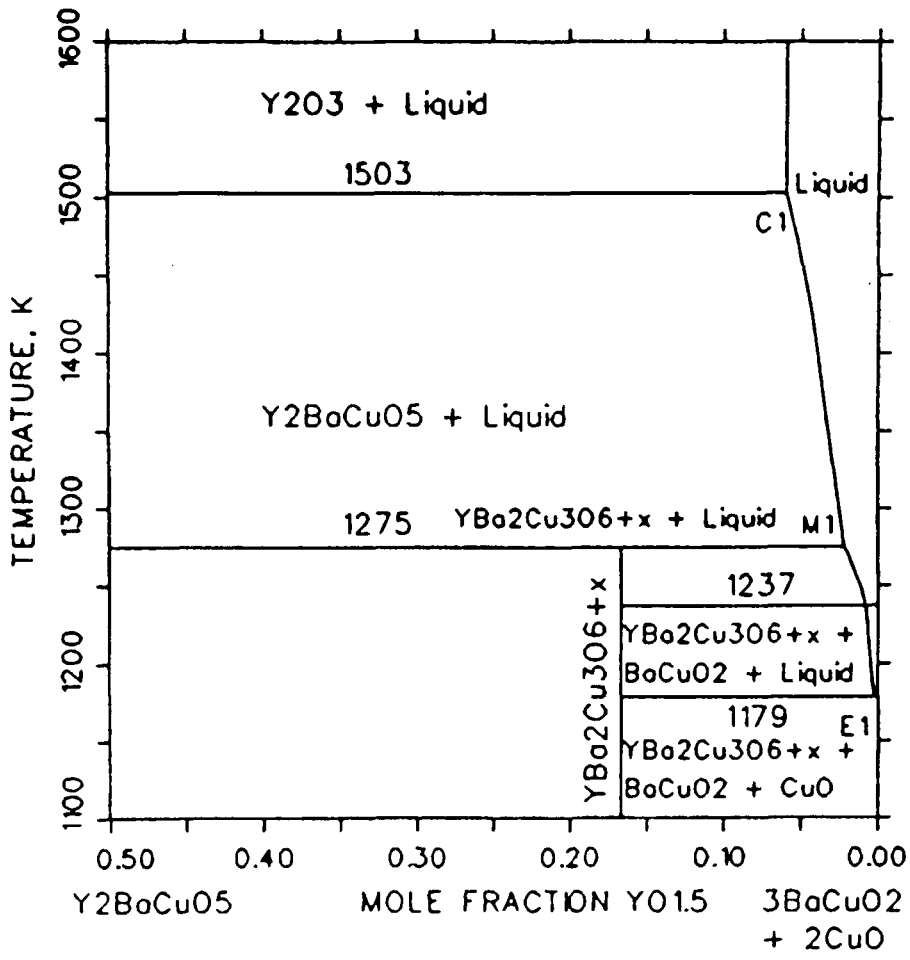

Figure 5.1: The calculated vertical section of the phase diagram for Y_2O_3, BaO and CuO (after [Lee 1991])

The samples were placed in a furnace on several loose parallel Al_2O_3 tubes during melt processing. This kind of substrate geometry made it easier to separate the as-grown samples from the substrate after the melt growth procedure, and reduced the interfacial reaction between superconductor and any other substrate.

5.2.2.1. Melt growth in the one-zone furnace.

The one-zone furnace has a Eurotherm temperature controller (accurate to within +/- 1 ^{o}C) with an eight-ramp programmer.

The melt growth program is illustrated in Fig. 5.2:

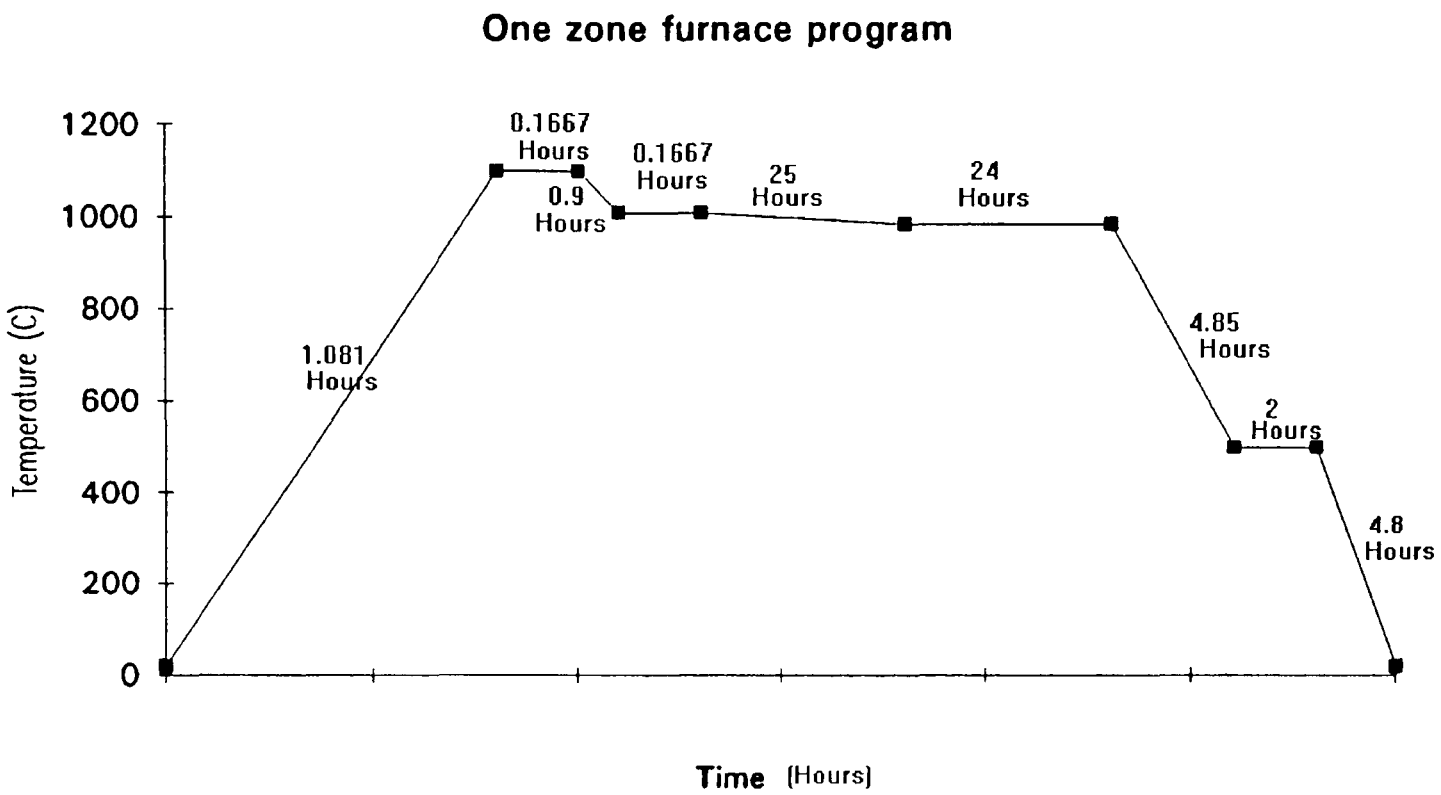

Figure 5.2: One zone furnace program for melt growth crystal supercondutor

Ramp 1 :	999 ^{o}C/hour	Fast heating of the precursor sample.
Level 1:	1100 ^{o}C	All $Y_1Ba_2Cu_3O_{7-x}$ phase decomposed into Y_2BaCuO_5 + melt $((3BaCuO_2+2CuO)_{liquid})$.
Dwell 1:	10 minutes	Stabilizing temperature.
Ramp 2:	999 ^{o}C/hour	Fast quenching the system to avoid the growth of Y_2BaCuO_5
Level 2:	1010 ^{o}C	Starting temperature for the growth of $Y_1Ba_2Cu_3O_{7-x}$ phase.
Dwell 2:	10 minutes	Stabilizing temperature.
Ramp 3:	1 ^{o}C/hour	The $Y_1Ba_2Cu_3O_{7-x}$ crystal growth procedure
Level 3:	985 ^{o}C	The temperature at which $Y_1Ba_2Cu_3O_{7-x}$ solidification is complete.
Dwell 3:	24 hours	Completion of the solidification procedure.

Ramp 4:	100 ^{o}C/hour	Slow cooling rate to encourage the oxygen absorption.
Level 4:	500 ^{o}C	The oxygenation temperature setting.
Dwell 4:	2 hours	Oxygen absorption.
Ramp 5:	100 ^{o}C/hour	Slow cooling to encourage the oxygen absorption.
Level 5:	25 ^{o}C	Room temperature.
Dwell 5:	End	program completes.

By carefully placing the sample in different positions inside the furnace, the melt growth procedure has been carried out both with a temperature gradient (40^{o}C/cm, 12cm away from the furnace centre) and without the presence of any significant temperature gradient (centre of the furnace).

After running the program, the sample was then oxygenated in a pure oxygen or atmosphere for 15 hours at 600 ^{o}C and cooled at the rate of 100 ^{o}C/hour to room temperature.

5.2.2.2 Melt growth in the two-zone furnace

The two zone furnace has two Eurotherm temperature controllers with two-ramp programmers. Since the programmer has only two ramp control, the temperature gradient inside the furnace has to be carefully measured under different temperature settings in order to complete the melt growth process which was done in a five-ramp program in the one zone furnace. The zone 1 and zone 2 temperature controllers are set up in the programs illustrated in Fig. 5.3 & 5.4:

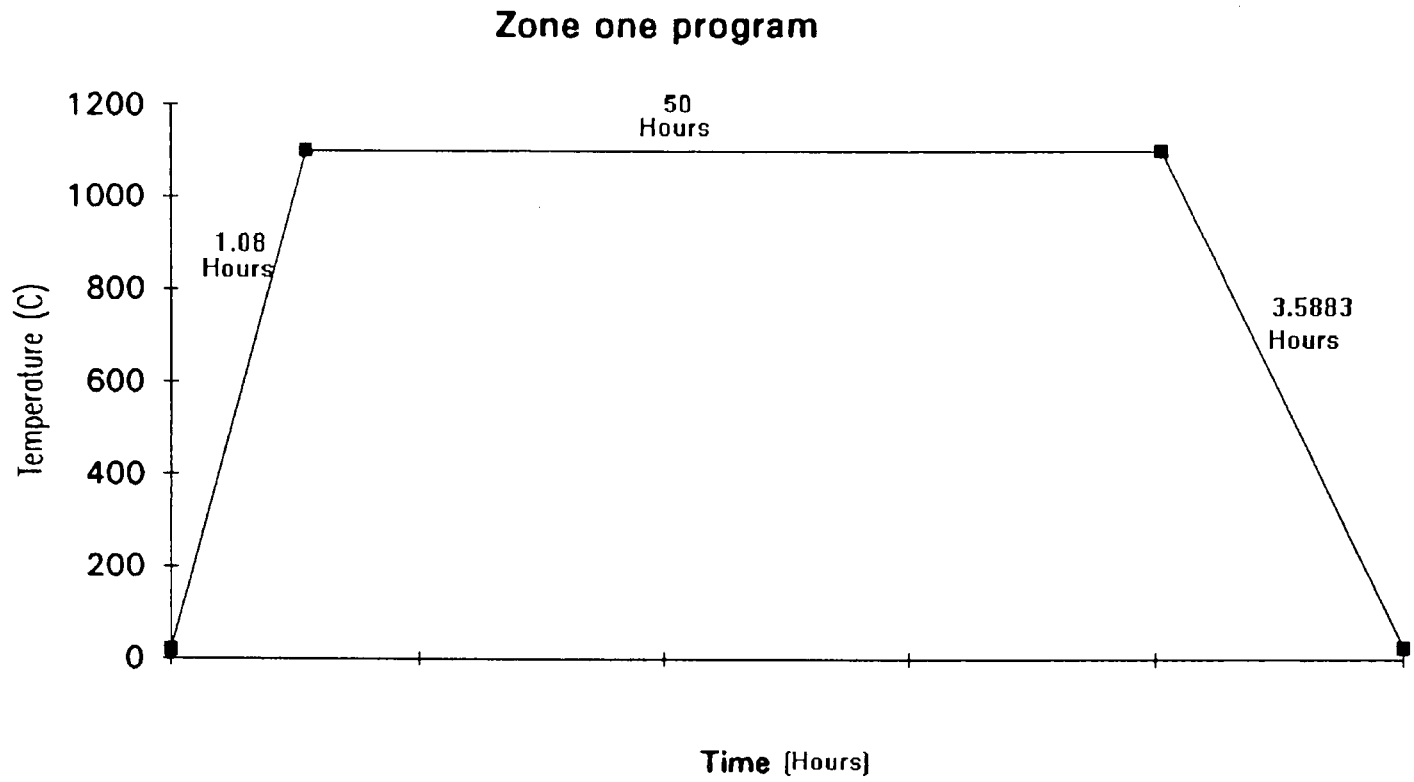

Figure 5.3: Zone one program setting in two-zone furnace

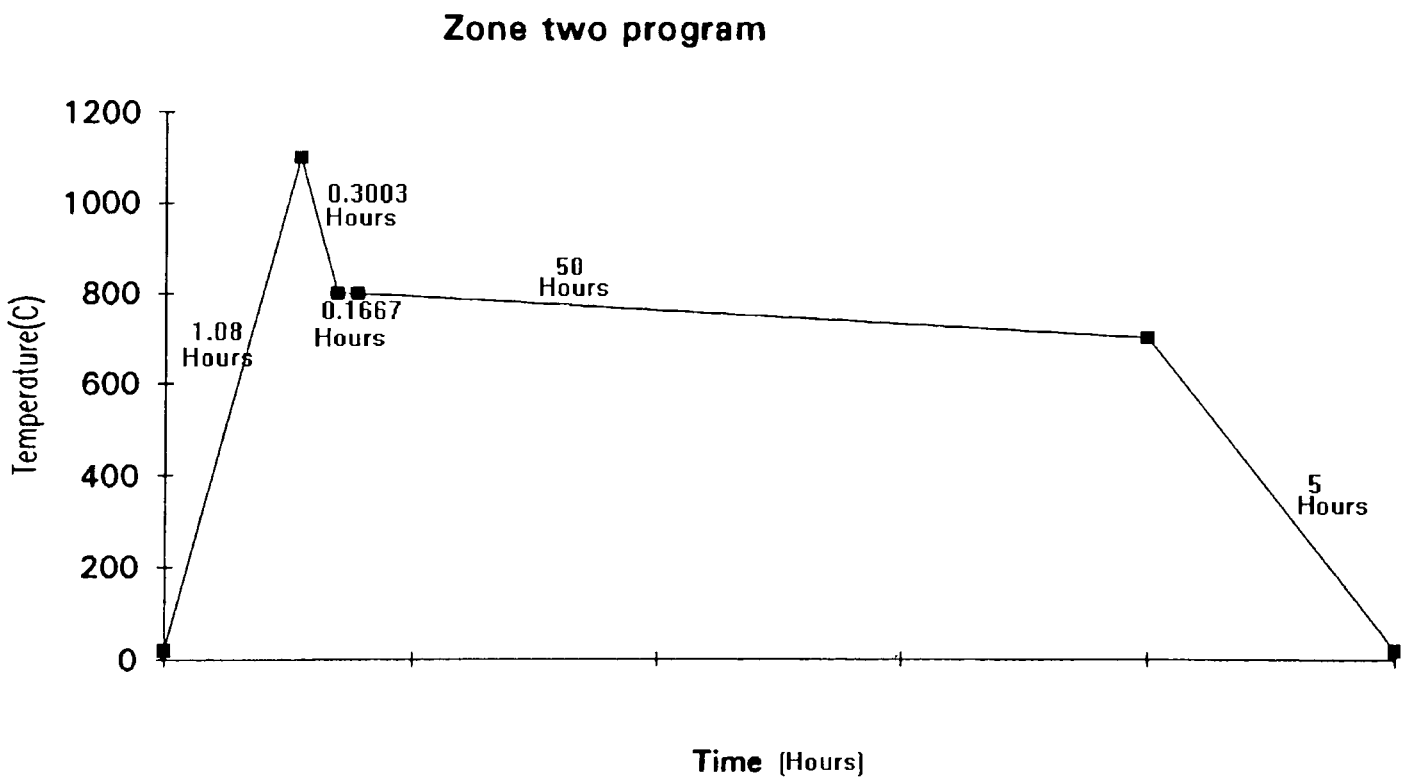

Figure 5.4: Zone two program setting in two-zone furnace

Zone 1 program setting:

Ramp 1:	999 ^{o}C/hour	Fast heating of the precursor sample
Level 1:	1100 ^{o}C	Melt sample (two phases in phase diagram)
Dwell 1:	50 hours	Crystal growth process
Ramp 2:	300 ^{o}C/hour	Cooling down rate
Level 2:	25 ^{o}C	Room temperature
Dwell 2:	End	

Zone 2 program setting:

Set point	1100 ^{o}C	Raise the temperature to two phase zone (Y_2BaCuO_5+L) in the phase diagram.
Ramp 1:	999 ^{o}C/hour	Cooling rate
Level 1:	800 ^{o}C	Set temperature gradient
Dwell 1:	10 minutes	Stabilizing temperature
Ramp 2:	2 ^{o}C/ hour	Starting melt growth process
Level 2:	700 ^{o}C	Complete melt growth process
Dwell 2:	End	

The precursor pellet was placed inside the two zone furnace at the position (D) 14 cm from the front entrance of the furnace. The temperature gradient in the furnace was controlled by both controllers in zone 1 and zone 2. When the temperatures in both zone 1 and zone 2 were raised to 1100 ^{o}C, the whole precursor pellet was heated into the two-phase region (Y_2BaCuO_5+L) in phase diagram (Fig.5.1). Fast cooling of zone 2 to 800 ^{o}C while maintaining zone 1 at 1100^{o}C discouraged the growth of the Y_2BaCuO_5 phase and set the front part of the precursor pellets at about 1010 ^{o}C to start the growth of the $YBa_2Cu_3O_{7-x}$ superconductor crystals. The temperature gradient in the furnace then is given by line A in Fig.5.5. As the temperature in zone 2 is slowly cooled to 700^{o}C while zone 1 remained at 1100^{o}C, the temperature

gradient in the furnace slowly shifts to line B in Fig.5.5, which makes the position at 1010 ^{o}C move through the sample. Meanwhile the temperature at the front part of the precursor pellet gradually cools down to below 960^{o}C (C-C' line in Fig.5.5). Then the furnace is gradually cooled to room temperature. From the temperature profiles (Fig. 5.5) we can see that the melt grown procedure is carried out between line A and line B. The growth of $YBa_2Cu_3O_{7-x}$ superconductor crystals ends at about 985^{o}C according to Fig.5.1, and so the maximum crystal length of the $YBa_2Cu_3O_{7-x}$ superconductor crystal will be limited by the D-D' line in Fig. 5.5, which is about 10 mm long. By optimizing the program setting of zone 1 and zone 2, the length of D-D' can be increased and so increase the melt grown crystal length of $YBa_2Cu_3O_{7-x}$. Since this part of the research is not the major part of my subject, the work is left to be improved.

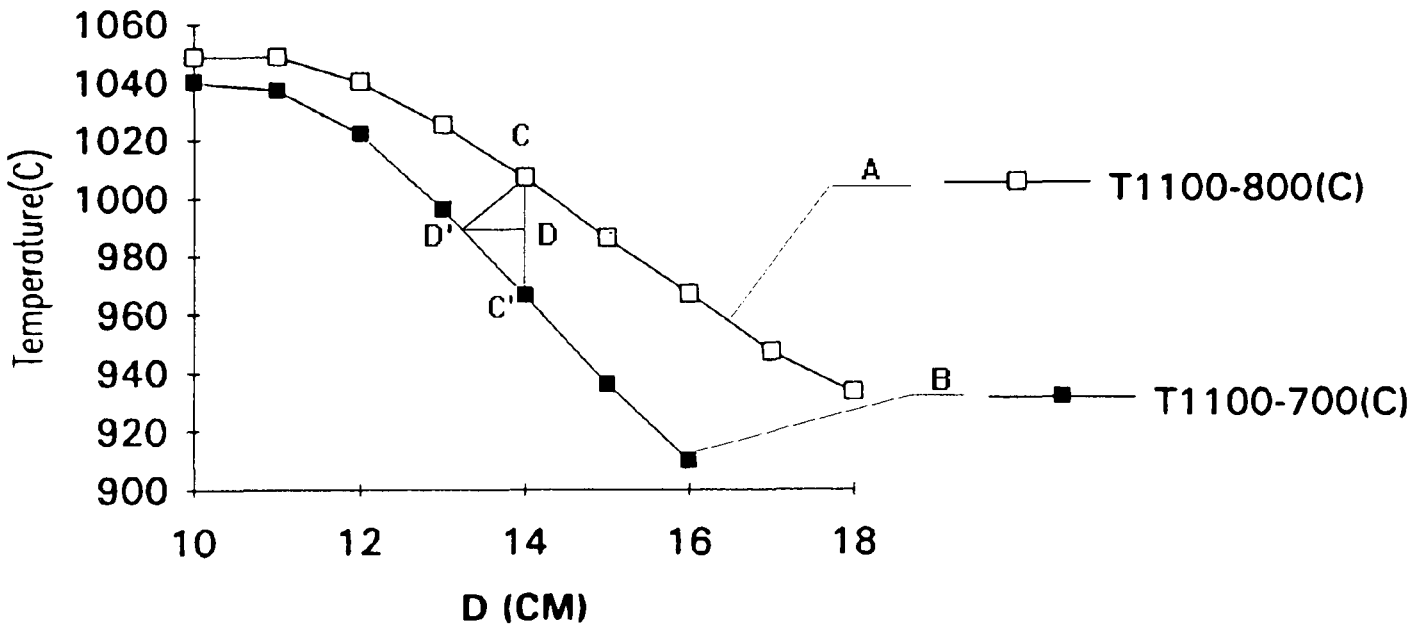

Figure 5.5: The furnace temperature gradient profile

After the melt growth procedure, the sample was oxygenated in a pure oxygen or atmosphere for 15 hours at 600 ^{o}C and cooled at the rate of 100 ^{o}C/h to room temperature.

5.3 Results and discussion

5.3.1 Crystal growth

The properties of the samples are summarised in Table 5.1:

Processing method	Temperature gradient	Texture	Crystal length mm	Tc K	Sample density % theoretical	Jc A/cm^2 at 77K
Sintering	No	None	Negligible	90	70%	10^2 no magnetic field
Melt growth (one-zone)	No	None	0.2-0.3	--	--	--
	Yes	<001>	over 10	90	99%	3600 at 0.5 Tesla *
Melt growth (two-zone)	Yes	<001>	over 10	90	99%	3600 at 0.5 Tesla *

* Measured by magnetic methods by Dr. J.Evetts' Group in the University of Cambridge

Table 5.1: Sample properties

Table 5.1 shows that the samples made by the melt growth technique have unusually large crystal size with greatly improved superconducting properties. The densities of the samples were also estimated by calculating the total outer volumes and carefully weighing them.

For the samples grown without the presence of a temperature gradient in the single zone furnace, the crystals have grown to about 0.2-0.3 mm in diameter (Fig.5.6a), its microstructure is completely different from those of sintered superconductor pellet (Fig. 5.6b) and the pore density is significantly reduced.

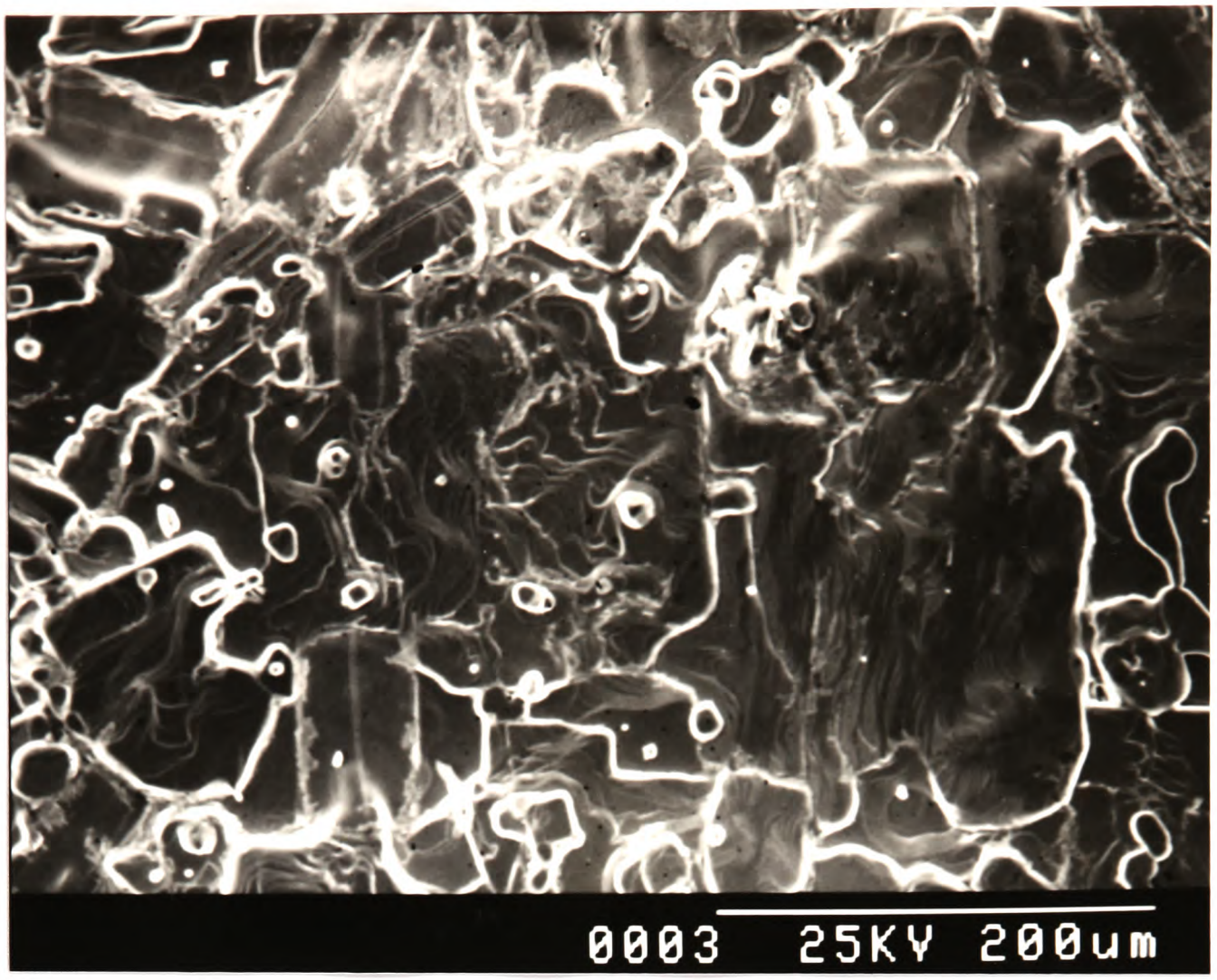

Figure 5.6a: Melt grown small crystal sample

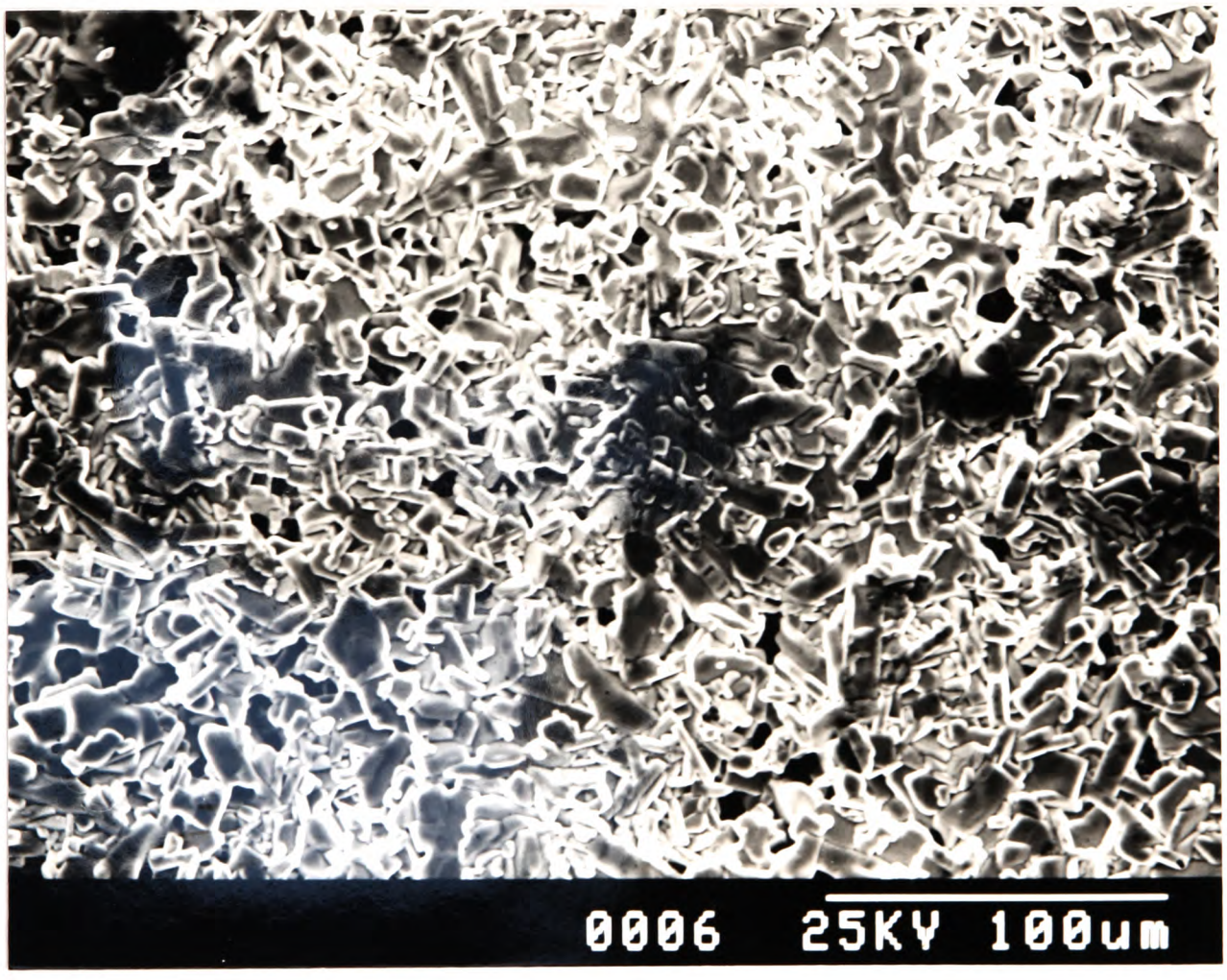

Figure 5.6b: Sintered $YBa_2Cu_3O_{7-x}$ superconductor

With the presence of a temperature gradient of about 40°C/cm, which was achieved by putting the samples away from the centre of the furnace, the crystals have

grown to over 10 mm (Fig.5.7a & Fig.5.7b). Extreme care has to be taken to measure and choose the position inside the one zone furnace to ensure the correct temperature gradient.

The results show that there are no obvious differences between the samples made in the one-zone furnace with the temperature gradient and the two-zone furnace. However, it confirms that the shift of the temperature gradient is a vital factor for the growth of the large textured crystals. Further investigation is required to optimize the annealing conditions to further increase the superconductor crystal size in the two-zone furnace.

Large grains were observed in the samples made in both one-zone and two-zone furnaces. Slight deviation from the conditions described above, especially the sample position (temperature gradient condition) and the cooling speed, resulted in much smaller grain size and possible loss of the texturing.

Figure 5.7a: Melt grown textured large crystal sample (whole sample)

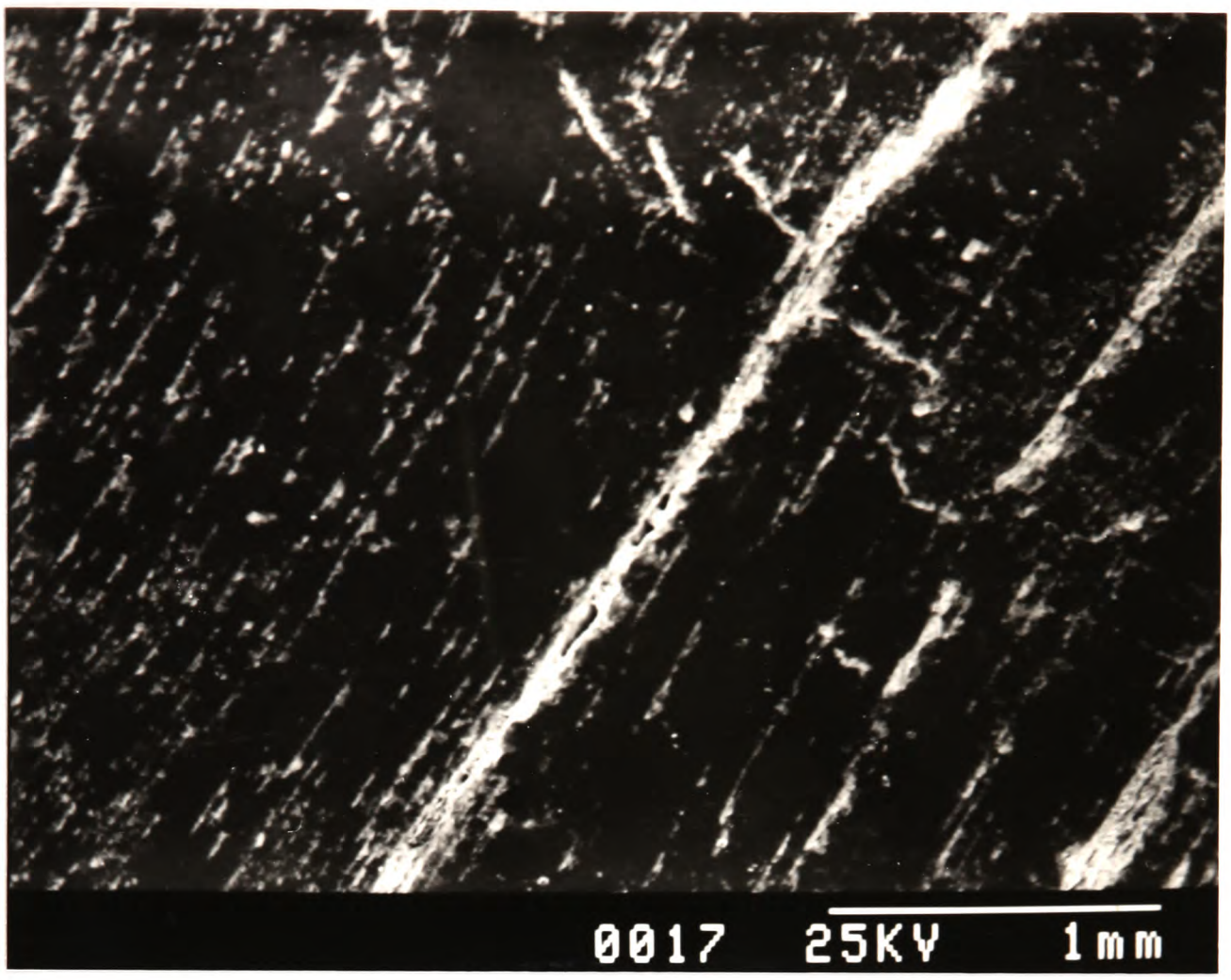

Figure 5.7b: Melt grown textured large crystal sample (partial sample)

The crystallization of the $YBa_2Cu_3O_{7-x}$ grains starts from the tip of the sample and many small grains are nucleated in each sample. However, there were probably only a few grains with preferable crystalline direction to further develop into the large textured crystals (Fig.5.8). They all grew in the same direction with very slight deviation from the direction of the temperature gradient. Some of them grew into large crystals with size over 10mm long in the longitudinal direction. At the end of the crystal growth process, the grain size is usually reduced and the texture disappears. This is probably due to the mismatching of the growing speed and the shifting of the temperature gradient, although in very few of the samples did the crystal growth go through to the end of the samples (Fig 5.9).

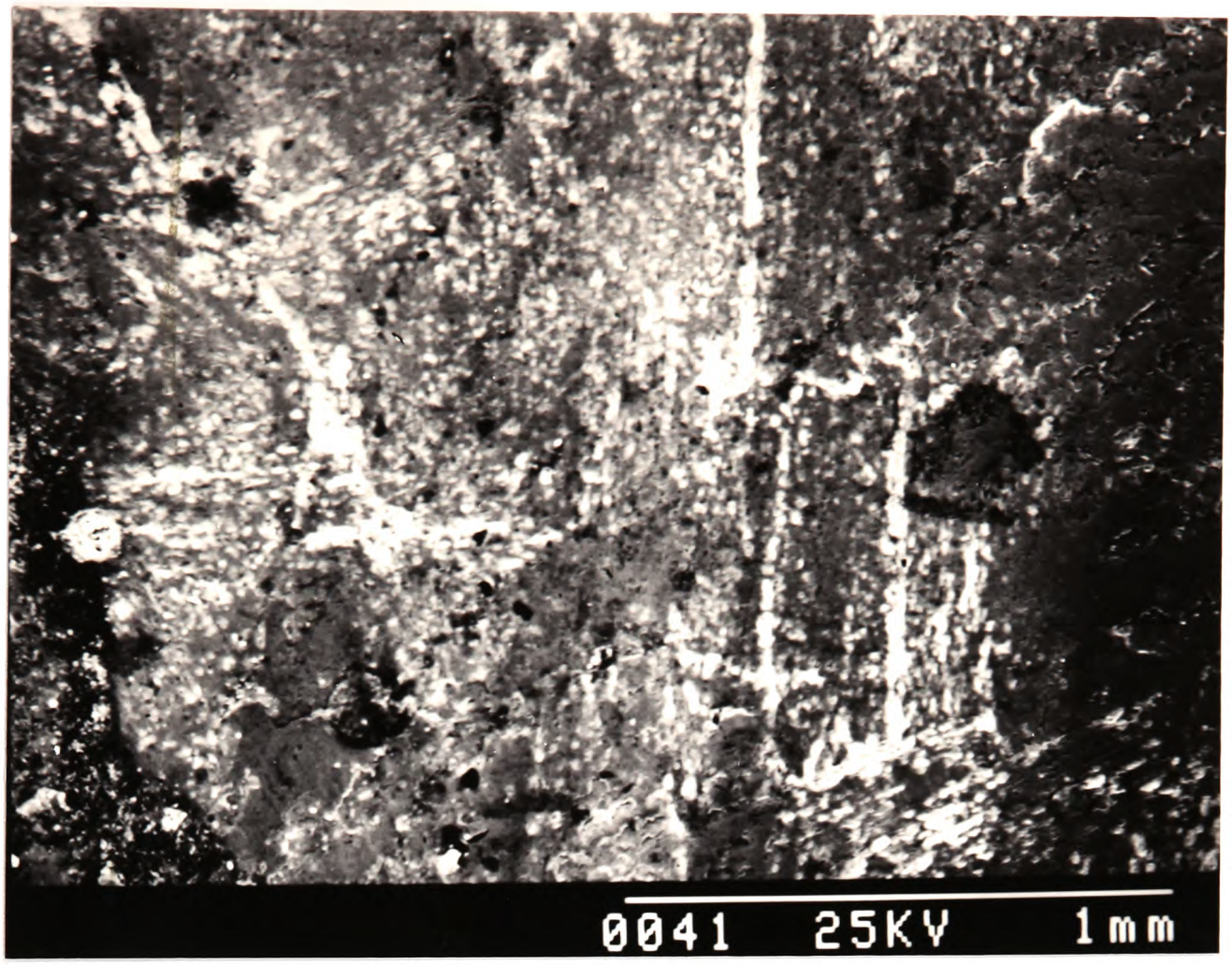

Figure 5.8: The nucleation point of large crystals

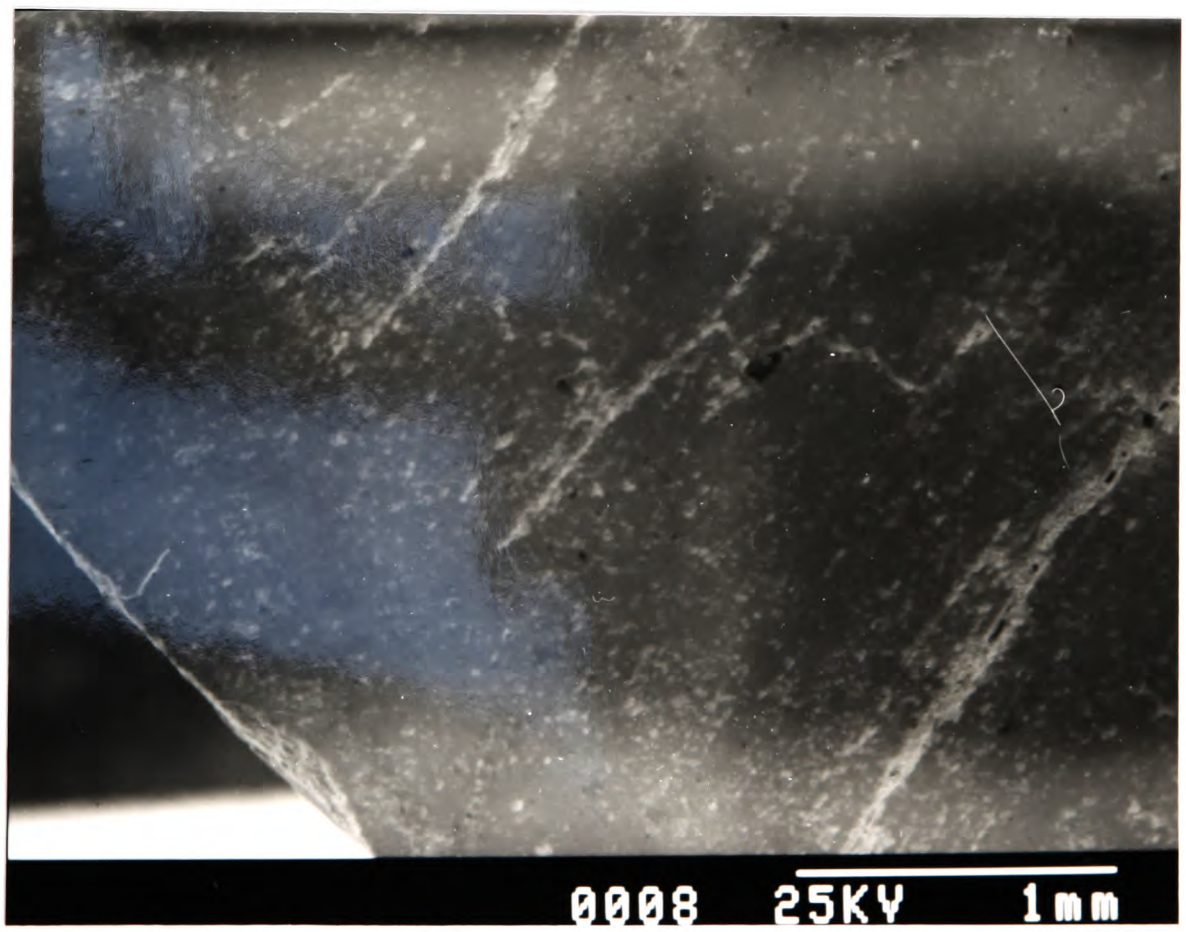

Figure 5.9: The clean end of the crystal growth

The temperature gradient shift technique for melt growth processing has an advantage over the mechanical method of moving the sample inside the furnace. It avoids the samples suffering from mechanical vibrations which might cause disturbance of the crystal growth.

5.3.2 The microstructure of melt grown $YBa_2Cu_3O_{7-x}$ samples

When observed by optical microscopy, scanning electron microscopy and the electron microprobe, there are mainly two types of large scale crystal defects in the melt textured crystal samples: fine Y_2BaCuO_5 precipitates as spheroidal inclusions in the $YBa_2Cu_3O_{7-x}$ crystal matrix (Fig.5.10) and microcracks (Fig.5.11).

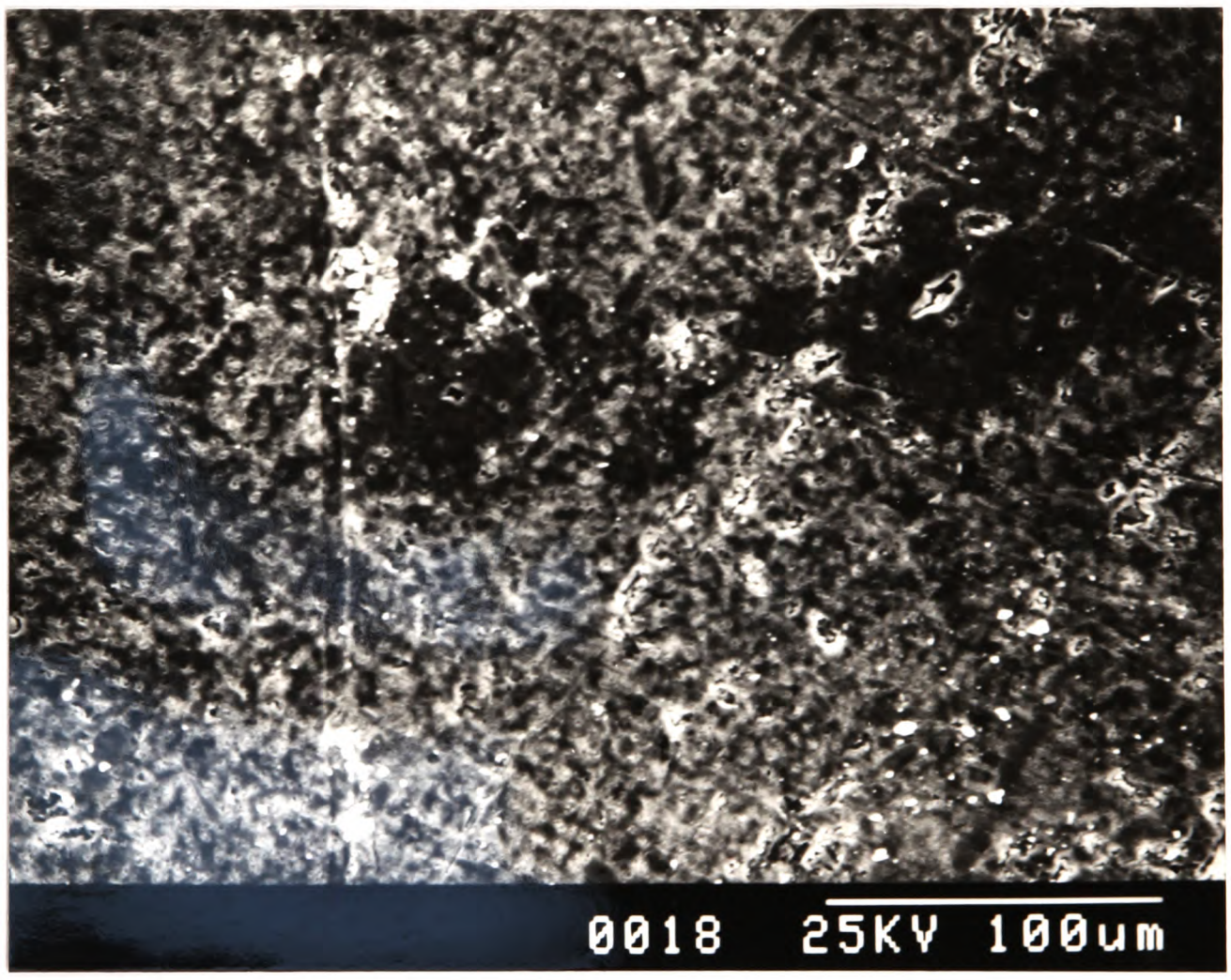

Figure 5.10: Fine Y_2BaCuO_5 inclusions in $YBa_2Cu_3O_{7-x}$ crystal matrix

Fig.5.11 shows that the cracks originated from the boundary of the melt ($BaCu_xO_x$) and the $YBa_2Cu_3O_{7-x}$ crystal matrix, which implies that the cracks in this sample were caused by contraction from solidification of the last remaining melt.

Figure 5.11: A crack source in a $YBa_2Cu_3O_{7-x}$ crystal

To reduce the crack formation, the sample was slowly cooled to 950^{o}C at a rate of 1 ^{o}C/hour instead of to 985 ^{o}C in the 5-ramp program, and an additional slow cooling procedure was added to pass the tetragonal to orthorombic structure transition at the rate of 10^{o}C/hour.

The results show that the crack density has been reduced, which means the slow cooling procedure does help to reduce the crack caused by the stress from the liquid state-solid state transition and the tetragonal-orthorhombic structure transition. The crystal size of the sample made in this method is very large, therefore the stresses generated inside the material get more and more difficult to release and there are still many cracks in the sample (Fig.5.12). This is the problem for further improvement of crystal size, it is very hard to avoid cracking if the grain size is large.

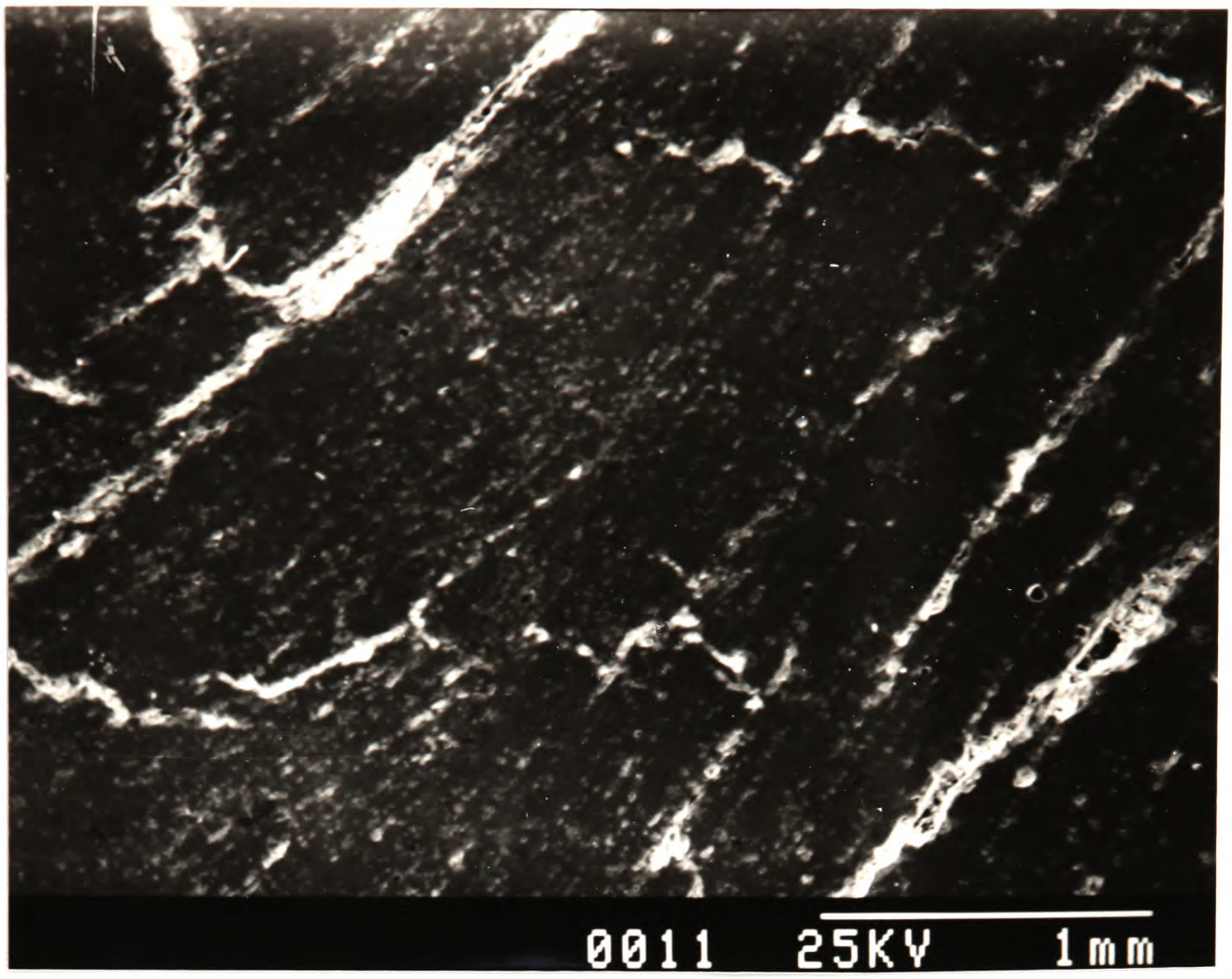

Figure 5.12: The cracks in a slow cooled $YBa_2Cu_3O_{7-x}$ crystal

This technique described above consists of melting the material to erase the previous granular structure and improve the density of the material from 60-70% to essentially 100% theoretical density, which not only eliminates the pores in the materials but also formed a strong texture in the $YBa_2Cu_3O_{7-x}$ superconductor.

5.3.3 Texture and properties of the melt grown $YBa_2Cu_3O_{7-x}$

The texture of the melt grown samples has been studied by X-ray diffraction (XRD) analysis. Fig.5.13 shows an XRD spectrum of a sample of sintered $YBa_2Cu_3O_{7-x}$ superconductor - there is no evidence of texture in this material.

The XRD spectrum of the melt growth sample (Fig.5.14) shows the sample is highly <00l> oriented because only the <00l> peaks have significant height. Some of the crystals have been removed from this sample mechanically, and the XRD spectrum of these crystals is shown in Fig.5.15.

Although most the samples have c-axis texture (Fig.5.14 & 5.15), other grain orientations have also been observed in this experiment. The XRD spectrum of an

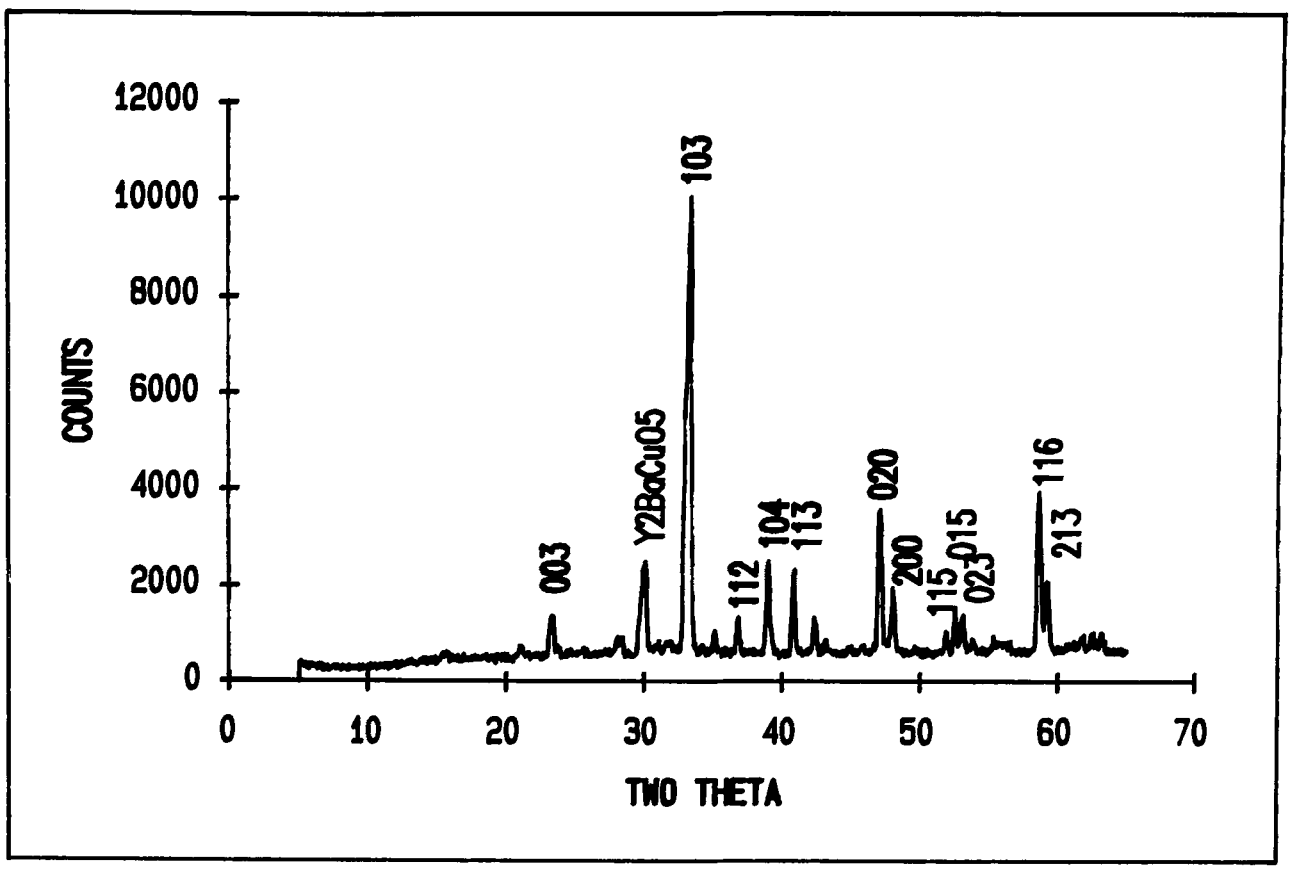

Figure 5.13: XRD spectrum of sintered YBa2Cu3O7-x superconductor

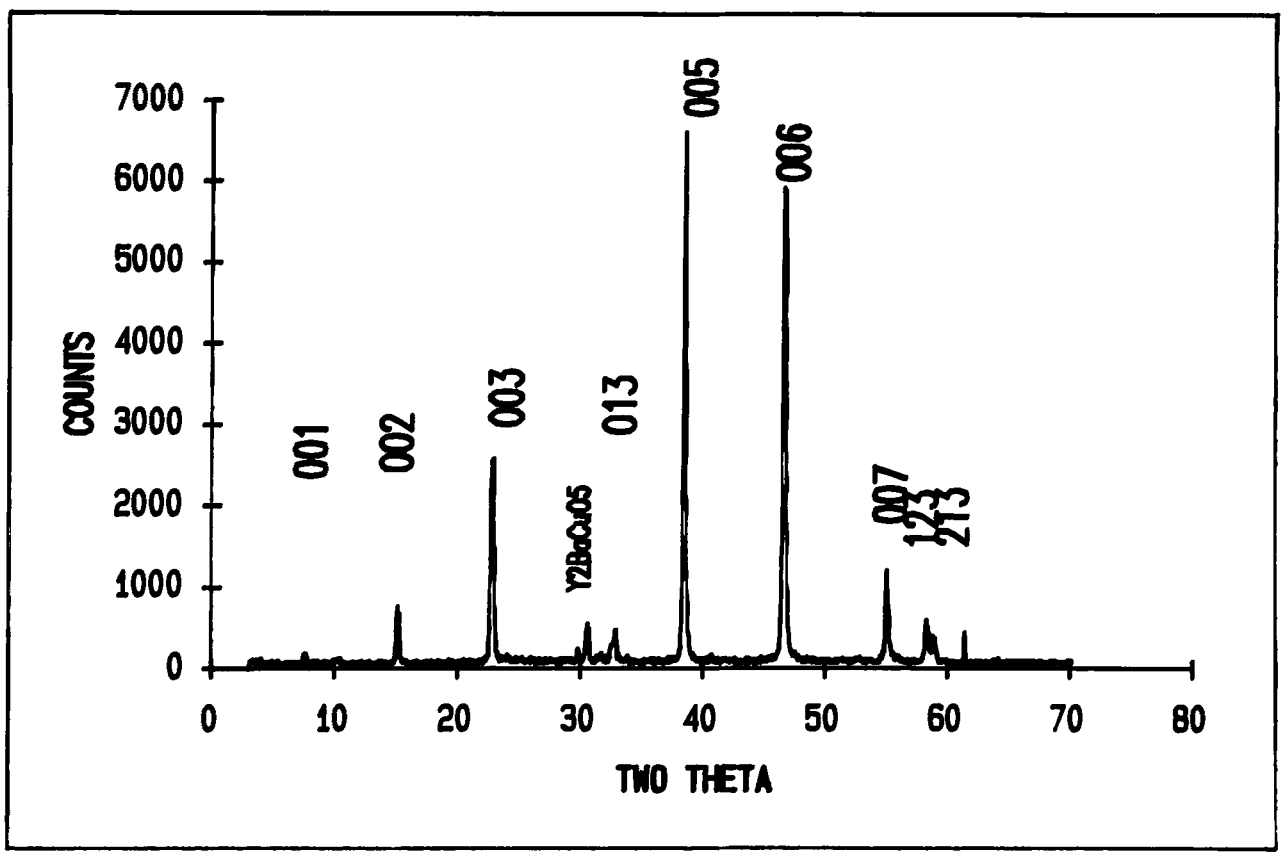

Figure 5.14: XRD spectrum of melt growth YBa2Cu3O7-x superconductor

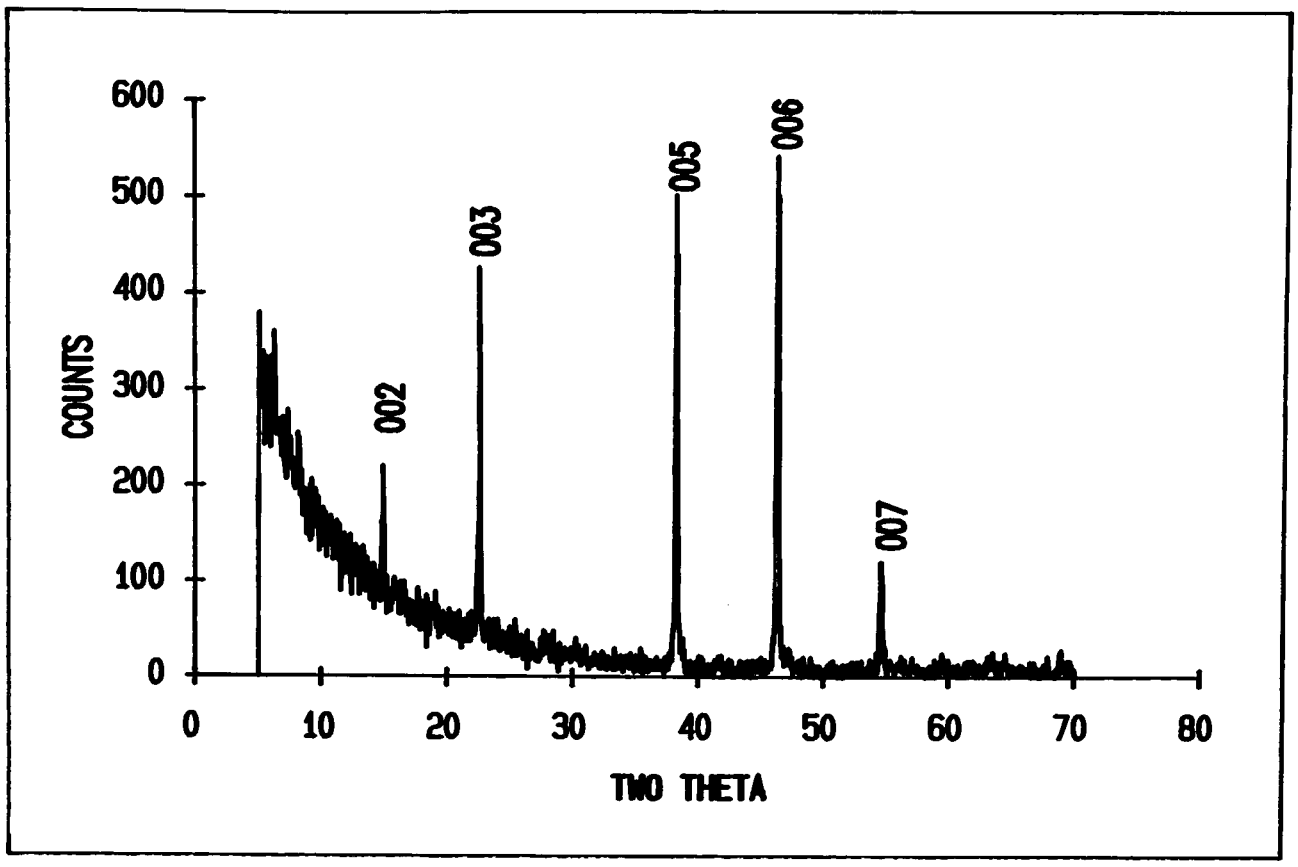

Figure 5.15: XRD spectrum of crystal taken from a melt processed YBa2Cu3O7-x

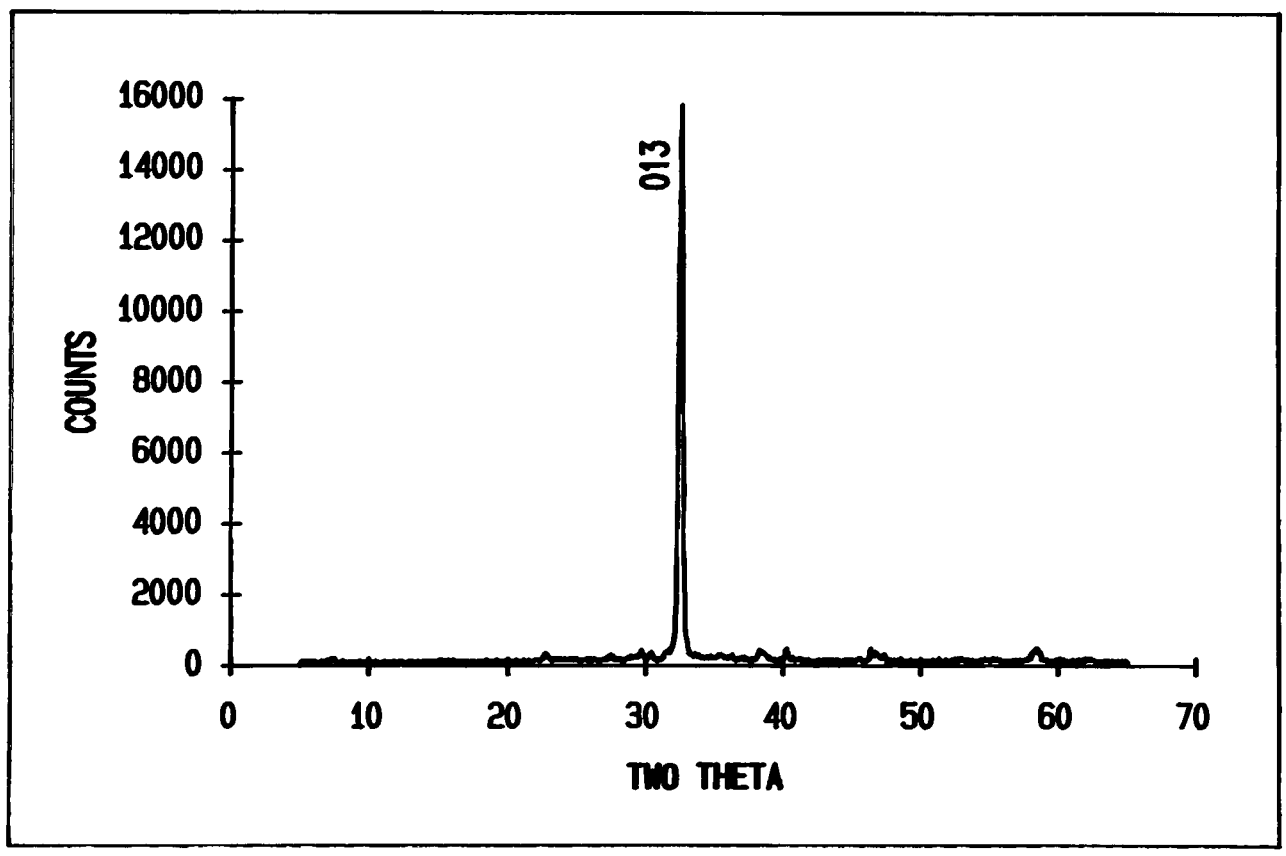

Figure 5.16: XRD spectrum of melt growth YBa2Cu3O7-x superconductor showing only the (013) peak

<013> textured sample and a <116> textured sample are shown in Fig.5.16 and 5.17.

This texture in the melt processed sample has partially solved the extreme anisotropy problem of the $YBa_2Cu_3O_{7-x}$ superconductor which requires each grain to be aligned with the CuO_2 planes parallel, because the $Y_1Ba_2Cu_3O_{7-x}$ superconductor has a strong tendency for preferential crystal growth parallel to the CuO_2 planes. Therefore the high critical current density has been achieved. The large grained material also has a significantly lower density of grain boundaries in any given length of current path.

The Jc of this material is over 3600 A/cm^2 at 0.5 Tesla, 77K, which was measured in Dr. J.E. Evett's group at Cambridge University.

5.4 Conclusions

A melt growth technique has been developed based on the peritectic reaction mechanism. This temperature gradient crystal growth technique in both one-zone and two-zone furnaces has produced large grained texture $YBa_2Cu_3O_{7-x}$. The samples have crystal size over 10 mm with greatly improved superconducting properties and show potential for further improvement.

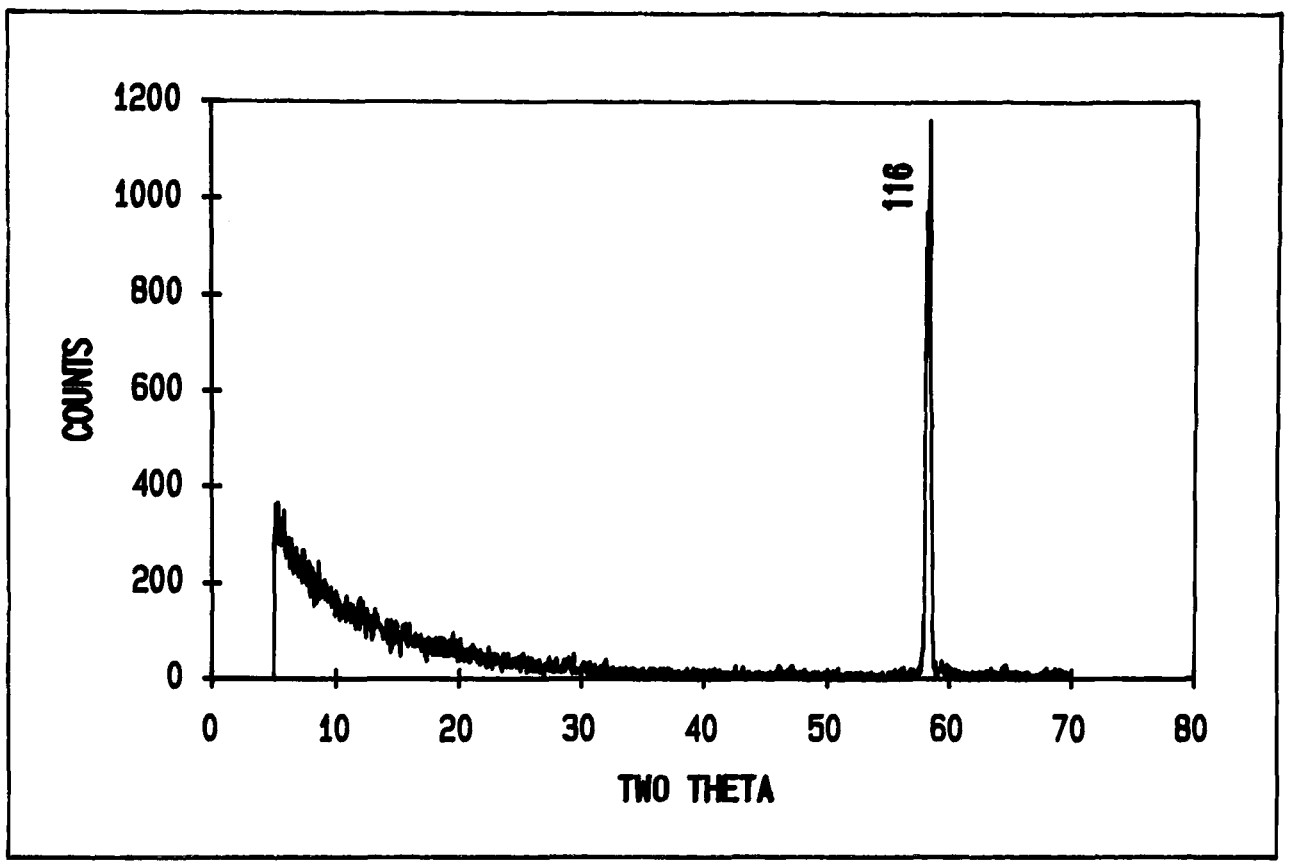

Figure 5.17: XRD spectrum of melt growth YBa2Cu3O7-x superconductor showing only the (116) peak

Chapter 6

Electrical contacts to high temperature superconductor

6.1 Introduction

The difficulty in making low resistivity electrical contacts is one of the main obstacles to the application of high T_c superconductors. As we have seen from previous chapters, reactive metal contacts have very high contact resistivities, especially after oxygenation annealing which is vital for $YBa_2Cu_3O_{7-x}$ to obtain the right oxygen stoichiometry in order to maintain superconducting properties. Noble metal contacts, or more precisely only gold and silver contacts, have been shown to have contact resistivities below 10^{-8} Ohm cm^2 after proper heat treatment. But there is doubt about the long term mechanical stability of noble metal contacts on high Tc superconductors, especially for those noble metal contacts made without further annealing procedure on the less porous, high Jc, superconductors such as single crystals or melt textured $YBa_2Cu_3O_{7-x}$. Oxygen stoichiometry changes in $YBa_2Cu_3O_{7-x}$ during contact making is a also major problem in obtaining low resistivity contacts.

The purpose of this part of work is to investigate the relations between contact properties, contact materials and processing methods, find out a reproducible method for making rugged and low resistivity electrical contacts, and investigate the microstructure and the conduction mechanisms at the contact interface.

6.2 Experimental methods

The electrical contact work carried out in this chapter went through following procedures: superconductor sample preparation, superconducting property measurement, contact preparation, electrical measurement, and microstructure analysis.

6.2.1 Superconductor sample preparation

High quality superconductor samples are essential for making meaningful comparisons between different contacts. The $YBa_2Cu_3O_{7-x}$ samples are prepared and tested by the methods described in chapter 5.

Due to the rapid degradation of $YBa_2Cu_3O_x$ in the presence of water and carbon dioxide, $YBa_2Cu_3O_x$ ceramic pellets were cut into test samples of dimensions 10 x 1 x 1 mm^3 using a diamond saw without any lubricant. The top surfaces of the superconductor samples were mechanically ground by a series of SiC papers to the finest 1200 grade, then polished by 6μm diamond paste with non-aqueous glycerol lubricant. The highly polished surfaces of the samples were cleaned with absolute alcohol, dried with cotton wool, and stored in a vacuum or sealed container with silica gel.

Before making the contacts, a thin surface layer of the superconductor was removed by mechanical polishing with 6 μm diamond paste, which helped to get rid of the surface degradation layer of the superconductor due to the exposure to atmosphere.

6.2.2 Superconducting property measurement

The superconducting transition of the bulk superconductor sample was measured by four probe measurement (Fig.6.1).

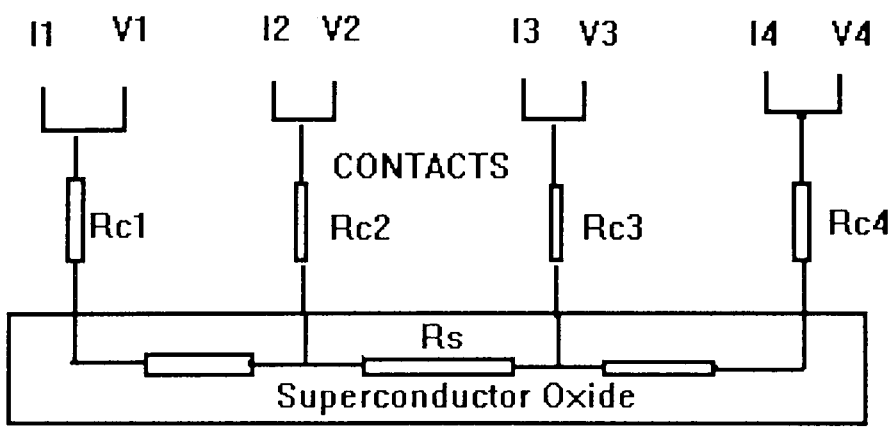

Figure 6.1: A schematic diagram of contact configurations for electrical measurement where R_C refers to specific contact resistance, R_S refers to the superconductor

resistance, and I, V are the current or voltage for the four- terminal contacts.

The normal measurement method is to pass current (I) through terminals 1 and 4, and measure the voltage (V) between terminals 2 and 3 (Fig.6.1). The superconductor resistance can then be calculated by $R_S = V/I$. A typical result is shown in Fig.6.2.

Fig.6.2 shows that the superconducting transition is very sharp which indicates the bulk superconductor sample is a single phase $YBa_2Cu_3O_{7-x}$ with correct oxygen stoichiometry. The conditions for sample preparation used in chapter 5 were fixed to ensure all the $YBa_2Cu_3O_{7-x}$ samples used for contact resistivity research have good and consistent superconducting properties.

6.2.3 Contact sample preparation

The materials used for making electrical contacts and their relevant properties are listed in Table 6.1.

Table 6.1: Contact materials

Contact materials	Type	Melting point K	Bulk resistivity mΩ cm	Contact type	Contact thickness(m)
Titanium	Reactive	1993	54.0	Evaporation	10^{-6}
Titanium plate	Reactive	1993	54.0	Diffusion bonding	10^{-3}
Palladium	Noble	1827	10.8	Evaporation	10^{-6}
Silver	Noble	1234.9	1.6	Evaporation	10^{-6}
Silver epoxy	Noble	----	----	Curing epoxy	10^{-3}
Gold	Noble	1337.4	2.20	Evaporation	10^{-6}
Gold plate	Noble	1337.4	2.20	Diffusion bonding	10^{-3}
Molybdenum plate	Reactive	2883	5.2	Sputtering	10^{-6}

The thin film metal contacts on superconductor were deposited through a mask

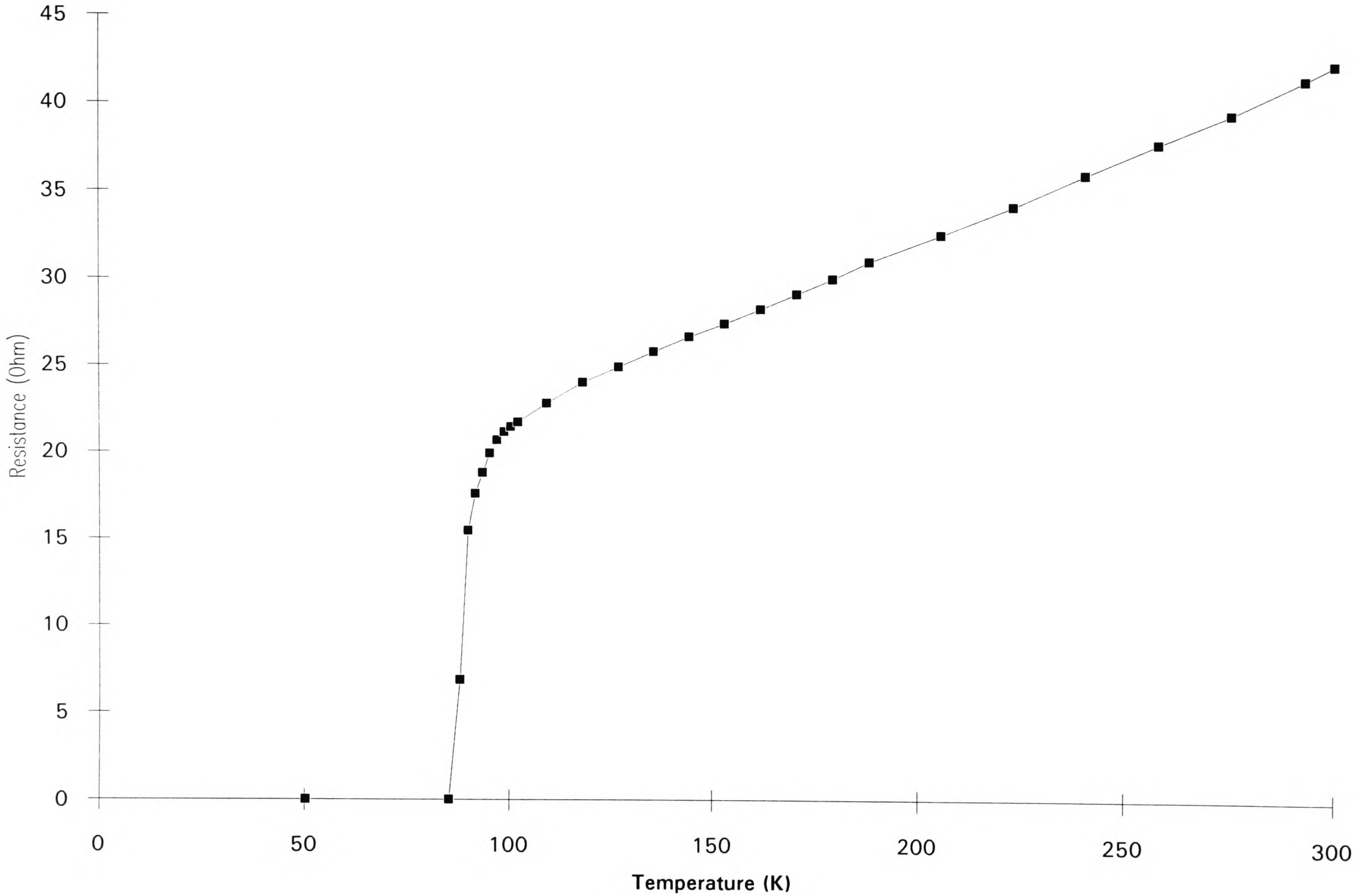
45
40
35
30
25
20
15
10
5
0
Resistance (Ohm)
0
50
100
150
200
250
300
Temperature (K)

by thermal evaporation or sputtering (Fig.6.3).

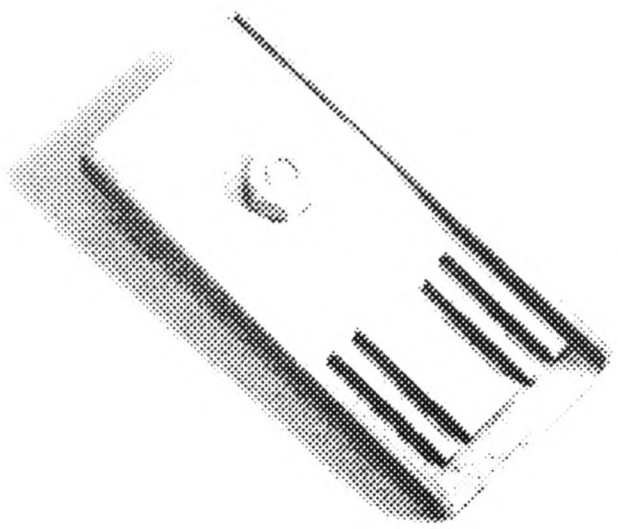

Figure 6.3: Evaporation/sputtering mask

The gaps in the mask are about 1mm wide, which made each electrical contact 1 mm^2 in area. The evaporation and sputter deposition of metal contacts was all carried out in a vacuum of $< 10^{-5}$ mbar.

For the diffusion bonded contact samples, the contact metal plates were reduced to the desired size and mechanically polished by the method described above. Then the metal plates were placed on the selected area of the $YBa_2Cu_3O_{7-x}$ pellet and pressure was applied on the top of metal contacts to press them firmly against the superconductor using the equipment which will be shown in chapter 7. Then the contact samples were placed inside the furnace and annealed at the different temperatures required to bond each contact material.

After the electrical contacts were prepared, silver wires of 0.5 mm in diameter were connected to the evaporated/sputtered thin film contacts on the superconductor by high conductivity silver paint. For the diffusion bonded metal plate contacts, silver wire leads were directly connected by ordinary Sn-Pb soldering.

6.2.4 Electrical measurement:

Contact resistances were measured by the three-probe method, by driving current (I) through terminals 2 and 3 and measure the voltage (V_c) between terminals 1 and 2 or 3 and 4, see Fig.6.4.

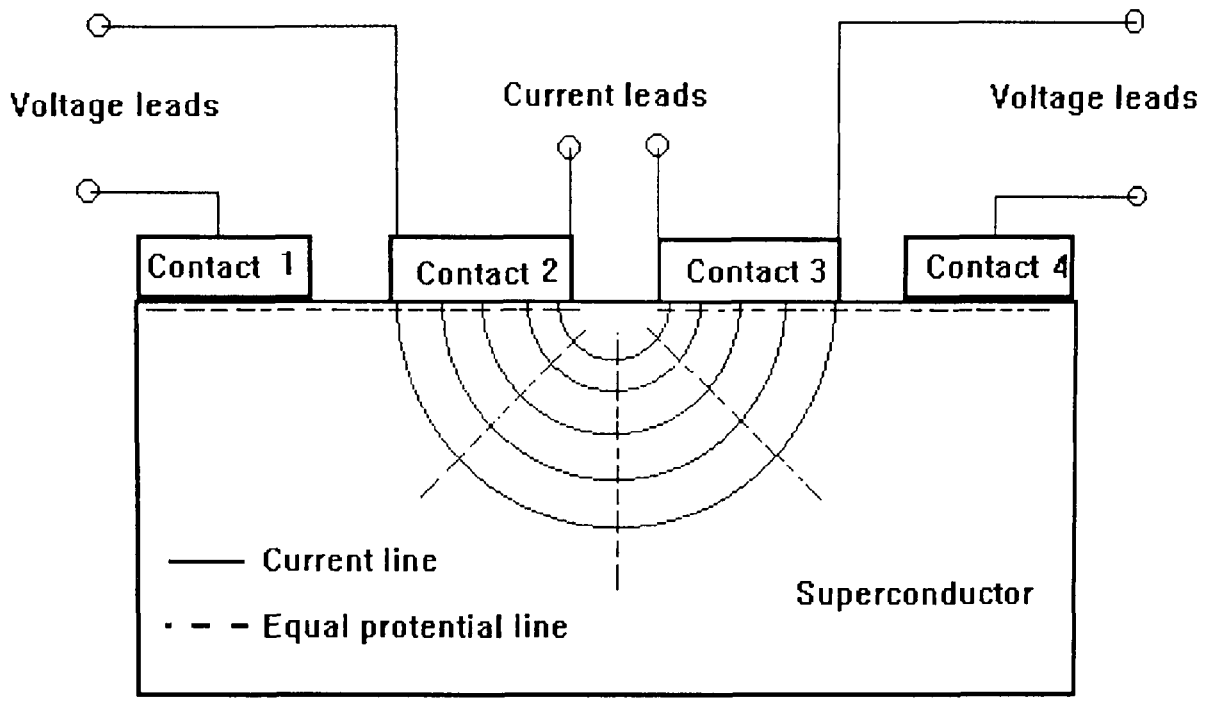

Figure 6.4 Contact resistance measurement configuration (after Lakshmikumar, 1989)

Since the equi-potential line at terminals 1 and 4 is infinitely close to the surface of the superconductor, the voltage differences between terminal 1 and 2 or 3 and 4 (Vc) can be considered as the voltage drop from the current (I) passing through terminal 2 or 3. So the contact resistance R_C of contact 2 or 3 is calculated by $R_C=V_C/I$, and the contact resistivity ρ_C of the terminal is calculated by $\rho_C=R_C x A_C$, where A_C is the contact area.

Pre-measurement was carried out to test the homogeneity of the sample before contact resistivity measurement, which is important for these measurements above Tc. This ensured that no extraneous voltage was developed between terminals 1 and 2 when current was passed through terminals 3 and 4.

To minimize the resistance between the leads and the contact surface, high conductivity silver paint was used to connect silver wires to the electrical contacts. The silver painted contacts were left in air for over 12 hours until completely dry.

The contact resistance were measured as a function of temperature in a Cryodyne closed cycle He cryostat. Each contact sample was glued with high thermal conductivity "GE" varnish to a copper disc substrate, and the copper disc was tightly pressed against the cold head of the cryostat by four copper screws.

The equipment used in the electrical measurement of the superconducting and

contact properties were comprised of following parts:

1) Cryodyne closed cycle Helium cryostat.

2) Lake Shore Cryotronics temperature controller, model DRC 91C

3) "Princeton Applied Research 5208" Two Phase Lock-in Analyser made by EG & G

4) Brook Deal 9473 signal source made by EG & G

5) An IBM compatible computer.

The electrical leads were connected into the low temperature chamber which enabled the monitoring of the superconductor resistance or contact resistance as a function of temperature. The resistances were monitored during the cooling procedure. After it was cooled to the lowest temperature the system could reach (20K for thin sample and 50~60 K for bulk sample), the samples were heated up in a controlled manner (computer controlled), the temperature of the cryostat and the voltage signal were measured by the lock-in amplifier. The electrical measurement equipment is schematically illustrated in Fig.6.5

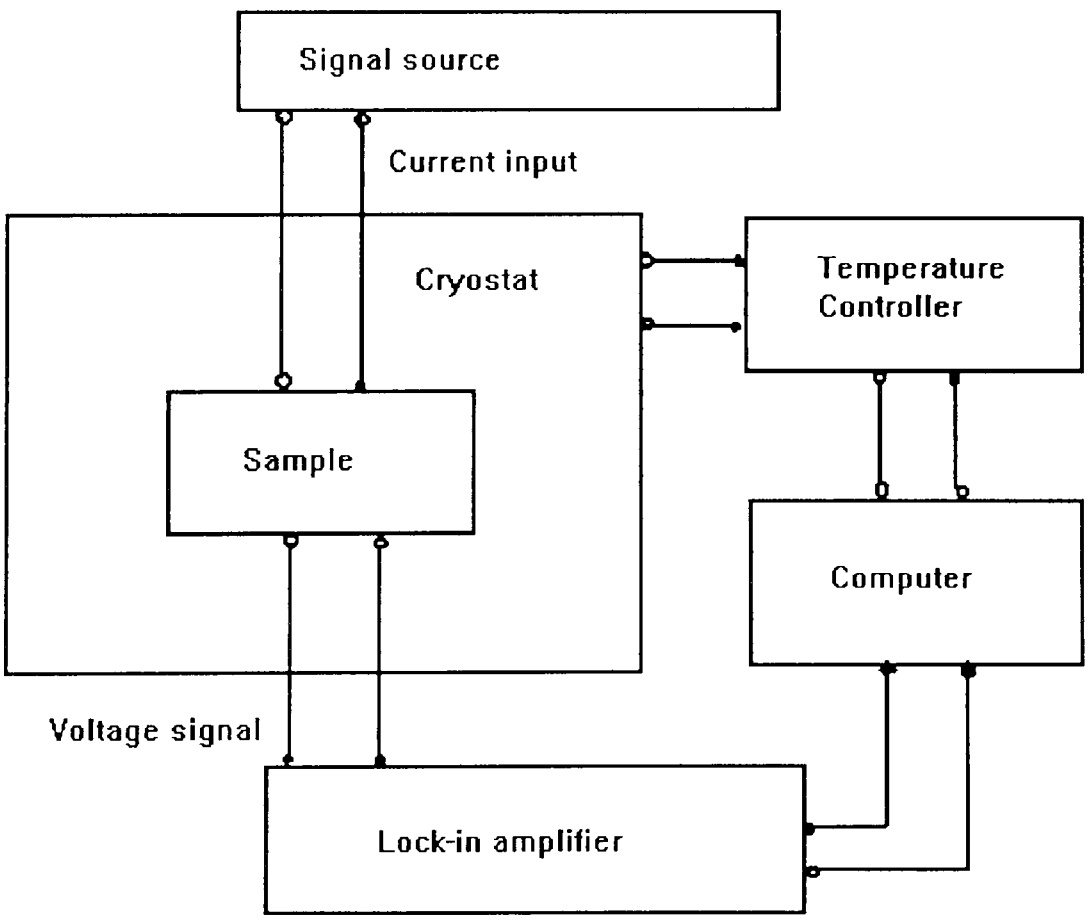

Figure 6.5 Schematic diagram of equipment setting for electrical measurement.

Initially, the temperatures were monitored from a silicon diode attached directly

to the cold head which measured the temperature of the copper disc. A separate experiment was carried out to calibrate the sample temperature later. The temperature recorded by this method typically is 30K lower than the actual temperature of the superconductor. These differences vary with temperatures, sample thickness, varnish connecting quality and the equilibration time. To overcome these problems the cryostat was rewired and another diode incorporated which was glued or pressed on the top of the sample. This improved the accuracy of the temperature measurement.

6.2.5 Microstructural examination of the contact interface

In order to examine the microstructure and interfacial reactions at the contact/superconductor interface, cross sectional samples of the contacts were prepared for optical microscope, SEM and electron microprobe analysis.

In the cases that the contact metal layers were very thin after the annealing procedure, typically below 1 μm, it is very difficult to reveal the contact interface structure and the composition of the interface layer, so diffusion bonded superconductor/metal plate composite samples were used to simulate the actual contact condition, and cross sections of the composite samples were polished and studied instead of the thin film contact.

Another special case was the contact of titanium/melt-textured superconductor. The interface was studied directly from the surfaces prepared by splitting the composite.

The optical microscope was frequently used during the cross section sample preparation. The contact interface is very brittle due to the extremely different properties of the materials on each sides, and the composites easily fall apart during the sample mounting and polishing procedure. Optical microscopy can provide a convenient inspection method to identify the presence of these kinds of cracks at the interface, and help to optimise the sample preparation conditions to provide less damaged interface samples for SEM and electron microprobe analysis.

The SEM was used to examine the morphology of the interface structure, and

the back scattered electron image mode was used to identify the presence and distribution of second phases at the interface. All the SEM experiments were carried out on either Hitachi S510 or JSM 35X scanning electron microscopes.

Compositional analysis of the interfaces between superconductors and contact metals were carried out in the Cameca Camebax Microprobe - Energy Dispersive X-ray Spectrometry (EDS) was used for qualitative analysis; Wavelength Dispersive X-ray Spectrometry (WDS) was used for quantitative analysis. The characteristic X-rays are generated by the electron beam-atom interaction during the electron scattering processes, and the X-rays continue to be generated until the electron energy falls below the critical excitation energy E_C for a given X-ray wavelength. This results in the generation of X-rays from a volume of the sample much larger than the beam itself. This volume is approximately pear shaped and varies its size with electron beam energy, sample atomic number Z and density. The typical width and depth are 1-3 μm. Any second phase present at the contact/superconductor interface in regions smaller than 1μm will not be detected accurately, the result will include the signals generated from the surrounding materials. Since the accurate analysis of low energy $O_{K\alpha}$ X-rays is difficult, the oxygen concentration of the materials is calculated by the remainder method. In another words, the microprobe measures the metal concentrations directly from the signals and then calculates the oxygen concentration by the difference between the total metal percentages and 100%.

6.3 Silver thin film contacts

As discussed in chapter 3, silver is reported to be one of the best contact materials.

My first task was to use silver contacts to find out the proper contact-making procedure, and the processing factors which have the most significant effects on the contact properties.

6.3.1 Experiment

Silver contacts were first deposited on superconductor tape ST provided by GEC through a mask by thermal evaporation. Then the contact samples were put inside the furnace and annealed in air. The silver contacts were tested extensively in this experiment over various experimental conditions to search for a reproducible condition for making low resistivity contacts to the superconductor. The optimum annealing condition for thin film silver contacts in my experiments is 500^{o}C for one hour. After cooling to room temperature, silver wires were attached onto the contacts on the superconductor by high conductivity silver paint.

6.3.2 Experimental results

The silver contact resistivities of the specimens treated at the optimised condition were measured as a function of temperature, and a typical result is shown in Fig.6.6. The silver contact resistivity is $8x10^{-6}\Omega$ cm^2 at temperatures below T_c. This result is highly reproducible, and common properties of silver contacts made by this method are: (1) a small positive temperature dependence above the superconducting transition temperature T_c, (2) a sharp resistance drop at temperatures about T_c, and (3) low contact resistivities in the range 10^{-4}-10^{-6} Ωcm^2 at temperatures below Tc.

However, without the heat treatment at 500^{o}C for one hour, silver contacts have a very large contact resistivity. The typical value is about 10^{-1}-10^{-2} Ωcm^2 with a negative temperature dependence, Fig.6.7.

The silver metal contact layer on the $YBa_2Cu_3O_{7-x}$ became very thin after annealing. To make it easier for SEM analysis, two of the contact samples with silver contact facing each other were pressed and glued together with epoxy, this may increase the chance of finding undamaged interfacial area for study.

SEM and electron microprobe analysis shows no obvious impurity layer at the interface for both good and bad contact samples, and silver thin film can hardly be seen on the SEM image of the cross section of the sample Fig.6.8, only WDS analysis shows that there is silver at the interface. So it is important to employ high density

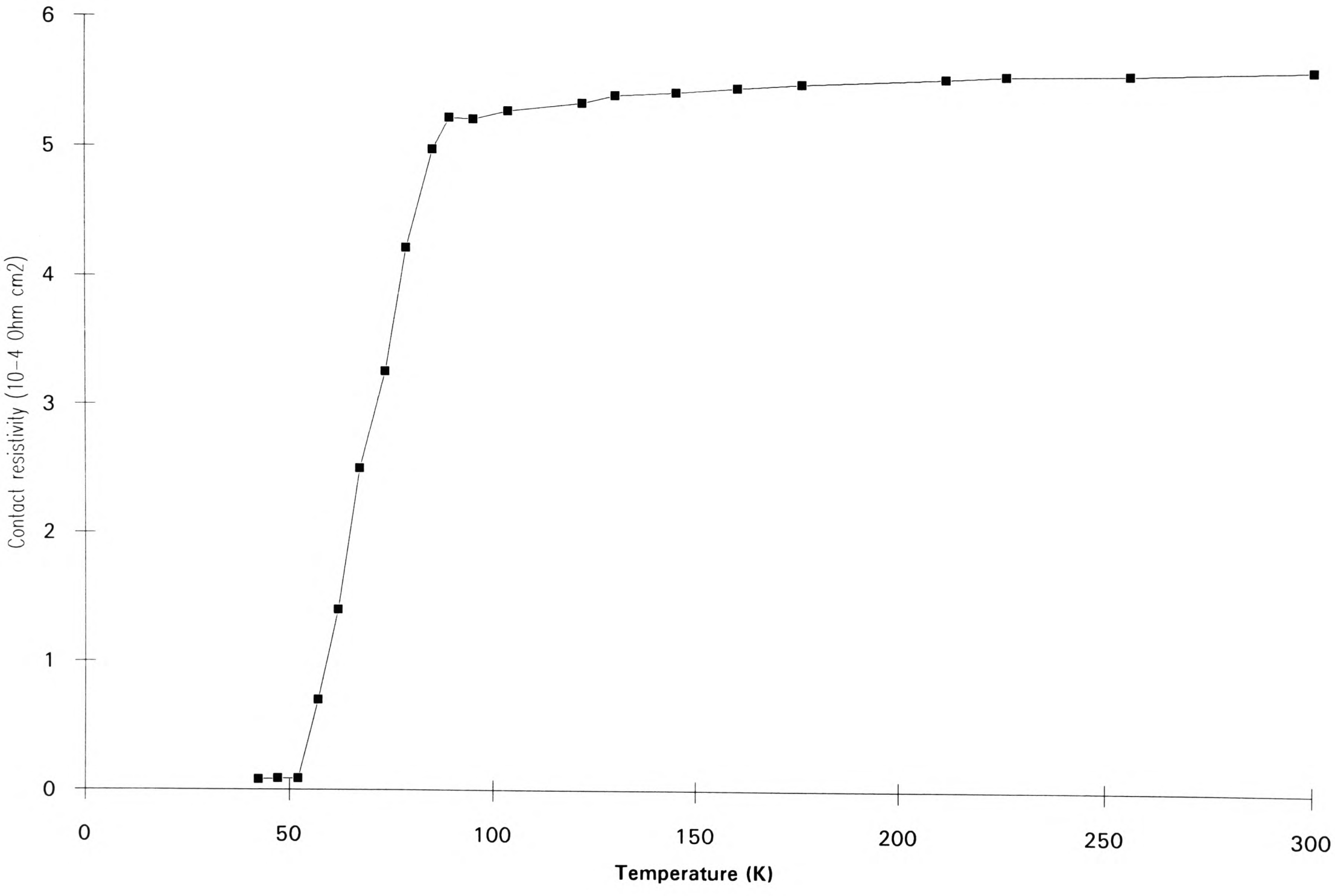
Contact resistivity (10-4 Ohm cm2)
6
5
4
3
2
1
0
0
50
100
150
200
250
300
Temperature (K)

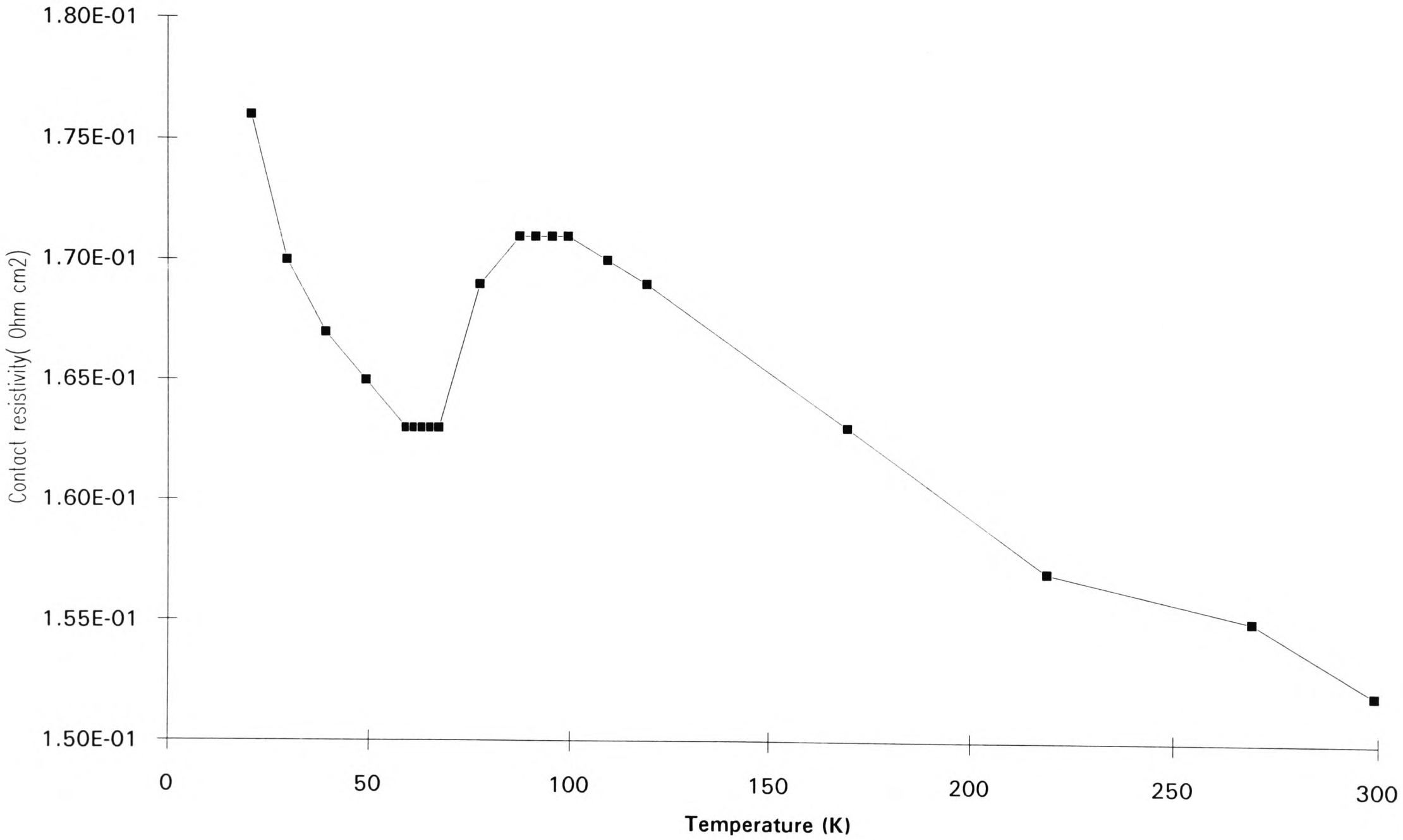

Figure 6.7: Silver contact without annealing ST

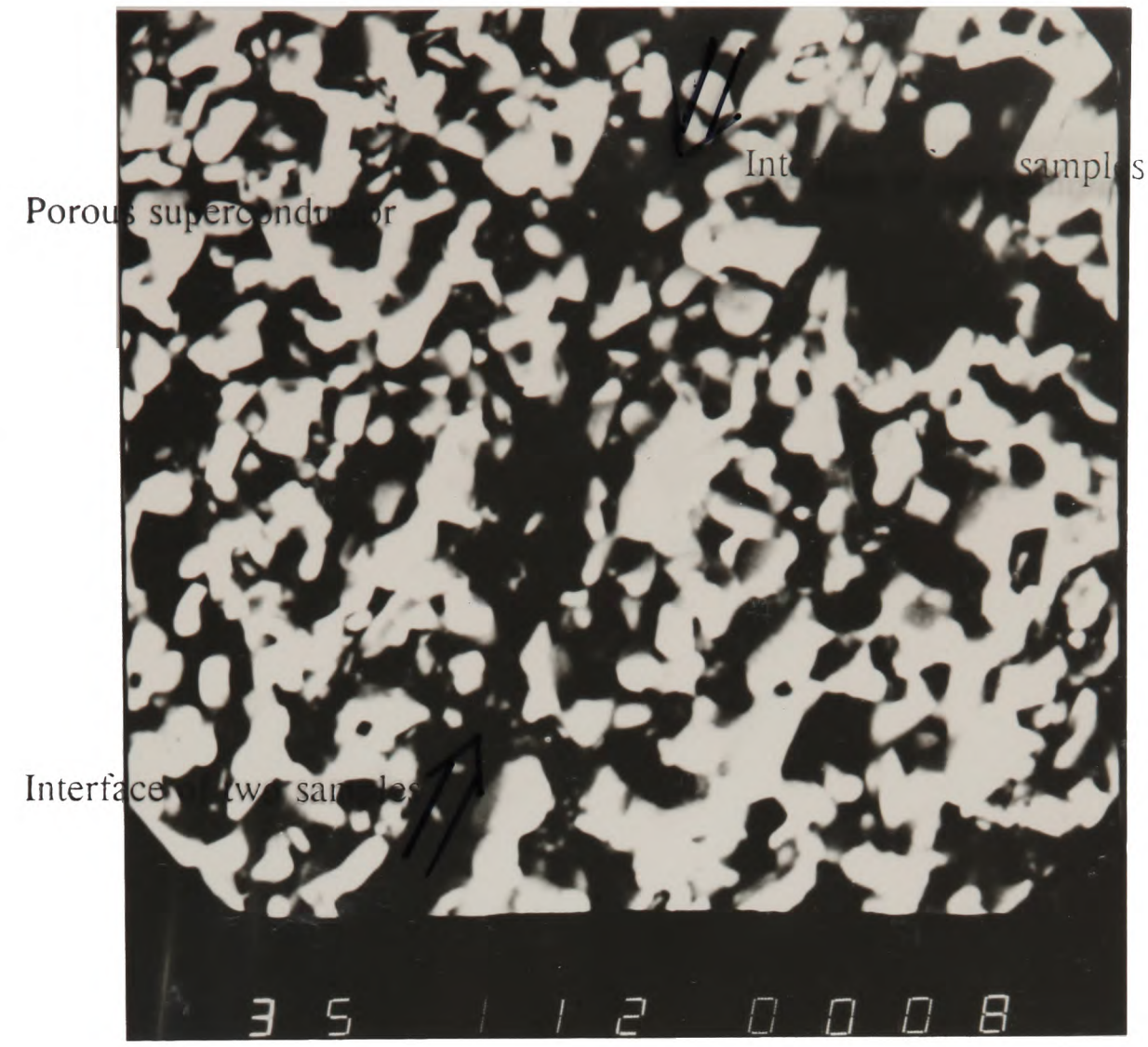

Figure 6.8: Interfaces of silver thin film contacts **ST**

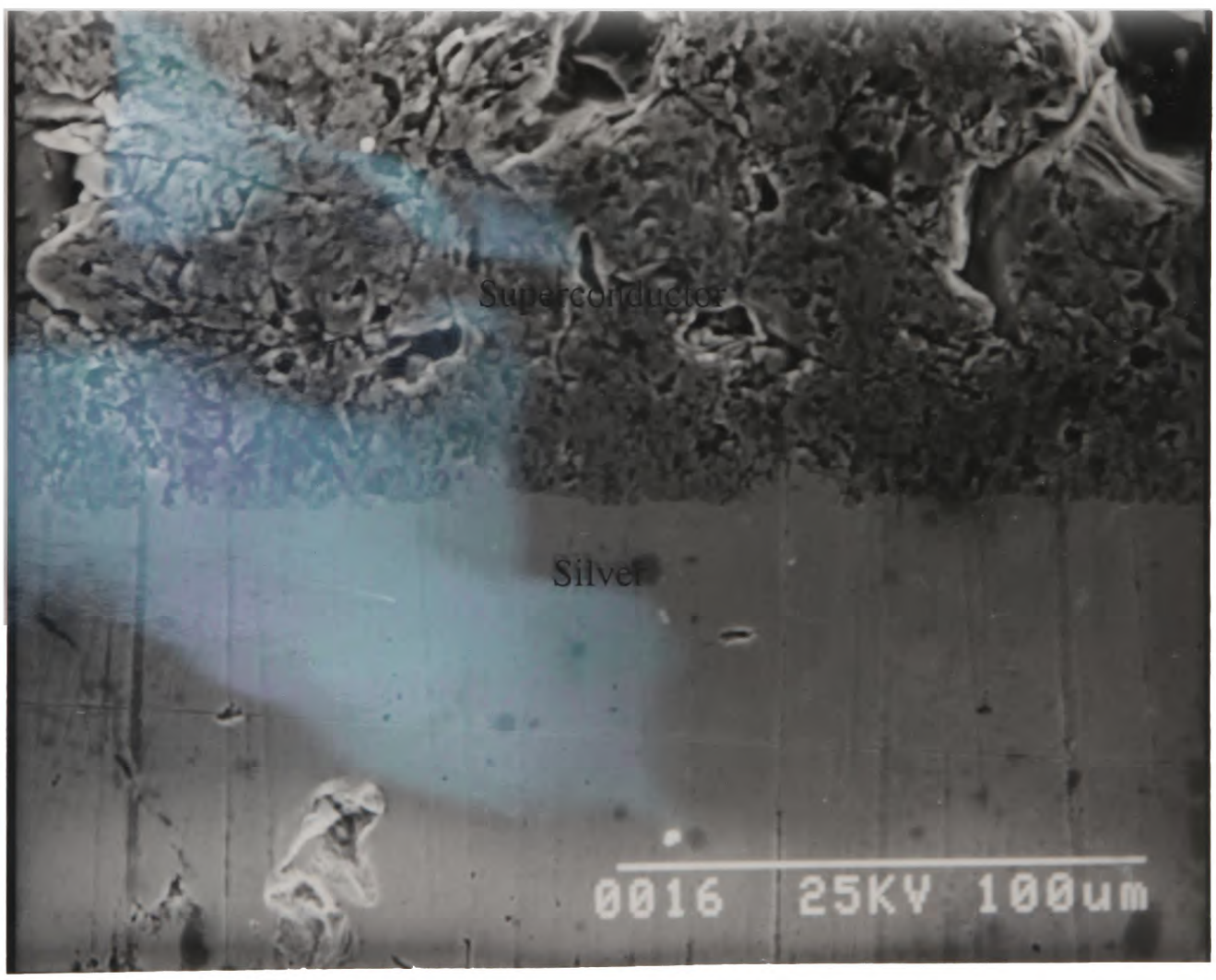

Figure 6.9: Interface of silver-superconductor diffusion couple **MG**

Figure 6.8: Interfaces of silver thin film contacts ST

Figure 6.9: Interface of silver-superconductor diffusion couple MG

samples to study the contact interface. Fig.6.9 shows the interfacial microstructure of a diffusion bonded silver sheet on higher density superconductor sample. The interface between silver and superconductor appears clean and there is no impurity interfacial layer visible.

6.3.3 Discussion

The obvious feature in the contact resistivity measurement (Fig.6.6) is its similarity to the superconducting transition measurement (four-probe measurement Fig. 6.2). Both of them have a sharp resistance drop around the superconducting transition temperature T_c. This feature and its possible physical explanation will be discussed with contact interface models in chapter 8.

The low temperature annealing procedure is vital to obtain low resistivity contacts. Contacts without annealing show semiconducting behaviour, which means that there must be a continuous semiconducting layer at the surface of the superconductor due to either the contamination from the vacuum chamber or the presence of a oxygen deficient layer formed during thermal evaporation. However, the defect layer can not be observed by either SEM or the electron microprobe since accurate oxygen measurement is a difficulty and the presence of a very thin (below the resolution of SEM and electron microprobe) continuous insulator can have a detrimental effect on contacts because of the short coherence length of the high T_c superconductor material. The annealing treatment recovers the oxygen stoichiometry at the superconductor surface and/or encourages the silver to diffuse into the superconductor to make a intimate contact with the 'fresh' material. This procedure can change the contact resistivity/temperature dependence and reduce the contact resistivity by 2 orders of magnitude.

6.4 Silver epoxy

Silver epoxy was tested as a contact material in this work to see if it could be used to prepare low resistance contacts with good mechanical properties.

6.4.1 Experiment

Silver wires were held in the desired place above the superconductor surface and silver epoxy was attached to the wires. Then the wires were placed on to the surface of the superconductor and the silver epoxy was solidified by blowing hot air or by situating the sample on a hot plate at a temperature over 200^{o}C for a few minutes. A set of comparison silver epoxy contact samples were made by attaching silver epoxy on the sample without incorporating silver wires, and the silver wires were attached later with silver paint. Then the contact samples were annealed at different temperatures before contact resistivities were measured.

6.4.2 Experimental results

The silver epoxy contacts showed very high resistivity without heat treatment and had a negative temperature dependence similar to the unannealed silver thin film contact behaviour. The silver epoxy contact resistivity was improved after high temperature annealing. The best silver epoxy contact with resistivity below 10^{-7} Ohm cm^2 was achieved after annealing at 900^{o}C for 3 hours. This result of contact resistivity as a function of temperature is shown in Fig.6.10. The contact resistivity has a metallic behaviour at high temperature, and has a sharp resistance drop at T_c. Below T_c, the result gives a resistivity limit of 10^{-7} Ohm cm^2 for a typical 1 mm^2 contact. The silver epoxy contacts without incorporating silver wires in the contact making procedure need silver wires connected subsequently onto them with silver paint. The contacts still displayed a transition of the resistivity at T_c, but have a range of residual resistivities up to 10^{-5} Ohm cm^2.

6.4.3 Discussion

The advantage of using silver epoxy as a contact material is that it incorporates wires in the contact making procedure, and so we do not need to attach wires on the contact by silver paint after the contact making. Therefore the mechanical strength of

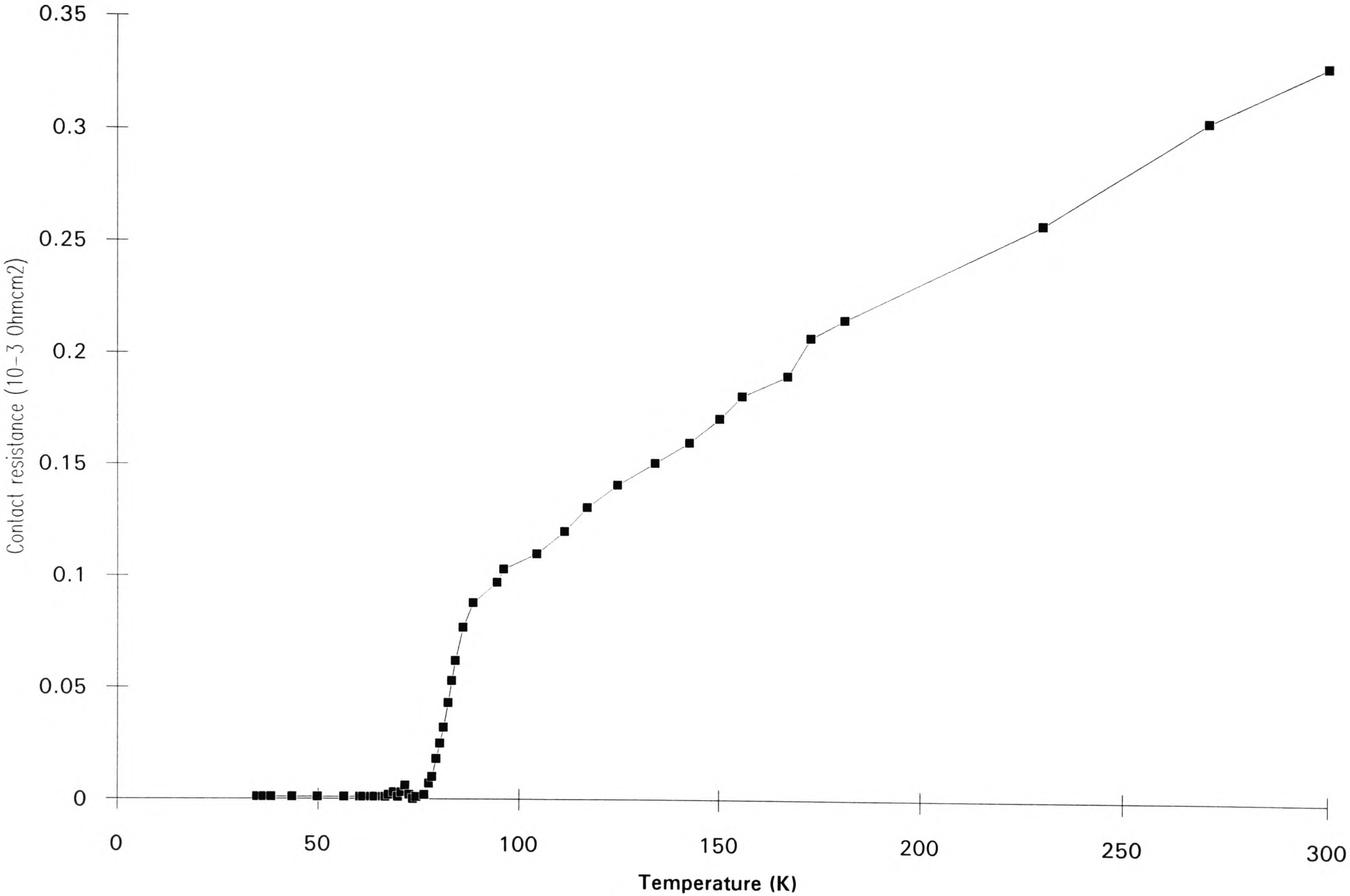
0.35
0.3
0.25
0.2
0.15
0.1
0.05
0
Contact resistance (10-3 Ohmcm2)
0
50
100
150
200
250
300
Temperature (K)

the contact is improved and we can eliminate the possible additional resistance from the silver paint. The results show the contact resistivity of silver epoxy contacts incorporating silver wires is at least 1 order of magnitude lower than those of silver thin film contacts and silver epoxy contacts with silver paint attached leads at room temperature. The resistivity of silver epoxy contacts incorporating wires has a much larger positive temperature dependence than the silver thin film contacts (Fig.6.10 and Fig.6.6). Its temperature dependence is more like that of the pure superconductor transition (Fig.6.2). The physical implication of this behaviour will be discussed in chapter 8.

Since the solvent in the silver epoxy, which can have a bad effect on contact resistance, has been evaporated after such intensive heat treatment, the silver epoxy contact after annealing should be regarded as pure silver contact to superconductor. The silver epoxy contact resistivity value is among the best value achieved in noble metal contacts.

6.5 Titanium contacts

We have seen from chapter 3 that contacts with no chemical reaction often result in weak bonding at the interface. For the purpose of making rugged and stable contacts, a limited interface reaction is preferred. The ideal contact materials should ideally have limited interface reaction to form a strong chemical bond, the chemical stoichiometry of the superconductor oxides should not be severely changed by the contact making procedure and should be recovered by a following oxygenation treatment.

The interface reaction product could either be a continuous layer of conducting metal oxide or isolated insulating compounds particles at the contact interface, so the electrical current is not blocked at the interface and contact properties are not severely damaged. These desired features make the choice for the contact materials very limited.

6.5.1 Titanium metal contact

6.5.1.1 Background

The first material I considered was titanium. Titanium is a well known bonding material to ceramics and is the major component of brazing material to oxide ceramics [Moorhead 1988, Moorhead 1986, Kapoor 1988 and Nicholas 1984]. The bonding between titanium and oxide ceramics is due to chemical interaction at the interface with the formation of titanium oxide. The bonding is very strong.

When contacting to the high Tc superconductor, the titanium metal will inevitably be oxidized. The titanium mono-oxide, TiO, is a metallic conductor and would not introduce a large resistance to the contact even it forms continuous a TiO layer at the interface. What is more, the interface bonding is expected to be very strong.

6.5.1.2 Thermodynamic and kinetic analysis

Although there are many compounds in the Ti-O system, it is possible to control the formation of the TiO layer in two ways: - the thermodynamic way, controlling the titanium activity in the contact materials; or - the kinetic way, controlling the oxygen availability at the contact interface.

First: thermodynamic control

In the Ti-O system, two of the relevant reactions can be expressed in following two equations:

$$3TiO \Leftrightarrow Ti_2O_3 + Ti \qquad (6.1)$$

$$2Ti_2O_3 \Leftrightarrow 3TiO_2 + Ti \qquad (6.2)$$

The free energies for these reactions are:

$$\Delta G_1 = G_{Ti2O3} - 3G_{TiO} + RT\ln a_{Ti} \qquad (6.3)$$

$$\Delta G_2 = 3G_{TiO2} - 2G_{Ti2O3} + RT\ln a_{Ti} \qquad (6.4)$$

where ΔG_1 refers to the free energy change for reaction 6.1, and ΔG_2 refers to the free energy change for the reaction 6.2. G_{Ti2O3} is the Gibbs free energy of Ti_2O_3,

G_{TiO2} is the Gibbs free energy of TiO_2, G_{TiO} is the Gibbs free energy of TiO and $RTlna_{Ti}$ is the free energy term for titanium metal inside an alloy. It is very tempting to use a Ti-noble metal alloy to form a TiO interfacial product. However, from the free energy term in equation 6.3 and 6.4, it is obvious that the higher the activity of titanium a_{Ti}, the more likely it is that TiO will be stabilised in the Ti-O system. Since pure titanium metal obviously has the highest Ti activity among all titanium alloys, there will be no encouragement to form TiO by using titanium alloys. From the thermodynamic analysis above, the material for making these contacts was chosen to be pure titanium metal.

Second: Kinetic control

The oxidation of titanium metal can also be controlled by the availability of oxygen. The free energies of oxide formation in the Ti-O system, (TiO, Ti_2O_3 and TiO_2), are calculated in the terms of kJ/gram per atom oxygen from standard thermodynamic data [Smithells Metals Reference Book 1983, Sixth Edition]. The calculated results are listed in Table 6.1.

Table 6.1: Free energies for the formation of titanium oxides in terms of kJ/gram atom oxygen

	$-\Delta G_{300}$ 27°C (kJ)	$-\Delta G_{500}$ 227°C (kJ)	$-\Delta G_{1000}$ 727°C (kJ)	$-\Delta G_{1500}$ 1227°C (kJ)	$-\Delta G_{2000}$ 1727°C (kJ)
TiO	509.5	491.9	447.1	402.7	352.9
Ti_2O_3	475.7	458.6	415.2	372.2	328.8
TiO_2	431.1	413.7	369.8	326.4	282.4

From this calculation TiO is the most stable compound at all temperatures in an oxygen deficient condition. This is why a TiO layer forms at the interface when titanium metal is in contact with highly polished Al_2O_3 ceramic. [Moorhead 1986]

From thermodynamic data on the Ti-O system [Smithells Metals Reference Book 1983, Sixth Edition], the free energies for titanium oxide formation in an excess oxygen environment were calculated and the results are listed in table 6.2. From table 6.2, TiO_2 is the most stable compound in the Ti-O system when there is sufficient oxygen supply, TiO is a metastable phase. So experiments must be carried out under conditions of reduced oxygen supply at the contact interface in order to form contacts with only TiO at the interface.

Table 6.2: Free energies for the formation of titanium oxides in terms of kJ/gram atom titanium

	$-\Delta G_{300}$ 27°C (kJ)	$-\Delta G_{500}$ 227°C (kJ)	$-\Delta G_{1000}$ 727°C (kJ)	$-\Delta G_{1500}$ 1227°C (kJ)	$-\Delta G_{2000}$ 1727°C (kJ)
TiO	509.5	491.9	447.1	402.7	352.9
Ti_2O_3	713.6	687.9	622.9	558.3	493.2
TiO_2	862.1	827.3	739.5	652.7	564.8

6.5.2 Thermally evaporated Ti contacts.

6.5.2.1 Experiment and results

Ti metal stripes were deposited in a vacuum chamber by thermal evaporation on the top of the superconductor through a simple mask. The Ti contact samples were then annealed at 500°C for one hour in air.

The contact resistivity of this Ti metal contact is measured by the three - point contact resistance measurement, and the result shows that the contact resistivity is quite high (10^1-10^2 Ωcm^2) and shows a semiconductor behaviour. The titanium contact resistivity and its temperature dependence is shown in Fig. 6.11.

The interface between the $YBa_2Cu_3O_{7-x}$ and titanium metal layer was studied

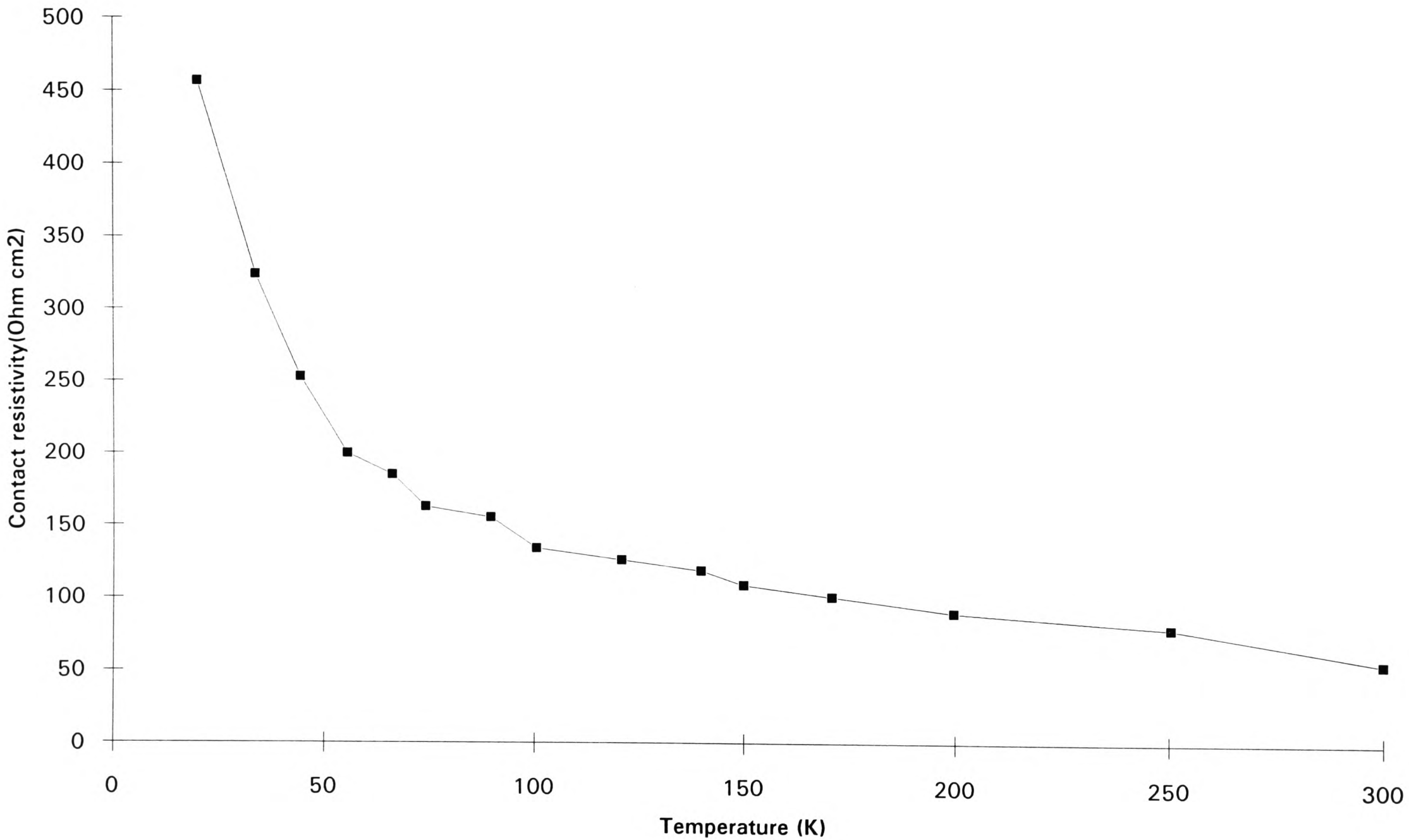

Figure 6.11: High resistivity Ti contact ST

by electron microprobe analysis. The interfacial layer composition is shown in table 6.3. The results show that the Ti overlayer was oxidised completely to TiO_2. Fig.6.12 shows the SEM image of the titanium contact interface prepared in the same way as the silver contact in 6.23.

Table 6.3: Composition of interfacial regions of Ti/YBCO contacts

	Y (at%)	Ba (at%)	Cu (at%)	Ti (at%)	O (at%)	Formula
Point 1	0.72	2.18	3.32	26.49	67.29	TiO_2
Point 2	0.78	2.13	2.47	29.02	65.59	TiO_2
Point 3	0.65	2.12	3.46	27.74	66.02	TiO_2

6.5.2.2 Discussion

The electrical measurement shows that titanium contacts made by thermal evaporation have a high contact resistivity with negative temperature dependence, which implies the formation of insulating TiO_2 at the interface. Electron microprobe analysis results show that TiO_2 is formed at the interface, which can explain the high contact resistivity and the negative temperature dependence of the titanium contact. But the thin titanium metal contact layer made by thermal evaporation might be oxidized from both the superconductor surface and the exposed top surface. To examine the oxidation of the titanium metal purely caused by the interface reaction and its effect on contact resistivity, thick titanium metal sheet can be used instead of the deposited thin film titanium contact.

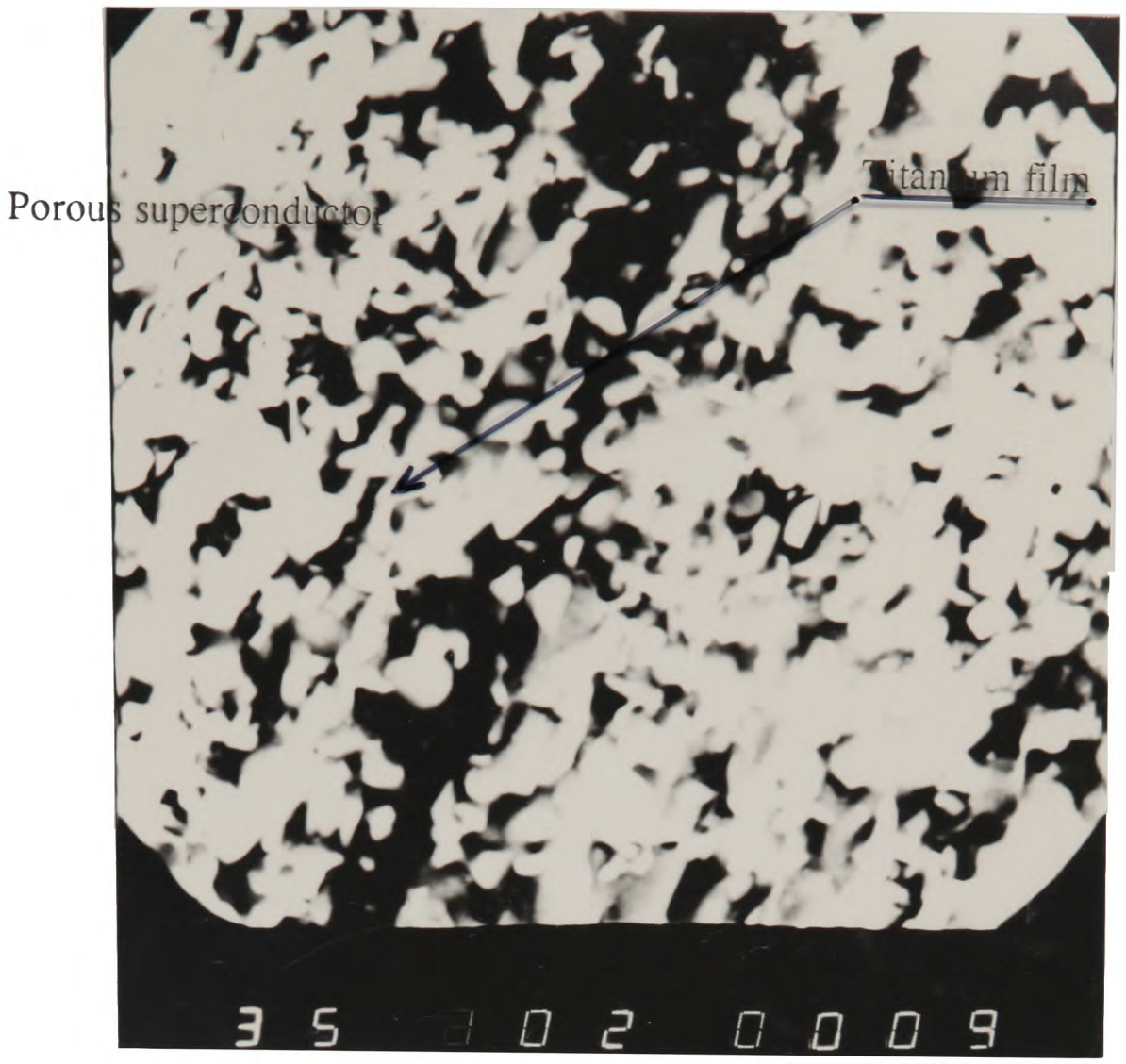

Figure 6.12: Interfaces of Ti thin film contacts ST

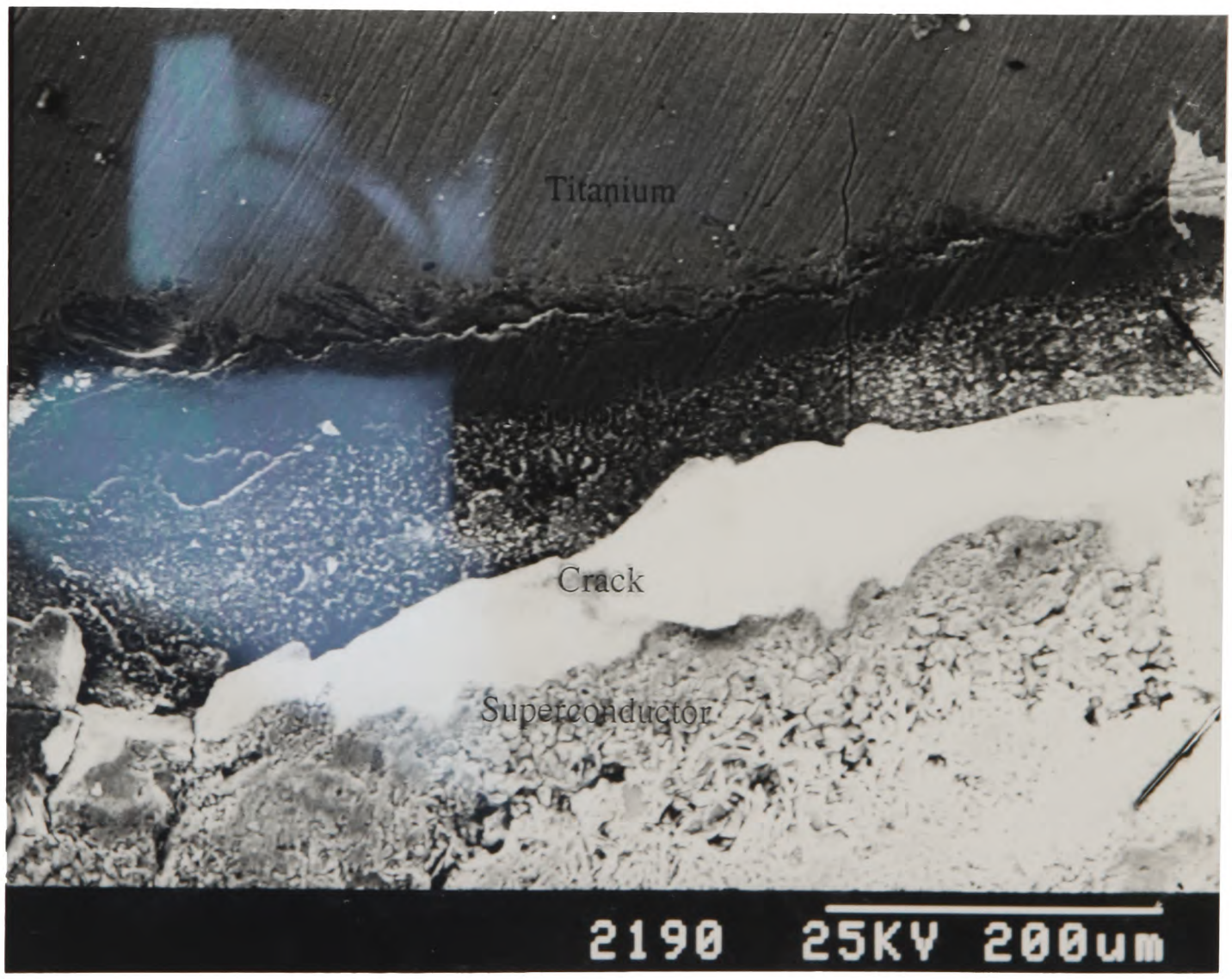

Figure 6.13: Interface of Ti metal plate and superconductor OS

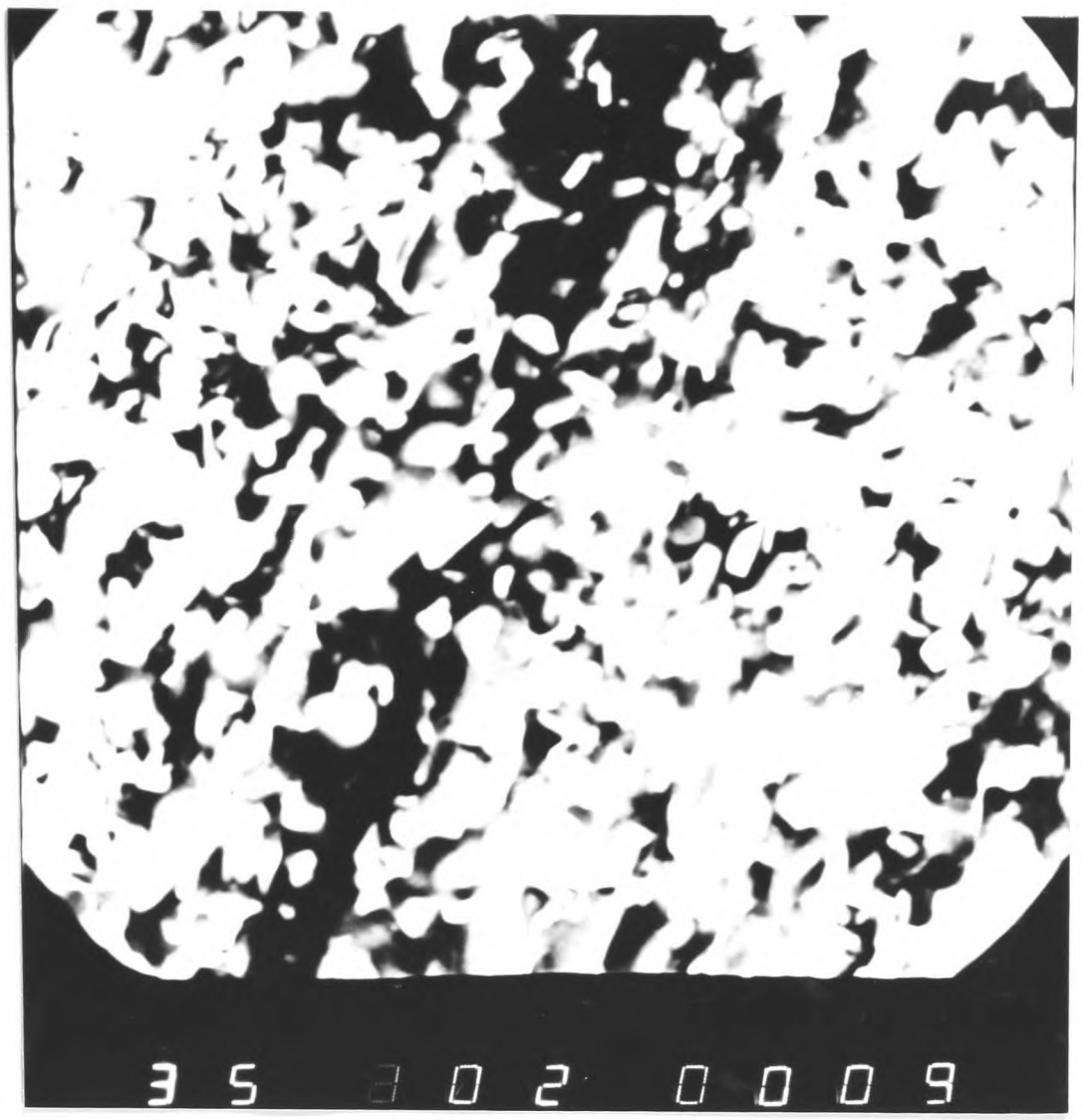

Figure 6.12: Interfaces of Ti thin film contacts ST

Figure 6.13: Interface of Ti metal plate and superconductor OS

6.5.3 Diffusion bonded titanium metal contacts:

6.5.3.1 Experiment and results

Sintered superconductor pellets prepared by the method described in chapter 5 were initially used for this contact resistivity work. Titanium metal strips were cut from pure titanium metal plate 0.5mm in thickness. Then the titanium metal strips were mechanically polished by a series of graded silicon carbide paper to 1μm diamond paste and the metal strips were degreased by ultrasonic cleaning with acetone.

The titanium metal strips were put in the desired place on top of the sintered superconductor pellet sample with the flat surfaces of the titanium metal stripes facing the polished surface of the superconductor, and they were tied together firmly with titanium wires.

The titanium metal strips were diffusion bonded by annealing under pressure at 600^{o}C for 3 hours. After cooling to room temperature, the titanium contact was firmly bonded onto the superconductor.

The top layer of oxidized titanium metal was carefully removed before silver wires were attached to the metal contact with silver paint.

Contact resistivity measurements show that the resistivity is very high, and has a very large negative temperature dependence similar to Fig.6.11. This indicates a thick TiO_2 layer is formed at the interface between the superconductor and titanium metal.

The cross section of the interface was analyzed by electron microprobe. The results are listed in table 6.4. The results show that a continuous TiO_2 layer was formed at the interface. SEM images of the interface shows there is a thick reaction layer at the contact interface, Fig.6.13.

Table 6.4: Composition of interfacial reaction layer

	Y (at%)	Ba (at%)	Cu (at%)	Ti (at%)	O (at%)	Formula
Point 1	0.01	0.15	0.17	33.90	65.76	TiO_2
Point 2	0.01	0.14	0.08	32.03	67.75	TiO_2
Point 3	0.03	0.51	0.10	32.94	66.41	TiO_2

6.5.3.2 Discussion

Titanium metal plate contacts on $YBa_2Cu_3O_{7-x}$ have very high contact resistivity. The microprobe analysis shows that there is a thick TiO_2 layer formed at the interface. To make low resistivity contacts with a TiO layer at the interface, a low oxygen activity must be tried according to the kinetic analysis of the Ti-O system in section 6.5.1.2.

6.5.4 Titanium contacts made in a vacuum furnace.

6.5.4.1 Experiment and results

To reduce the oxygen availability in the contact forming procedure, titanium contacts were made onto sintered superconductor pellets inside a vacuum furnace with pressure less than 10^{-5}mbar at all annealing temperatures. Other conditions remained as described in section 6.5.3.1. Although vacuum annealing will result in the loss of oxygen from $YBa_2Cu_3O_{7-x}$, making it a semiconductor, the oxygen content could be recovered by subsequent low temperature oxygen annealing, and hopefully, the low temperature annealing will not affect the formed interfacial product.

The Ti/superconductor diffusion couples were annealed in the vacuum furnace at 600^{o}C for 5 hours. After cooling to room temperature, the diffusion couple was firmly bonded together.

Microprobe analysis shows the diffusion couples treated in the vacuum furnace

have only one interfacial reaction product which is TiO_2 and there is no measurable TiO formation (Table 6.5). The SEM image of the contact interface is shown in Fig.6.14.

Table 6.5: Composition of interfacial reaction layer

	Y (at%)	Ba (at%)	Cu (at%)	Ti (at%)	O (at%)	Formula
Point 1	0.02	0.35	0.16	34.73	64.74	TiO_2
Point 2	0.26	0.60	0.54	30.26	68.35	TiO_2
Point 3	0.05	0.25	0.14	34.33	65.24	TiO_2

6.5.4.2 Discussion

This result shows that the titanium contact made on a sintered superconductor will preferably form TiO_2 compound even in a low oxygen activity environment. But the oxygen to oxidize the titanium metal may not purely come from the surface of the superconductor, and the pores within the sintered ceramics are fast oxygen transport paths. Both these effects will increase the oxygen availability at the contact interface. To reduce the pores in the superconductor material, melt textured material can be used.

6.5.5 Titanium contacts on melt-textured superconductor

To further reduce the oxygen availability at the contact interface during the contact making procedure, large grain size $YBa_2Cu_3O_{7-x}$ produced by the method described in chapter 5 was used instead of ordinary sintered superconductor samples. The density of the large crystal samples is very high (99% of theoretical density) and they contain essentially no pores. This feature could help to reduce the oxygen availability at the contact interface. By contacting intimately with the melt-textured superconductor, the titanium can only react with oxygen from the surface of the superconductor.

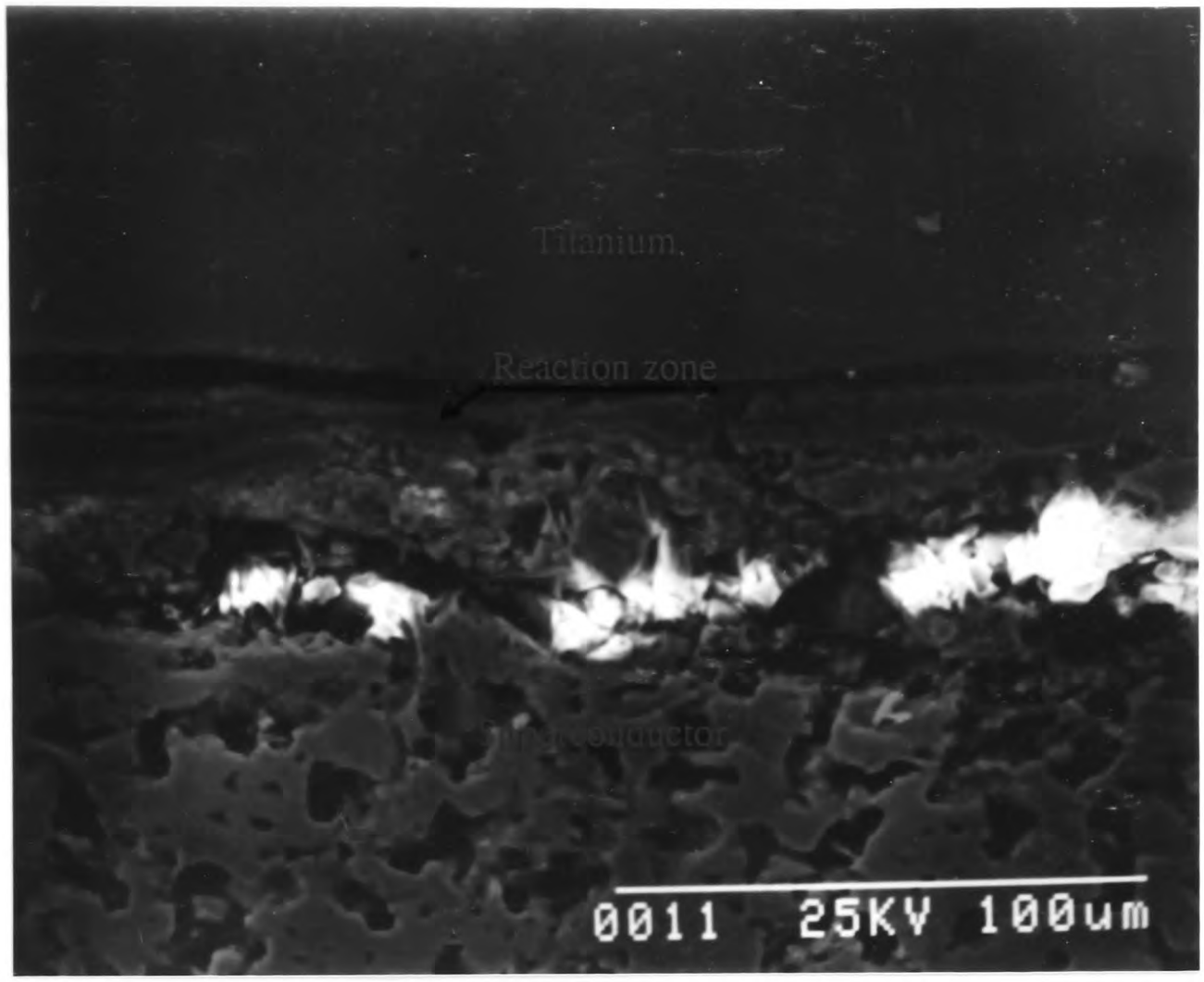

Figure 6.14: Interface of Ti/superconductor diffusion couple OS

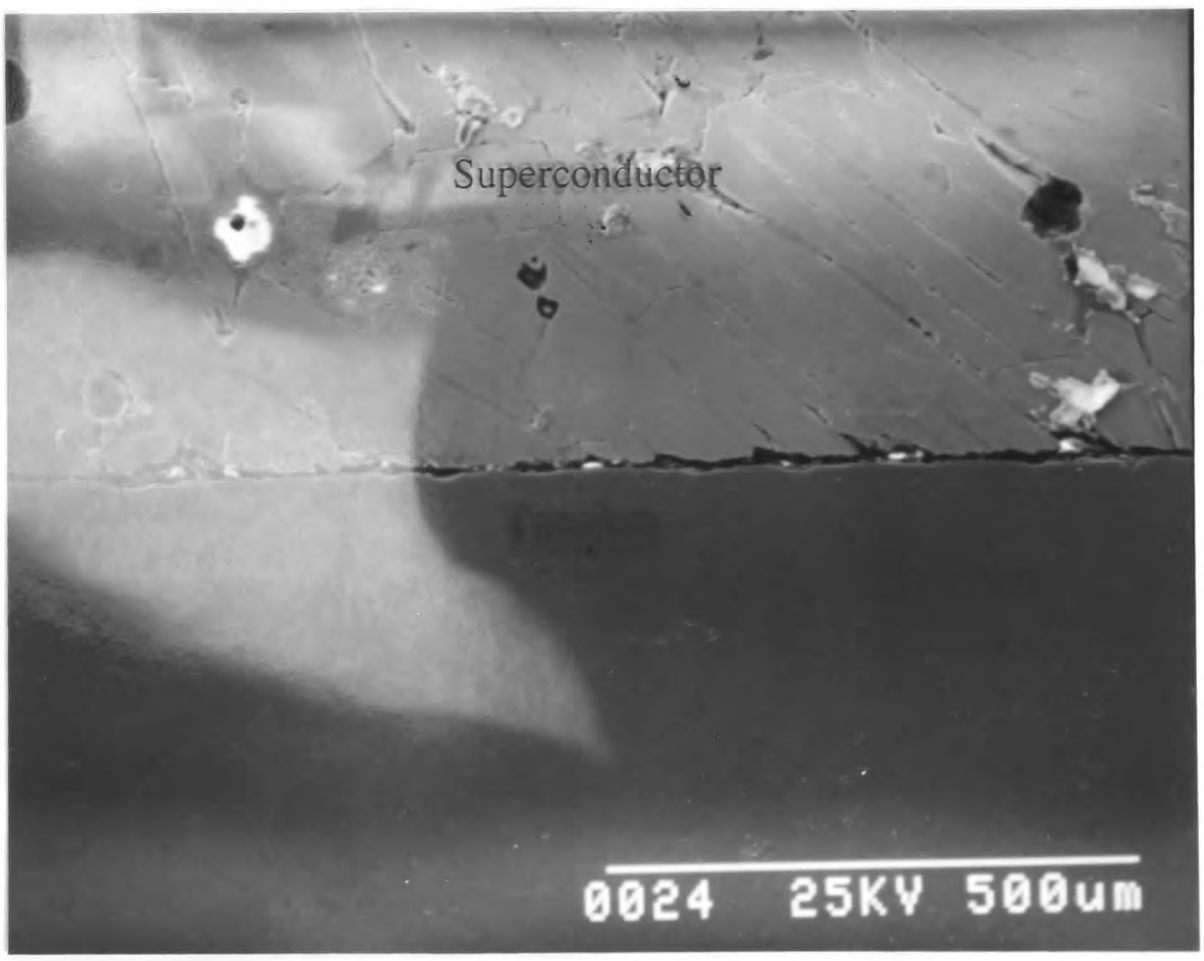

Figure 6.15: Interface of Ti/textured superconductor

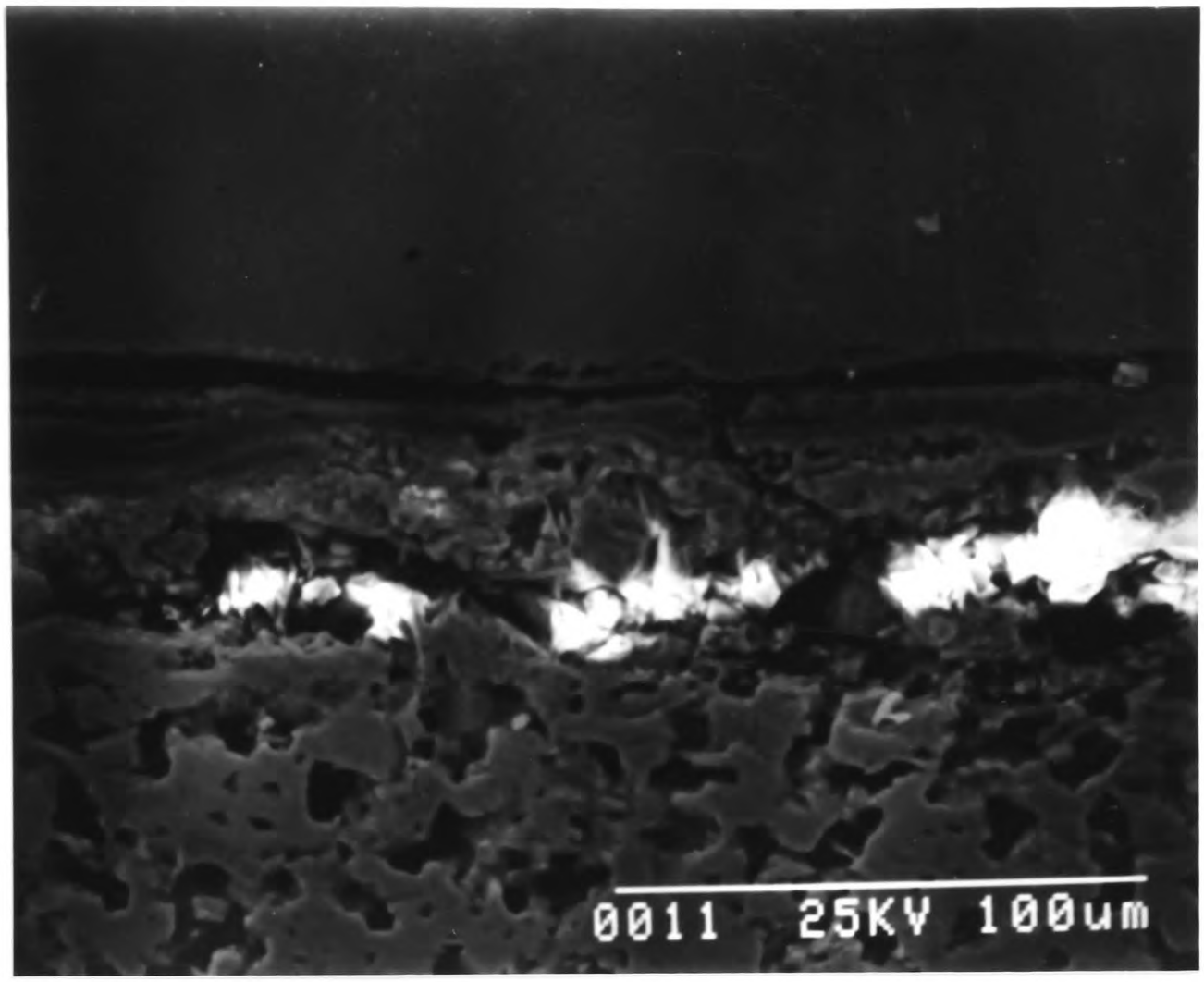

Figure 6.14: Interface of Ti/superconductor diffusion couple OS

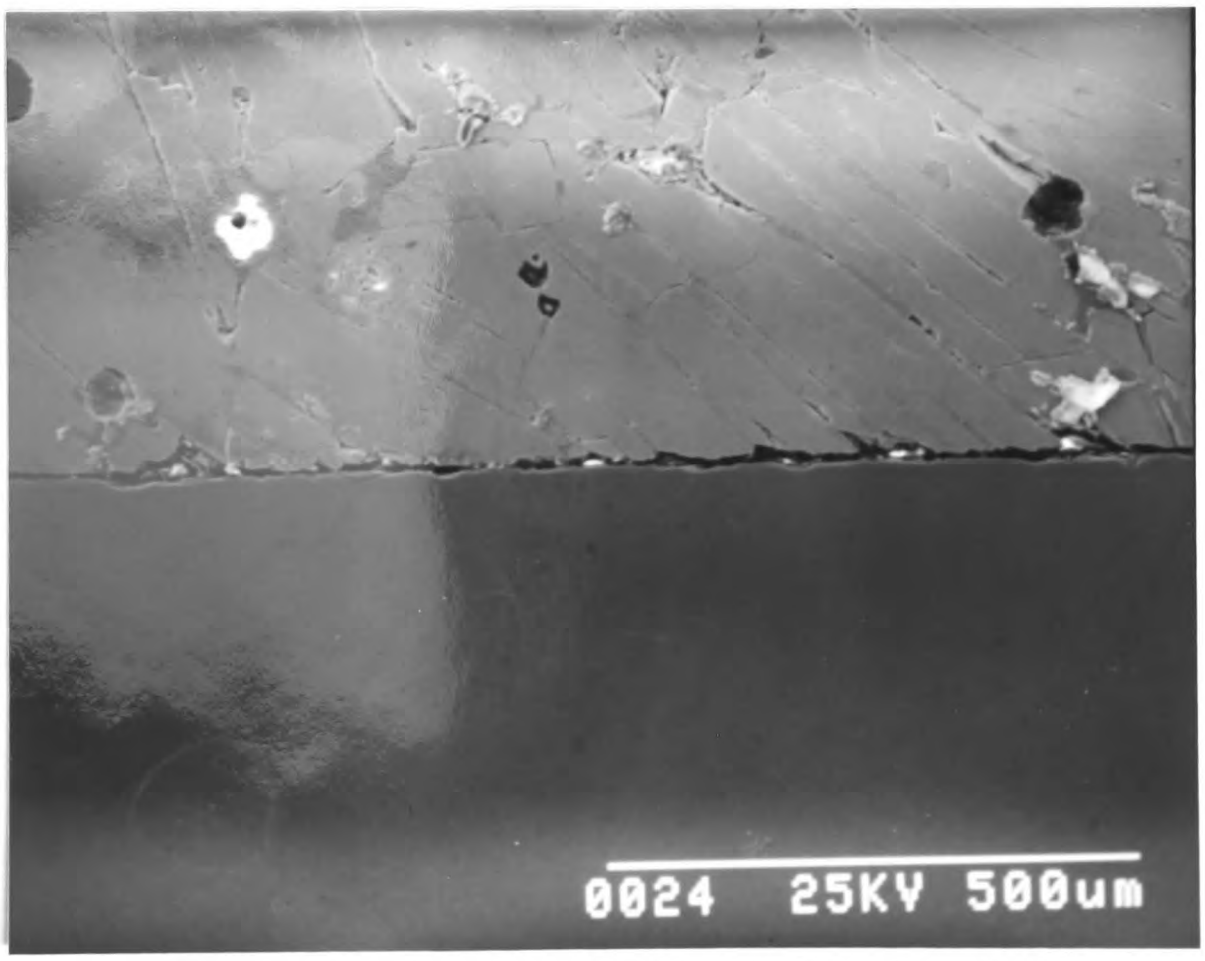

Figure 6.15: Interface of Ti/textured superconductor

6.5.5.1 Experiment and results

Titanium metal plate contacts were made onto the textured superconductor samples by the diffusion bonding technique. The titanium metal strips were pressed onto a highly polished surface of the superconductor, and annealed at 600°C for 8 hours. After cooling to room temperature, silver paint was used to connect silver wire leads onto the polished contacts.

Using the contact resistance measurement method, the contact resistance is measured with decreasing temperature. The results show that this contact has very high contact resistivity (10^1-10^2 Ωcm^2) and a negative temperature dependence similar to Fig. 6.11.

The cross section of the sample was examined by SEM and electron microprobe microanalysis, and results show an apparently clean interface between superconductor and titanium metal. There are no detectable reaction products at the interface (Fig.6.15).

Since the contact resistivity of the contact is very high, which indicates that there must be some kind of reaction at the contact interface. The titanium metal contacts were mechanically separated from the superconductor surface, and the interface between titanium metal and superconductor was exposed and was examined directly. Optical microscopy shows that both titanium metal and the superconductor have a golden coloured product at the interface (Figs. 6.16, 6.17). Electrical measurement of the golden coloured product on the Ti metal plate reveals that this golden reaction product is a good electrical conductor, the contact resistivity is in the range 10^{-1} - 10^{-3} Ωcm^2, measured by a two point method. But the golden coloured product on the superconductor surface is a poor electrical conductor.

Electron microprobe analysis showed that the titanium metal surface has a layer of TiO (table 6.6), but there is apparently a very thin layer of $BaTiO_3$ on top of the superconductor (table 6.7) where it was in contact with the titanium metal.

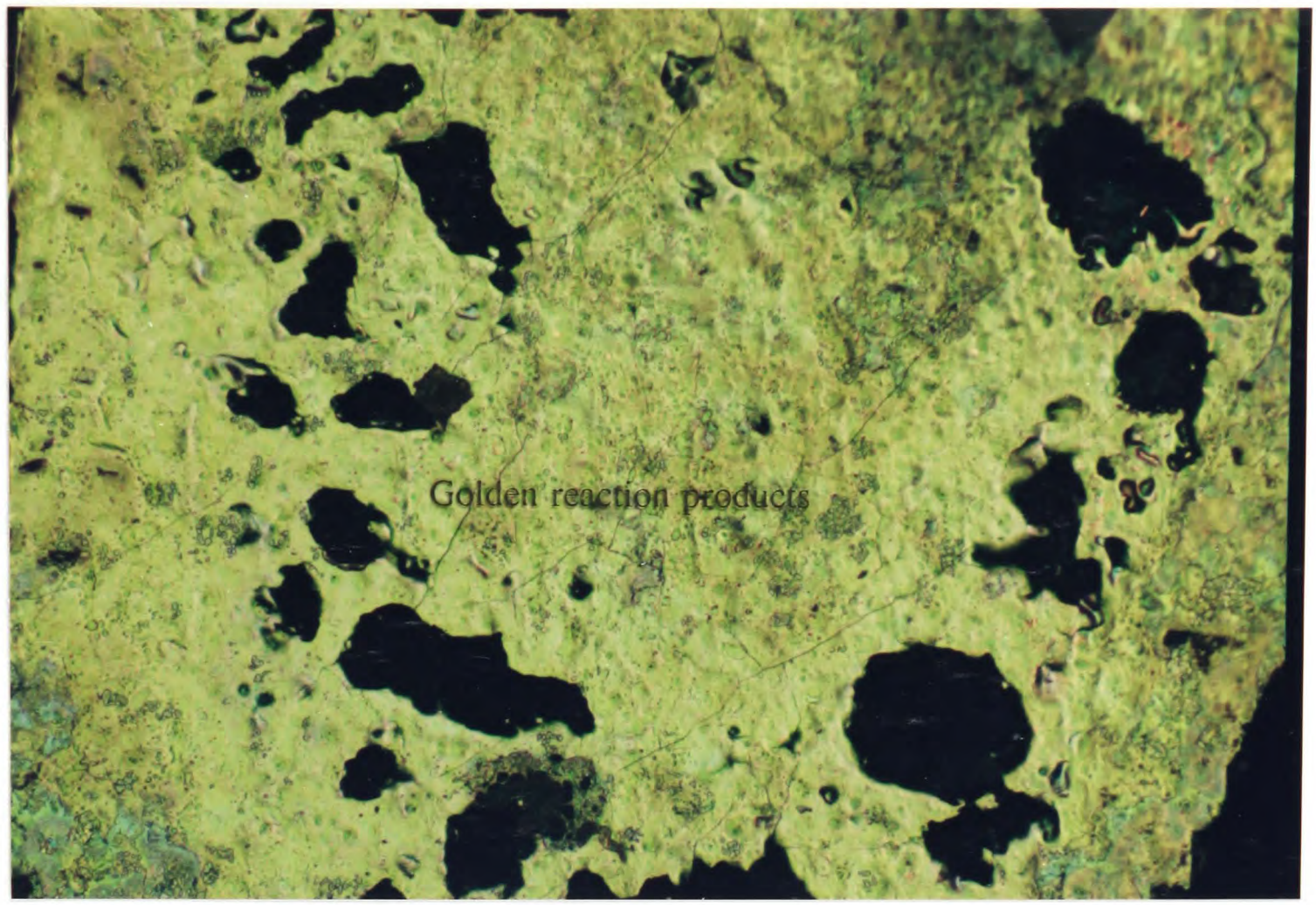

Figure 6.16: Reaction product at superconductor surface

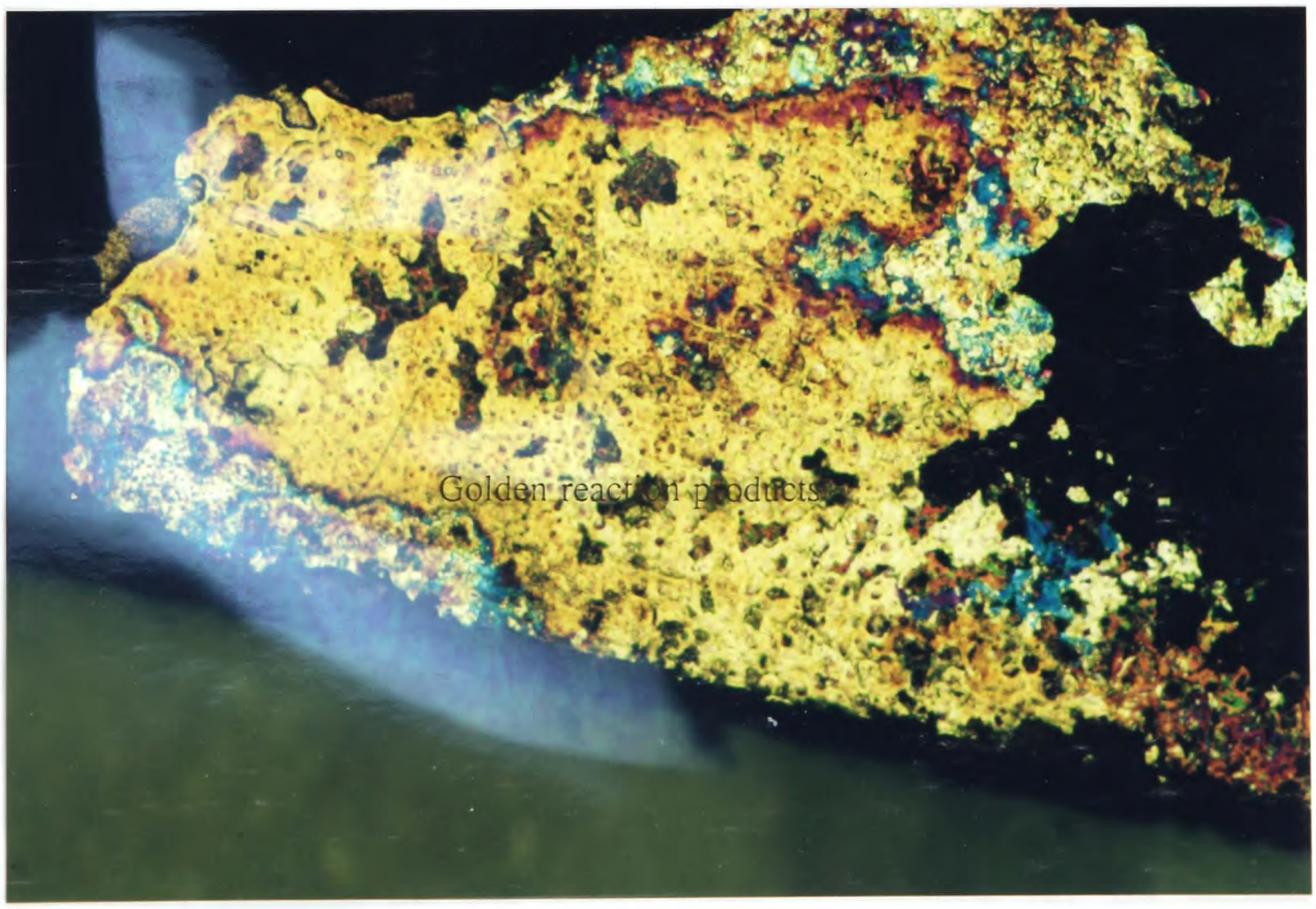

Figure 6.17: Reaction product at Ti metal surface

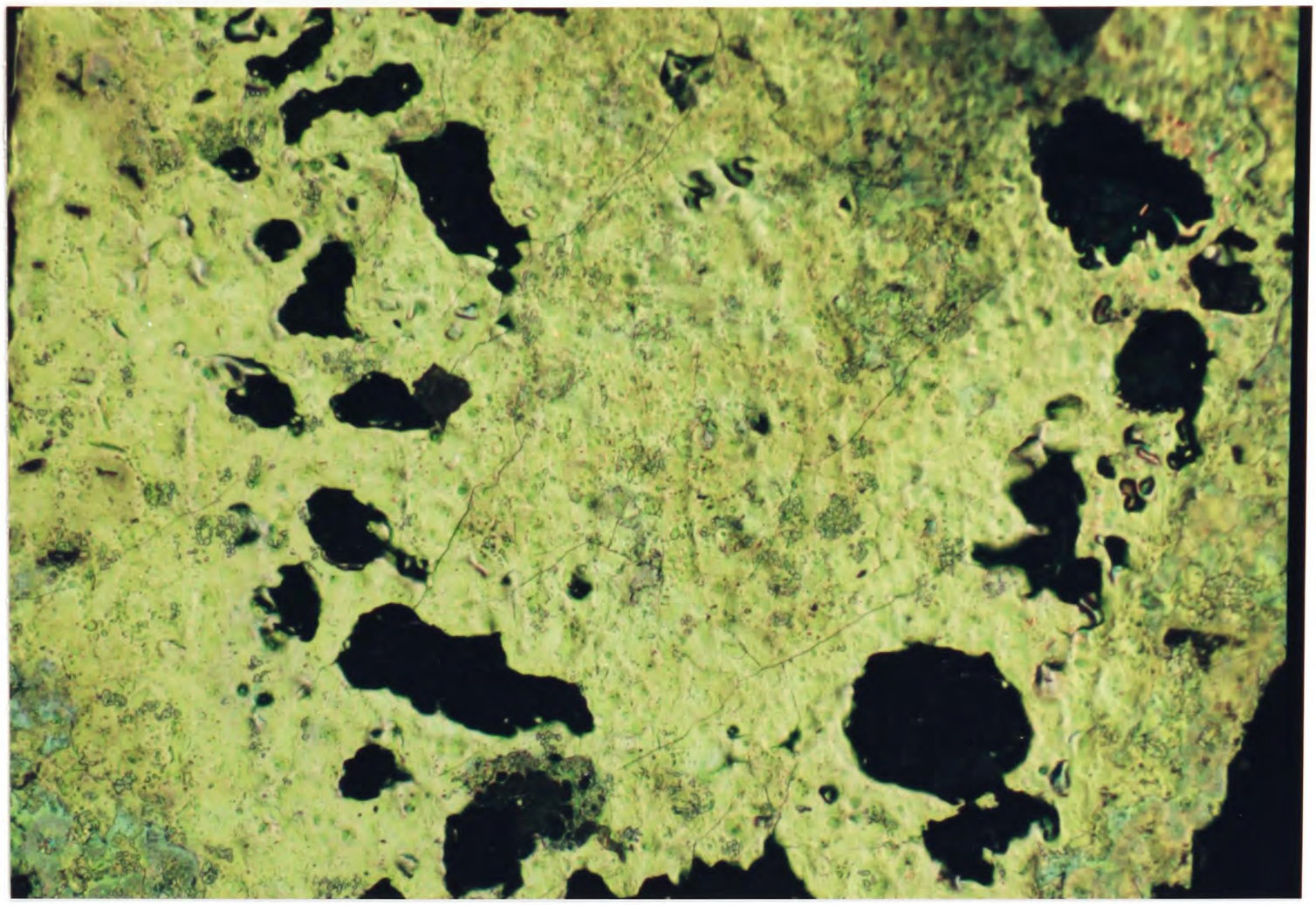

Figure 6.16: Reaction product at superconductor surface

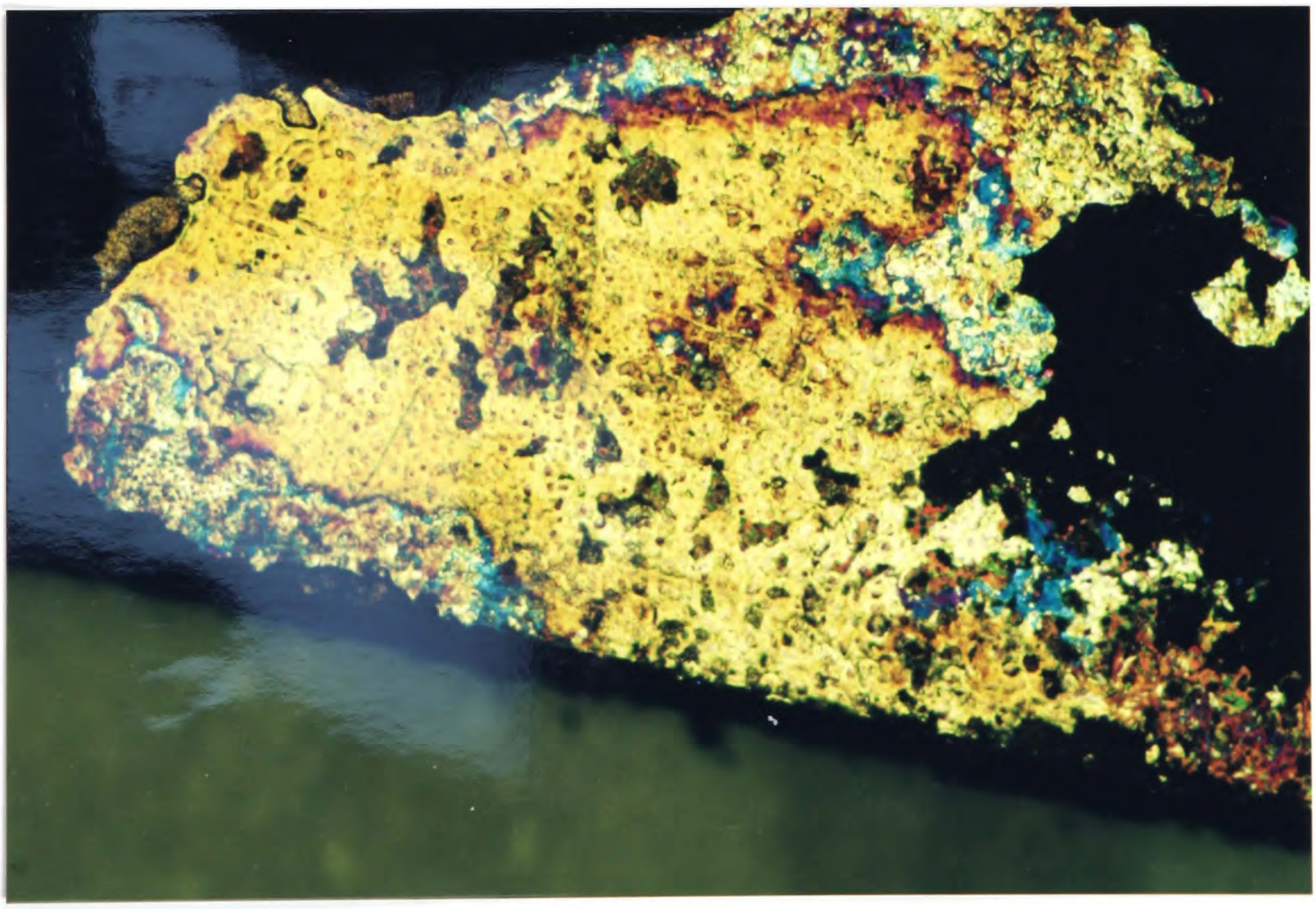

Figure 6.17: Reaction product at Ti metal surface

Table 6.6: Composition of interfacial reaction layer on Ti

	Y (at%)	Ba (at%)	Cu (at%)	Ti (at%)	O (at%)	Formula
Point 1	0.02	0.29	0.52	50.15	49.01	TiO
Point 2	0.02	0.22	0.36	43.40	56.11	TiO
Point 3	0.01	0.32	0.27	64.86	34.54	Ti+ TiO

Table 6.7: Composition of interfacial reaction layer on YBCO

	Y (at%)	Ba (at%)	Cu (at%)	Ti (at%)	O (at%)	Formula
Point 1	0.08	7.46	0.06	6.82	85.58	$BaTiO_3$
Point 2	0.06	3.12	0.15	4.53	92.13	$BaTiO_3$
Point 3	0.09	3.62	0.16	5.13	90.99	$BaTiO_3$

6.5.5.2 Discussion

These results show that titanium metal has a very limited reaction with melt textured superconductor even after extended annealing at 600^{o}C. The reaction is so limited that even with cross section examination it is not easy to detect the reaction products, although part of the reason is that the interfacial reaction layer is very brittle and can easily be broken off during polishing of the cross section sample like the cracked interface in Fig.6.15. A thin layer of TiO compound on the surface of titanium metal was identified by electron microprobe analysis, and the electrical measurement confirms that this golden coloured compound has low electrical resistance.

A thin layer of $BaTiO_3$ was formed on the superconductor surface where in contact with titanium metal. The uneven and porous reacted surface of the superconductor was studied by electron microprobe to preserve the reacted products at the interface, but due to the surface roughness, the overwhelming mount of oxygen calculated in this surface is a false value caused by low count rates of the metal signals. The formation of $BaTiO_3$ has a very bad effect on the contact resistivity and alters the chemical stoichiometry of the superconductor surface, which can not be recovered by subsequent annealing. This compound must also form at the interface of titanium contacts with sintered superconductors, but this limited reaction cannot be detected by cross section analysis.

6.5.6 Conclusion

The titanium metal contacts with $YBa_2Cu_3O_{7-x}$ have limited interfacial reaction. In oxygen rich conditions, TiO_2 has been detected as the main reaction product at the interface; in oxygen deficient conditions, TiO is the most likely reaction products at interface, but $BaTiO_3$ is also present at the interface which alters the surface chemical stoichiometry of the superconductor. In both cases, the contact resistivities to the high Tc superconductor are too high for application. This means that pure titanium metal is not suitable as a contact material to $YBa_2Cu_3O_{7-x}$.

6.6 Molybdenum contacts

Based on the idea of forming a conducting oxide at contact interface as discussed at the beginning of section 6.5, there are several other promising metals with conducting oxides such as Pb, Nb, and Mo. However, Pb and Nb both react vigorously with the high Tc superconductor as we have seen from the chapter 4, therefore they are obviously not suitable for contact materials to $YBa_2Cu_3O_{7-x}$.

Molybdenum has conducting oxide compounds, the electrical resistivity of MoO_2 is below 10^{-6} Ωcm at low temperatures ($<$ 100K) [Taller 1974]. If the reaction is well under control and the loss of oxygen to molybdenum from the high Tc

superconductor at the interface can be recovered by subsequent heat treatment, it may be possible to prepare low resistivity Mo/$YBa_2Cu_3O_{7-x}$ contacts.

6.6.1 Experiment and results

Molybdenum metal contacts were sputtered onto the superconductor surface through a mask, followed by heat treatment at 600°C for an hour. After cooling to room temperature, silver wire leads were attached onto the contacts with silver paint. The contact resistivity was measured by the method described in section 6.2.1, and the results show that the molybdenum-superconductor interface has a large contact resistivity (10^1 - 10^3 Ωcm^2) with negative temperature dependence similar to Fig.6.11.

To analyse the interfacial reaction of molybdenum and superconductor, a sample of diffusion bonded superconductor and molybdenum metal sheet composite was made by placing a piece of 0.5mm thick molybdenum metal between two pieces of superconductor and using titanium metal plates and wires to firmly bond them together.

Table 6.8: Composition of interfacial reaction layer

	Y (at%)	Ba (at%)	Cu (at%)	Mo (at%)	Ti (at%)	O (at%)	Formula
Point 1	0.1	0.1	0.3	99.5	0.1	0.0	Mo
Point 2	0.0	0.0	0.1	31.9	0.0	68.0	MoO_2
Point 3	9.1	4.9	2.4	21.0	0.1	62.6	$Y_2Mo_4O_{15}+BaMoO_4$
Point 4	0.4	13.1	0.2	14.7	0.1	71.5	$BaMoO_4$
Point 5	4.0	6.3	1.4	14.6	0.0	73.7	$Y_2Mo_4O_{15}+BaMoO_4$
Point 6	1.88	3.46	41.28	0.07	0.07	53.25	CuO

After high temperature diffusion, a cross section of the composite sample was polished and analyzed by SEM and electron microprobe analysis. The results show

that molybdenum reacts vigorously with $YBa_2Cu_3O_{7-x}$ (Fig.6.18). A series of insulating oxide layers was identified at the interface by electron microprobe analysis, the final products sequence is molybdenum metal, MoO_2, $Y_2Mo_4O_{15}+BaMoO_4$, $BaMoO_4$, CuO and unreacted $YBa_2Cu_3O_{7-x}$ superconductor (table 6.8).

6.6.2 Discussion

The sequence of the reaction products from the strong interaction between molybdenum and $YBa_2Cu_3O_{7-x}$ can be explained as follows: molybdenum is first oxidised into MoO_2. MoO_2 is not stable in contact with $YBa_2Cu_3O_{7-x}$ and reacts to form a series of molybdenum containing compounds as molybdenum diffuses out. This can be seen from the decreasing molybdenum concentration in the reaction products in table 6.8. This forces the unused material - primarily CuO outward, so a pure CuO layer forms at the edge of the reaction zone in contact with $YBa_2Cu_3O_{7-x}$. From the phase diagram of the Y-Ba-Cu-O system (Fig.2.6b) CuO is stable in contact with $YBa_2Cu_3O_{7-x}$, and the reaction stops there. So this reaction is controlled by the out diffusion of molybdenum into the superconductor.

Compared with titanium metal in similar samples, molybdenum reacts much more vigorously with superconductor. The reaction is too fast to control. So molybdenum can not be used as a contact material; although the conducting oxide MoO_2 layer finally forms, the detrimental interfacial reactions have already destroyed the superconductor substrate.

6.7 Multilayer contacts

6.7.1 Experiment design

The design of the multilayer contacts in this work is based on the idea that the interdiffusion of noble metal layer and reactive metal layer during the contact making may form isolated reaction products (insulators) at the reaction interface in a metallic conducting matrix. In this way the contact resistance is not spoilt by the insulating reaction products, and the contact to the superconductor could be very stable with

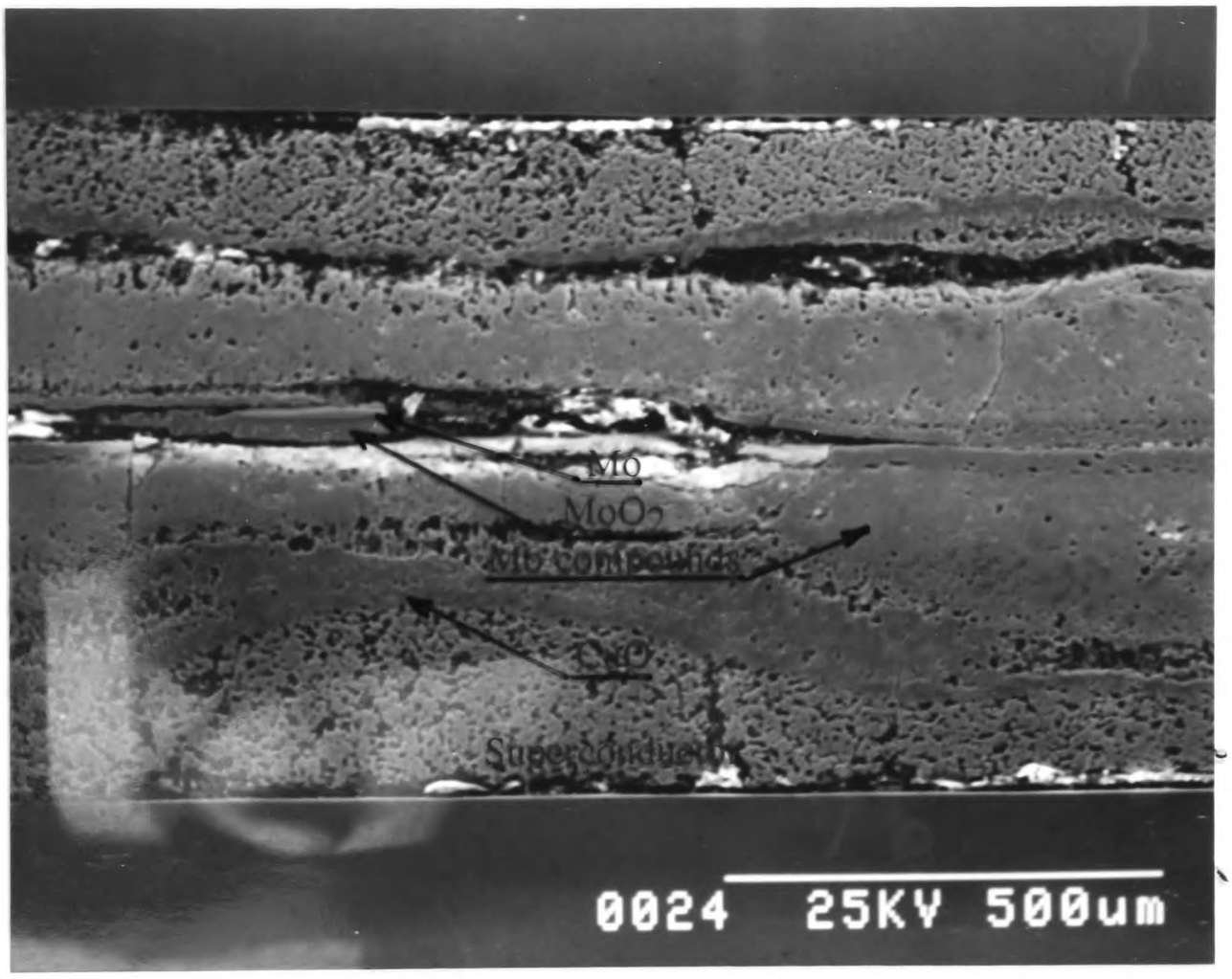

Figure 6.18: Interfaces of Mo/superconductor OS

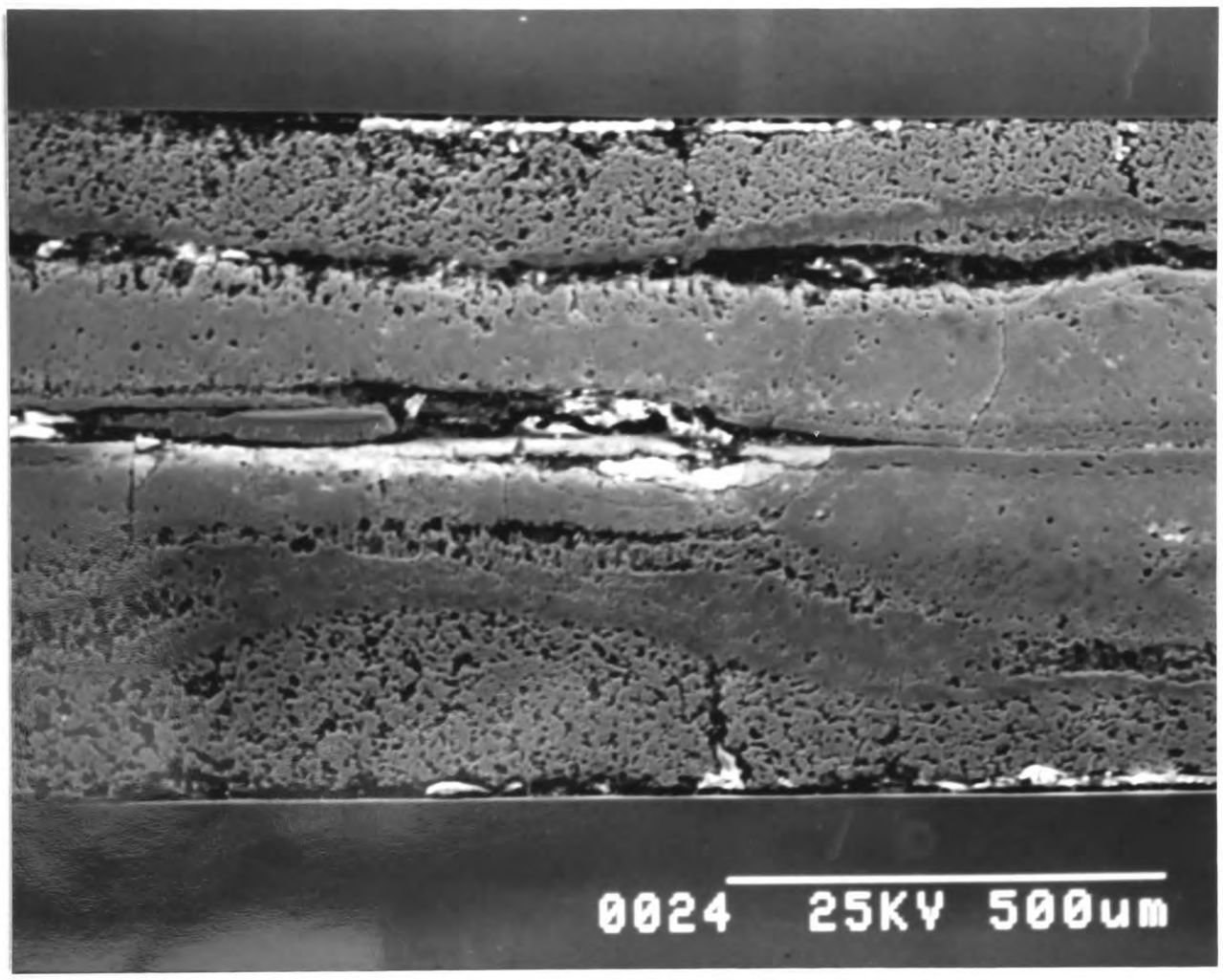

Figure 6.18: Interfaces of Mo/superconductor OS

relatively high mechanical strength.

The work on titanium contacts shows that this material has a very limited reaction with high density melt textured $YBa_2Cu_3O_{7-x}$ superconductor. It is a favourable candidate for a multilayer contact incorporated with a noble metal layer.

6.7.2 Experiments on Ti/Ag and Ti/Au contacts

Based on this idea, a thin layer of titanium metal ($< 1\mu m$) was deposited onto the superconductor by thermal evaporation, then a layer of silver or gold metal was deposited on the top of the titanium metal layer. After heat treatment for one hour at 500°C, silver wires were attached onto the contacts with silver paint.

6.7.3 Results

Contact resistivity was measured as a function of temperature, and the results are shown in Fig.6.19 & 6.20.

The annealed Ti/Ag and Ti/Au contacts show a metallic character, the contact resistivity drops slightly with decreasing temperature, and the contact resistivity is in the same range of the contact resistivity of noble metals made under similar conditions.

Like the unannealed silver contact, all the unannealed Ti/Ag and Ti/Au contacts show a semiconducting character. If the typical contact resistance is larger than a certain value ($>1\Omega$), no significant resistance change takes place at the superconducting transition temperature, and the contact resistivity is about 1000 times higher than that of annealed contact.

Microprobe analysis shows that the silver or gold has diffused into the Ti layer and the two elements are well mixed together. The electron microscope can not identify the boundary between the silver or gold and titanium.

6.7.4 Discussion

Comparing the contact resistivity of Ti with and without silver coating (Fig.6.11), the titanium with silver coating contact resistivity is much lower than the

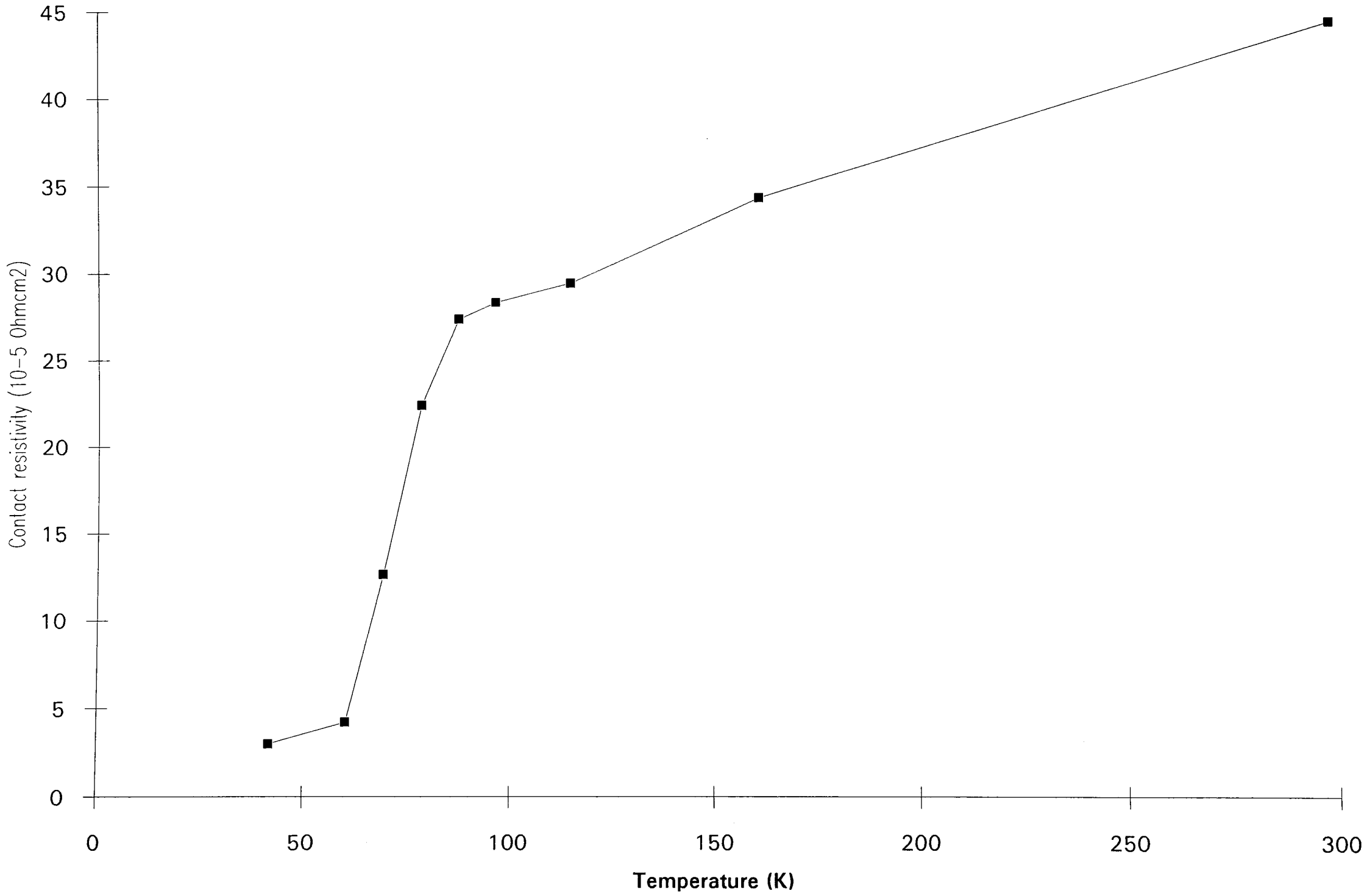

Figure 6.19: Ag/Ti contact resistivity OS

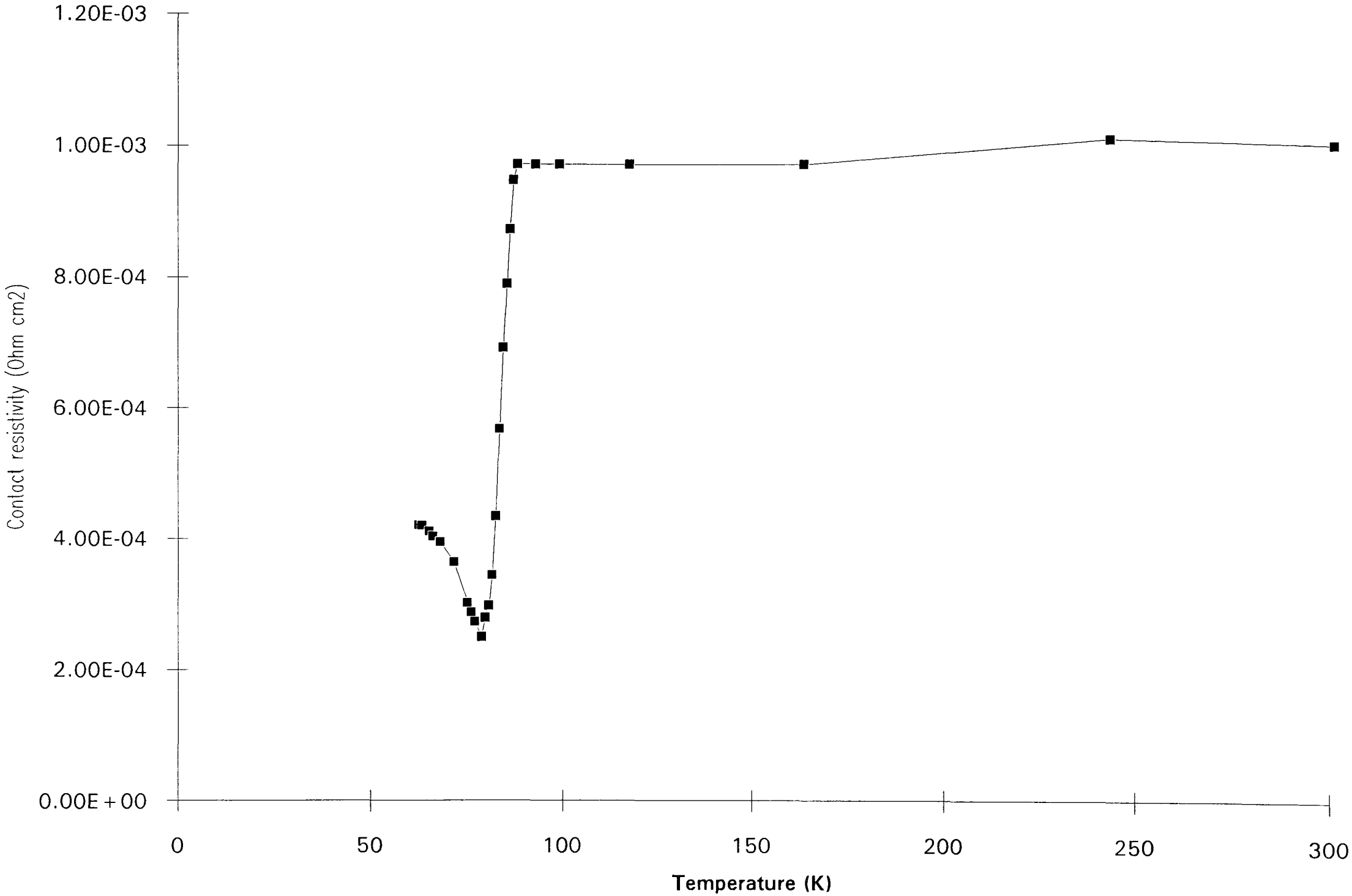

Figure 6.20: Au/Ti contact resistivity OS

one without silver coating. In addition, Ti/Ag and Ti/Au contacts show metallic behaviour while titanium contacts show semiconducting behaviour.

This result indicates that after the titanium oxide layer has been formed, the silver or gold diffuses into the layer and become fully intermixed with the titanium oxide. The interface resistance is then not greatly affected by the insulating Ti oxide.

It is a promising method to deposit a combination of the noble metal and reactive metal multilayers to make rugged thin film contacts to the superconductor.

6.8 'Semi-noble' metal-palladium contacts

In searching for materials which have limited reactions with $YBa_2Cu_3O_{7-x}$ for making rugged contacts, palladium was considered one of the candidates. Palladium is a common component in electric contact materials because it belongs to the noble metal family, and is very inert, (but not as inert as Pt or Au). It is expected that there will be limited reaction at the interface between palladium and superconductor. If the reaction is under control, the contact reaction at the interface will benefit the contact stability as well as mechanical properties.

6.8.1 Experiment

Palladium metal contacts were evaporated onto $YBa_2Cu_3O_{7-x}$ though a mask. After annealing at 600^oC for 1 hour, silver wires were attached to the palladium contact by silver paint before the electrical measurement.

A sample of diffusion bonded palladium/superconductor was made under similar conditions for the interfacial analysis. A palladium metal plate was mechanically polished, then the highly polished palladium metal plate surface was put against the polished $YBa_2Cu_3O_{7-x}$ surface. This palladium/$YBa_2Cu_3O_{7-x}$ composite was pressed together and annealed at 600^oC for 3 hours, after which the palladium plate was firmly bonded onto the $YBa_2Cu_3O_{7-x}$.

6.8.2 Results and discussion

The contact resistivity and its temperature dependence was determined by three-probe electrical measurement. The results of two experiments are shown in Fig.6.21 and Fig.6.22. From these contact resistivity results, one of the obvious features is the very strange contact resistivity behaviour near the superconducting transition temperature, T_c. This behaviour of the contact resistivity of palladium metal must be due to the structure at the contact interface.

A cross section of the diffusion bonded palladium/superconductor composite was polished and analyzed by SEM and electron microprobe. The results showed that unlike the titanium contacts on sintered superconductor which forms layered products at the interface, the palladium metal reacts with $YBa_2Cu_3O_{7-x}$ at the interface and forms isolated island-shaped palladium-rich phases (Fig.6.23 and 6.24). The compositions of the palladium-rich phases are identified as $BaCuPd_xO_{2+x}$, $PdCu_2O_3$, $Ba_4Cu_3Pd_2O_{11}$, $CuPd_xO_{1+x}$ and Pd+PdO phases ($x<1$) by microprobe analysis (table 6.9).

Table 6.9: Composition of interfacial reaction layer

	Y (at%)	Ba (at%)	Cu (at%)	Pd (at%)	O (at%)	Formula
Point 1	0.8	0.0	0.2	99.0	0.0	Pd
Point 2	0.0	0.1	32.9	15.0	51.9	$PdCu_2O_3$
Point 3	0.0	15.3	11.3	7.7	65.7	$Ba_4Cu_3Pd_2O_{11}$
Point 4	0.02	11.39	10.83	4.39	73.38	$BaCuPd_xO_{2+x}$
Point 5	0.0	0.1	41.2	6.3	52.4	$CuPd_xO_{1+x}$
Point 6	0.0	0.0	0.2	69.2	30.6	Pd+PdO

These oxide particles and particularly their shape and distribution at the

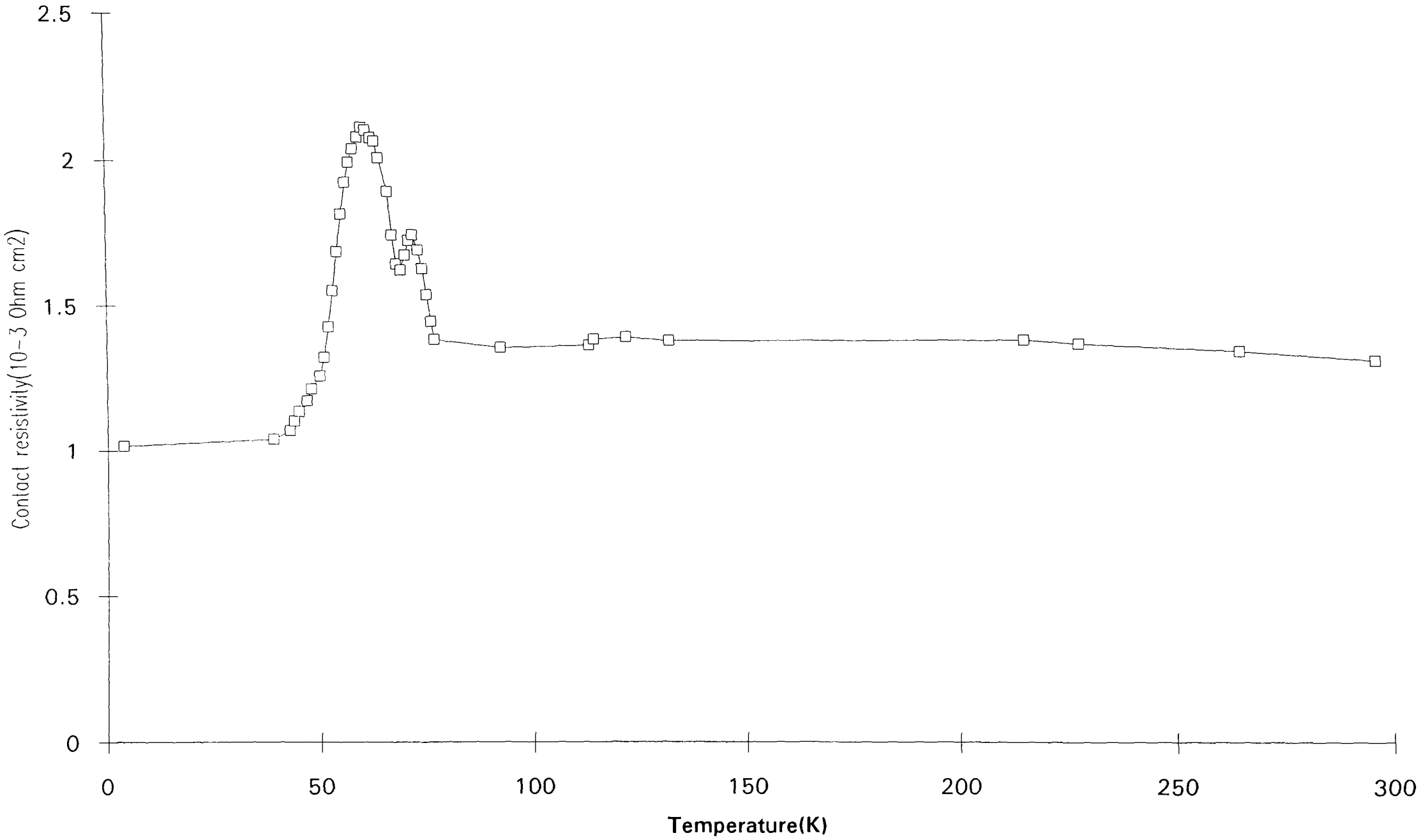

Figure 6.21: Pd contact resistivity MG

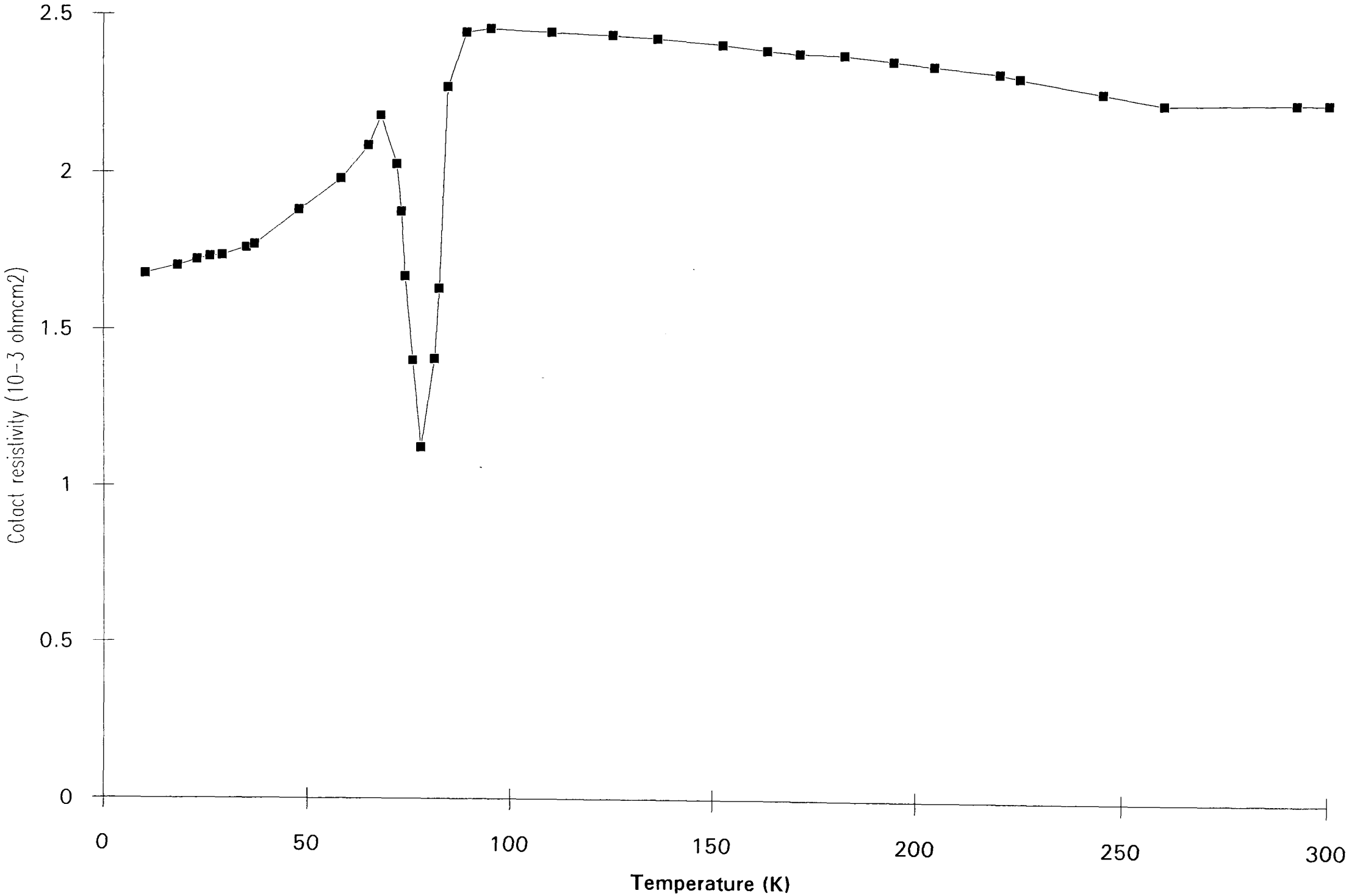

Figure 622: Pd contact resistivity MG

Figure 6.23: Interface of Pd/superconductor (annealed at 600°C for 1 hour)
MG

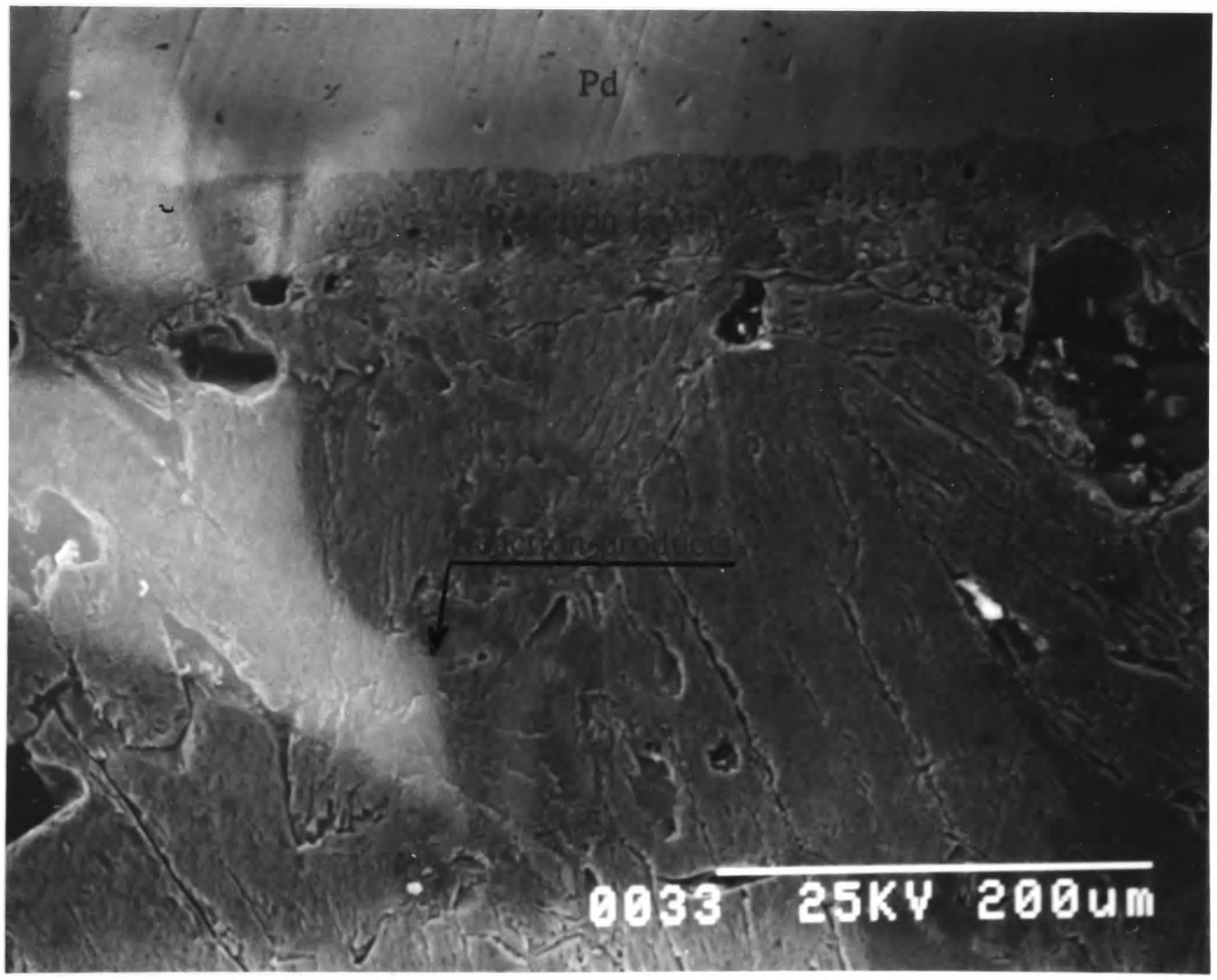

Figure 6.24: Interface of Pd/superconductor (annealed at 600°C for 8 hours)
MG

Figure 6.23: Interface of Pd/superconductor (annealed at 600^{o}C for 1 hour) MG

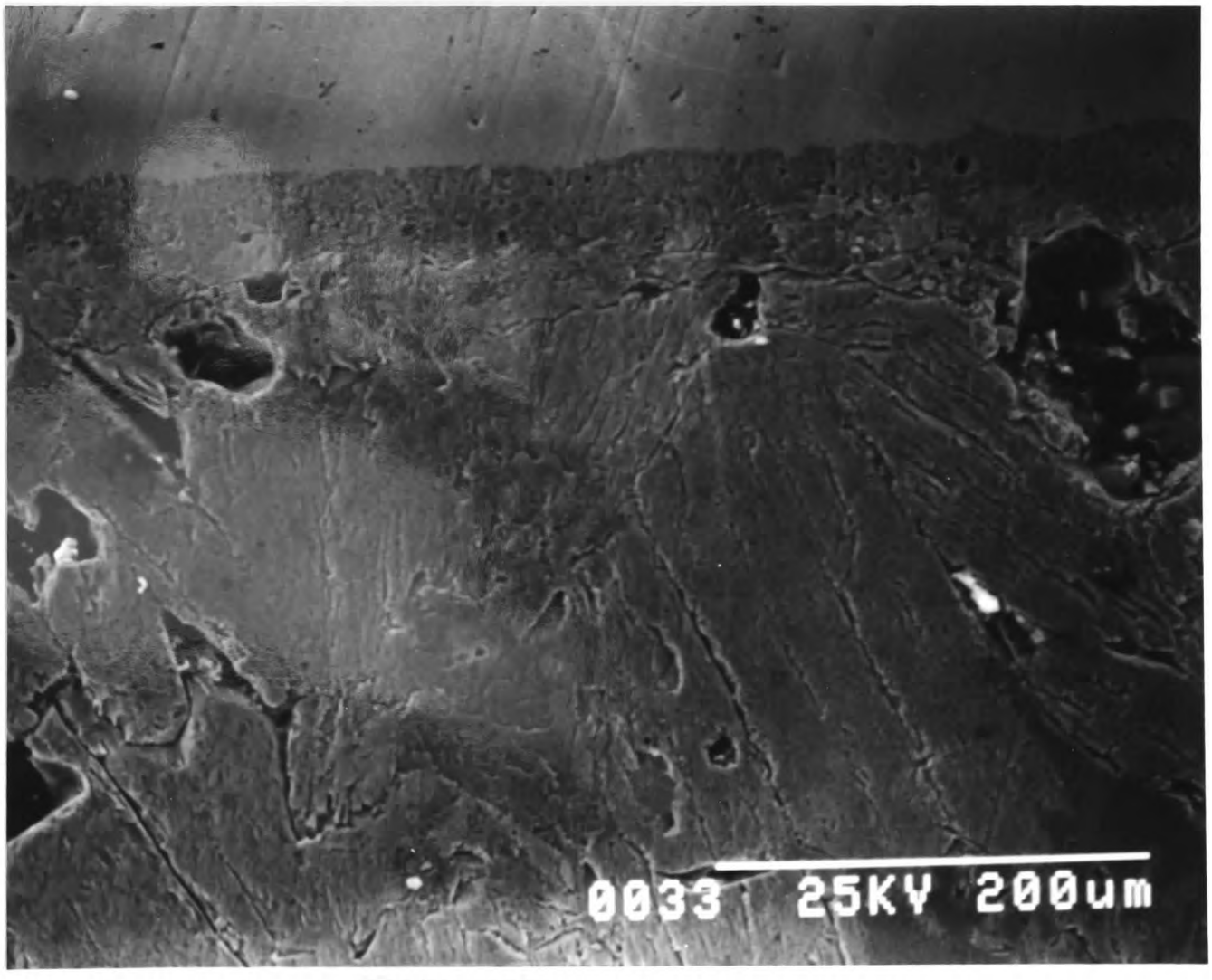

Figure 6.24: Interface of Pd/superconductor (annealed at 600^{o}C for 8 hours) MG

interface may caused the strange behaviour of the contact resistivity with temperature.

A simple model has been set up to explain the contact resistivity behaviour, and this model will be discussed in detail in chapter 8.

6.9 Solderable gold contacts

6.9.1 Introduction

We have seen that most methods for making electrical contacts to the superconductor require wire leads to be attached to the contacts, and thin film contacts are not suitable for conventional soldering methods [Ekin 1988 b]. Indium solder may alloy through the thin metal contact layer and degrade the $Y_1Ba_2Cu_3O_{7-x}$ surface for instance. From section 6.4 we see that using silver paint to attach electrical leads onto the contacts after contact making may cause high electrical resistance and low mechanical strength of the contact. Silver epoxy contacts is one solution to the problem, but in order to incorporate electrical leads, the wires should be involved in the whole contact making procedure including annealing at over 900^{o}C, which may be an restriction in many applications.

6.9.2 Background

Gold is often thought to be the best contact material, see data in Table 3.2. Its low resistance, bondability, chemical inertness, ductility and solderability are advantages over other materials. The usage of noble metals as contact materials to superconductors helps to stabilize the interfaces by preventing oxygen diffusion across the interface. Silver may act as a "switchable" passivation buffer, allowing oxygen to penetrate to the $Y_1Ba_2Cu_3O_{7-x}$ interface at elevated temperatures, but protecting the $Y_1Ba_2Cu_3O_{7-x}$ surface at room temperature. This is very useful for the making and oxygenating superconductor/silver composites, allowing the $Y_1Ba_2Cu_3O_{7-x}$ to be fully oxygenated. But for making contacts on a fully oxygenated sample, especially for the case of using high power soldering to attach electrical leads onto the as-made contacts, the oxygen may escape from the superconductor surface through the silver

contact during soldering. Gold on the other hand has been shown to be an effective oxygen buffer material at high temperatures, even a thin layer of the gold can prevent oxygen absorption resulting in an oxygen deficient layer which has semiconducting behaviour [Mizushima, 1988]. Gold contacts certainly have the advantage over silver contacts that they can block oxygen diffusion across the interface.

6.9.3 Experiment and results

To investigate the gold/superconductor interactions which are reported by many authors [Verkouteren 1989, Ray 1989 and Cieplak 1990], a piece of polished gold plate was put on the top of a clean surface of the high Tc superconductor, and then pressure was put onto the gold plate to press the gold plate and superconductor tightly together in the geometry showed in Fig 6.25.

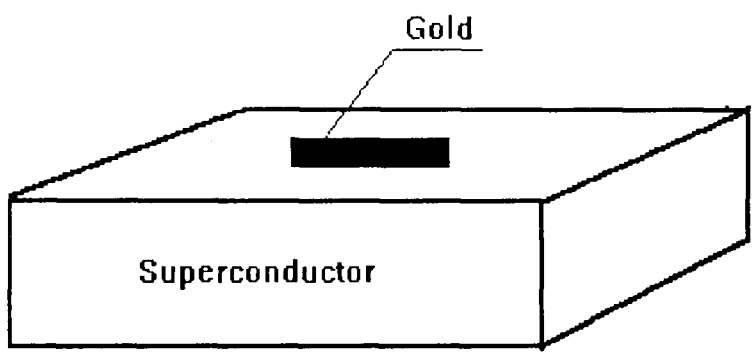

Figure 6.25: Schematic diagram of the gold/superconductor composite

The gold/superconductor systems were put inside a furnace and sintered at 800^{o}C for 12 hours both in pure oxygen and air. After furnace cooling to room temperature, the interface was examined by optical microscopy, SEM and electron microprobe analysis.

The optical microscope shows the gold reacted with $YBa_2Cu_3O_{7-x}$ superconductor. The surface area of the $YBa_2Cu_3O_{7-x}$ under the gold plate changes to a green colour, which implies there are reactions between gold and $Y_1Ba_2Cu_3O_{7-x}$. It is possible that the reaction might form the green Y_2BaCuO_5 phase on the surface (Fig 6.26).

Figure 6.26a: Reaction products on superconductor surface
MG

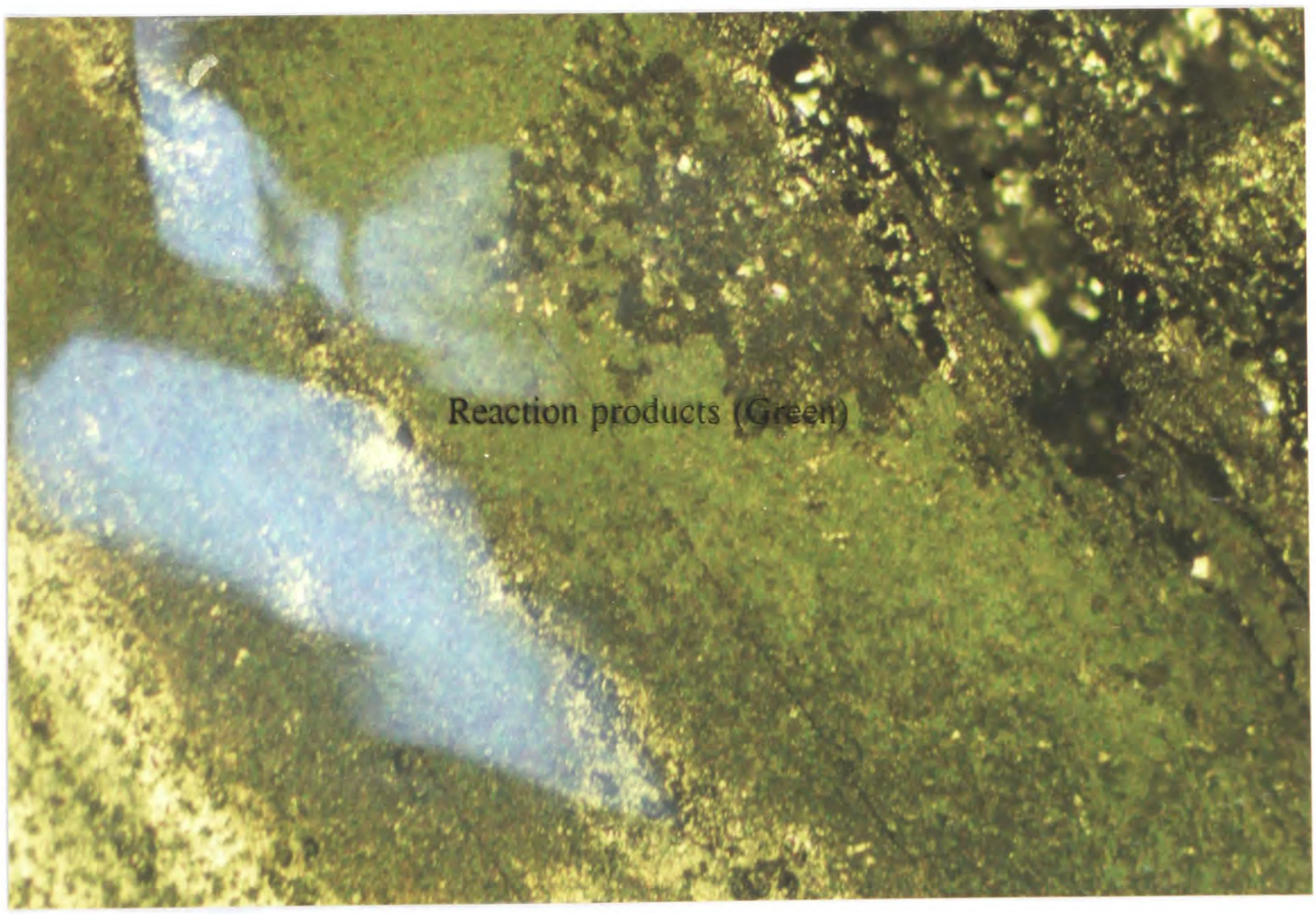

Figure 6.26b: Reaction products on superconductor surface
MG

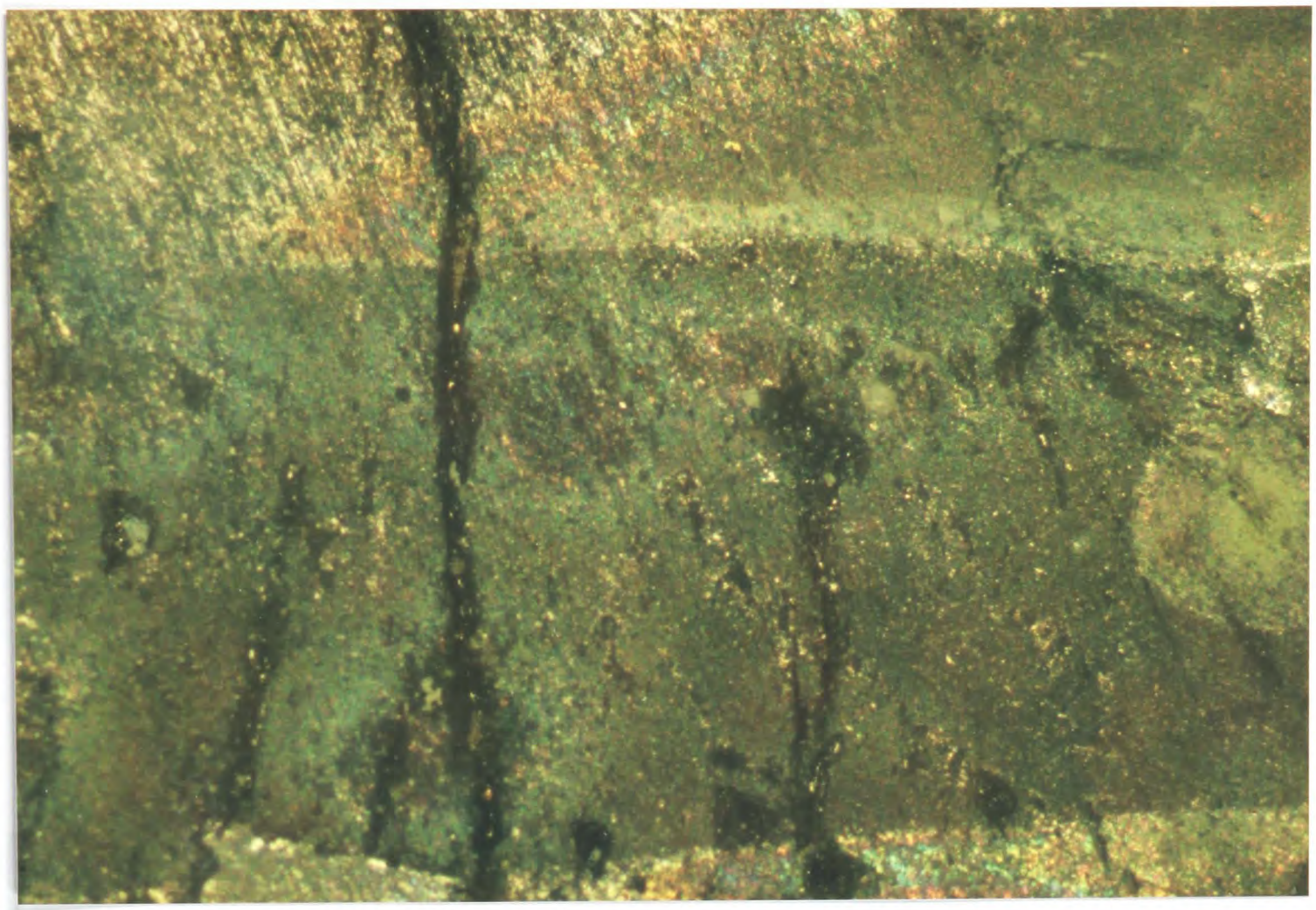

Figure 6.26a: Reaction products on superconductor surface
MG

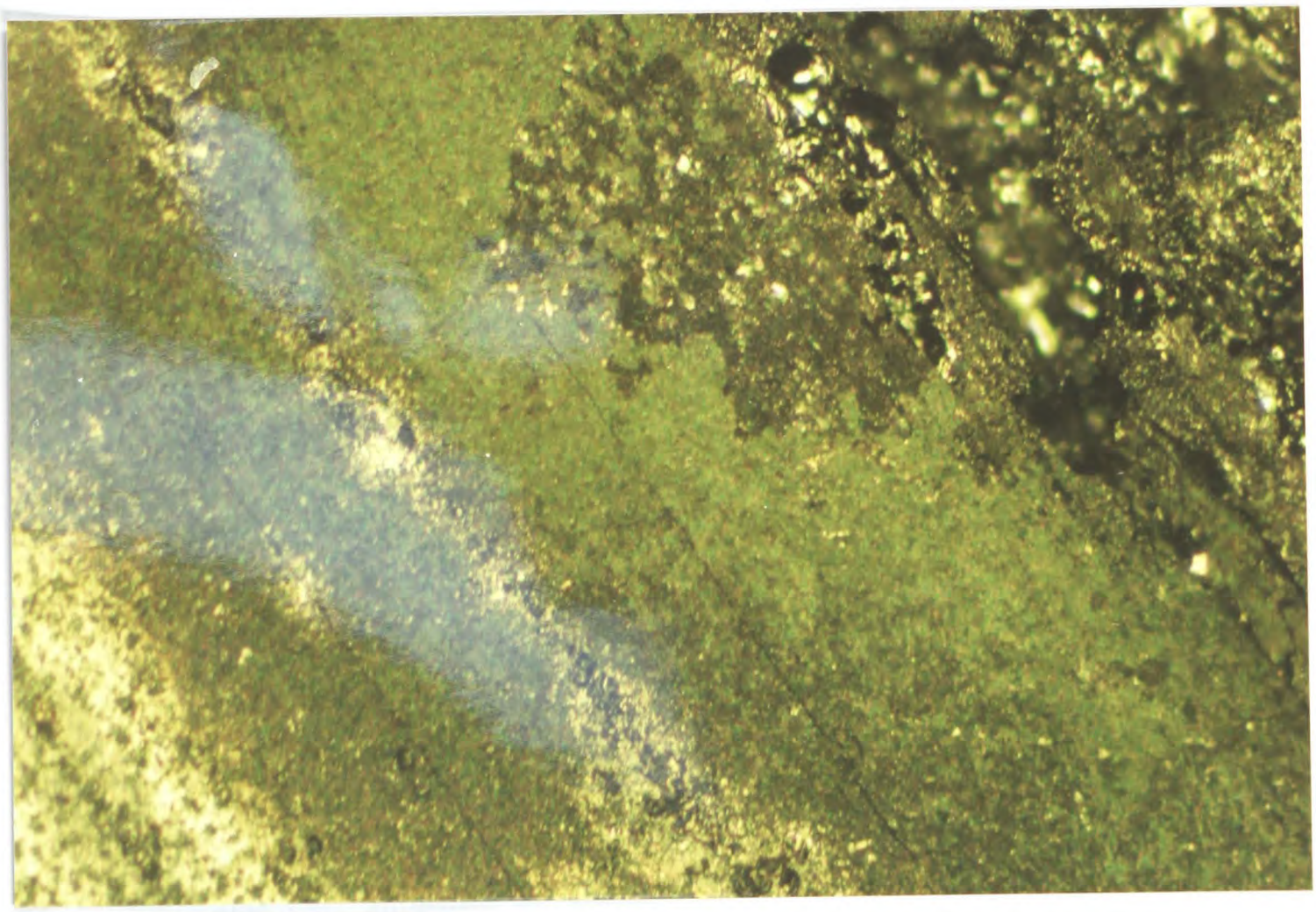

Figure 6.26b: Reaction products on superconductor surface
MG

The SEM analysis showed there were compounds formed on the gold plate (Fig.6.27) and a layer of reaction product on the surface of the high Tc superconductor (Fig. 6.28) when compared to the clean surface of as made samples (Fig.5.7b).

Quantitative microprobe analysis shows that the compounds seen in the SEM pictures (Fig.6.27 and 6.28) are mainly the Y_2BaCuO_5 phase. However sometimes the electron microprobe does not detect the correct composition of Y_2BaCuO_5 phase because the reaction layer is too thin. Sometimes the composition is apparently more like $Y_1Ba_1Cu_1O_X$ (table 6.10).

Table 6.10: Composition of interfacial reaction products

	Y (at%)	Ba (at%)	Cu (at%)	O (at%)	Formula
Point 1	18.91	12.12	10.05	58.93	Y_2BaCuO_5
Point 2	17.26	10.61	12.05	60.08	Y_2BaCuO_5
Point 3	13.24	12.56	11.87	62.33	Y_2BaCuO_5

Another experiment was also carried out to examine the reaction between gold and $YBa_2Cu_3O_{7-x}$ superconductor in another contact geometry, gold strips were embedded inside $YBa_2Cu_3O_{7-x}$ as shown in Fig.6.29.

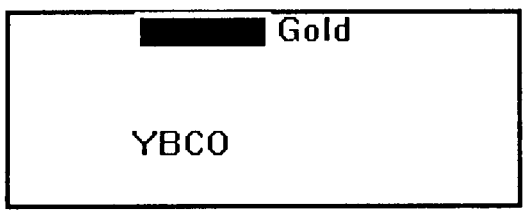

Fig.6.29 Schematic diagram of gold/superconductor composite

The gold plate was pressed into $YBa_2Cu_3O_{7-x}$ powder and sintered at 900°C for 12 hours and then annealed at 800°C for 72 hours. The interface between the gold and superconductor was analysed by SEM and electron microprobe, and

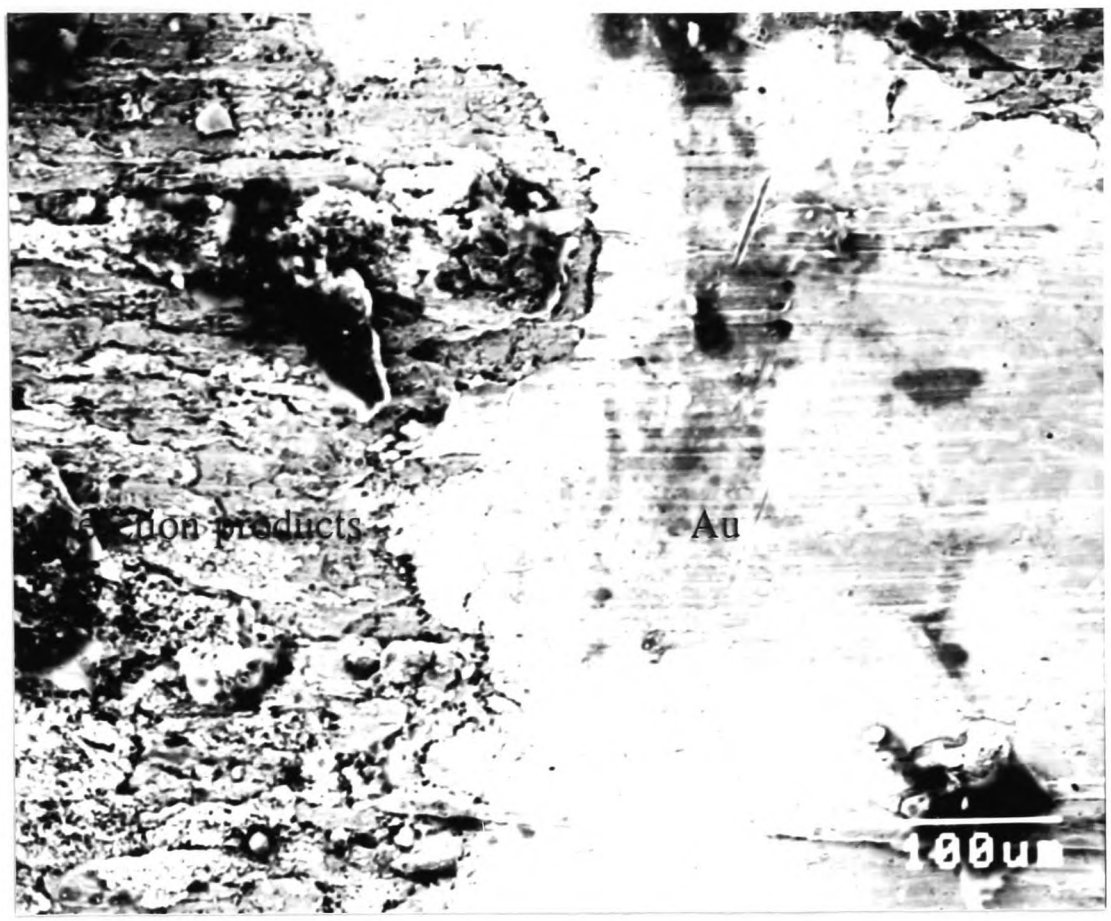

Figure 6.27: Reaction products on Au surface

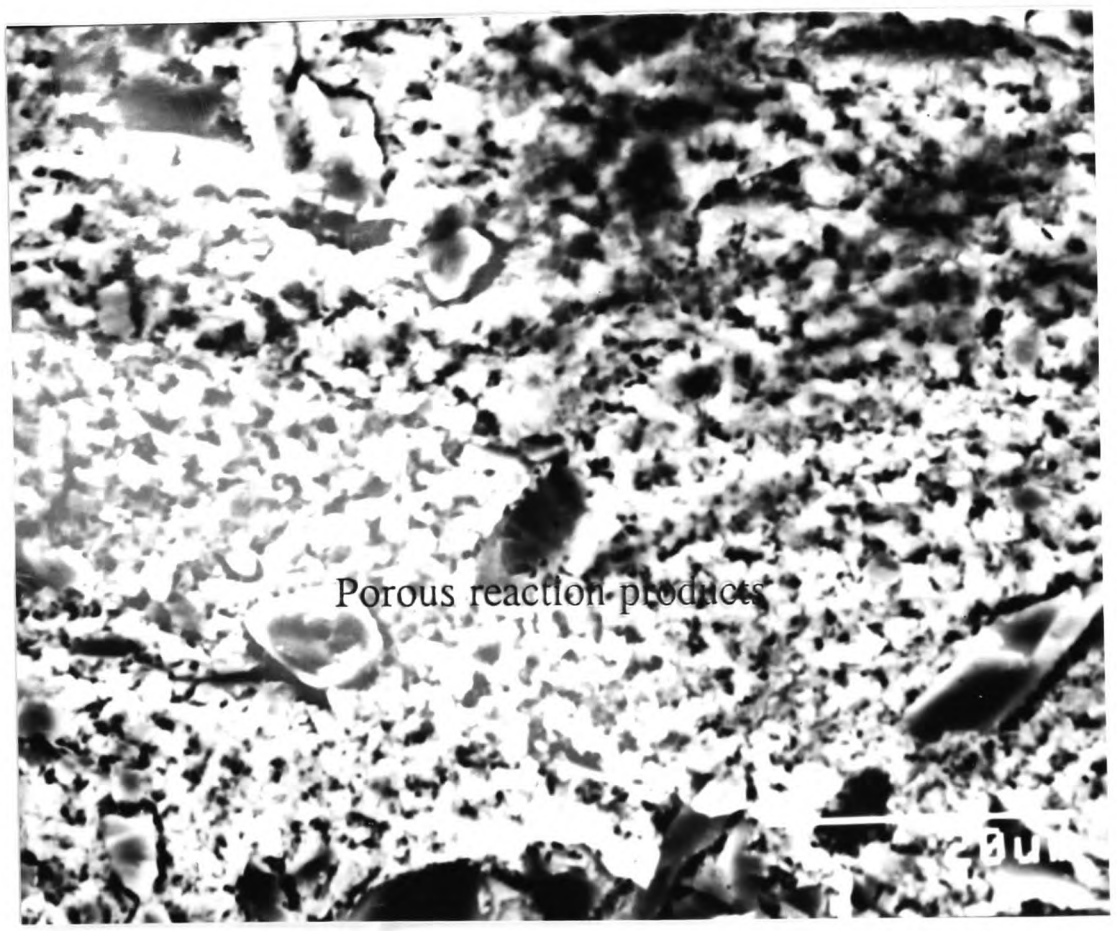

Figure 6.28: Reaction products on superconductor surface
MG

Figure 6.27: Reaction products on Au surface

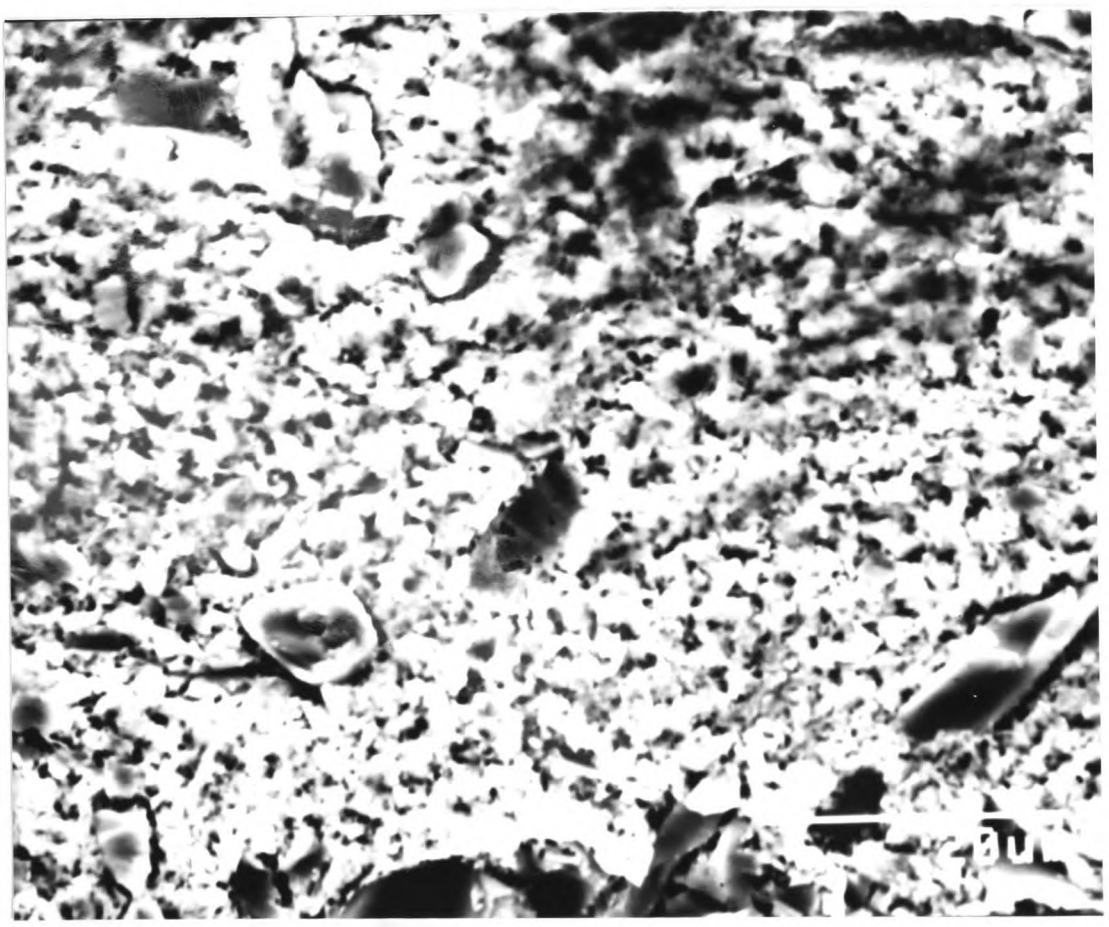

Figure 6.28: Reaction products on superconductor surface
MG

surprisingly the interface appears clean and no Y_2BaCuO_5 phase was detected.

By increasing the annealing time, gold contacts were made by diffusion bonding the Au/superconductor composites at 800°C for 72 hours. The gold contact was firmly bonded to the $Y_1Ba_2Cu_3O_{7-x}$ (The bonding is not firm enough if it was annealed for less time). Silver wires were soldered onto the gold contacts using indium solder. The electrical resistivity of the gold contact was measured by the three-terminal method. The gold contact resistivity and its temperature dependence is shown Fig.6.30. The contact resistivity shows positive temperature dependence with contact resistance 10^{-7} Ωcm^2 below Tc. The cross section of the contact interface was analyzed by electron microprobe, and there are no detectable interfacial reactions. The interfacial structure were shown in the SEM image, Fig. 6.31. There is no sign that gold takes part in any reaction. The gold diffusion distance in the superconductor is also quantitatively measured by electron microprobe analysis, and the result is shown in Fig.6.32. The initial interface is situated at position 10 μm and there is clearly some penetration of Au into the $Y_1Ba_2Cu_3O_{7-x}$.

6.9.4 Discussion

The contact resistivity measurements show that gold contact resistivities seem only slightly damaged by the slight decomposition of $YBa_2Cu_3O_{7-x}$ at the contact interface. However, the diffusion bonding time for the Au contacts is much longer than the annealing time for Au/superconductor samples used for interface reaction analysis. It is not clear if the same reaction has happened in the Au contact sample since it is difficult to separate the contact without damaging the interface, and cross section analysis cannot detect a thin reaction layer.

The interfacial analysis shows that the presence of gold on the surface of $YBa_2Cu_3O_{7-x}$ somehow makes it thermodynamically unstable, decomposing into 211 and other compounds. However, if the gold plate is embedded inside the superconductor and sintered together, there is no detectable reaction at the interface. This indicates that whether the gold - $Y_1Ba_2Cu_3O_{7-x}$ reaction occurs has some

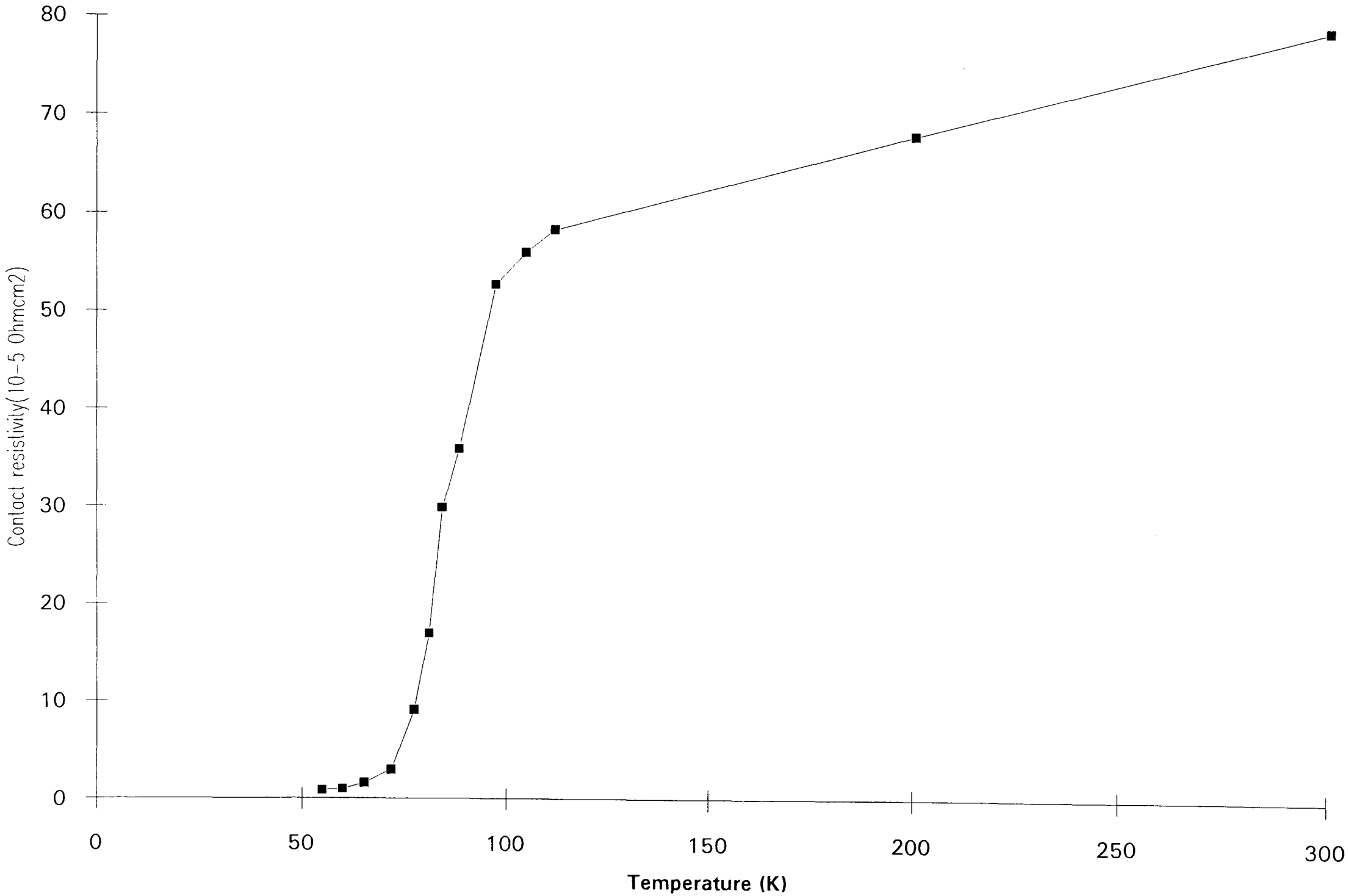
Contact resistivity(10-5 Ohmcm2)
80
70
60
50
40
30
20
10
0
0
50
100
150
200
250
300
Temperature (K)

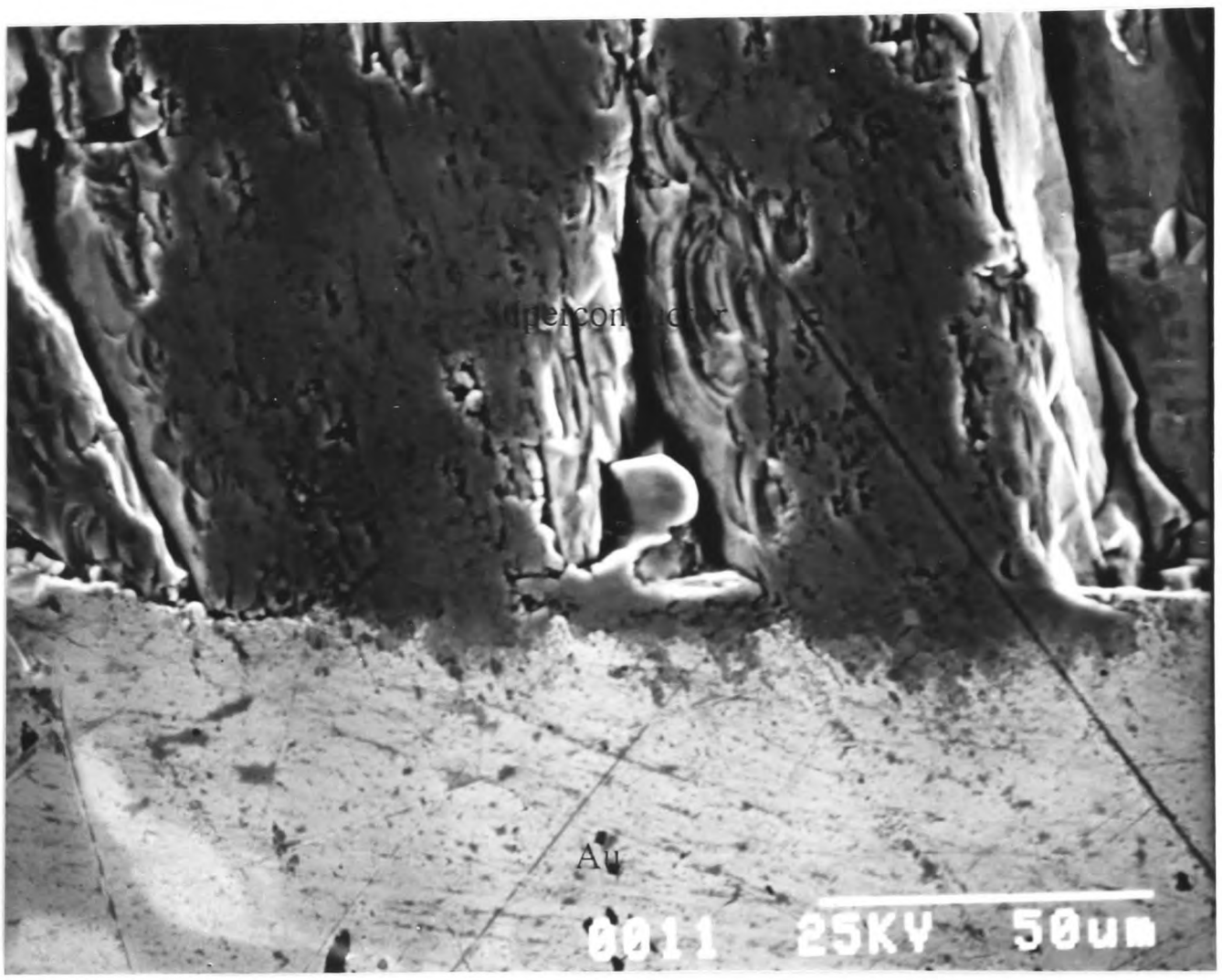

Figure 6.31: Interface of Au/superconductor MG

Figure 6.31: Interface of Au/superconductor MG

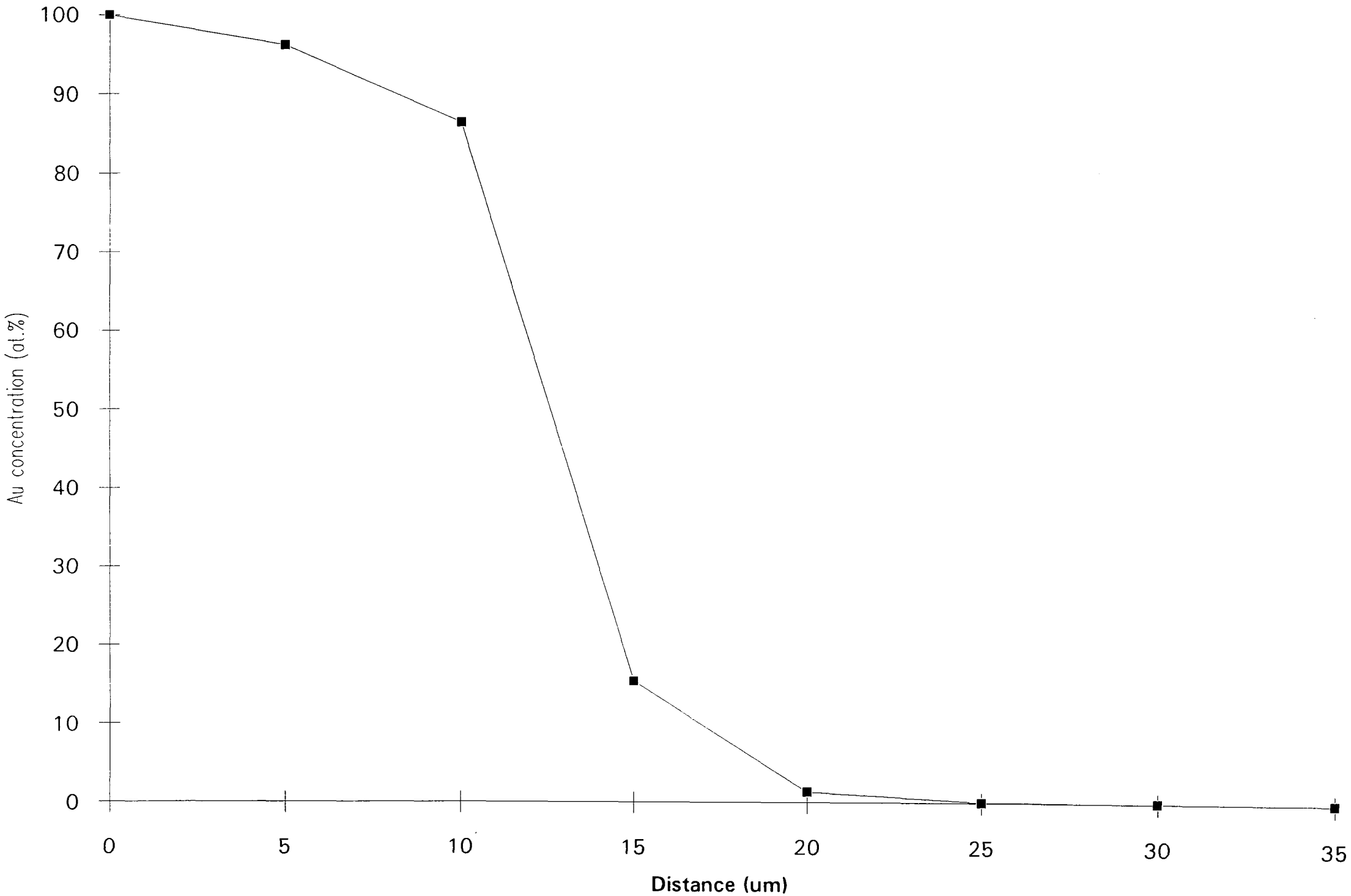

Figure 6.32: Au diffusion

relation to the oxygen supply to the contact interface. Since gold is a good oxygen buffer material, and at high temperatures (over 800°C) the whole superconductor is in the oxygen deficient tetragonal structure according to the P-T-X diagram of $YBa_2Cu_3O_{7-x}$ (Fig. 2.14), the contact interface must also be oxygen deficient. The gold contact prevents oxygen diffusing back through the contact into the superconductor during the cooling.

Thus a possible explanation for the experimental observation is that during high temperature annealing the surface of the $YBa_2Cu_3O_{7-x}$ which in direct contact with the gold plate may be in a oxygen deficient environment due to the presence of the gold buffer layer. If the oxygen concentration is below the stable limit (10^{-4} atm), Fig.2.3, then the $YBa_2Cu_3O_{7-x}$ may decompose into 211 and other impurity phases. However, it is quite unlikely that the oxygen deficient environment itself can cause the decomposition of $YBa_2Cu_3O_{7-x}$, since there are no signs of decomposition happened in other geometries of Au/superconductor composites.

A second explanation is that the $YBa_2Cu_3O_{7-x}$ is not stable in contact with gold because copper diffuses into the gold plate and decomposes the superconductor material. This mechanism has been suggested by Verkouteren et al [Verkouteren 1989, Ray 1989 and Cieplak 1990]. However this explanation is also quite unlikely since not all gold/$YBa_2Cu_3O_{7-x}$ composites show an interfacial reaction.

Another explanation is that the oxygen concentration gradient may cause the decomposition of $YBa_2Cu_3O_{7-x}$. At high temperatures (800°C) the oxygen equilibrium pressure is very low and so the superconductor is in the oxygen deficient tetragonal state. During cooling, the oxygen is absorbed back and transforms the $YBa_2Cu_3O_{7-x}$ into the superconducting orthorhombic structure. But the gold is a good oxygen buffer material, and the surface of the $YBa_2Cu_3O_{7-x}$ under the gold plate may need the diffusion of oxygen from surrounding exposed surface area to be fully transformed. The presence of an oxygen concentration gradient at the interface may cause a change in other elements' chemical potentials.

According to the Gibbs Duhem relation, in $YBa_2Cu_3O_{7-x}$:

$$d\mu_Y + 2d\mu_{Ba} + 3d\mu_{Cu} + 7d\mu_O = 0 \qquad (7.3)$$

Cu is the most mobile cation element in the system, and may move under the presence of a chemical potential gradient, as schematically shown in Fig.6.33. Cu may diffuse in the opposite direction to the oxygen, and this may cause the decomposition of $YBa_2Cu_3O_{7-x}$. The excess Cu easily disappears into the gold plate, leaving mainly 211 at the interface as suggested by other people's work [Verkouteren 1989, Ray 1989 and Cieplak 1990] and the experimental results presented here.

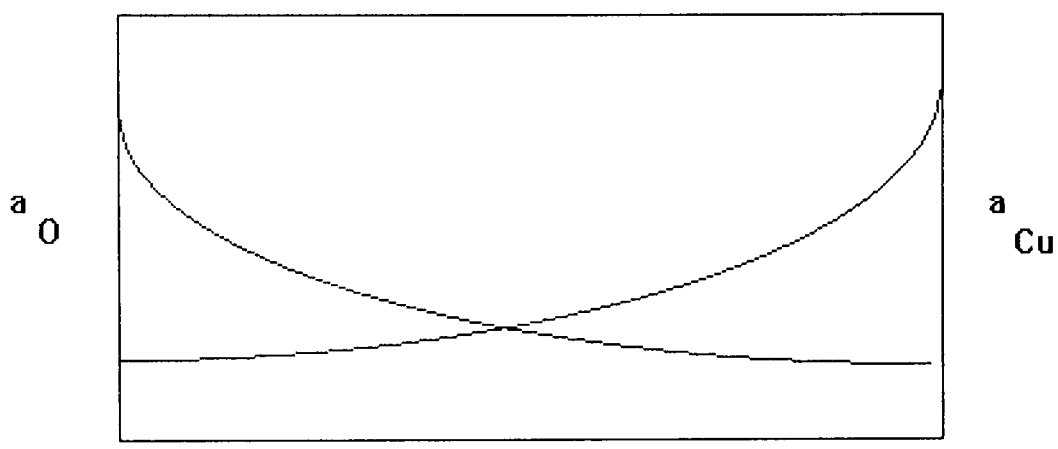

Fig. 6.33 Schematic chemical potential changes
in the presence of oxygen concentration gradient

This explanation predicts a very limited reaction zone, only the very near surface layer will have the potential to cause copper diffusion and decompose the $YBa_2Cu_3O_{7-x}$ which in good agreement with the experimental results.

Further investigation is needed to identify which is the mechanism for the decomposition of $YBa_2Cu_3O_{7-x}$ in the presence of gold. Based on the third proposed explanation, a problem could be solved by introducing sufficient oxygen into the sample even during high temperature annealing to stabilise the $YBa_2Cu_3O_{7-x}$ and reduce the chance of decomposition.

In the next stage of the work presented in this thesis, electrochemical methods were used to dope oxygen atoms into the superconductor at high temperature. The details are described in chapter 7.

6.10 Conclusions

In summary, I proposed and investigated two kinds of design of reactive metal contacts, aiming to make low resistivity contacts with strong mechanical strength. Three possible reactive contact metals have been tested for contact making, and the microstructures at the interfaces have been studied to find the relations between contact resistivity and contact processing conditions. Gold and silver contact making techniques were carefully studied to find possible rugged low resistivity contacts.
The results can be summarized as:

Titanium metal can be used as one of the components in multilayer contacts if the resistivity is not required to be lower than $10^{-5}\Omega cm^2$. This is a promising type of contact processing technique for low resistivity and strong mechanical bonds.

Molybdenum metal is not suitable for making contact to $YBa_2Cu_3O_{7-x}$.

Palladium metal can form strong bonds with $YBa_2Cu_3O_{7-x}$ with contact resistivities around 10^{-3}-10^{-4} Ωcm^2. The anomalous resistivity behaviour of these contacts may due to the distribution of reaction products with widely varying properties.

As I have mentioned in chapter 3, part of my work on Mo and Pd contacts overlapped with Bessergenev's work. The resistivity values I obtained for Mo and Pd contacts are similar to Bessergenev's results, but my study of the contacts is much more thorough in the interfacial structure and its relation with the irregularity of the contact resistivity - time behaviours.

Gold and silver contacts give resistivities among the best reported results in the literature, and they turned out to be extremely stable in time, could withstand repeated thermal cycling from room temperature to 10K and yield very reproducible R-T curves. Among them, silver epoxy contacts and solderable gold plate contacts are the promising techniques for making strong contacts with ultra low resistivity behaviour.

Chapter 7

Solid state electrochemical studies on $YBa_2Cu_3O_{7-x}$

7.1 Introduction

One of the important parameters of $YBa_2Cu_3O_{7-x}$ is its oxygen stoichiometry which can change the properties of the material from superconducting to semiconducting. The optimum oxygen stoichiometry is 7-x=6.9~7.0. The availability of structurally and compositionally homogeneous orthorhombic $YBa_2Cu_3O_{7-x}$ materials with this stoichiometry is crucial for their application. Most commonly the sample must be annealed for a long time at 673-773K to be fully oxygenated. But the kinetics of oxidation are very slow at 700K. It has been reported that it is extremely difficult for high density samples to be fully oxidized [Town 1990 and O'Bryan 1988]. Higher temperature annealing will need impractically high oxygen pressures to achieve the optimum oxygen content, since the equilibrium value of x varies with both temperature and oxygen pressure (Fig 2.14).

Solid state electrochemical methods can control the oxygen stoichiometry at the surface of the superconductor more or less independently of the temperature, and has the advantage that a high oxidation temperature can be used without expensive high pressure oxygen equipment to achieve high oxygen stoichiometry in $YBa_2Cu_3O_{7-x}$.

The experiments in this chapter may be divided into four main areas: 1) To improve the oxygen content of bulk textured $YBa_2Cu_3O_{7-x}$; 2) To improve the oxygen content of $YBa_2Cu_3O_{7-x}$ thick film samples; 3) To measure the thermodynamic properties of the $YBa_2Cu_3O_{7-x}$ and to study the formation of $YBa_2Cu_4O_8$; 4) To make low resistivity gold contacts.

7.2 Background

7.2.1 Theory of electrolytes

There is a very interesting physical phenomenon associated with the operation of ionic conductors that the changes in surface activities of mobile ionic species

respond to changes in applied potential. Thus the migration of ionic species inside oxygen ion conducting solid electrolytes is influenced by the presence of an electrochemical gradient. The relation between the partial current i_i and the electrochemical potential gradient $d\eta_i/dx$ is given by the partial specific electrical conductivity σ_i for the species i [Wepper 1987]:

$$i_i = \frac{-\sigma_i}{Z_i e} \times \frac{d\eta_i}{dx} \tag{7.1}$$

where Z_i is the charge number and e is the elementary charge.

The electrochemical potential η_i may be divided into an electrostatic potential component ϕ and a chemical potential component μ_i:

$$\eta_i = \mu_i + Z_i e\phi \tag{7.2}$$

$$\text{and} \quad \mu_i = \mu_i^o + KT\ln a_i \tag{7.3}$$

where μ_i^o, K, T are the chemical potential at the standard state ($a_i = 1$), Boltzmann's constant, and the absolute temperature respectively.

The conductivity may be written as product of the concentration of species C_i and the diffusivity D_i by the Nernst-Einstein equation [Nernst 1888 and Einstein 1905]

$$\sigma_i = \frac{D_i C_i Z_i^2 e^2}{KT} \tag{7.4}$$

Combining equations (7.1) to (7.4), we can get equation 7.5:

$$i_i = \sigma_i \cdot \frac{d\phi}{dx} - Z_i e D_i \frac{d\ln a_i}{d\ln C_i} \cdot \frac{dC_i}{dx} \tag{7.5}$$

For a practical solid electrolyte there is a large concentration of mobile ions in the electrolyte. The ionic current is far in excess of the electron current, thus the chemical potential of mobile ionic species is independent of position, so equation (7.5) can rewritten as:

$$i_i = \sigma_i \frac{d\phi}{dx} \tag{7.6}$$

From this equation we can see that the ionic transference is predominantly due to the influence of internal electrostatic field. This is Ohm's law for the ionic conducting species i.

The relationship between the chemical potential of oxygen μ_{O2} and the oxygen partial pressure p_{O2} is :

$$\mu_{O2}=RT\ln p_{O2} \qquad (7.7)$$

where T is the absolute temperature of the electrolyte and R is the gas constant.

By considering the transport of one mole of oxygen across the electrolyte, the energy balance requires

$$\mu'(O_2)-\mu''(O_2)= - Z\times F\times E \qquad (7.8)$$

$\mu'(O_2)$ and $\mu''(O_2)$ are the chemical potentials on either side of the electrolyte respectively, Z (=4) is the valence of molecular oxygen, F is the Faraday constant and E is the EMF (electromotive force) across the electrolyte. Combining equations (7.7) and (7.8), one derives the so-called Nernst equation:

$$E =-\frac{RT}{4F}\ln\frac{p'_{O_2}}{p''_{O_2}} \qquad (7.9)$$

From equation (7.9) we can see that the activity at the opposite surface may be determined when the activity at one surface of the electrolyte is fixed at a known reference value.

This attractive feature enables the electrolyte to act as an electrochemical transducer, so the thermodynamic and transport quantities can be converted into precisely measurable electrical quantities such as voltage and current.

7.2.2 Experimental principles

In insulating oxide crystals, oxygen ions form a close-packed array and are usually practically immobile compared with cations. Unlike the insulating oxides, the oxygen ions in $YBa_2Cu_3O_{7-x}$ are the most mobile species, and $YBa_2Cu_3O_{7-x}$ ceramics have a very good electrical conductivity within which it is possible to maintain a high current density. This fact provides the basis of a study using electrochemical methods to monitor oxygen activities in $YBa_2Cu_3O_{7-x}$.

The oxygen activity at the interface between a solid electrolyte and

$YBa_2Cu_3O_{7-x}$ is determined by the Nernst equation, $-E=(RT/ZF)\ln(A_{ref}/A_{123})$, which relates the open circuit potential across the coupling, E, to the ratio of oxygen activities at each surface of the electrolyte, where R is molar gas constant, T is the absolute temperature, Z is the number of electrons involve per volume cell, F is the Faraday constant, and A_{ref} and A_{123} are the oxygen activity at the reference side and the interface between $YBa_2Cu_3O_{7-x}$ and electrolyte respectively. By measuring the open-circuit voltage between the reference and the sample, the oxygen activity at the sample surface can be determined. Conversely, by controlling the potential difference E across the electrolyte, the activity of oxygen at the electrolyte/sample interface can be fixed with respect to the reference electrode.

7.2.3 Selection of solid state ion conductor

Among the most commonly used oxide substrates, yttria-stabilized zirconia (YSZ), MgO, Al_2O_3 and $SrTiO_3$, YSZ has shown to be one of the least reactive ceramic materials used as substrates for $YBa_2Cu_3O_{7-x}$ films [Cheung 1989, Naito 1987 and Gurvitch 1987].

Besides, yttria-stabilized zirconia (YSZ) has shown the lowest interfacial electrical resistance between the $YBa_2Cu_3O_{7-x}$ films and substrates [Ying 1990]. MgO and Al_2O_3 have high resistivity interfaces, and Al_2O_3 shows a large reaction layer. $SrTiO_3$ also has a interfacial resistance larger than the interfacial resistance of YSZ. These results show that YSZ is a good candidate for electrochemical titration of the YBCO superconductor.

Although other compounds may be used as electrolytes, such as Bi_2O_3, the poor chemical stability of these compounds casts doubts on use in practical applications, and a strong reaction with the superconductor has been found [MacManus 1989].

Yttria-stabilized zirconia electrolytes can work at the temperature ranging from 873K to 1773K as shown in Fig. 7.1. Below 773K the conductivity falls below 10^{-3} $(\Omega cm)^{-1}$ and the ionic flux will be too low for practical use.

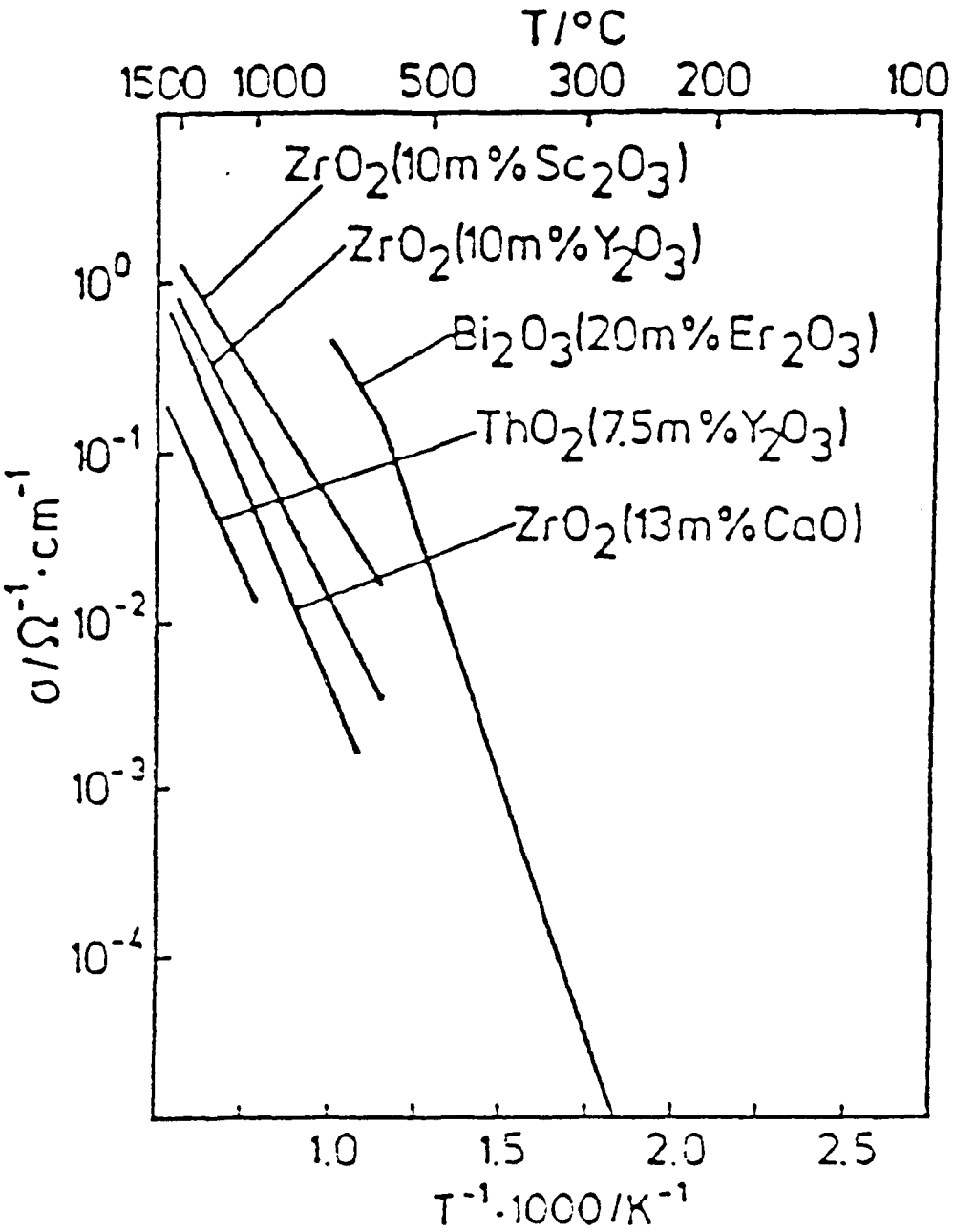

Fig.7.1: Conductivity of several electrolytes and their temperature dependence

These data provide a basic foundation to use YSZ as an electrolyte for the purpose of electrochemical titration of $YBa_2Cu_3O_X$ thin film and bulk samples.

7.3 Experimental equipment

7.3.1 Apparatus for electrochemical titration

The apparatus was designed with following abilities: holding the samples at a carefully chosen position in the furnace and providing pressurised contacts which are essential for both electrochemical titration and contact processing experiments; allowing electrical signals to pass into and out of the samples through electrical contacts at high temperature; and containing samples in a gas controlled chamber which can be used in different gaseous environments. The structure of the apparatus is

illustrated in Fig.7.2. The main body of the apparatus was made of pyrophyllite ceramic (1) and brass sealing parts (2). The pressure loading system included a spring (3) and a closed-ended alumina tube (4) which also served as a temperature probe for the sample. The cooling system (5) was bonded onto the brass sealing piece to prevent overheating of the brass and the O ring (6) during high temperature electrochemical titration. The metal sealing part contains three holes which serves as passage for gas control (7), electrical wires (8) and thermocouple wire leads (9). Photographs of the whole apparatus together with a close-up of the top sample-holding section are shown in Fig.7.3 and 7.4. Pyrophyllite ceramic was chosen to make the apparatus because it is easily machinable before sintering, and has high strength, high temperature endurance and electrical insulating properties after sintering [Appendix I].

7.3.2 Furnace

A special horizontal furnace was made to fit around the apparatus in which the electrochemical experiments were carried out. The furnace was built by myself in the departmental students workshop with a diameter of 30mm and length of 60 mm. The furnace was controlled by a Eurotherm temperature controller and K-type thermocouple. The thermocouple measured the actual sample temperature by contact with the sample through a closed-ended alumina tube. The temperature in the furnace was controlled within $\pm$ 1K and ranged from 273K to 973K.

Some of the high temperature electrochemical titration experiments were carried out in the two-zone furnace which was described in chapter 5. The actual temperature of the sample was monitored by a second K-type thermocouple which was in direct contact with the sample though a closed-ended alumina tube.

7.3.3. Electronic equipment for electrochemical titration

A Heathkit regulated L.V. power supply with voltage output of 0V-35V was used in the electrochemical titration experiments, which was controlled with an accuracy of $\pm$0.2Volts. A Thurlby 1905a intelligent digital multimeter ($\pm$0.01mv,

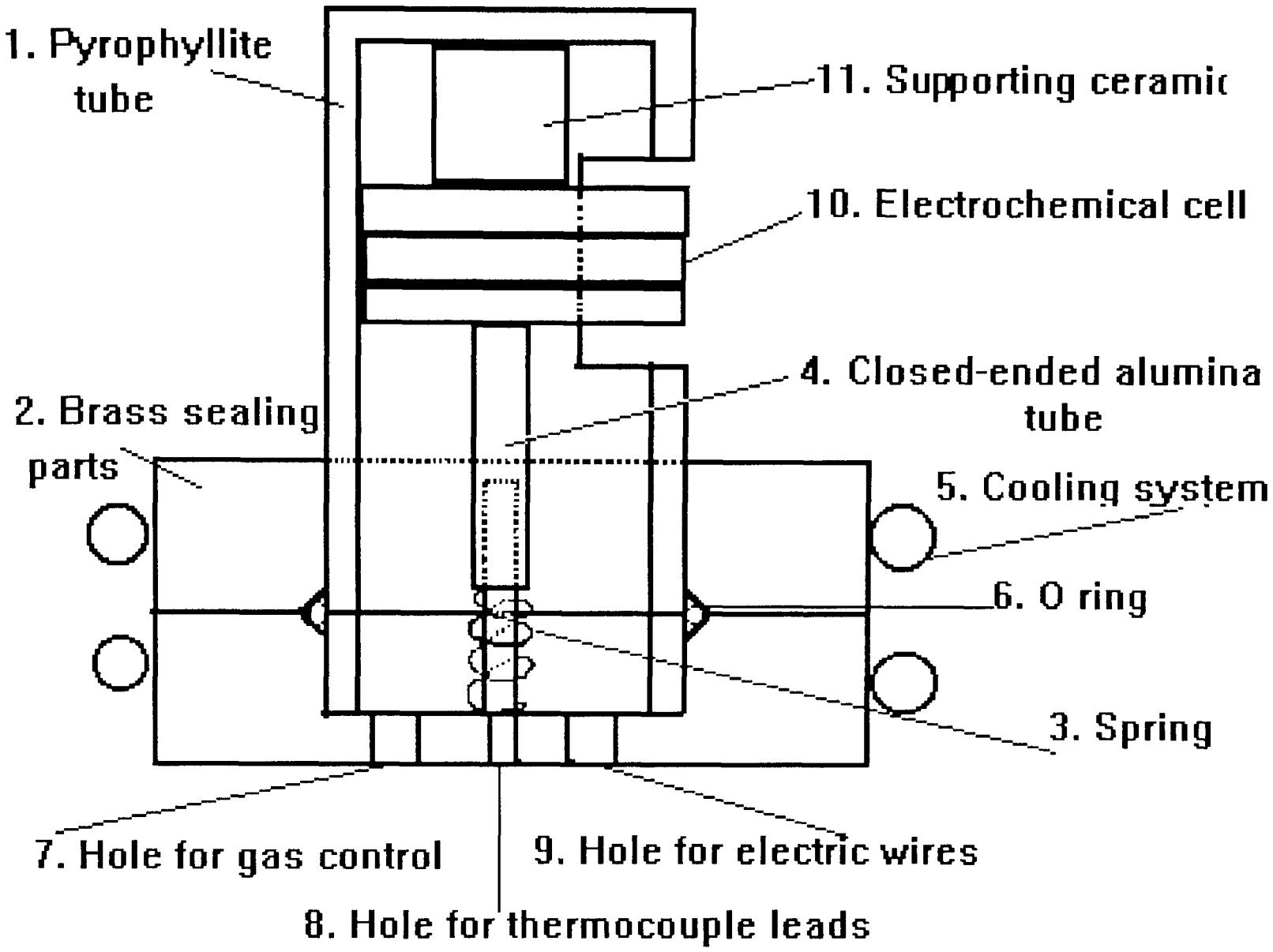

Figure 7.2: Schematic diagram of titration apparatus

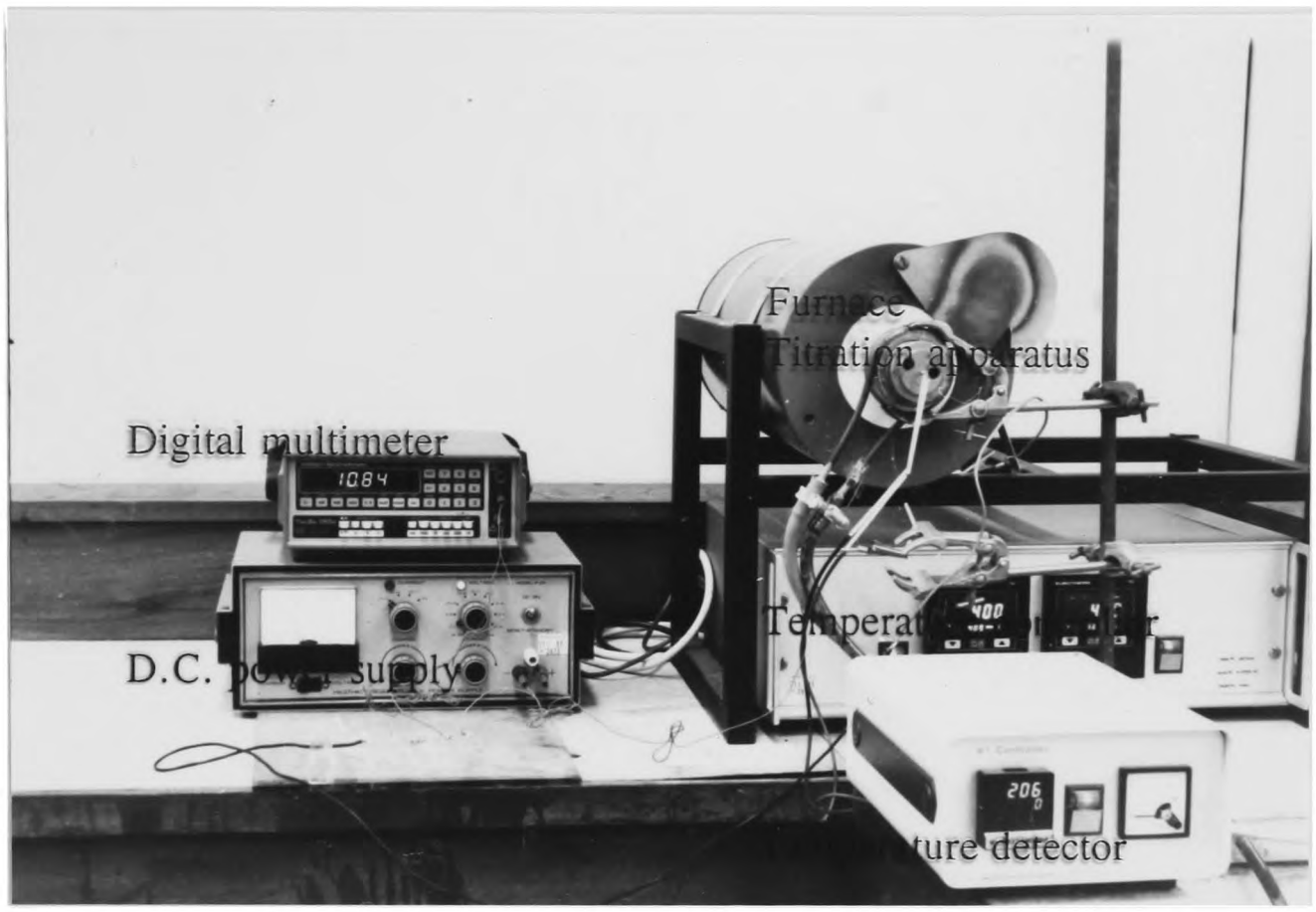

Figure 7.3: Experiment apparatus for electrochemical titration (front)

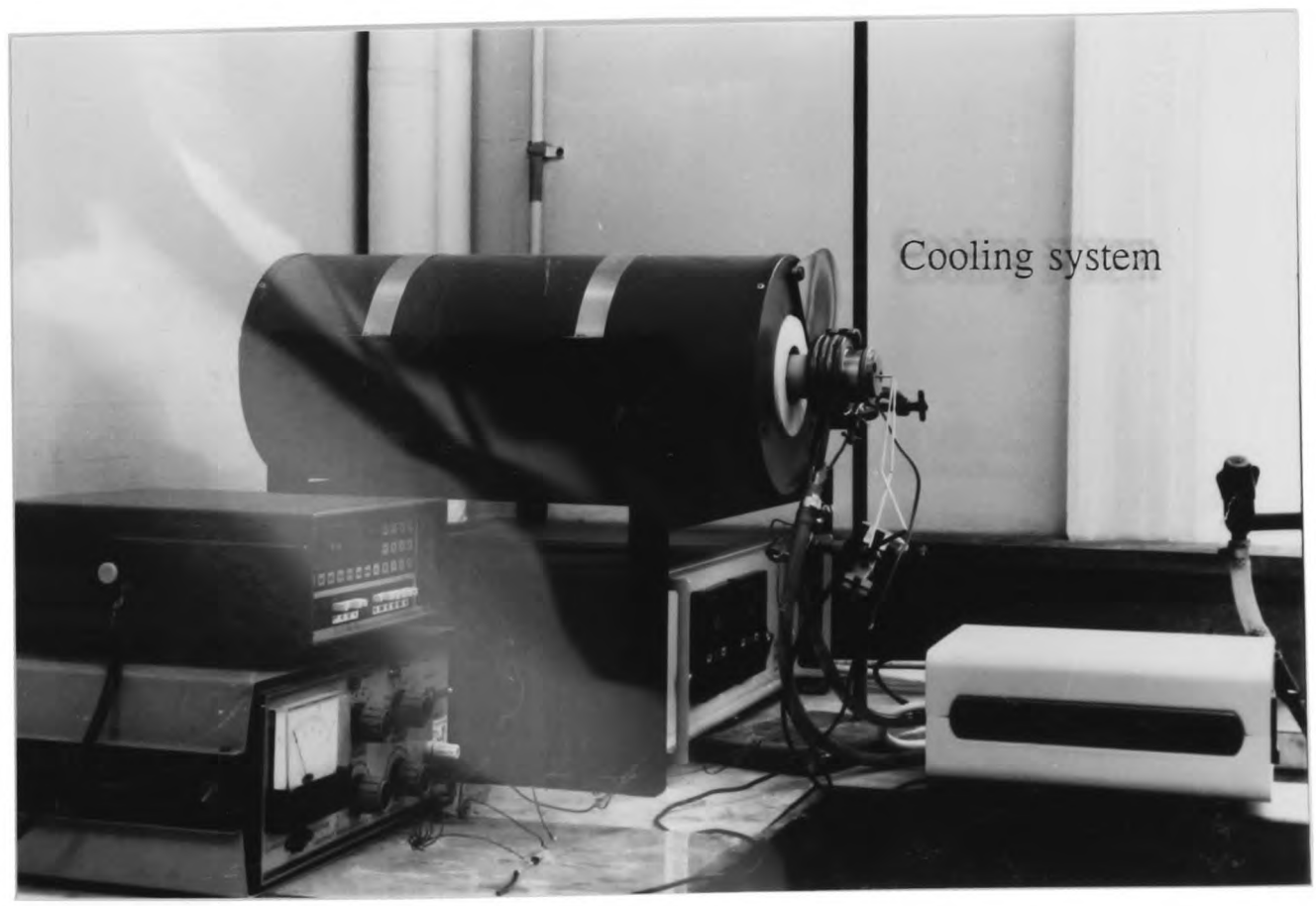

Figure 7.4: Experiment apparatus for electrochemical titration (side)

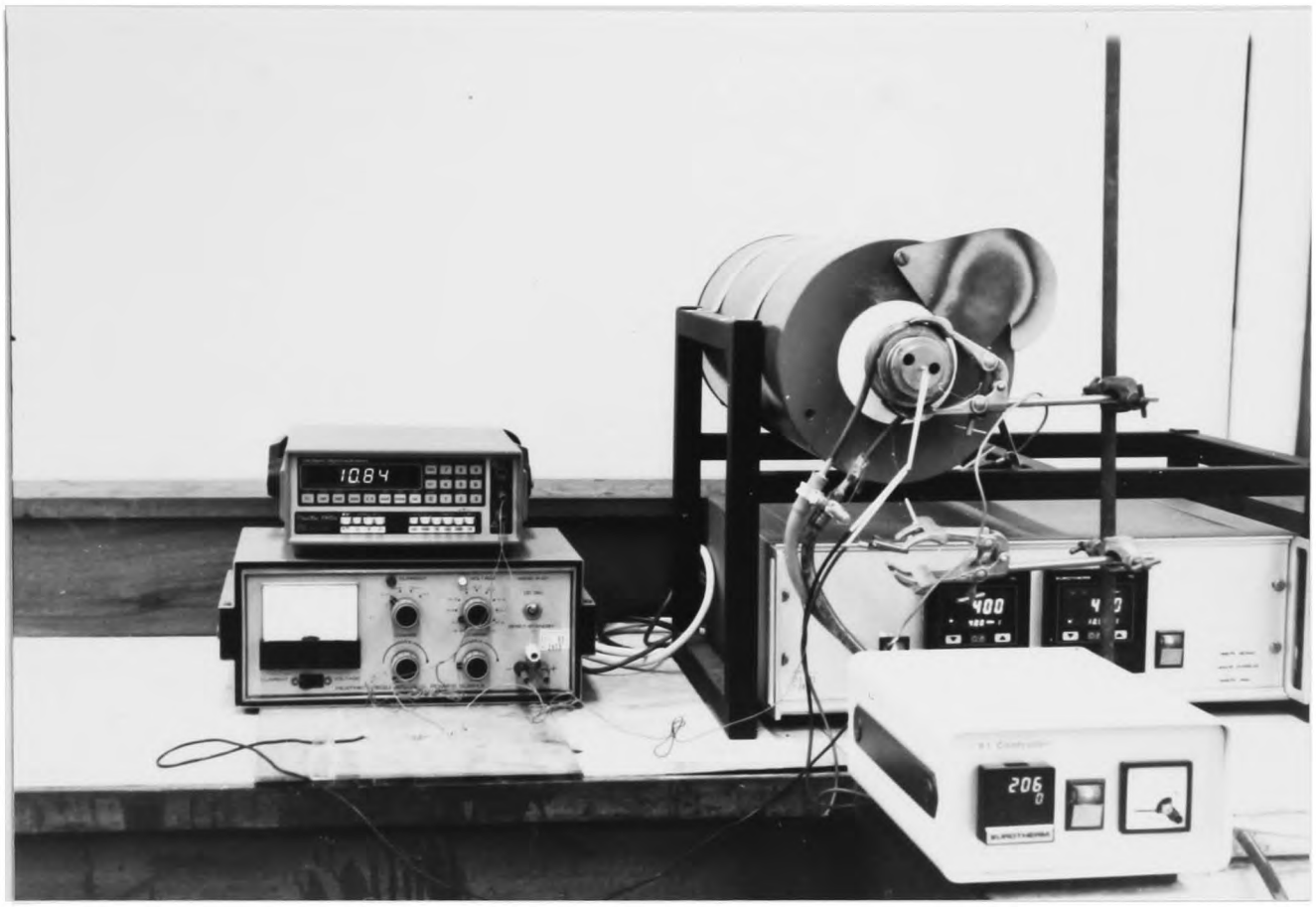

Figure 7.3: Experiment apparatus for electrochemical titration (front)

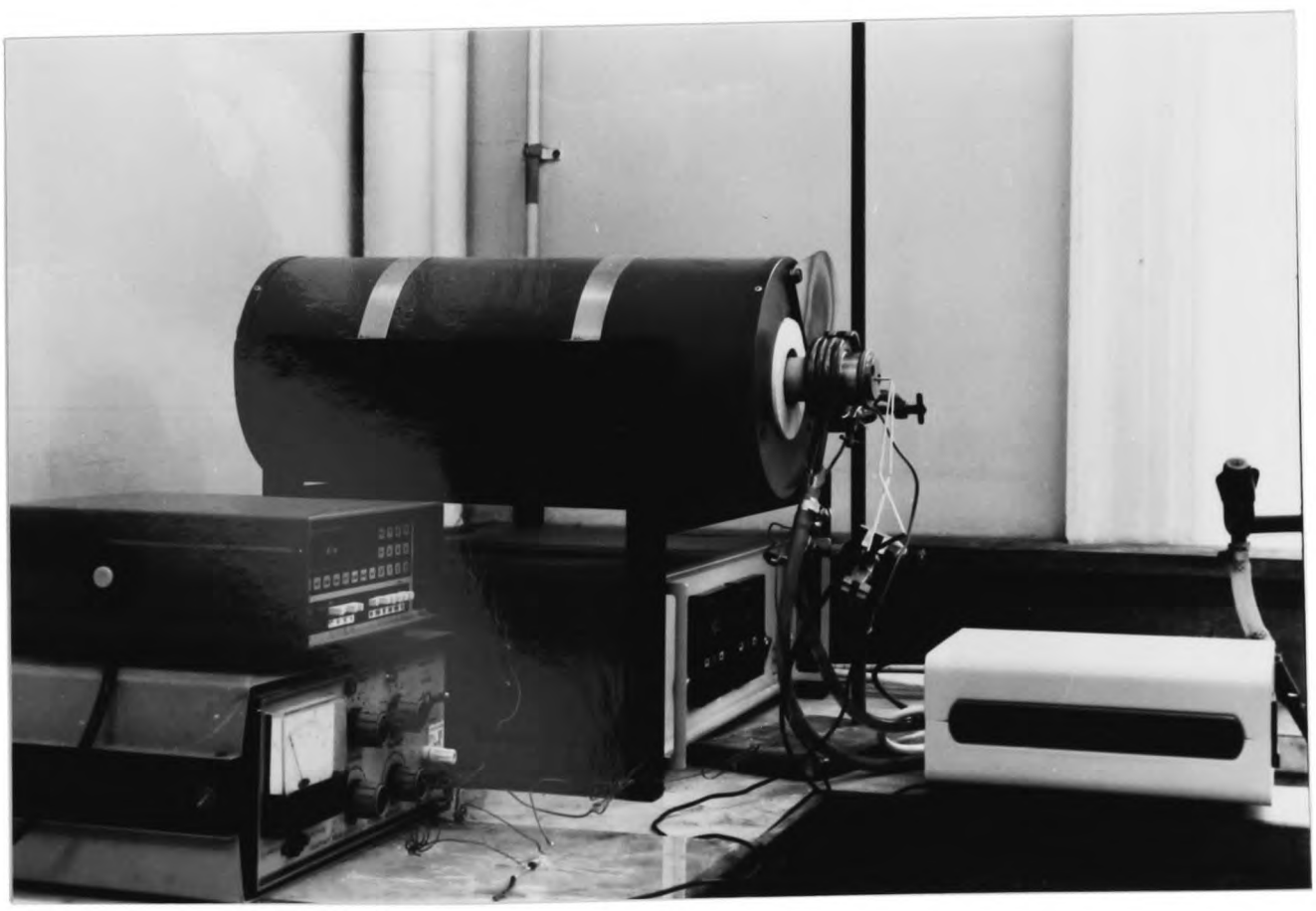

Figure 7.4: Experiment apparatus for electrochemical titration (side)

±0.01 Ohm) was used to measure the signals from the electrochemical cell.

A resistor was also put in the electronic circuit so that the current through the cell could be measured from the voltage drop between the two sides of the resistor. This served as a simple coulometer, and the value was recorded manually.

7.4 Sample preparation

7.4.1 $YBa_2Cu_3O_{7-x}$ samples

High density samples are a crucial factor in electrochemical titration experiments, ensuring an intimate contact between $YBa_2Cu_3O_{7-x}$ and the electrolyte to prevent the oxygen loss from the interface during the titration. Bulk textured $YBa_2Cu_3O_{7-x}$ samples were employed for this purpose. The samples were prepared in the same way as described in chapter 5.

The textured $YBa_2Cu_3O_{7-x}$ pellets were polished by silicon carbide paper to remove the contaminated surface and polished in glycerol with diamond paste to ensure that there are two flat surfaces which is important for preventing the oxygen loss from the interface. All preparation process must avoid water since $YBa_2Cu_3O_{7-x}$ reacts very actively with water.

Textured $YBa_2Cu_3O_{7-x}$ thick film samples were provided by GEC Hirst Research Centre. The thick film samples were fully oxygenated and had good superconducting properties with $Tc > 88K$. The surface of the superconductor film was gently polished with diamond paste to form a flat surface.

7.4.2 Zirconia electrolytes

The Yttria-stabilised zirconia precursor pellets were made by uniaxially pressing the starting powder into discs with average dimensions of ϕ15x2 mm at $10^4 Ncm^{-2}$. The starting powder with composition $(ZrO_2)_{0.85}(Y_2O_3)_{0.135}$ was made by 'TOSOH' in Japan. The crystallite size of the powder is about 2.47 μm. The pellets were then sintered at 1500^oC for 12 hours in air. The sample density is around 5.6 gm cm^{-3}.

The sintered YSZ pellets were mechanically polished by SiC paper followed by diamond paste down to 1 μm paste. This process ensured a highly polished flat surface which is to be in contact with the $YBa_2Cu_3O_{7-x}$ ceramics.

7.4.3. Platinum and silver paste electrodes

Two platinum sheets of the same size as the YSZ and $YBa_2Cu_3O_{7-x}$ samples were polished and spot welded with platinum wire leads. One of the platinum sheets was punched with many holes to act as a working electrode to drive oxygen ions into the electrolyte. Platinum metal was selected for its stability at high temperature.

Although platinum paste was the best candidate for electrodes, I used silver paste instead for its high conduction of oxygen ions and its cheap price. The paste was painted onto one of the surfaces of the electrolyte and put in the furnace at 300^{o}C for 12 hours to dry it and get rid of the solvent in the silver paste before the electrochemical titration.

7.4.4 Gold buffer layers

We have seen from previous chapters that gold may be the only oxygen buffer material at high temperature which has very limited effect on the properties of $YBa_2Cu_3O_{7-x}$. To prevent oxygen leaking out from the sides of the bulk crystal $YBa_2Cu_3O_{7-x}$ samples, the side surfaces were coated with gold by thermal evaporation.

Another effect of gold coating is that the gold layer may act as a short circuit to prevent holes from travelling in the opposite direction to the oxygen ions which may to some extent slow down the O^{-2} diffusion process [Govinda Rajan 1990].

7.5 Coulometric titration

7.5.1 Experiment

The coulometric titration experiments were performed by using galvanic cells which were made of either bulk textured crystal $YBa_2Cu_3O_{7-x}$ samples and

$(ZrO_2)_{0.89}(Y_2O_3)_{0.11}$ pellets or thick film $YBa_2Cu_3O_{7-x}$ samples with YSZ substrates. The cells incorporated a gaseous reference source of oxygen with $(ZrO_2)_{0.89}(Y_2O_3)_{0.11}$ pellets or YSZ substrates serving as oxygen ion conducting electrolytes. The electrical circuit used for coulometric titration is shown in Fig. 7.5.

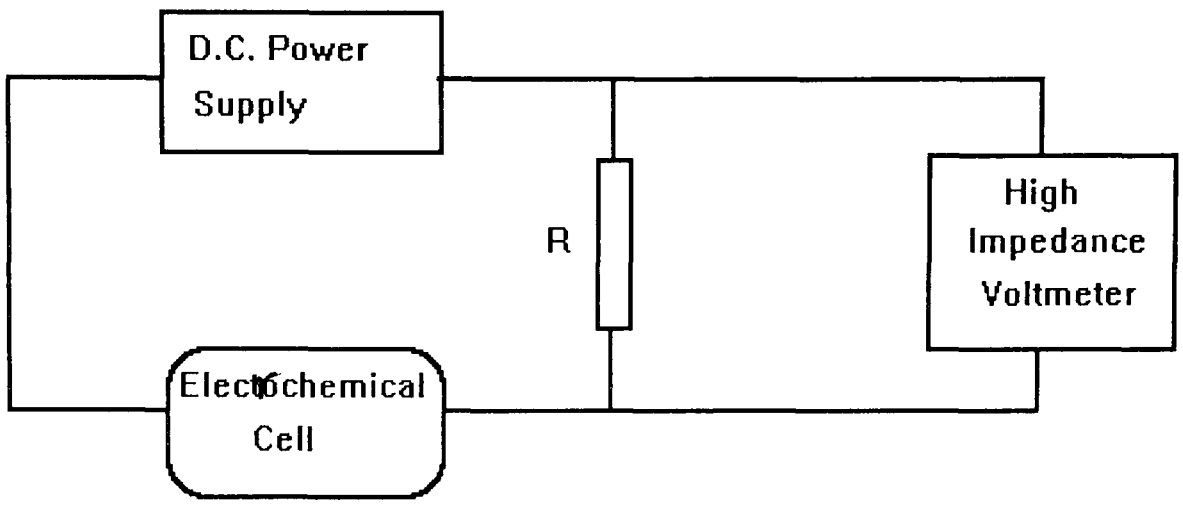

Figure 7.5 Electrical circuit used for coulometric titration

The D.C. power supply applied 0.2V-1.0V potential across the electrochemical cell and the current through the cell was monitored by the voltmeter.

For the bulk textured superconductor sample, the electrochemical cell is illustrated in Fig. 7.6, in which the YSZ pellet was placed against the superconductor pellet inside the cell.

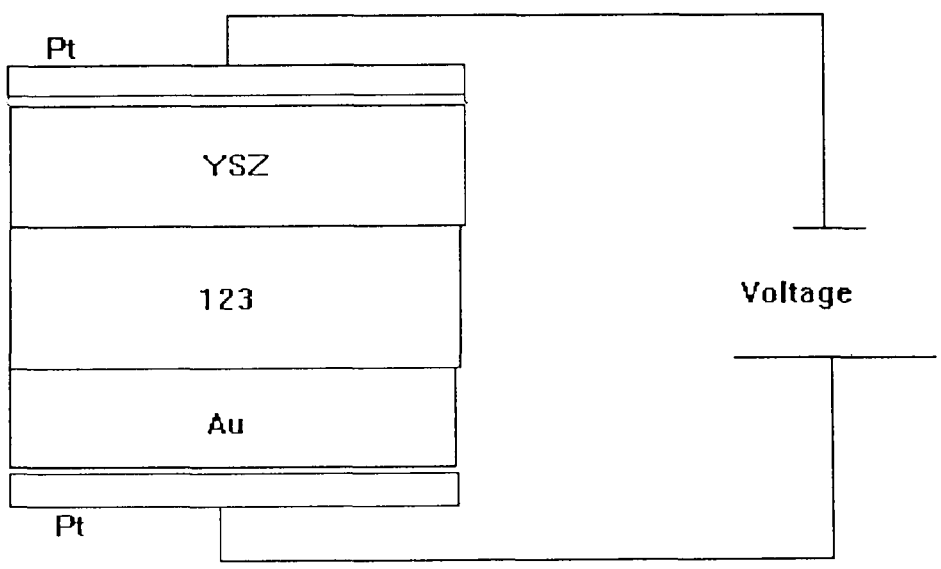

Figure 7.6: Schematic diagram of the electrochemical cell.

A gold plate was inserted between $YBa_2Cu_3O_{7-x}$ and the platinum

electrode to prevent the interaction between them at high temperatures.

For the thick film $YBa_2Cu_3O_{7-x}$ on the YSZ substrate, the sample was directly put in the cell without the $(ZrO_2)_{0.89}(Y_2O_3)_{0.11}$ pellet. The YSZ substrate served as the electrolyte because of the good conductivity between the YSZ substrate and the superconductor. So the electrochemical cell structure is the same as Fig. 7.6.

All experiments were performed in air. The temperature was 773K-1073K. 723K was chosen as the lowest temperature for sample titration, since below this temperature the kinetics of oxygen transport through the cell were too slow, and the current value through the cell was small so it would take very long time for oxidation. 1073K was chosen as the top temperature since the YSZ electrolyte would react with the $YBa_2Cu_3O_{7-x}$ samples above this temperature. Most of the samples were titrated at 973K for 8 hours. Control pellets were also sintered in the apparatus under the same conditions but without electrochemical titration, in order to isolate the effect of the electrochemical treatment.

After the coulometric titration experiments, the electrochemical cells were either quenched or slow cooled while maintaining the electrical potential across the cells. The oxygen concentration of the $YBa_2Cu_3O_{7-x}$ bulk textured samples and thin film and thick film $YBa_2Cu_3O_{7-x}$ samples were determined by X-ray diffraction techniques.

7.5.2 Experimental results

7.5.2.1 Bulk textured $YBa_2Cu_3O_{7-x}$ samples

The X-ray diffraction results show that for bulk melt textured $YBa_2Cu_3O_{7-x}$ samples there are some differences when comparing the results before and after electrochemical titration (Fig.7.8).

The c axis textured peaks are slightly shifted to higher angles after the electrochemical titration, which implies that the c axis lattice parameter is reduced, see table [7.1]. By using the empirical equation, $z=-5.733\times C + 73.829$ [Suzuki 1990], in which z is the oxygen stoichiometry of the $YBa_2Cu_3O_{7-x}$ and C is the lattice

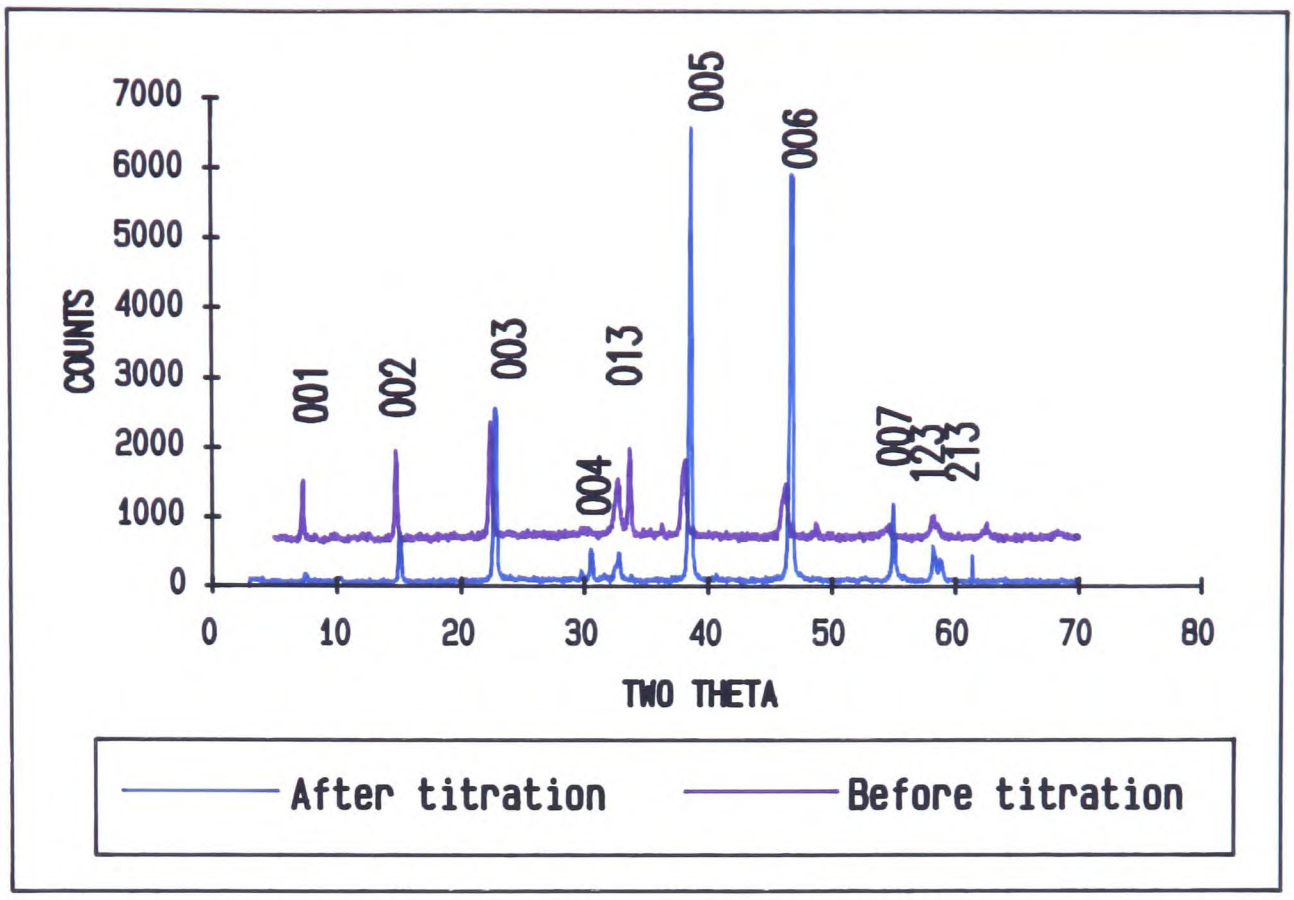

Figure 7.8: XRD result for textured sample before and after electrochemical titration

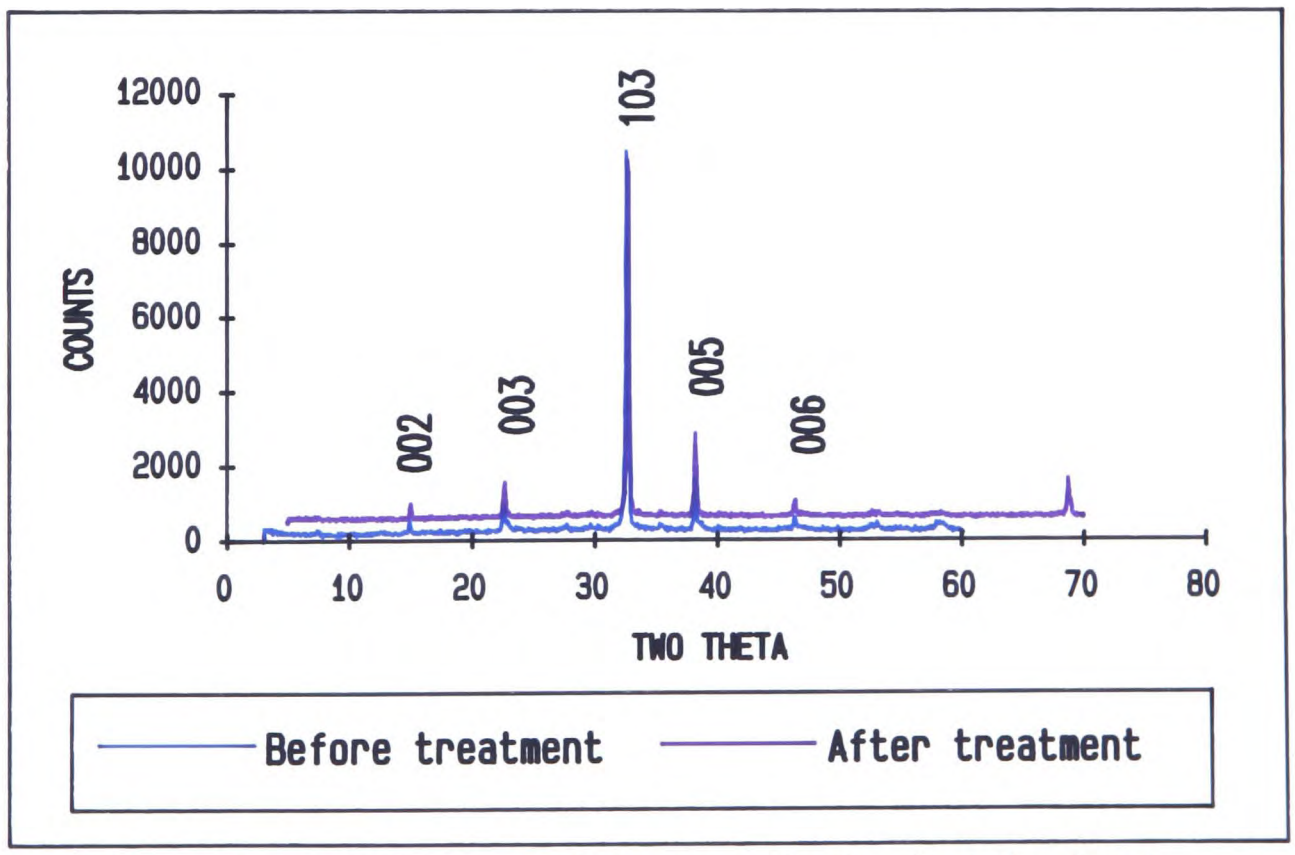

Figure 7.9.: XRD result for textured sample before and after heat treatment

parameter of the c-axis, the oxygen stoichiometry was calculated from lattice parameters. The oxygen contents were improved from around 6 to about 6.9 (Table 7.2) after electrochemical titration.

The samples treated under the same conditions without electrochemical titration show no significant change in the XRD spectrum Fig.7.9. There is a much smaller c-axis peak shift compared with the titrated sample. The extent of the peak shift is listed in Table 7.3. The oxygen stoichiometry of the sample before and after annealing is calculated from the lattice parameter by using the empirical equation, and results show that the sample oxygenation has only slightly altered the oxygen stoichiometry of the sample from 6.2 to 6.4 (Table 7.4).

7.5.2.2 $YBa_2Cu_3O_{7-x}$ thick film sample

The X-ray diffraction results for the melt textured $YBa_2Cu_3O_{7-x}$ thick film sample before and after titration are shown in Fig.7.10. The c-axis peak shifts are still observable. The c-axis lattice parameters are listed in table 7.5. The oxygen stoichiometry has been improved from 6.8 to 7.0 (Table 7.6).

The sample treated at the same temperature for the same length of time without titration shows no peak shift in the X-ray diffraction spectrum (Fig. 7.11), and there is no obvious change in lattice parameters or in the oxygen content (Table 7.7 & 7.8).

7.5.3 Discussion

The results from the bulk samples show that it is obvious that the electrochemical titration gives much faster oxidation kinetics than ordinary heat treatment at the same temperature. The absolute value of the oxygen stoichiometry determined in this method may involve some error from the empirical equation and also systematic errors in the zero alignment of the XRD goniometer, but the relative values and the trend are adequate to show the difference for samples prepared under different conditions.

In the case of the thick film samples, since the samples were previously fully

Table 7.1 Angle and d-value of c axis peaks for titrated and untitrated sample

c axis	Before titration		After titration	
textured	Angle (2θ)	d-value(Å)	Angle (2θ)	d-value(Å)
002	14.920	5.933	15.015	5.8956
003	22.560	3.9381	22.645	3.9235
005	38.225	2.3526	38.285	2.3491
006	46.330	1.9582	46.355	1.9572

Table 7.2 Oxygen stoichiometry change

c axis peaks	Stoichiometry (before titration)	Stoichiometry (after titration)
002	5.4595	6.80679
003	5.726	6.8595
005	6.314	6.947
006	6.4158	6.976
Stoichiometry (Average)	x=5.98	x=6.9040

Table 7.3 Angle and d-value of c axis peaks for annealed and unannealed sample

c axis	Before titration		After titration	
textured	Angle (2θ)	d-value(Å)	Angle (2θ)	d-value(Å)
001	7.370	11.9852	7.570	11.6690
002	14.845	5.9628	15.145	5.8453
003	22.435	3.9597	22.820	3.8938
005	38.180	2.3553	38.555	2.3332
006	46.290	1.9598	46.700	1.9435

Table 7.4 Oxygen stoichiometry change

c axis peaks	Stoichiometry (before annealing)	Stoichiometry (after annealing)
002	5.8015	6.2300
003	6.0976	6.34872
005	6.4917	6.492
006	6.4708	6.50523
Stoichiometry (Average)	x=6.1900	x=6.3938

Table 7.5 Angle and d-value of c axis peaks for titrated and untitrated films

c axis	Before titration		After titration	
textured	Angle (2θ)	d-value(Å)	Angle (2θ)	d-value(Å)
003	22.890	3.8820	22.935	3.8745
005	38.455	2.3391	38.635	2.3286
006	46.545	1.9496	46.715	1.9429
007	54.950	1.6696	55.145	1.6642

Table 7.6 Oxygen stoichiometry change

c axis peaks	Stoichiometry (before titration)	Stoichiometry (after titration)
003	7.062	7.19147
005	6.77870	7.07968
006	6.76666	6.99713
007	6.82628	7.04299
Stoichiometry (Average)	x=6.8584	x=7.0778

Table 7.7 Angle and d-value of c axis peaks for titrated and untitrated films

c axis	Before titration		After titration	
textured	Angle (2θ)	d-value(Å)	Angle (2θ)	d-value(Å)
003	22.890	3.8820	22.795	3.8980
005	38.455	2.3391	38.505	2.3361
006	46.545	1.9496	46.590	1.9478
007	54.950	1.6696	54.915	1.6706

Table 7.8 Oxygen stoichiometry change

c axis peaks	Stoichiometry (before titration)	Stoichiometry (after titration)
003	7.062	6.78730
005	6.77870	6.86469
006	6.76666	6.82858
007	6.82628	6.78615
Stoichiometry (Average)	x=6.8584	x=6.8167

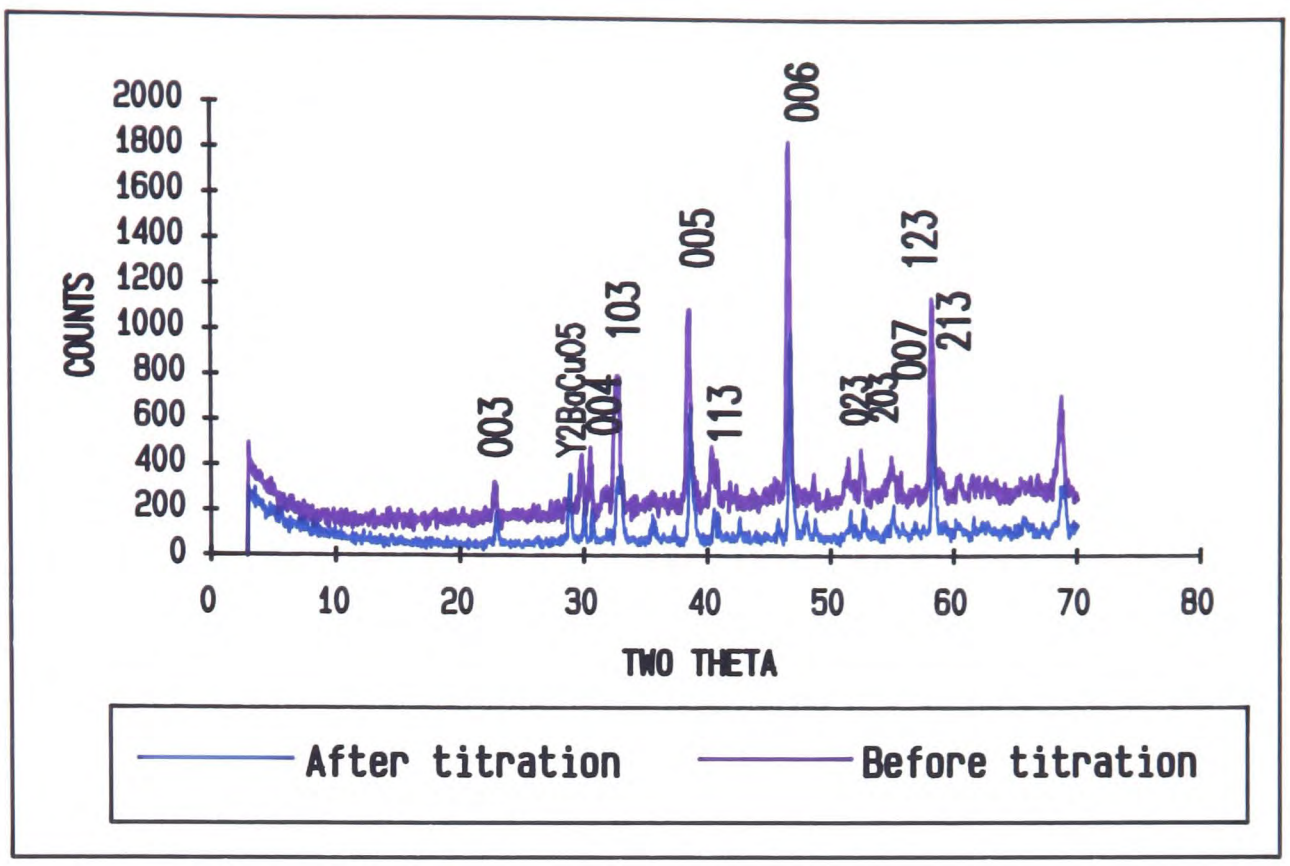

Figure 7.10: XRD result for textured thick film before and after electrochemical titration

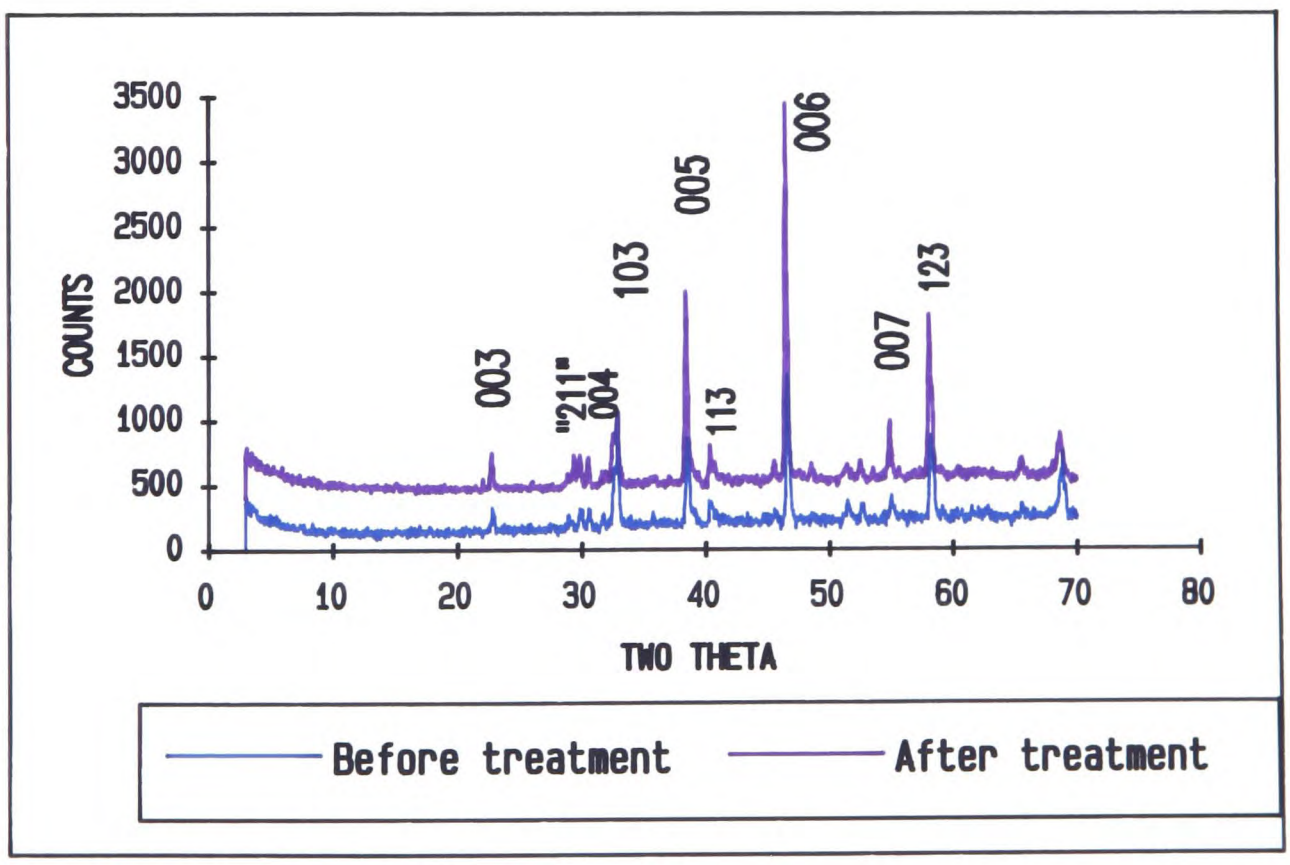

Figure 7.11: XRD result for textured thick film before and after heat treatment

oxygenated and had good superconducting properties, heat treatment alone cannot greatly improve the oxygen stoichiometry, but the higher oxygen activity achieved in the titration can further improve the oxygen content.

The fast oxidation kinetics of the electrochemical method may be achieved by the faster oxygen diffusion speed in titrated $YBa_2Cu_3O_{7-x}$ since titrated samples have a much higher oxygen concentration at the sample surface controlled by the applied voltage according to the Nernst equation. Another possible reason is that the electrochemical method may eliminate the surface process of solid-gaseous reaction at the $YBa_2Cu_3O_{7-x}$ surfaces during the oxidation:

$$O_2 \rightarrow 2O, \quad 2O+4e^- \rightarrow 2O^{2-} \tag{7.10}$$

Instead, the interfacial reaction in the electrochemical cell has a simple connection :

$$O^{2-}(\text{electrolyte}) \rightarrow O^{2-}(YBa_2Cu_3O_{7-x}) \tag{7.11}$$

So it is a promising method for oxidation of the densified $YBa_2Cu_3O_{7-x}$ samples, especially for melt textured $YBa_2Cu_3O_{7-x}$ thick film samples to increase the oxygen content and hence improve the superconducting properties.

7.6 Thermodynamic properties of $YBa_2Cu_3O_{7-x}$ and the formation of $YBa_2Cu_4O_8$

7.6.1 Electrical circuit

The electrical circuit used for the measurement of the thermodynamic properties of $YBa_2Cu_3O_{7-x}$ is shown in Fig.7.12a.

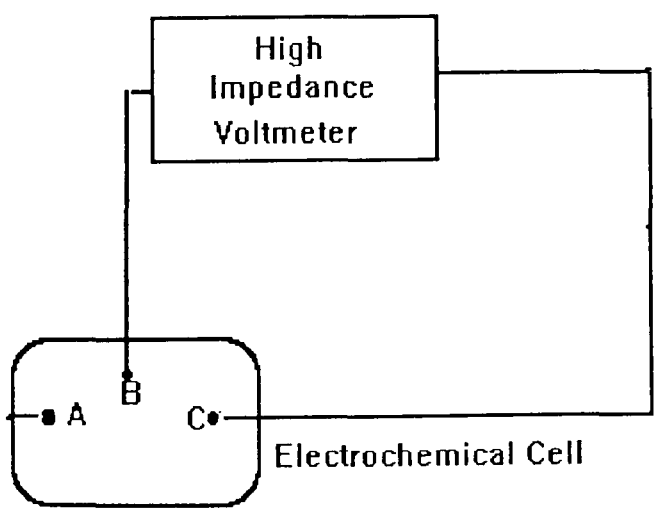

Figure 7.12a Electrical circuit for thermodynamic measurements

The wiring inside the electrochemical cell is shown in Fig. 7.12b.

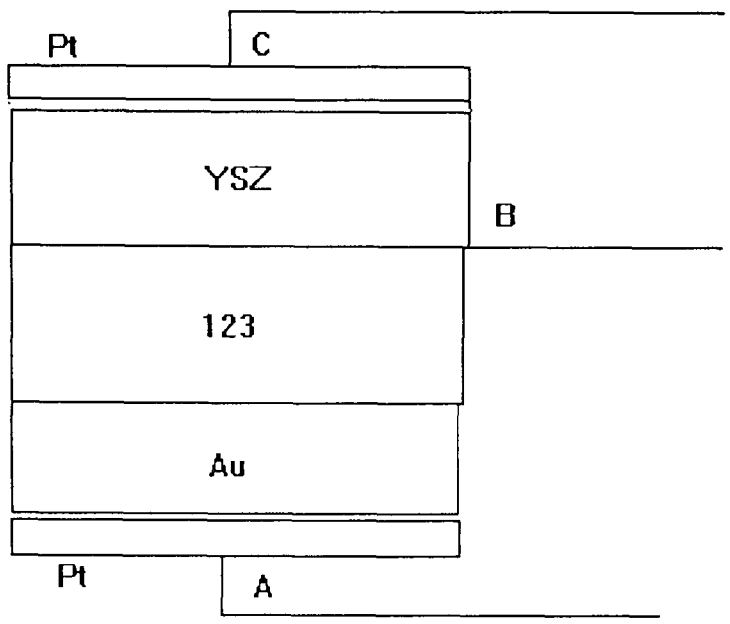

Figure 7.12b: The wiring structure in the electrochemical cell

The open circuit potentials, E, were monitored between terminal B and C using a high impedance voltmeter.

The oxygen activity at the surface of the $YBa_2Cu_3O_{7-x}$ is related to the oxygen stoichiometry of the sample and the equilibrium oxygen pressure above the existing phases. If the experiment is accurate enough, it could measure not only the oxygen surface activity but also the oxygen content at the surface.

7.6.2 Experiments

Experiment 1: Measurements on untitrated $YBa_2Cu_3O_{7-x}$

The oxygen activity of as-made $YBa_2Cu_3O_{7-x}$ textured samples was measured in the electrochemical cell with increasing temperature. The temperature of the system was gradually raised from 400°C to 900°C at a rate of 100°C per hour. The open circuit voltage E was recorded simultaneously. The results are shown in Fig.7.14. At low temperatures the oxygen activity drops with increasing temperature, then rises with increasing temperature.

Experiment 2: Measurements on titrated $YBa_2Cu_3O_{7-x}$

To measure the oxygen activity of $YBa_2Cu_3O_{7-x}$ after electrical titration, the

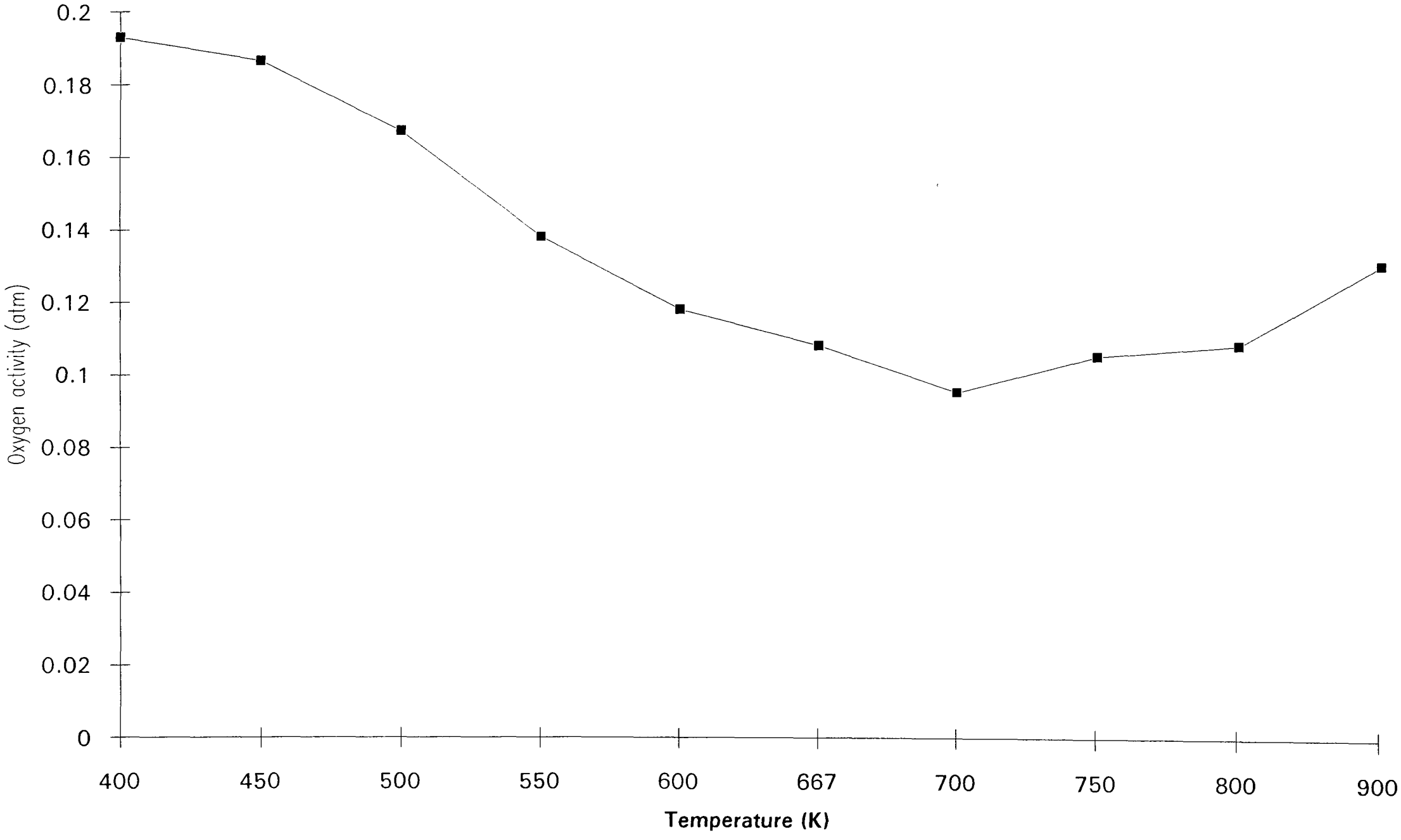

Figure 7.14: Temperature dependence of oxygen activity

sample was first titrated using the method shown in Fig.7.5. After cooling to room temperature, the electrochemical cell was rewired to the thermodynamic measurement circuit (Fig. 7.12a). Then the electrochemical cell was reheated to high temperature and the oxygen activity was measured with increasing temperature.

For the samples titrated with the cell voltage under 2 Volts, the oxygen activities and their temperature dependence all have similar features as shown in Fig.7.14. For the samples titrated with the cell voltage above 3 Volts, the oxygen activity and its temperature dependence is shown in Fig.7.15. The oxygen activity at the sample surface increased with temperature and after reaching a peak value of 10^{8} (atm), gradually decreases with increasing temperature down to 10^{-1}(atm).

Experiment 3: Isothermal measurement of titrated samples

Since the oxygen content in $YBa_2Cu_3O_{7-x}$ varies with temperature at a given oxygen partial pressure (Fig.2.14), it is difficult to measure the effect of titration on oxygen content after cooling and reheating the samples. The oxygen content will inevitably be altered during cooling and reheating, especially at the surface region. To avoid this additional cooling and heating, I developed the circuit shown in Fig.7.17 to measure the oxygen activity immediately after electrochemical titration.

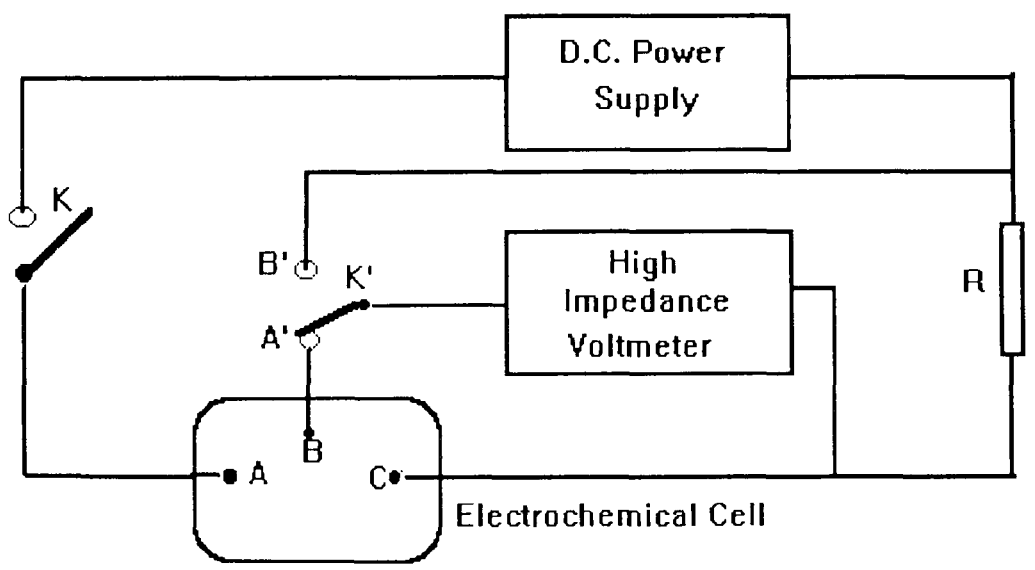

Figure 7.17 : Circuit for isothermal measurement .

First with switch K on and K' connected to B', the circuit is identical to circuit Fig.7.5 and the sample is titrated at 700^{o}C for typically 14 hours with voltages across

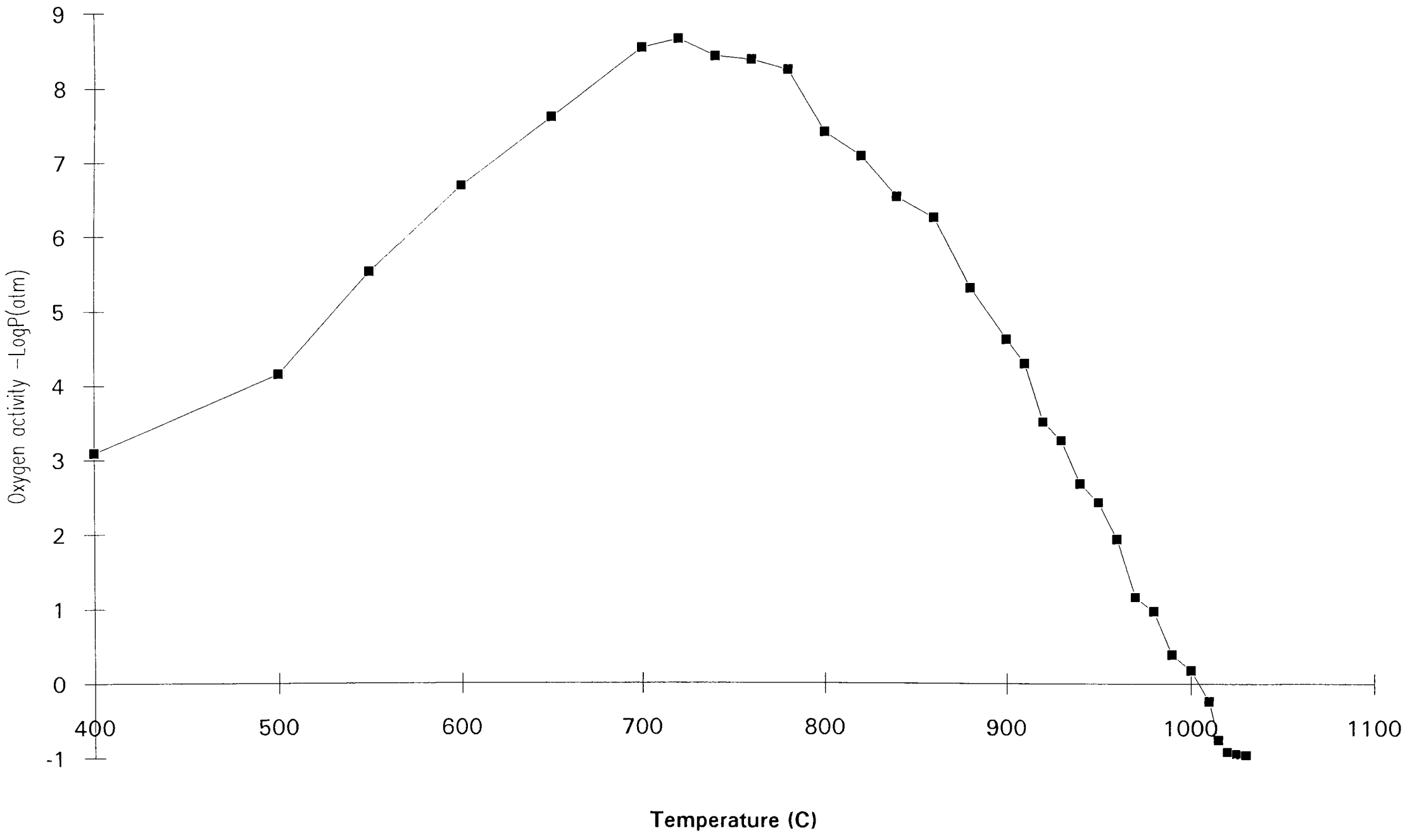

Figure 7.15: Temperature dependence of oxygen activity

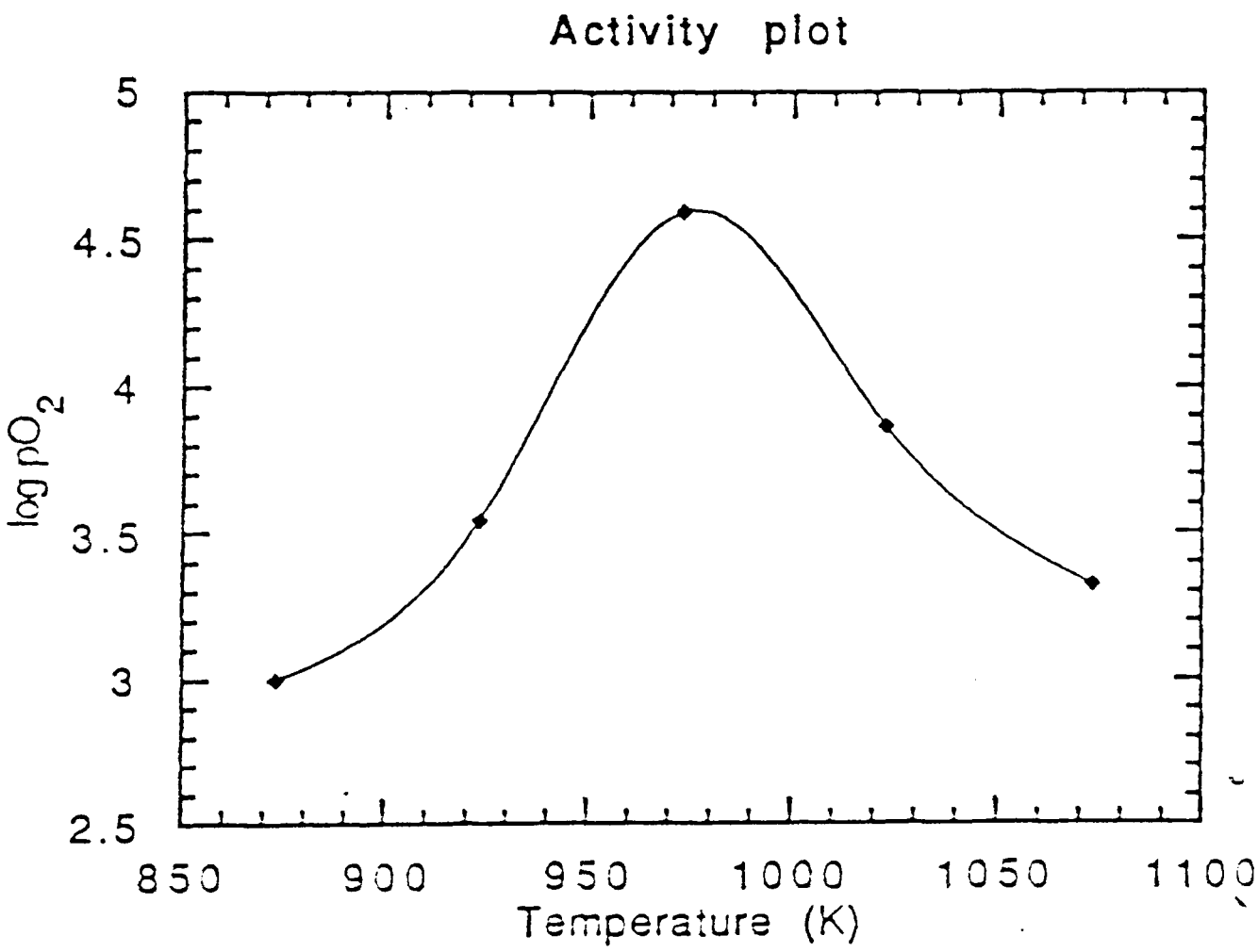

Fig. 7.16: After Mcmanus 1990

the cell ranging from 0.2-5V. Then K is switched off and at same time switch K' is moved to A', this circuit is identical to the circuit 7.12a, so the oxygen activity is measured immediately after the electrochemical titration. Instead of measuring the oxygen activity against temperature, the oxygen activity against time at constant temperature was measured to examine the way it changes with oxygen diffusion out of the $YBa_2Cu_3O_{7-x}$. The oxygen activities of the sample titrated at 700°C for 14 hours were also measured at 800°C .

The samples titrated below 2 Volts at 700°C have oxygen activity of 10^{-1} atm and flat time dependence (Fig.7.18). The sample titrated in one atmosphere oxygen pressure at 700°C for 14 hours with 5 Volts cell voltage shows a flat time dependence of oxygen activity at first. The oxygen activity of the step is about 10^{42} atm., then the oxygen activity decreases with time and shows a irregular time dependence (Fig. 7.19).

The sample titrated at 700°C in air for 14 hours with 5 Volts cell voltage shows two steps in its oxygen activity-time relation. The first is about 10^{21} atm; The second step is much flatter than the first one with oxygen activity 10^{12} atm. (Fig.7.20).

The sample titrated at 700°C in air for 48 hours with 5 Volts cell voltage shows similar features to Fig.7.20. The first step is blurred, but the second step is very flat. The oxygen activity of second step is 10^{15} atm (Fig.7.21).

The oxygen activity of the sample titrated at 800°C in air for 14 hours shows only one step with oxygen activity 10^{5} atm. (Fig.7.22).

Experiment 4: XRD analysis

The electrochemically titrated samples were all studied by XRD analysis. The XRD spectra for the sample titrated at 5 Volts cell voltage is shown in Fig. 7.23.

The results show that the $YBa_2Cu_3O_{7-x}$ decomposed during the titration and the following compounds are possibly formed at the interface between $YBa_2Cu_3O_{7-x}$ and ZrO_2: $BaZrO_3$, CuO, Y_2BaCuO_5, $YBa_2Cu_4O_8$, $Y_2Ba_4Cu_7O_{14+z}$, $BaCuO_2$

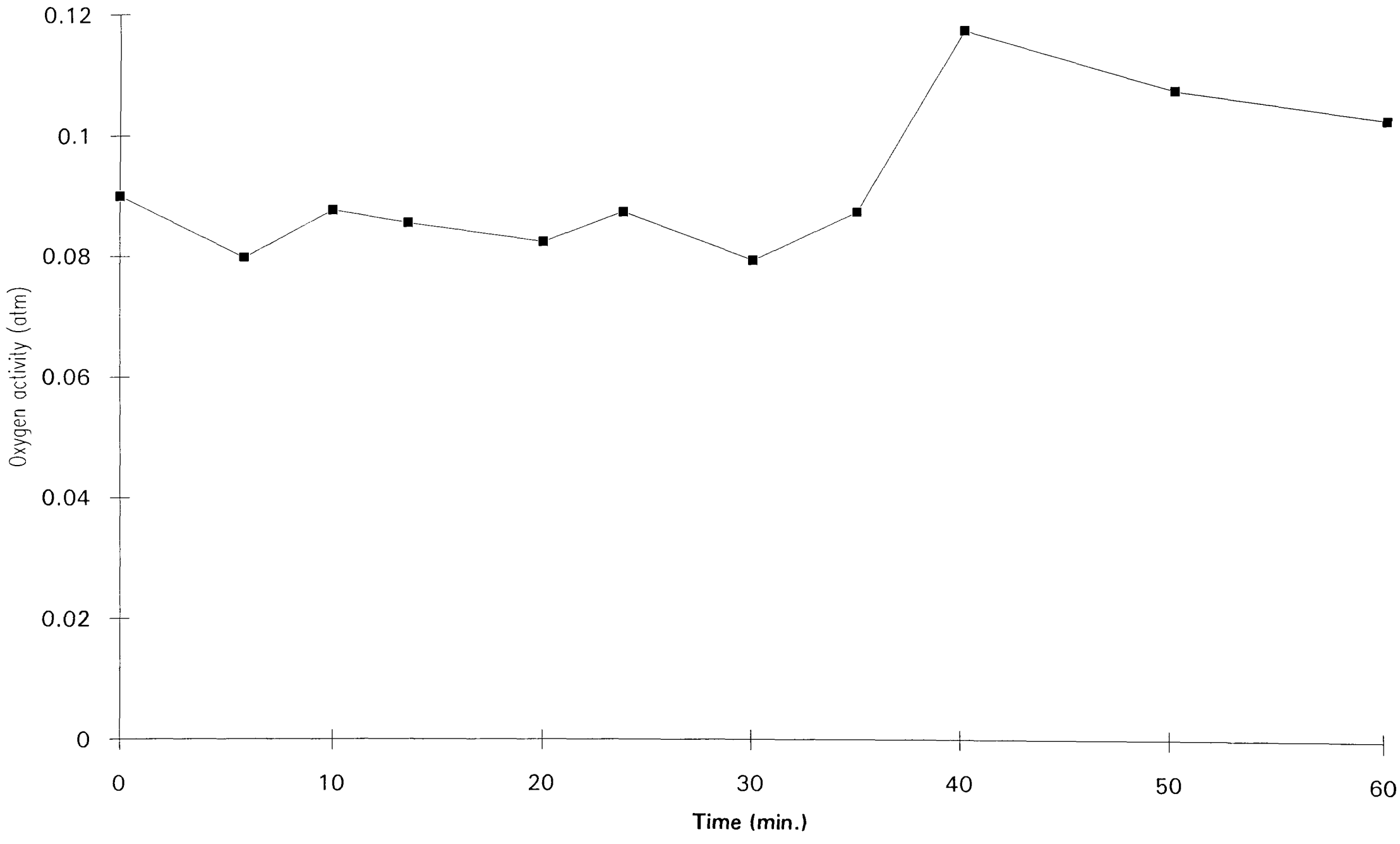

Figure 7.18: Oxygen activity for low voltage titrated sample

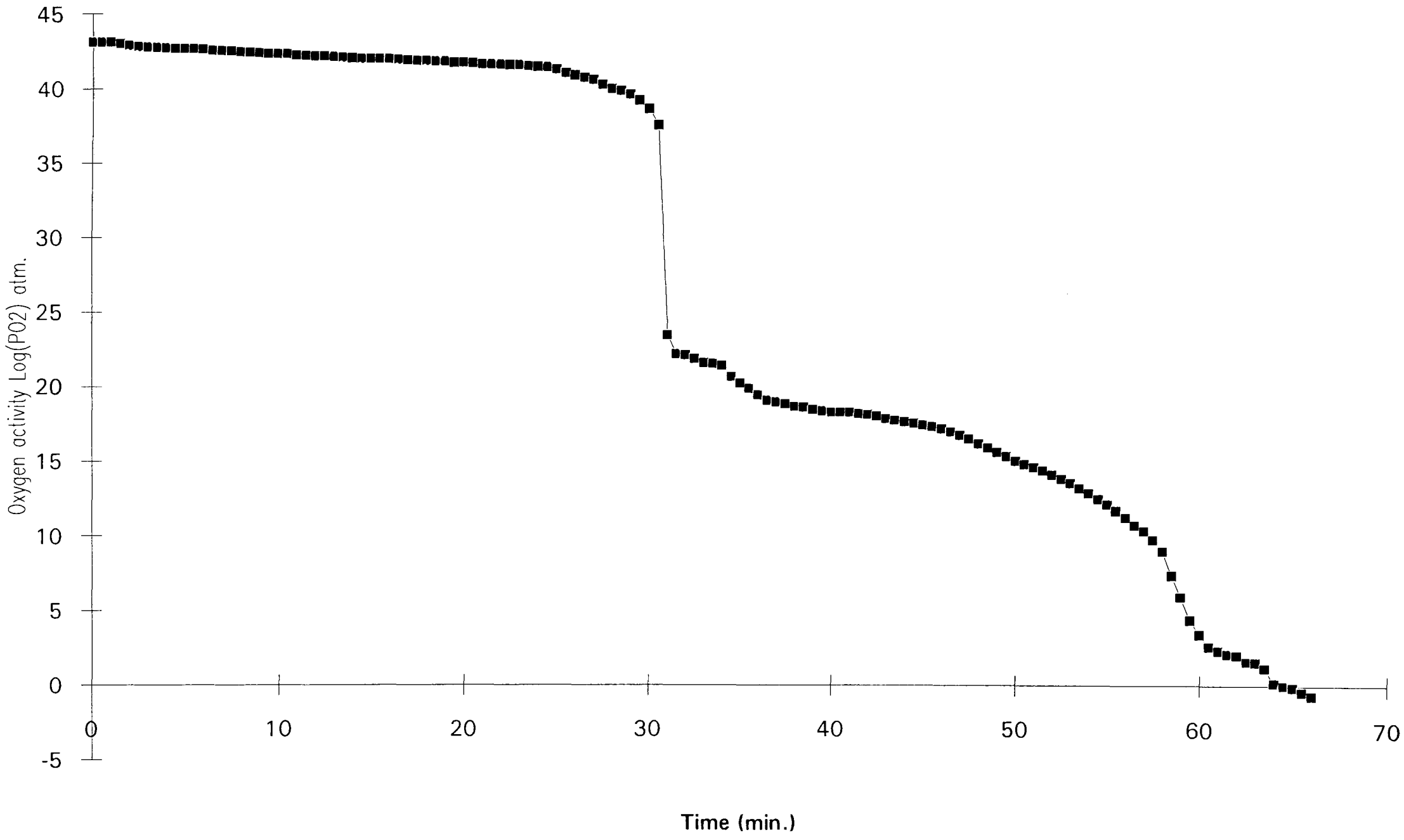

Figure 7.19: Oxygen activity for sample titrated at 700C in pure oxygen

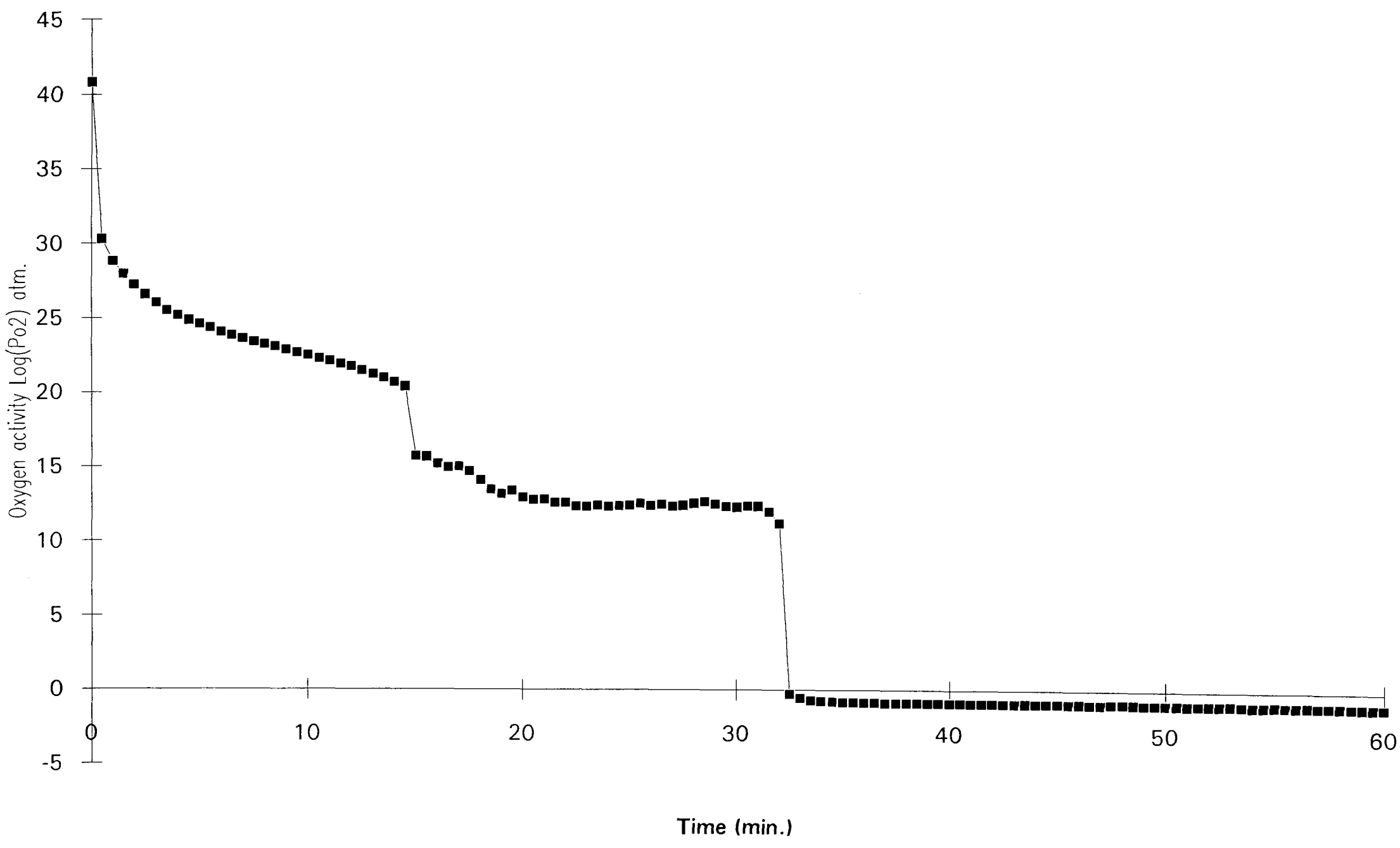

Figure 7.20: Oxygen activity of sample titrated at 700C in air

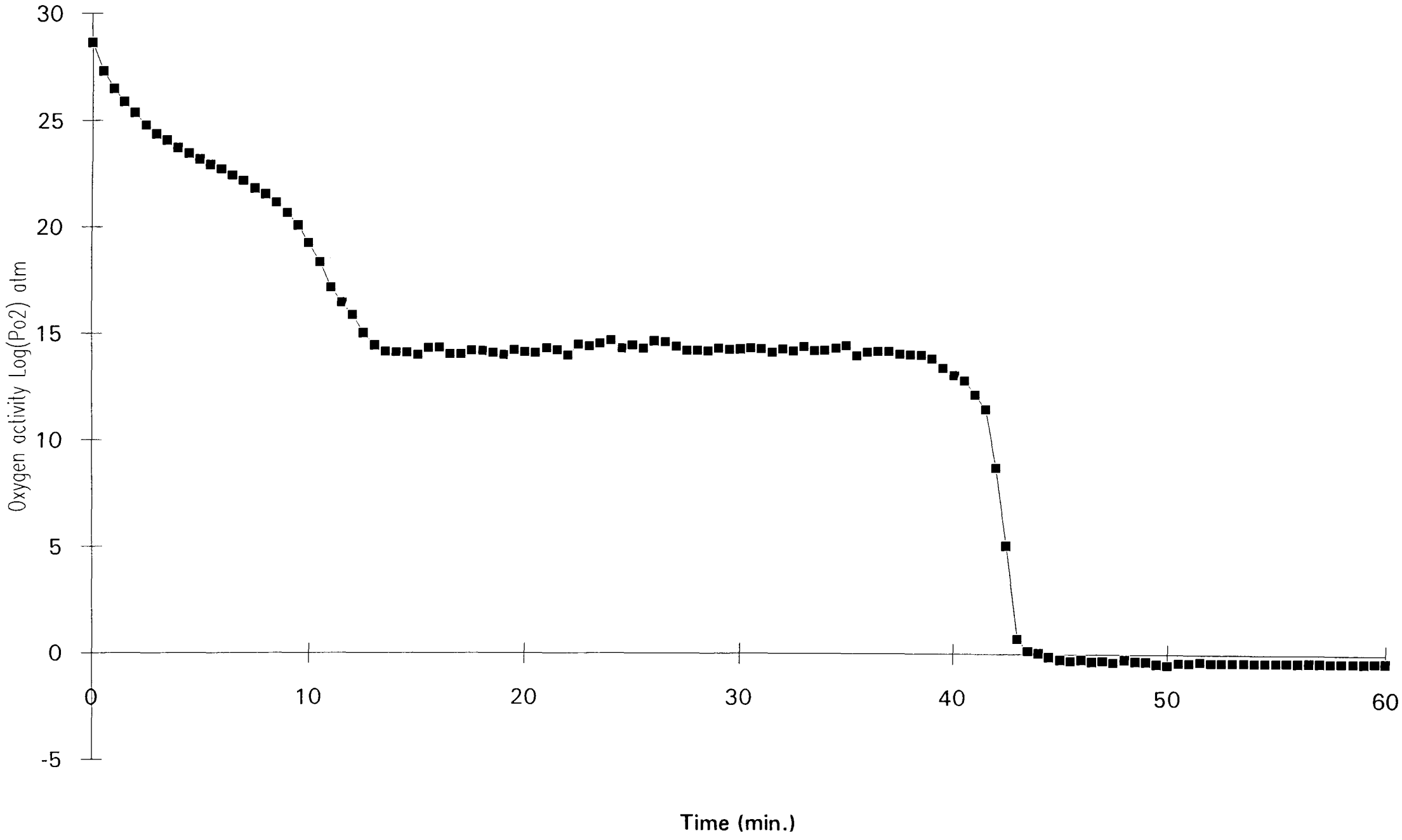

Figure 7.21: Oxygen activity of sample titrated at 700C for 48 hours in air

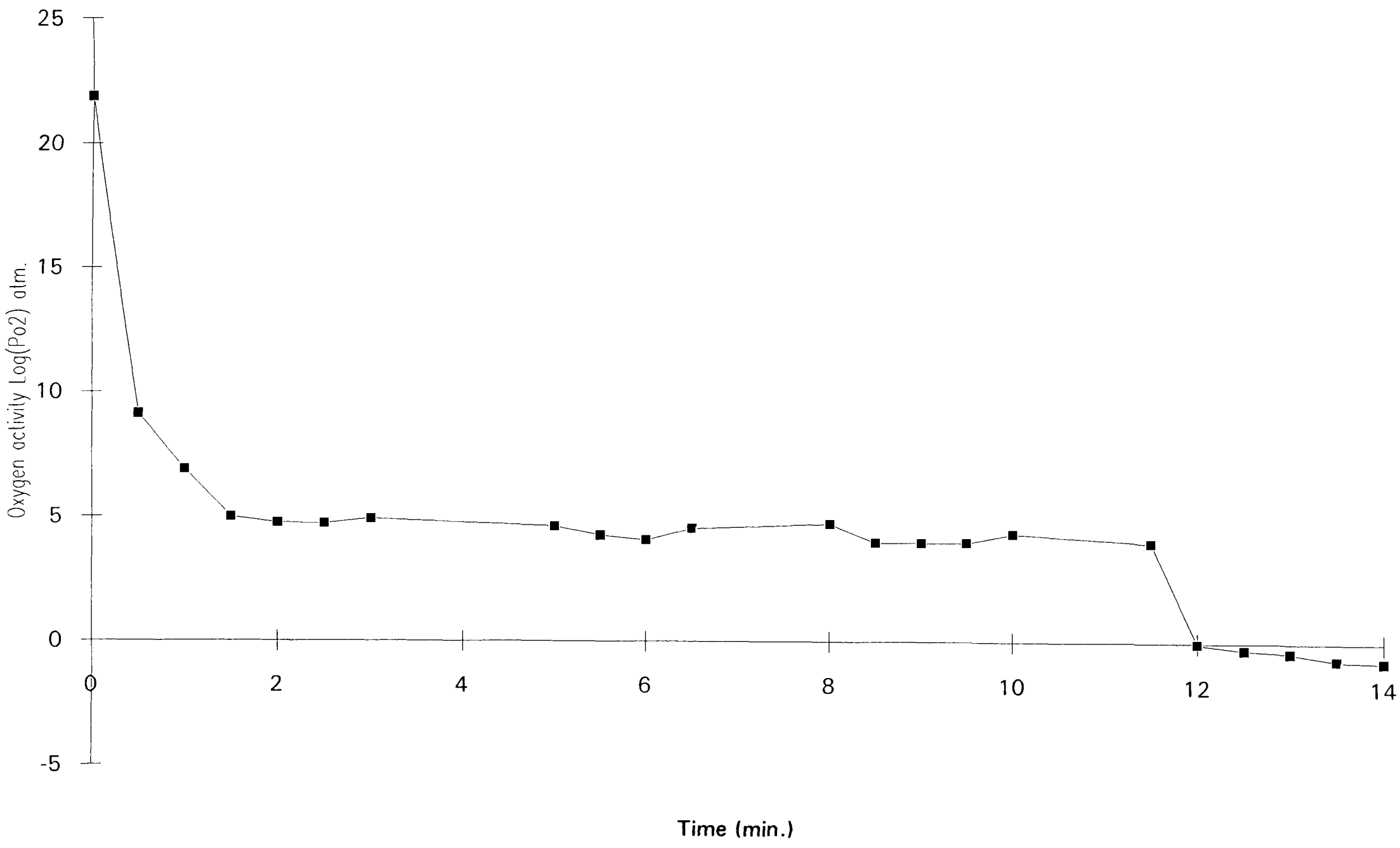

Figure 7.22: Oxygen activity of sample titrated at 700C for 14 hour measured at 800C

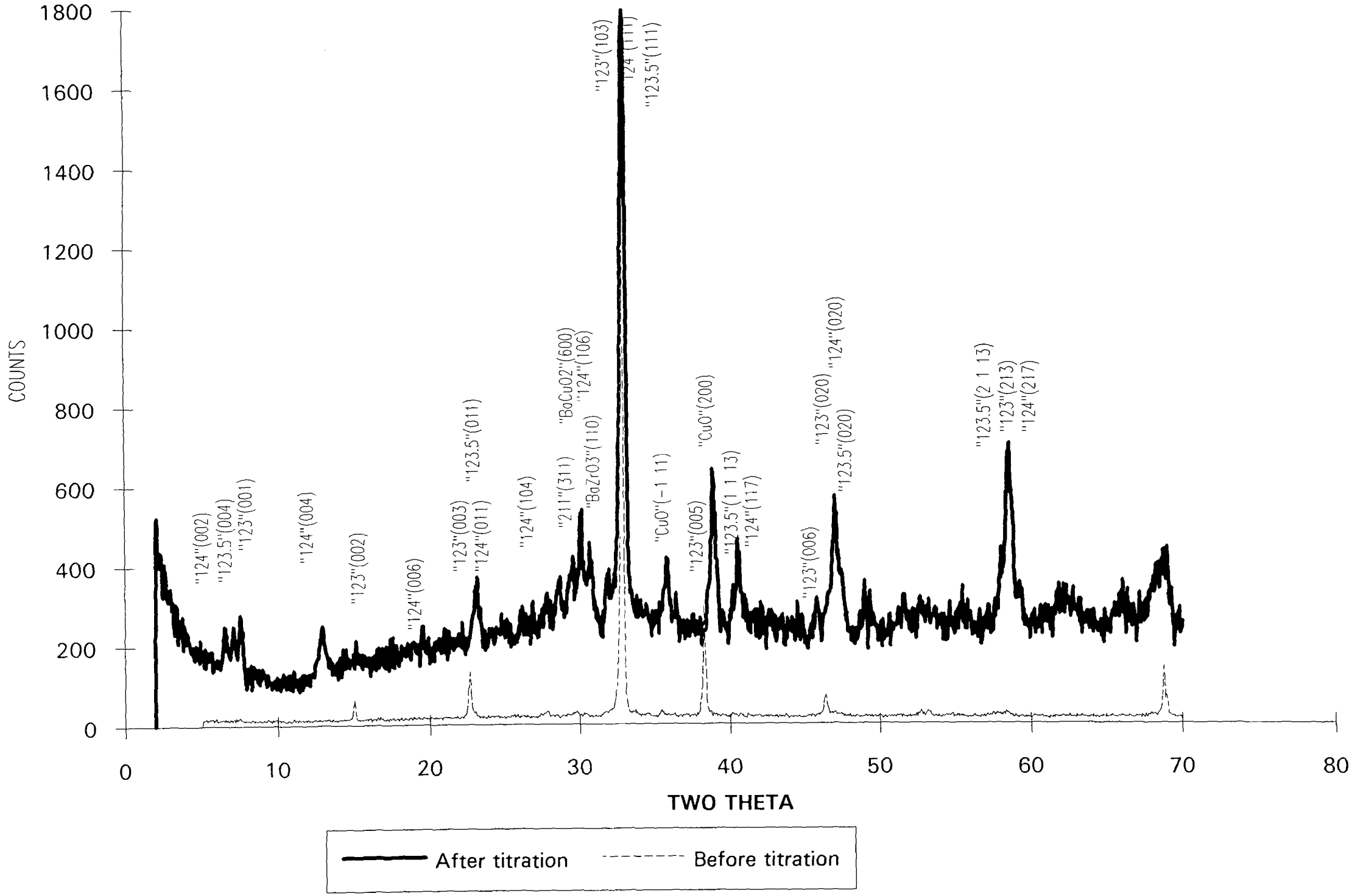

Figure 7.23: XRD spectrum for sample titrated at 5 Volts

and unreacted $YBa_2Cu_3O_{6+z}$.

The samples were processed by the melt growth method which provides the possibility of maintaining high oxygen activity at the interface because of the high sample density, but also makes it difficult to identify the formation of $YBa_2Cu_4O_8$ or $Y_2Ba_4Cu_7O_{14+z}$ phases in X-ray analysis. Unless the $YBa_2Cu_4O_8$ or $Y_2Ba_4Cu_7O_{14+z}$ low angle peaks can be observed, the other peaks coincide with and are buried under the peaks from textured $YBa_2Cu_3O_{6+z}$.

XRD analysis of the opposite surface of the $YBa_2Cu_3O_{7-x}$ sample shows that there are no reaction products at this surface (Fig.7.24).

The XRD spectrum for the sample titrated below 2 Volts is shown in Fig. 7.25. There are only traces of the reaction products at the interface, the main phase is $YBa_2Cu_3O_{7-x}$.

Experiment 5: Electron microprobe analysis

The titrated samples were also studied by electron microprobe analysis. The titrated surfaces were directly studied without any further treatment, and the results are listed in following tables:

Table 7.9

Electron microprobe results for sample titrated at 5 Volts

Typical points	Y at%	Cu at%	Ba at%	Zr at%	O at%	Formula
1	10.301	29.373	19.282	---	41.044	$YBa_2Cu_3O_{7-x}$
2	5.060	20.620	10.790	---	63.540	$YBa_2Cu_4O_8$
3	5.456	18.623	10.717	---	65.203	$Y_2Ba_4Cu_7O_{14+z}$
4	0.006	0.244	17.810	19.520	62.421	$BaZrO_3$
5	22.370	12.070	10.580	---	54.970	Y_2BaCuO_5
6	0.003	48.33	0.0021	---	51.42	CuO

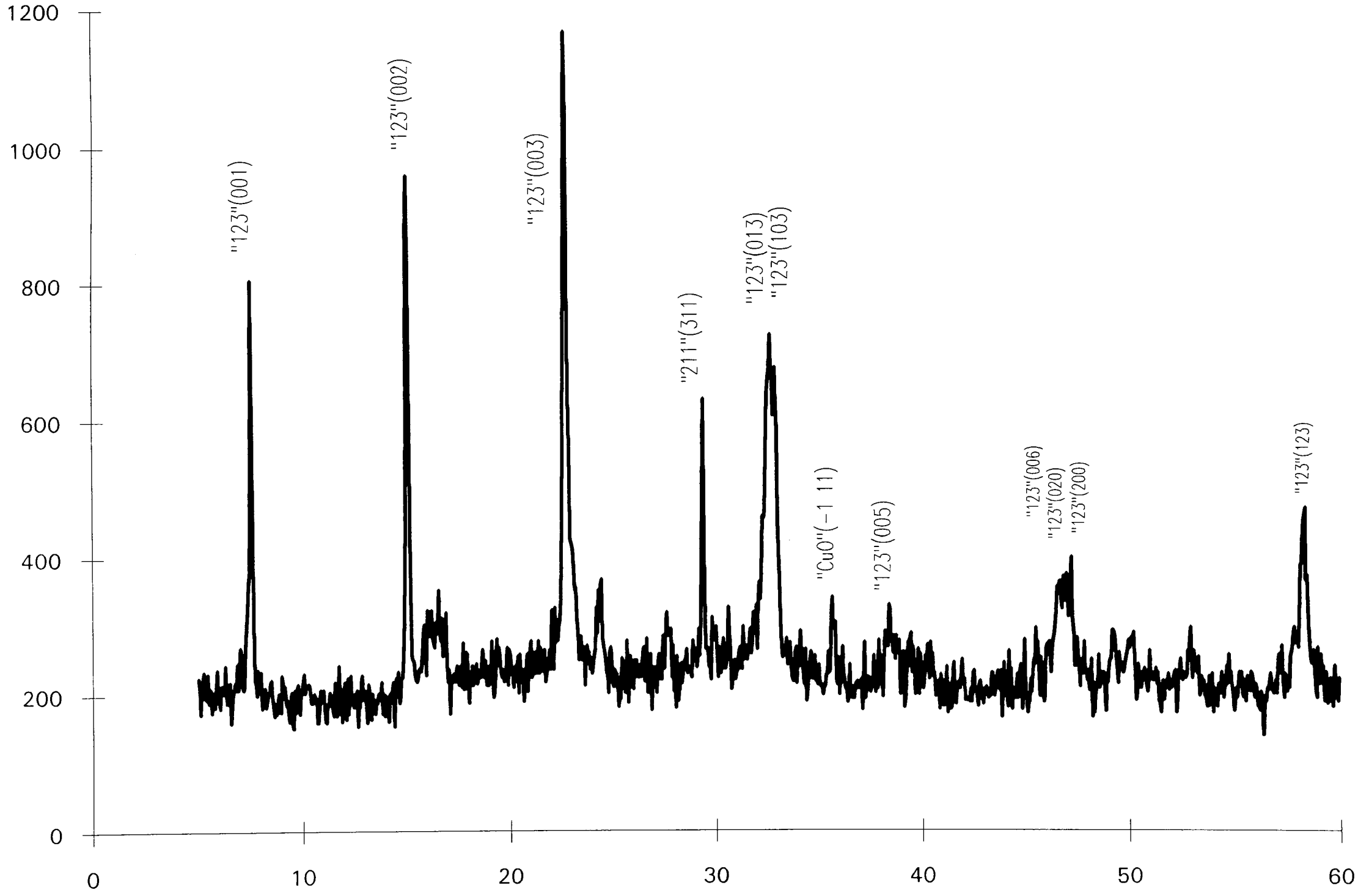

Figure 7.24: XRD spectrum for the back side of the titrated sample

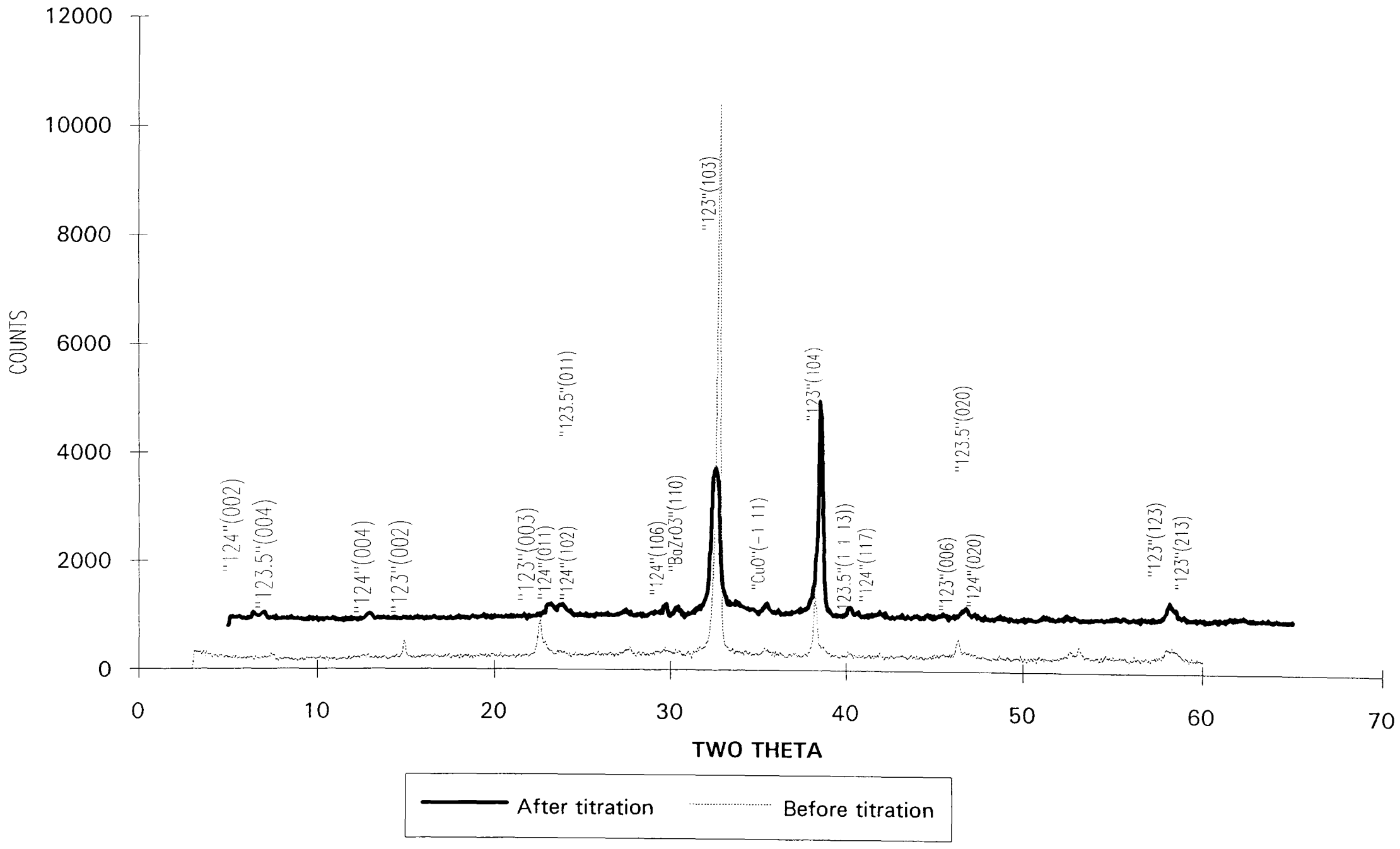

Figure 7.25: XRD spectrum for sample titrated at 2 Volts

Typical points analysed in the electron microprobe reveal that in the sample titrated at 5 Volts, $YBa_2Cu_3O_{7-x}$ was decomposed and the following compounds are formed at the interface between $YBa_2Cu_3O_{7-x}$ and ZrO_2: $BaZrO_3$, CuO, Y_2BaCuO_5, $YBa_2Cu_4O_8$, $Y_2Ba_4Cu_7O_{14+z}$, and residual $YBa_2Cu_3O_{6+z}$.

The sample titrated below 2 Volts remains unchanged with typical composition:

Table 7.10

Composition of sample titrated under 2 Volts

Y at%	Cu at%	Ba at%	O at%	Formula
8.270	24.090	15.790	51.850	$YBa_2Cu_3O_{7-x}$

7.6.3 Discussion

The increase of the oxygen activity with temperature at higher temperatures in experiment 1 can be interpreted as the normal behaviour of $YBa_2Cu_3O_{7-x}$ according to the experimental P-T-X phase diagram Fig. 2.14. This diagram predicts that the oxygen equilibrium pressure should rise linearly with temperature for a particular oxygen stoichiometry.

The feature that the oxygen activity drops with increasing temperature at low temperature might be due to insufficient ion conduction in the YSZ electrolyte at these low temperatures. The electrical circuit will then show a false voltage value near zero. According to the Nernst equation (7.9), the voltage can be converted to oxygen activity, and the value is about the same as the reference activity which is 0.2 atm. Since the conductivity of the YSZ electrolyte increases with temperature (Fig.7.1), the accuracy of the cell voltage measurement gradually improves, explaining the first feature in Fig. 7.14.

The data from the sample titrated at over 3 Volts in experiment 2 (Fig.7.15) is

very similar to the result observed by McManus [1990] which reported that the oxygen activity increased to $3*10^4$ atm. (Fig.7.16). The author was not able to repeat this feature, but it was interpreted as the high equilibrium oxygen pressure at high temperature of the sample with parameter x near 0.

I believe that the oxygen activity rise with increase of temperature in Fig.7.15 must contain inaccurate values caused by insufficient ion conduction in the YSZ electrolyte as discussed for experiment 1 (Fig. 7.14). Analysis of the result of experiment 3 below proves that this feature is not due to the high equilibrium oxygen pressure at high temperature in $YBa_2Cu_3O_{7-x}$ with x near 0.

The measurement of oxygen activity versus time in experiment 3 after high voltage (5 Volts) electrochemical titration reveals some interesting features that the previous measurements in experiment 2 of oxygen activity versus temperature missed out. The step-like change in the oxygen activity is not likely to be caused by the oxygen stoichiometry change in the $YBa_2Cu_3O_{7-x}$. This change in $YBa_2Cu_3O_{7-x}$ at high temperatures is a diffusion controlled process which is a gradual procedure and won't display a step-like change in oxygen activity. Besides, the observed oxygen activity should be too high for the $YBa_2Cu_3O_{7-x}$ phase according to the experimental P-T-X diagram Fig.2.12.

According to the Gibbs phase rule:

$$f = c + 2 - p \qquad (7.12)$$

where f is the degree of freedom, c is the number of components, p is the number of phases, and 2 is the freedom for temperature and pressure. In the $YBa_2Cu_3O_{7-x}$ system, c is 4, p is 4 and at a constant temperature and pressure f=0. The flat feature in the plot of oxygen activity against time indicates a four-phase equilibrium.

In the $YBa_2Cu_3O_{7-x}$ system at 1 atmosphere, the nonstoichiometric phases are $YBa_2Cu_3O_{7-x}$ and $YBa_3Cu_2O_{7-x}$ which can undergo changes in oxygen content. The four-phase equilibria concerning these two phases will interact with the surrounding oxygen activity. However, they are all at low oxygen pressures (10^{-3} - 10^{-4} atm. see chapter 2 section 2.1), obviously not responsible for the phase equilibria observed in

experiment 3.

In view of high oxygen activity generated in the electrochemical cell during the electrochemical titration procedure, the $YBa_2Cu_3O_{7-x}$ surface may decompose with the formation of $YBa_2Cu_{3.5}O_{7+x}$ or $YBa_2Cu_4O_8$ phases (see chapter 2 section 2.2). $YBa_2Cu_3O_{7-x}$ will decompose into $YBa_2Cu_{3.5}O_{7+x}$ or $YBa_2Cu_4O_8$ under oxygen activities over 100 atm.

The reactions are first the $YBa_2Cu_3O_{7-x}$ phase decomposing into $Y_2Ba_4Cu_7O_{14+z}$:

$$6YBa_2Cu_3O_{6+z} - (4z-3)/2O_2 = Y_2BaCuO_5 + 3BaCuO_2 + 2Y_2Ba_4Cu_7O_{14+z} \quad (7.13)$$

and then at higher oxygen pressures $Y_2Ba_4Cu_7O_{14+z}$ will decompose into $YBa_2Cu_4O_8$ and other compounds [Kaldis 1990 and Morris 1989].

$$4Y_2Ba_4Cu_7O_{14+z} - (4z-3)/2O_2 = Y_2BaCuO_5 + 3BaCuO_2 + 6YBa_2Cu_4O_8 \quad (7.14)$$

The reactions must have happened at the interface between the superconductor and YSZ electrolyte, where high oxygen activity is generated by the cell voltage. The XRD and microprobe analyses show that there are some $YBa_2Cu_4O_8$ and $Y_2Ba_4Cu_7O_{14+z}$ phases present in the titrated samples. The oxygen pressure of these two four-phase equilibria are shown in Fig.7.26 [Degterov 1991]. Lines 1 and 4 are the equilibrium oxygen activities of equations 7.13 and 7.14 respectively. The equilibrium oxygen pressures of the reactions at 1000K are in the range of 10^{-1}--10^{0} atmospheres which is obviously too low to be responsible for the oxygen activity measured at 1000K, Figure 7.19-7.22. The decomposition reactions for $Y_2Ba_4Cu_7O_{14+z}$ and $YBa_2Cu_4O_8$ phases are:

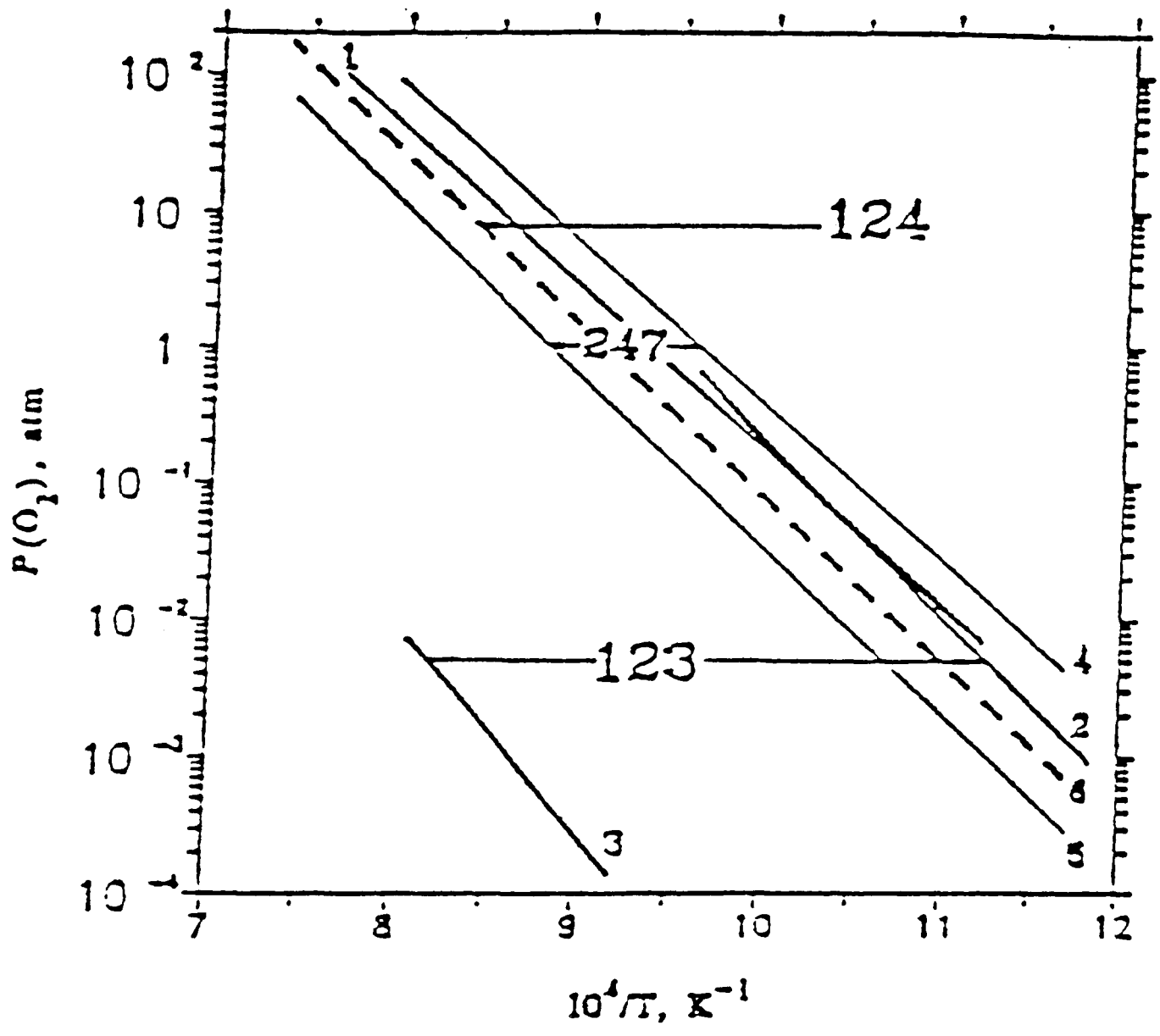

Figure 7.26: P-T Diagram (after Degterov 1991)

$$Y_2Ba_4Cu_7O_{14+z} = 2YBa_2Cu_3O_{6+z} + CuO + (1\text{-}z)/2O_2 \quad (7.15)$$

$$2YBa_2Cu_4O_8 = Y_2Ba_4Cu_7O_{14+z} + CuO + (1\text{-}z)/2O_2 \quad (7.16)$$

which generate even lower equilibrium oxygen activities, shown in Fig.7.26 by lines 5 and 6.

The oxygen activities measured in experiment 3 could thus not be any of the four-phase equilibria listed above.

Given that the $YBa_2Cu_3O_{6+z}$ pellet was placed in contact with the YSZ electrolyte pellet inside the electrochemical cell, the $YBa_2Cu_3O_{6+z}$ phase may have been decomposed by electrochemical titration into $Y_2Ba_4Cu_7O_{14+z}$, $YBa_2Cu_4O_8$ and other phases according to the equations 7.13 and 7.14, and the reaction product $BaCuO_2$ may then reacting with the ZrO_2. This might occur even though ZrO_2 ceramics are very stable in contact with $YBa_2Cu_3O_{6+z}$ up to 800°C [Cheung 1989]. The reaction is:

$$BaCuO_2 + ZrO_2 = BaZrO_3 + CuO \quad (7.17)$$

The Gibbs free energy terms of the reaction are:

$$\Delta G = \Delta G^{ox}_{BaZrO_3} - \Delta G^{ox}_{BaCuO_2} \quad (7.18)$$

where ΔG is the Gibbs free energy of the reaction, the superscripts ox stand for Gibbs free energy change when forming a phase from simple oxides, $\Delta G^{ox}_{BaZrO_3}$ is the $BaZrO_3$ Gibbs free energy of formation from oxides, and $\Delta G^{ox}_{BaCuO_2}$ is the $BaCuO_2$ Gibbs free energy of formation from oxides.

At T = 1000K,

$\Delta G^{ox}_{BaZrO_3} = -91.6 \pm 12.8$ (KJ/mol) [Saha 1989]

$\Delta G^{ox}_{BaCuO_2} = -36.6$ (KJ/mol) [Fan 1990]

the $\Delta G = -55$ (KJ/mol) < 0

So equation 7.17 indicates that $BaZrO_3$ and CuO will tend to form spontaneously according to the thermodynamics of the reaction.

Considering the possible reaction products, $BaZrO_3$, CuO, Y_2BaCuO_5, $YBa_2Cu_4O_8$, $Y_2Ba_4Cu_7O_{14+z}$ and some unreacted $YBa_2Cu_3O_{6+z}$, all are present

at the interface in contact with ZrO_2 ceramics in the titrated samples. There are three possible five phase equilibria at the interface between the YBCO sample and YSZ electrolyte:

$$2YBa_2Cu_4O_8 + 3ZrO_2 - \frac{1}{2}O_2 = Y_2BaCuO_5 + 7CuO + 3BaZrO_3 \quad (7.19)$$

$$Y_2Ba_4Cu_7O_{14+z} + 3ZrO_2 - \frac{1}{2}zO_2 = Y_2BaCuO_5 + 6CuO + 3BaZrO_3 \quad (7.20)$$

$$4YBa_2Cu_3O_{6+z} + 6ZrO_2 + (1 - 2z)O_2 = 2Y_2BaCuO_5 + 10CuO + 6BaZrO_3 \quad (7.21)$$

The Gibbs free energy terms of these reactions are:

$$\Delta G_{124} = \Delta G^{ox}_{Y_2BaCuO_5} + 3\Delta G^{ox}_{BaZrO_3} - 2\Delta G^{ox}_{YBa_2Cu_4O_8} + \frac{1}{2}RT\ln P_{O_2} \quad (7.22)$$

$$\Delta G_{247} = \Delta G^{ox}_{Y_2BaCuO_5} + 3\Delta G^{ox}_{BaZrO_3} - \Delta G^{ox}_{Y_2Ba_4Cu_7O_{14+z}} + \frac{1}{2}zRT\ln P_{O_2} \quad (7.23)$$

$$\Delta G_{123} = 2\Delta G^{ox}_{Y_2BaCuO_5} + 6\Delta G^{ox}_{BaZrO_3} - 4\Delta G^{ox}_{YBa_2Cu_3O_{6+z}} - (1-2z)RT\ln P_{O_2} \quad (7.24)$$

where ΔG_{124}, ΔG_{247} and ΔG_{123} are the Gibbs free energies of equations 7.19, 7.20 and 7.21 respectively, $\Delta G^{ox}_{BaZrO_3}$ is the $BaZrO_3$ Gibbs energy, $\Delta G^{ox}_{YBa_2Cu_4O_8}$ is the $YBa_2Cu_4O_8$ Gibbs energy, $\Delta G^{ox}_{Y_2Ba_4Cu_7O_{14+z}}$ is the $Y_2Ba_4Cu_7O_{14+z}$ Gibbs energy, $\Delta G^{ox}_{YBa_2Cu_3O_{6+z}}$ is the $YBa_2Cu_3O_{6+z}$ Gibbs energy, $\Delta G^{ox}_{Y_2BaCuO_5}$ is the Y_2BaCuO_5 Gibbs energy, R is the gas constant and T is the absolute temperature.

For the five-phase equilibria 7.19, 7.20 and 7.21, the equilibrium conditions require that ΔG_{124}, ΔG_{247} and ΔG_{123} are equal to zero. So equations 7.22 7.23 and 7.24 can be rewritten as :

$$\frac{1}{2}RT\ln P_{O_2} = 2\Delta G^{ox}_{YBa_2Cu_4O_8} - 3\Delta G^{ox}_{BaZrO_3} - \Delta G^{ox}_{Y_2BaCuO_5} \quad (7.25)$$

$$\frac{1}{2}zRT\ln P_{O_2} = \Delta G^{ox}_{Y_2Ba_4Cu_7O_{14+z}} - 3\Delta G^{ox}_{BaZrO_3} - \Delta G^{ox}_{Y_2BaCuO_5} \quad (7.26)$$

$$(1-2z)RT\ln P_{O_2} = 2\Delta G^{ox}_{Y_2BaCuO_5} - 6\Delta G^{ox}_{BaZrO_3} - 4\Delta G^{ox}_{YBa_2Cu_3O_{6+z}} \quad (7.27)$$

At T = 1000K,

$\Delta G^{ox}_{BaZrO_3}$ = -91.6 ± 12.8 (KJ/mol) [Saha 1989]

$\Delta G^{ox}_{YBa_2Cu_3O_{6+z}}$ = -84.035 (KJ/mol) [Voronin 1991]

$\Delta G^{ox}_{Y_2BaCuO_5}$ = -55.200 (KJ/mol) [Voronin 1991]

So using equation 7.27:

$(1-2z)RT\ln P_{O2}$ = 2×(-55200) - 6×(-91600) - 4×(-84035) = -403860 (J/mol)

where R=8.314 and T=1000, for a sample with stoichiometry 6.75 (z=0.75)

$(1-2z)\ln P_{O2}$=-48. 576 $P_{O2} = 1.5577\times10^{42}$ (atm)

According to Gibbs phase rule:

$$f = c + 2 - p \quad (7.12)$$

c and p are both 5, at constant temperature and pressure, the degree of freedom f=5-5=0, that means the oxygen activity is expected to have a flat time dependence as oxygen diffuses out, and this is the case in experiment 3 (Fig.7.19) for the first flat step. The oxygen activity of the flat stage is 10^{40}-10^{42} (atm), which is about the same order as the calculated oxygen activity. So the five-phase equilibrium 7.21 may be responsible for the first flat step in Fig.7.19.

From equation 7.25, the Gibbs standard energy for $YBa_2Cu_4O_8$ is:

$\Delta G^{o}_{YBa_2Cu_4O_8}$ = - 2079.74 (KJ/mol) [Degterov 1991]

to convert the Gibbs standard energy for $YBa_2Cu_4O_8$ ($\Delta G^{o}_{YBa_2Cu_4O_8}$) to its Gibbs energy formed from oxides ($\Delta G^{ox}_{YBa_2Cu_4O_8}$), the following equation is used:

$$2YBa_2Cu_4O_8 = Y_2O_3 + 4BaO + 8CuO + \frac{1}{2}O_2 \quad (7.28)$$

$$\Delta G^{ox}_{YBa_2Cu_4O_8} = \Delta G^{o}_{YBa_2Cu_4O_8} - \frac{1}{2}\Delta G^{0}_{Y_2O_3} - 2\Delta G^{0}_{BaO} - 4\Delta G^{o}_{CuO} - \frac{1}{4}RT\ln P_{O2} \quad (7.29)$$

at 1 atm O_2 environment, $\frac{1}{4}RT\ln P = 0$

at 1000K

$\Delta G^0_{Y_2O_3}$ = -1628.996 (KJ/mol) [Degterov 1991]

ΔG^0_{BaO} = -454.481. (KJ/mol) [Degterov 1991]

ΔG^o_{CuO} = -66.333. (KJ/mol) [Degterov 1991]

So the $2\Delta G^{ox}_{YBa_2Cu_4O_8}$ = -181.086 (KJ/mol)

Equation 7.25 becomes:

$$\frac{1}{2}RT\ln P_{O2} = 148914.4505 \text{ (J/mol)}$$

substitute T=1000K

$$\frac{1}{2}\ln P_{O2} = 17.9113$$

$$P_{O2} = 3.6103 \times 10^{15} \text{ atm.}$$

From the Gibbs phase rule, it is a five phase equilibrium and the equilibrium oxygen activity should have a flat time dependence. Comparing the calculated result and the experiment result, equilibrium 7.19 may be responsible for the observed flat second steps in the oxygen activity - time relations (Fig. 7.20 & 7.21) which have oxygen activities of 10^{12} - 10^{15} atm.

For equation 7.26:

At T = 1000K,

$\Delta G^{ox}_{Y_2Ba_4Cu_7O_{14+z}}$ = -175392 (J/mol) [Voronin 1991]

so the equation becomes:

$$\frac{1}{2}zRT\ln P_{O2} = 154608 \text{ (J/mol)}$$

$$\frac{1}{2}z\ln P_{O2} = 18.596$$

For $Y_2Ba_4Cu_7O_{14+z}$ with oxygen stoichiometry 14.8 (z=0.8), which is a reasonable value under conditions of electrochemical titration,

$$P_{O2} = 1.55 \times 10^{20} \text{ (atm)}$$

This reaction (Equation 7.20), may be responsible for the first step in Fig. 7.20 and Fig. 7.21. The sloping nature of the step may be due to the sluggish kinetics of the reactions which involve other phase equilibria, and this might be the case in the Fig. 7.19, which shows some irregularities in the oxygen activity - time dependence at about 10^{15} atm.

The sample titrated at 700°C but measured at 800°C with cell voltage 5 Volts gave a much lower oxygen activity step (Fig.7.22). This is likely to be due to the equilibrium oxygen pressure variation of one of the three five phase equilibria discussed above, however, due to the lack of thermodynamic data on the system at 1073K I cannot know which of the equilibria is responsible for this step.

For the samples titrated at cell voltages below 2 Volts, there is no observable oxygen activity change from the untitrated sample, which indicates that the oxygen potential has not decomposed the $YBa_2Cu_3O_{6+z}$ phase, or not formed enough decomposition products to allow the reactions discussed above. The samples titrated at less than 2 Volts show only traces of reaction products from the XRD and microprobe analyses, which means that the decomposition of $YBa_2Cu_3O_{7-x}$ (equations 7.13, 7.14) is somehow hindered by kinetic features even at relatively high oxygen activities, though the thermodynamics favours decomposition.

7.7 Resistance measurements during titration

7.7.1 Experiment and results

To understand the oxygen diffusion procedure and how the electrical properties vary during electrochemical titration, the sample resistance and the electrolyte resistance were measured during the titration experiment. The electrical circuit is schematically shown in Fig.7.27.

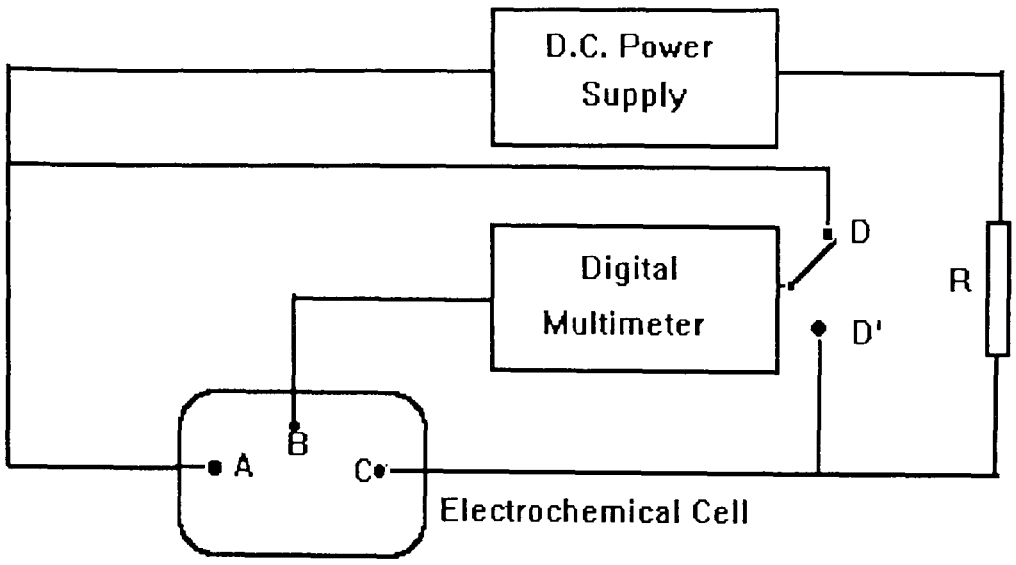

Figure 7.27: Electrical circuit for resistance measurement

The electrical resistance of the sample and the electrolyte were measured during the titration process by switching the switch to D or D', the results are shown in Fig.7.28

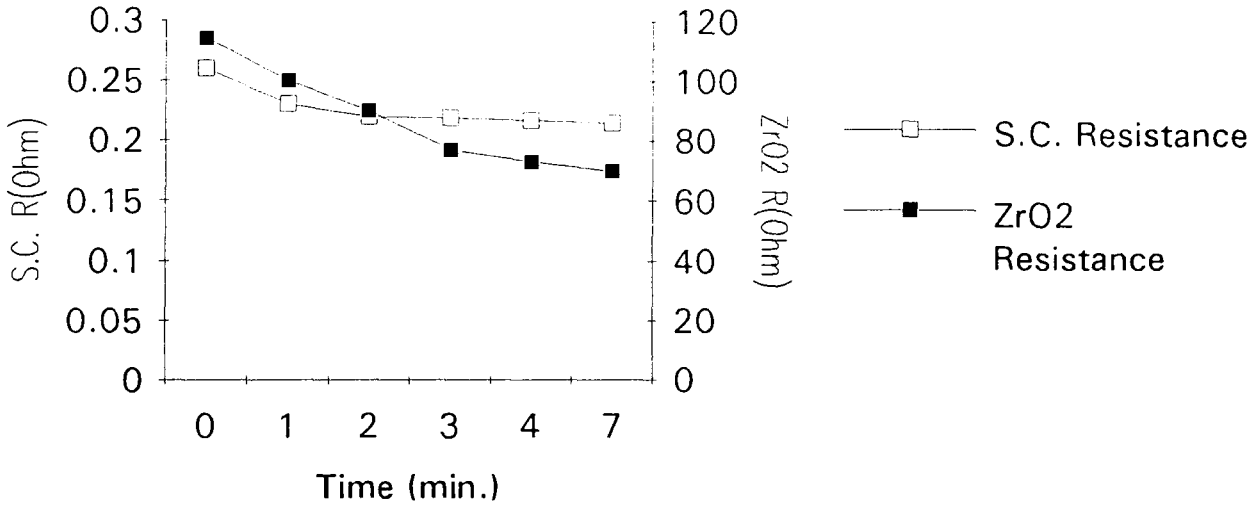

Fig.7.28: Electrical resistance of the cell during the titration

From the result we can see that the $YBa_2Cu_3O_{7-x}$ pellet changes in resistance from 0.3Ω to 0.2Ω, while the YSZ electrolyte changes its resistance from 120Ω to 60Ω.

7.7.2 Discussion:

The resistance drop in the $YBa_2Cu_3O_{7-x}$ during titration can be understood

since oxygen ions are injected into the $YBa_2Cu_3O_{7-x}$ and the oxygen stoichiometry is improved which leads to the reduction in electrical resistance (Fig. 1.11). This can be used as an early standard for a properly set up electrochemical cell. If the electrical resistance drops during the titration, this means the oxygen ions are entering the $YBa_2Cu_3O_{7-x}$ material, otherwise, the cell should be checked.

The sharp drop in the electrical resistance of the YSZ electrolyte during the titration may indicate the oxygen ion concentration is increased and thus increasing its conductance (equation 7.4).

Since the electrical resistance of the whole cell drops during titration, the constant voltage source in the DC power supply in the system will generate a increasing current during titration. This makes it difficult to monitor and interpret the current change during electrochemical titration by oxygen diffusion in the $YBa_2Cu_3O_{7-x}$. The measurement of the current during electrochemical titration is only used as a reference to ensure a properly connected circuit.

7.8 Contact making during electrochemical titration

7.8.1 Background

We have seen from chapter 6 that gold contacts on $YBa_2Cu_3O_{7-x}$ surfaces can sometimes cause decomposition of the superconductor material and result in mainly Y_2BaCuO_5. The mechanisms of the decomposition have been discussed in chapter 6, and the problem of limited oxygen supply is important in encouraging these reactions.

Electrochemical titration can introduce oxygen into the $YBa_2Cu_3O_{7-x}$ independently of the temperature, which is a big advantage over ordinary annealing and particularly high temperature annealing for which the necessary high oxygen activity might cause the decomposition of the $YBa_2Cu_3O_{7-x}$. The electrochemical titration method can push the oxygen into the $YBa_2Cu_3O_{7-x}$ and this may avoid the decomposition of the $YBa_2Cu_3O_{7-x}$ if the cell voltage is not too high.

7.8.2 Experiment

Gold pieces were cut into 1×2 mm^2 samples and polished. The $YBa_2Cu_3O_{7-x}$ superconductor samples used in this experiment were large grained textured samples. The $YBa_2Cu_3O_{7-x}$ was coated with gold on the surfaces to prevent oxygen loss. The samples were titrated at 600°C for 72 hours before the contact making experiment to ensure a high oxygen content when starting the contact making. Then they were put inside the electrochemical cell in Fig.7.29.

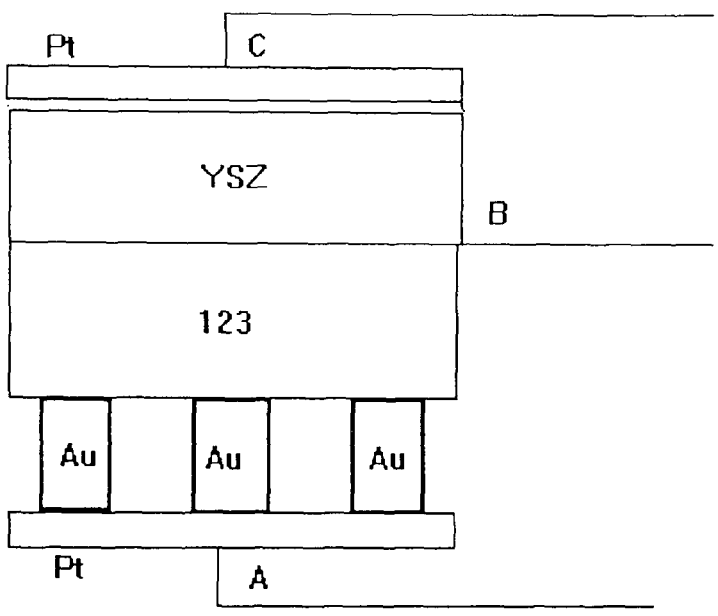

Figure 7.29: The electrochemical cell for contact making

This electrochemical cell was connected in the circuit in Fig.7.5. The sample was titrated at 800°C for 12 hours at the voltage below 2 Volts and the cell was cooled to room temperature with the applied cell voltage.

The gold plates were firmly bonded onto the $YBa_2Cu_3O_{7-x}$ after titration, and silver wires were then directly soldered onto the gold contacts with indium solder. The contact resistivity was measured by the three-terminal method described in chapter 6.

A contact resistivity of 2×10^{-8} Ω cm^2 was measured at 50K. The voltage is about 10^{-7} Volts measured on the lock-in amplifier with 100 mA current, which is very close to the sensitivity limit of the equipment, and is very unstable upon heating to measure the temperature dependence. The noise overloaded the lock-in amplifier so frequently that the temperature dependence could not be properly observed.

The gold contact was later mechanically separated from the $YBa_2Cu_3O_{7-x}$ surface, and the surface of the $YBa_2Cu_3O_{7-x}$ was analysed by optical microscopy and electron microprobe techniques.

The optical microscope analysis shows that there is no green phase (211) present at the surface (Fig.7.30), which is different from the result obtained from the sample made under the same conditions without electrochemical titration (Chapter 6). The electron microprobe analysis shows that the composition of the $YBa_2Cu_3O_{7-x}$ surface remains unchanged (Table 7.3).

Table 7.11: Composition of the $YBa_2Cu_3O_{7-x}$ surface

Y at%	Cu at%	Ba at%	O at%	Formula
7.597	21.241	13.861	57.301	$YBa_2Cu_3O_{7-x}$

7.8.3 Discussion

The gold contact made by diffusion bonding without titration for 8 hours was not adhered to the surface and there is decomposition of the $YBa_2Cu_3O_{7-x}$ superconductor into the 211 phase, as has been discussed in chapter 6. Gold contacts made by the diffusion bonding technique reached a contact resistivity of 10^{-7} Ohm cm^2 with prolonged high temperature annealing (48 hours).

The gold contacts on $YBa_2Cu_3O_{7-x}$ made by electrochemical titration have not caused decomposition. The $YBa_2Cu_3O_{7-x}$ surface and the gold contact sample made with this method have even better contact resistivity in a shorter annealing time (8 hours). The oxygen titration obviously increased the oxygen content in the $YBa_2Cu_3O_{7-x}$ at high temperature and avoided the decomposition. This proved that the mechanism of the decomposition of $YBa_2Cu_3O_{7-x}$ in the earlier experiment might have some relation with the local oxygen supply at the surface region.

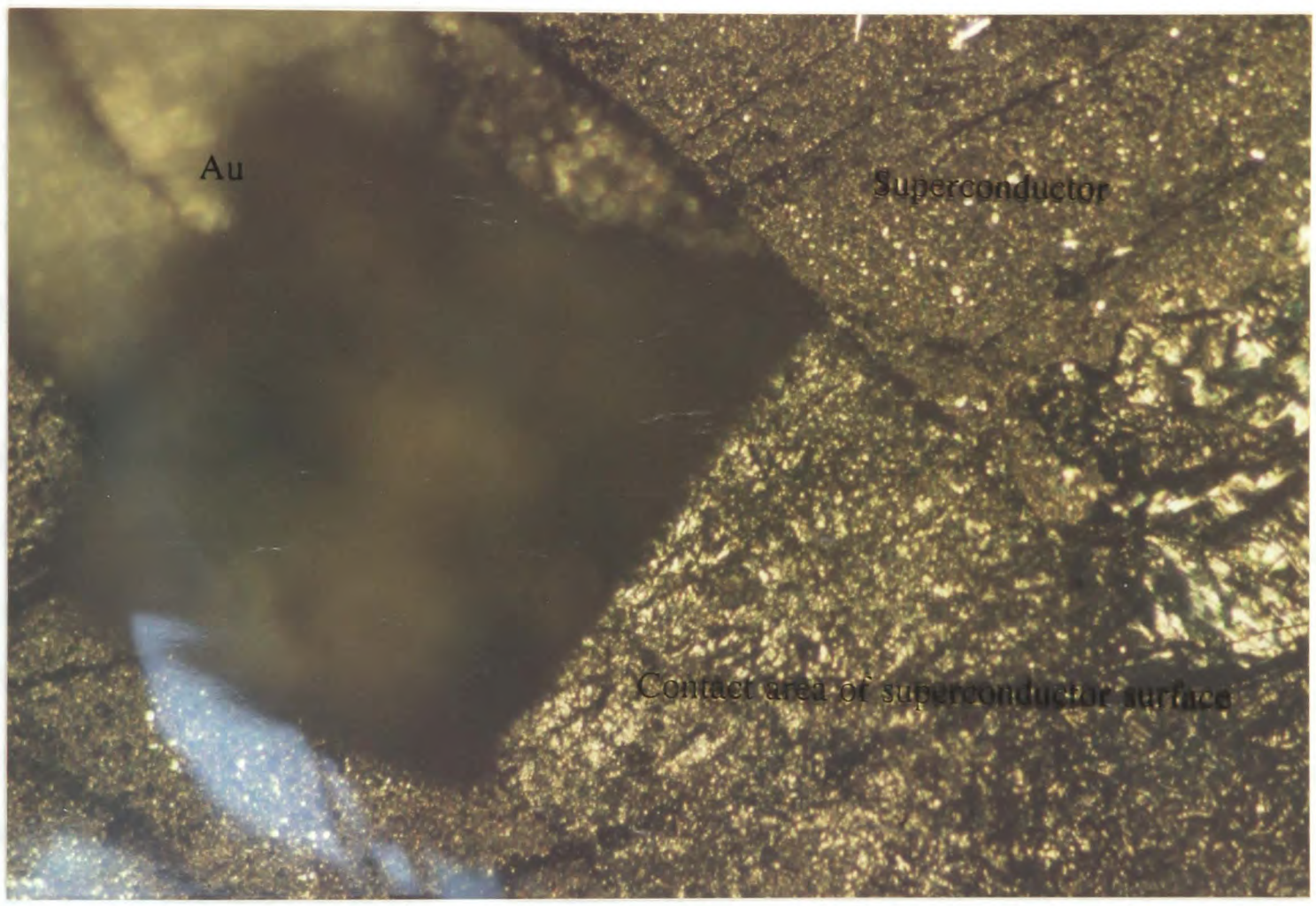

Figure 7.30: Interface of Au/superconductor

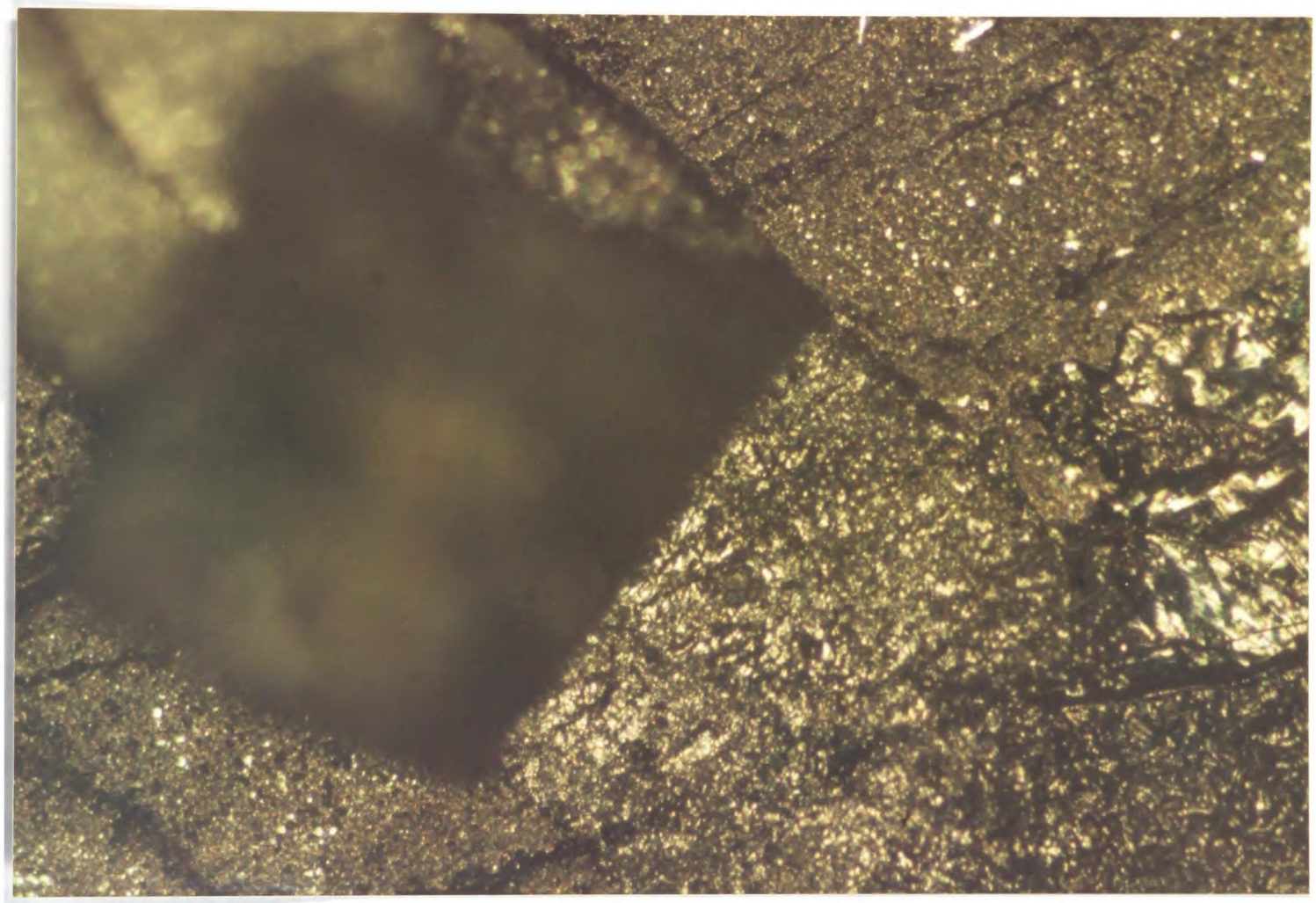

Figure 7.30: Interface of Au/superconductor

Gold contacts made using the electrochemical titration method avoided the decomposition of the $YBa_2Cu_3O_{7-x}$ and reduced the annealing time in the gold contact making procedure, and also achieved better contact properties. These experiments have then helped to explain some of the problems found with Au/YBCO contact fabricated by conventional annealing, and have suggested ways of overcoming those problems.

7.9 Conclusions:

1). The electrochemical titration method can be used to increase the oxygen stoichiometry of bulk textured $YBa_2Cu_3O_{7-x}$ samples.

2). The electrochemical titration method can further oxidize melt textured thick film $YBa_2Cu_3O_{7-x}$ samples in which it may be difficult to further improve oxygen content by conventional annealing.

3). The electrochemical titration method was proved to give faster oxidation kinetics in $YBa_2Cu_3O_{7-x}$ than annealing at the same temperature and oxygen pressure .

4). The electrochemical titration method can generate very high oxygen activity at the surface of $YBa_2Cu_3O_{7-x}$ and form $YBa_2Cu_4O_8$ and $YBa_2Cu_{3.5}O_{7+x}$.

5). The solid state electrochemical cell can be used to study the thermodynamic properties of the Y-Ba-Cu-O system at high oxygen pressure by measuring the oxygen activity versus time continuously immediately after the electrochemical titration.

6). There are three possible five-phase equilibria involved with $YBa_2Cu_3O_{7-x}$, CuO, ZrO_2, $ZrBaO_3$, $YBa_2Cu_4O_8$ and $YBa_2Cu_{3.5}O_{7+x}$ which may be responsible for the high oxygen activity observed after electrochemical titration.

7). The insufficient oxygen supply at high temperatures at the interface between gold and $YBa_2Cu_3O_{7-x}$ may be responsible for the decomposition of $YBa_2Cu_3O_{7-x}$.

8). The electrochemical titration method can be used to make low resistivity gold contacts on $YBa_2Cu_3O_{7-x}$.

Chapter 8

Modelling of $YBa_2Cu_3O_{7-x}$ contacts

8.1 Introduction

As we have seen from chapter 6, contacts made with different contact materials and processed in different ways show not only differences in contact resistivity values but also in the variation of resistivity with temperature. Currently there is no theory to explain the complex contact resistivity behaviours.

In this chapter, a series of simple models are set up according to the microstructure of the contact interface to simulate the complicated contact resistivity behaviours. As a result it may prove possible in the future to propose the nature of and geometry of reaction products at contact interfaces from the temperature dependence of the contact resistance.

8.2 A possible explanation for the contact resistance drop near Tc

It has been noticed that the measured contact resistances reported in chapter 6 have sharp changes at the superconducting transition temperature, Tc, especially in the cases of very low resistivity contacts with typical resistivity values 10^{-6}-10^{-7}Ohm cm^2 (Fig6.9 and Fig. 6.23). The change of contact resistivity is very similar to the pure superconducting transition Fig.6.2. It looks as if the measurement somehow includes a contribution from the superconductor resistance R_S, although a 3 point measurement geometry should avoid any such contribution from the bulk superconductor. This contact resistance feature near Tc is commonly observed [Hui 1989, Suzuki 1989], but currently there is no explanation for it. Scattered insulating particles at the contact interface will cause a constriction resistance in addition to the normal bulk resistance of the contact material [Mroczkowski 1989], but this cannot be used in explaining the complicated contact resistivity behaviour.

One possible explanation is discussed below: Since the normal state resistivity of $YBa_2Cu_3O_{7-x}$ changes with its oxygen stoichiometry, the resistivity rises sharply as

the oxygen stoichiometry decreases (Fig.1.12), and the oxygen stoichiometry at the surface of $YBa_2Cu_3O_{7-x}$ is very likely to change during the storage or expose to air or vacuum (Komolov 1990 & Chen 1991), it is possible that a thin layer of superconductor with different (higher) electrical resistivity was involved in the contact resistance measurement due to the change in oxygen stoichiometry. The resistance of the thin layer of $YBa_2Cu_3O_{7-x}$ with higher resistivity formed directly under the contact cannot be distinguished from the resistance of contact itself, and will be measured as part of the contact resistance. At temperatures above Tc, the resistance is dominated by the normal state resistance of $YBa_2Cu_3O_{7-x}$ if the contact is reasonably good. The thin surface layer of $YBa_2Cu_3O_{7-x}$ goes through its superconducting transition below Tc, and the apparent contact resistance drops by several orders of magnitude. The resistance measured now is the resistance of interface and contact materials, and it is determined primarily by the reaction products at the interface.

This assumption is consistent with the occurrence of a transition in contact resistance at a temperature near Tc, and the linear contact resistance behaviour above Tc (which is the normal state resistance behaviour of $YBa_2Cu_3O_{7-x}$ [Ong 1988, Hagen 1988].

8.3 Contact interface models

The temperature dependence of the contact resistivity can reflect the contact properties, especially when the contact metals react with, and form compounds with, the superconductor. The nature of and geometry of the reaction products can be revealed by the temperature dependence of the contact resistivity.

8.3.1 Model for contacts with poor resistivities

Contacts with high resistivities do not generally show a resistivity drop at the superconducting transition temperature. The contact resistances increased as the temperature dropped, as we have seen in Chapter 6 (Fig.6.10 for example). The very large contact resistance and the negative temperature coefficients above Tc probably

indicate the existence of a semiconducting layer beneath the electrode. The electron microprobe did find a thick layer of TiO_2 at the interfaces between Ti contacts and sintered superconductor, Fig.6.12. Considering that the contact interface impurities (reaction products) may act as semiconductor layers and contribute the dominant part of the measured resistance value, the model for this kind of high resistivity contact can be simplified to a layer of semiconductor as shown in Fig. 8.1.

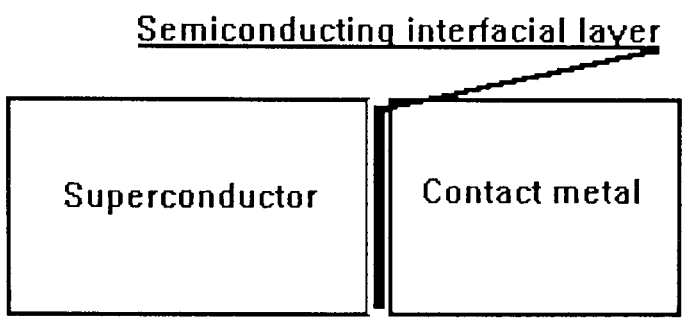

Figure 8.1: A schematic diagram of contact with high contact resistance

Assuming that semiconductor behaviour can be described by following equation:

$$R_{semi}=C_{semi}\exp(E/KT) \qquad (8.1)$$

where C_{semi} is a constant, E is the activation energy, k is Boltzmann's constant, and T is the absolute temperature.

The calculated result for a value of $E_0=E/K=80$ is shown in Fig. 8.2 and compared with the experimental data (Fig. 6.10), and approximates very well to the overall shape of the measured contact resistivity behaviour after normalisation.

8.3.2. Model for noble metal contacts

For the noble metal contacts like silver or gold, the electron microscope analyses show that the interfaces between noble metal and high Tc superconductor contain no new phases (Fig.6.8). The contact resistivity measurements show that noble metal contacts have very low resistivity. The contact resistance is linear and shows ohmic behaviour above Tc, drops sharply at Tc , and then continues to drop

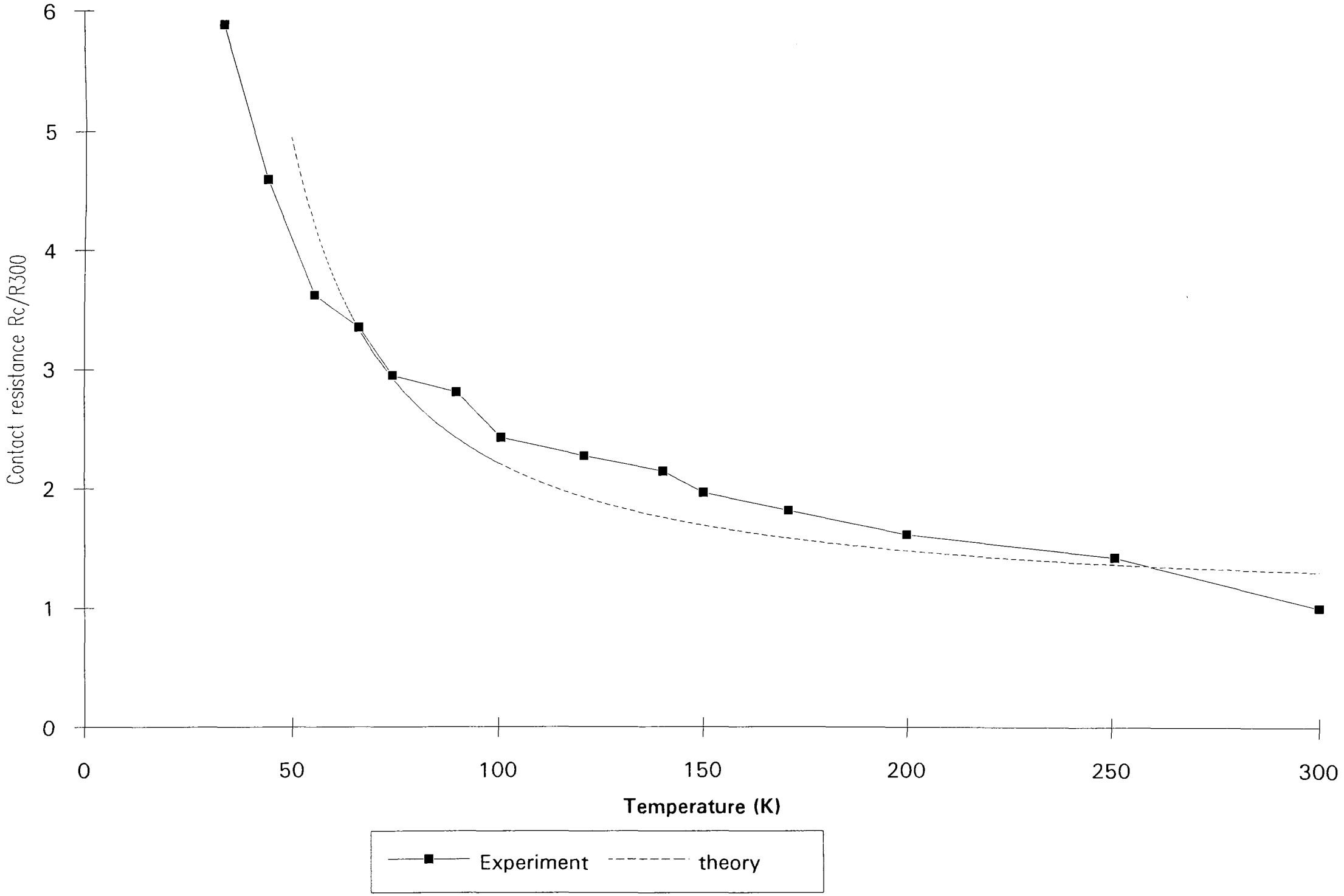

Figure 8.2: High resistivity contact model and experiment

slightly below Tc (Fig. 8.3). This indicates that the interface resistance is ohmic over the whole temperature range.

The model for this type of contact is based on the discussion in section 8.2, and is shown in Fig.8.4:

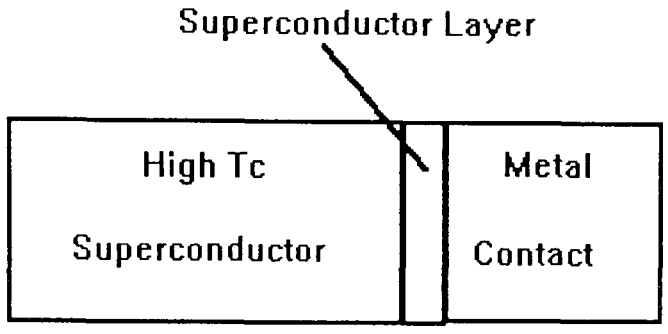

Figure 8.4: Schematic diagram of contact for noble metal

the total contact resistance is the series of sums:

$$R_c = R_{in} + R_m + R_i \tag{8.2}$$

where R_{in} is the resistance of the interfacial superconductor layer, R_m is the resistance of the contact metal layer and R_i is the resistance of the interface due to the current restriction, which may be regarded as a constant.

As we have seen from resistance measurements on noble metal contacts, Fig.8.3, the contact resistivity behaves like the superconductor (Fig. 8.5) above Tc, so the R is dominated by R_{in}.

Since the R_{in} is a superconductor layer, an assumption is made that R_{in} can be expressed by the following equation:

$$T > T_c \qquad R_{in} = C_{in} T \tag{8.3}$$

$$T < T_c \qquad R_{in} = C_{in} T_c \exp(a(T - T_c)) \tag{8.4}$$

where C_{in} and a are constants and T_c is the superconducting transition temperature. At temperatures above Tc the superconductor has a linear relation with temperature, and at the temperatures below Tc equation 8.4 is chosen to simulate the superconducting transition.

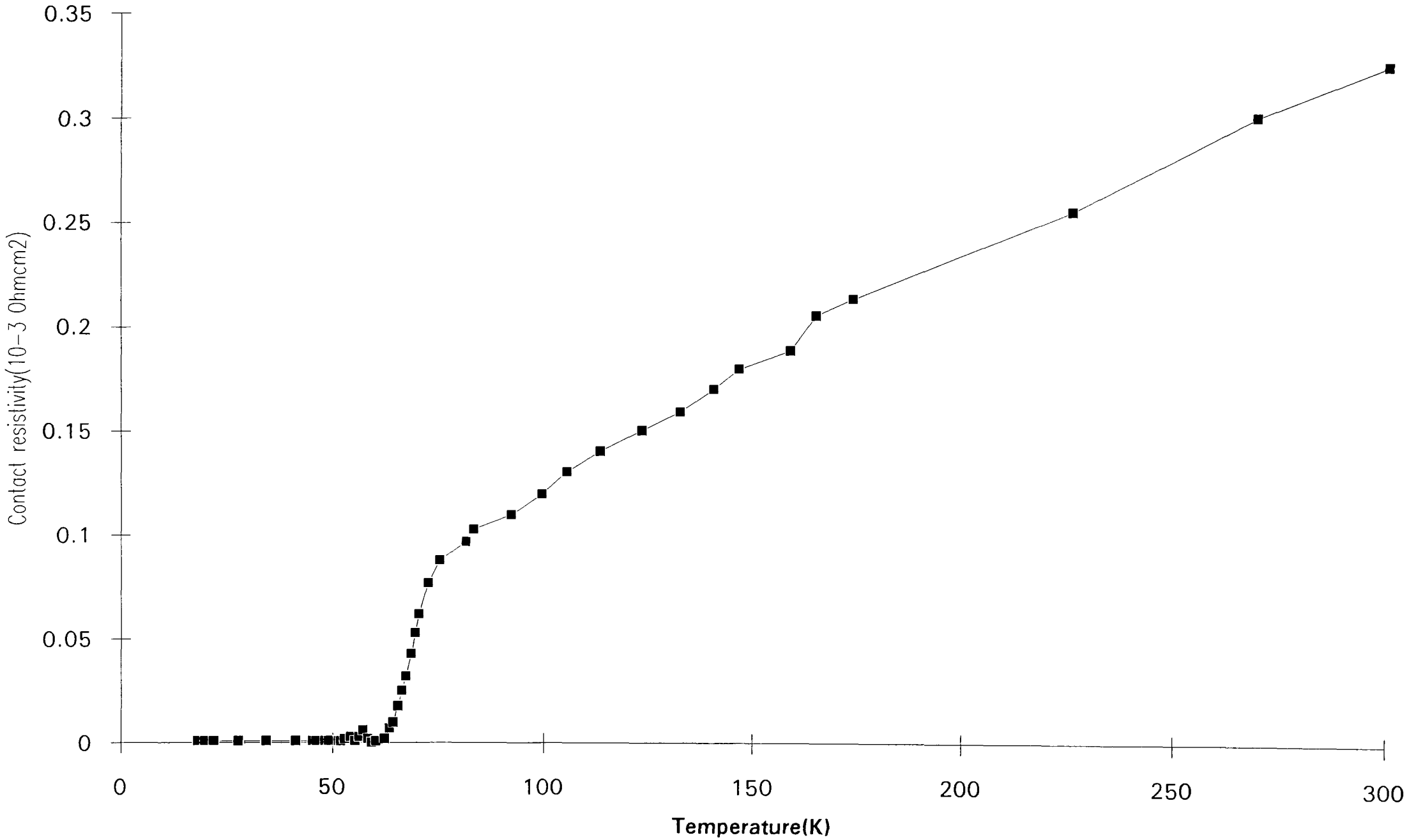

Figure 8.3: Silver epoxy contact (identical to Fig.6.9.

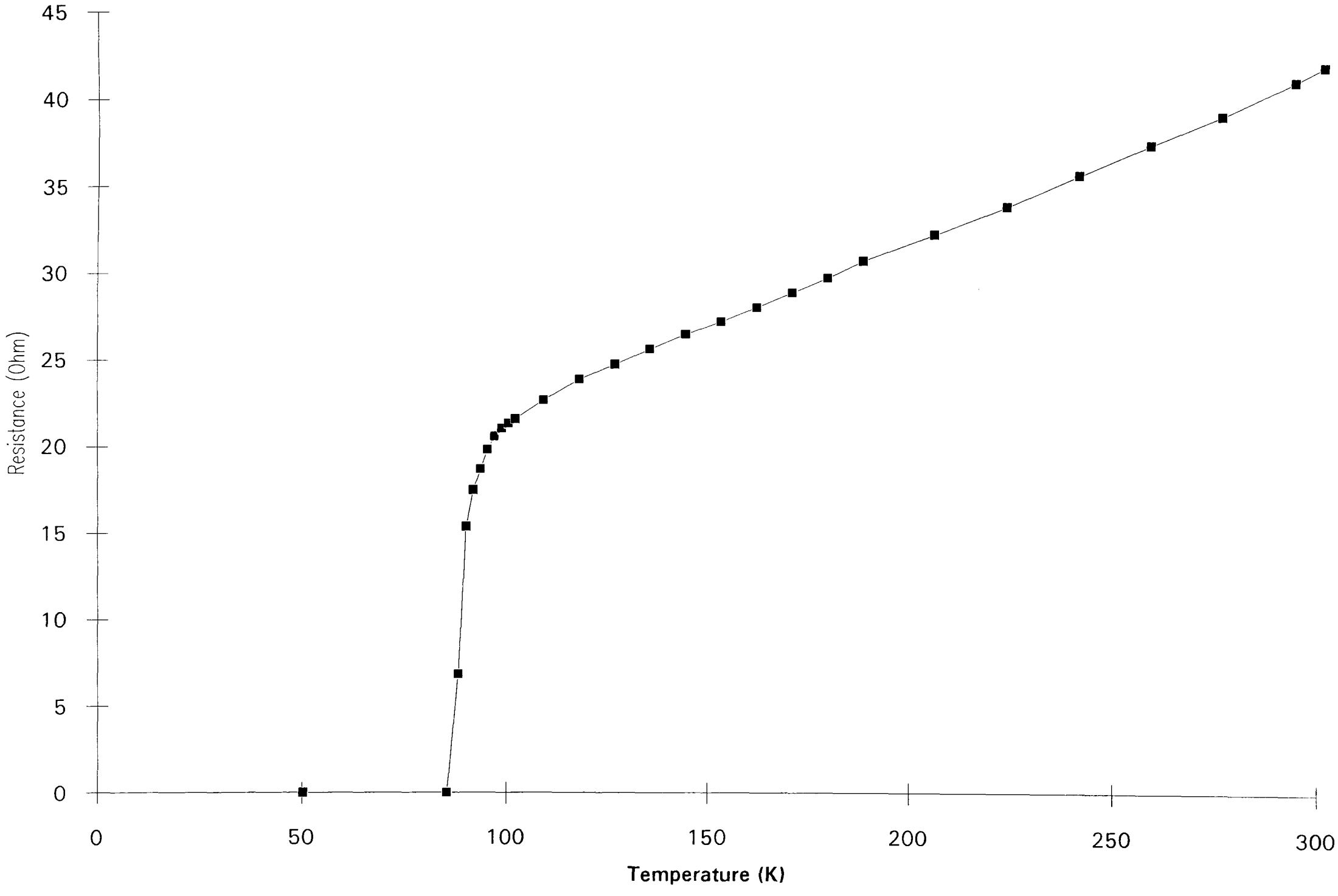

Figure 8.5: Superconducting transition

R_m is the resistance of the contact metal, and can be expressed as:

$$R_m = C_m T \tag{8.5}$$

C_m is constant, and as R_{in} is the dominant at $T > Tc$, we may arbitrarily assume that:

$$C_{in} = 100 C_m. \tag{8.6}$$

Model (8.2) can be rewritten as

$$R_c = C_{in}T + C_m T = C_m T(100+1) = 101 C_m T \qquad \text{for } T > Tc \tag{8.7}$$

$$\text{and } R_c = C_{in} T_c \exp(a(T-Tc)) + C_m T \qquad \text{for } T < Tc \tag{8.8}$$

The calculated result of the model is shown in Fig. 8.6 in comparison with experimental data, which fits the trend of a typical experimental result (Fig. 8.3) very well.

8.3.3 Model for contacts with resistivities (10^{-5}-$10^{-6}\Omega cm^2$)

The above model (8.2) is good for very low contact resistivities (10^{-6}-10^{-7} Ohm cm^2) as measured in gold diffusion bonds (Fig.6.23) and silver epoxy contacts with proper heat treatment (Fig.6.9). However, this model may not be good enough for contacts with slightly higher resistivities (10^{-5}-10^{-6}Ohm cm^2) of the kind shown in Fig.8.7. The resistance above T_c shows much flatter temperature dependence compared with the 4 point $YBa_2Cu_3O_{7-x}$ data shown in Fig.8.5.

Since there is a slight increase in contact resistivity compared with the case above, the contacts may have interfacial impurities or oxygen deficient regions which act as semiconducting material, and these may be in a parallel circuit with the $YBa_2Cu_3O_{7-x}$ surface layer.

A model for this type of contact is shown in Fig.8.8:

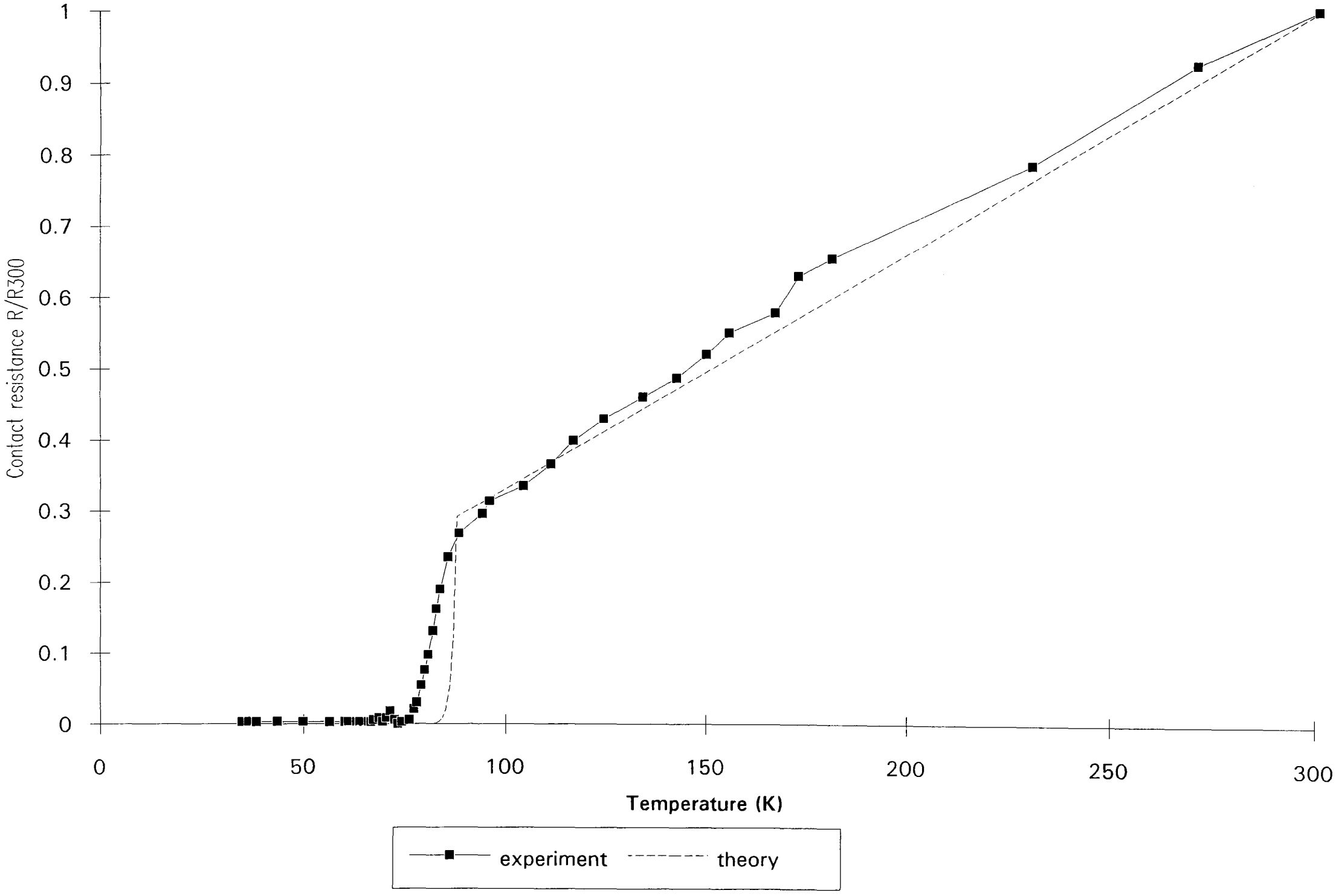

Figure 8.6: Noble metal contact resistivity and its model

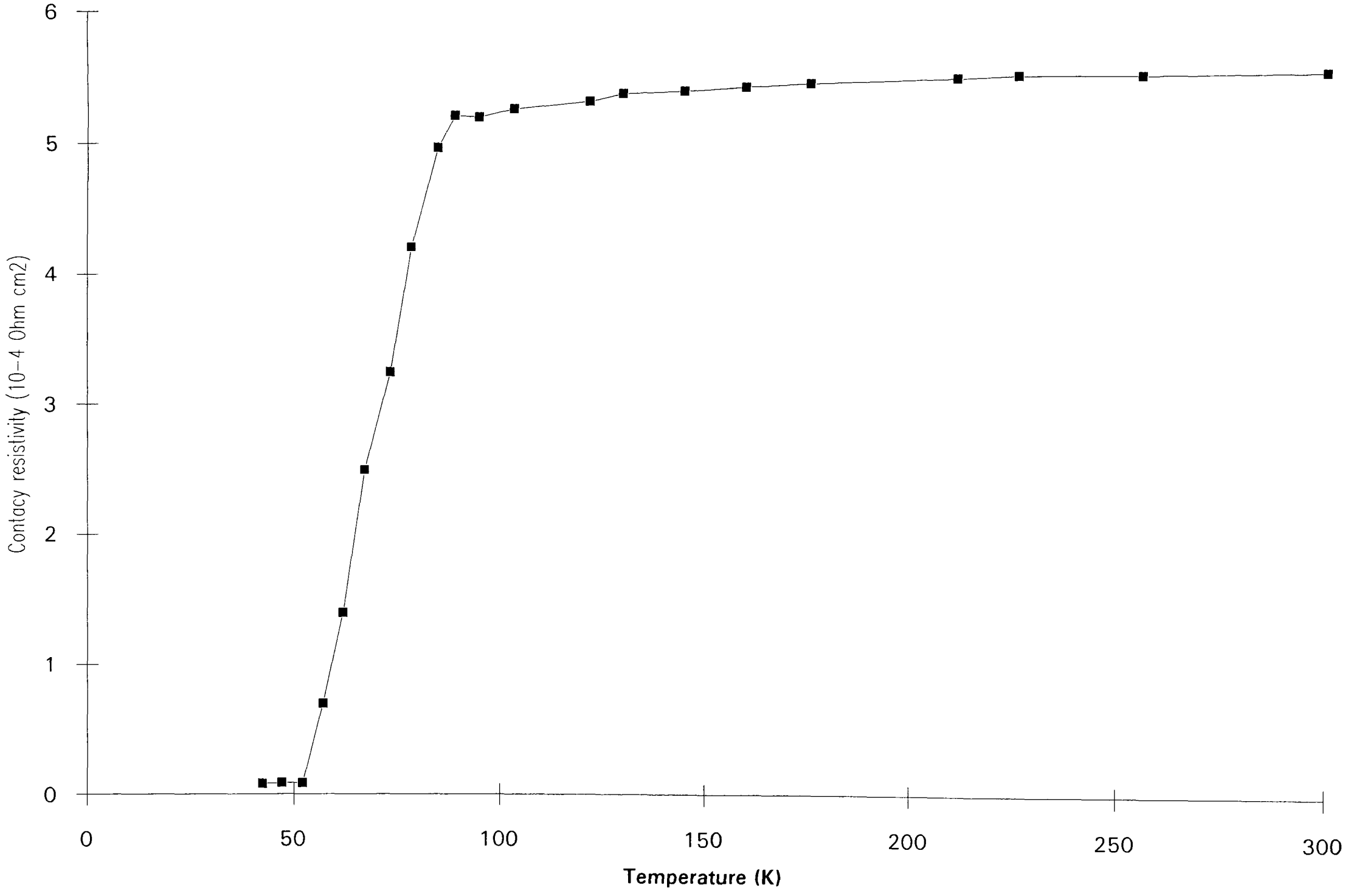

Figure 8.7: Silver contact resistivity (identical to Fig. 6.6)

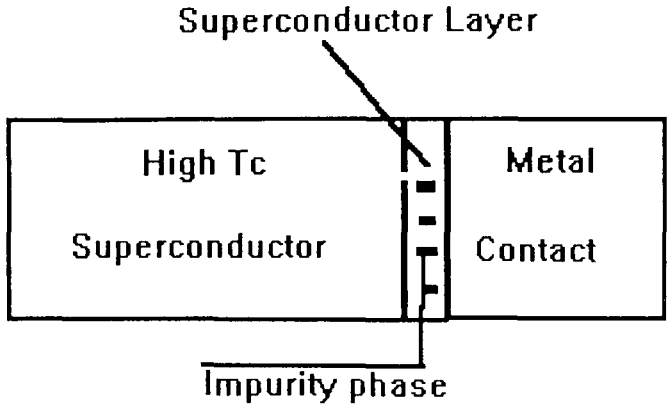

Figure 8.8: A schematic diagram of contact with resistivity $10^{-5}\Omega cm^2$

The impurities or oxygen deficient regions are assumed to be semiconducting with a resistance variation with temperature:

$$R_{semi}=C_{semi}\times\exp(E/KT) \tag{8.9}$$

where C_{semi} is a constant and E is the activation energy.

The contact resistance is the sum of the parallel circuit of semiconductor and superconductor:

$$R_c=C_{semi}\times T\times\exp(E^0/T)/(T+C\times\exp(E^0/T)) \qquad \text{For } T>T_c \tag{8.10}$$

and

$$R_c=C_{semi}\times T_c\times\exp(a\times(T-T_c))\times\exp(E^o/T)/(T_c\times\exp(a\times(T-T_c))$$
$$+C_{semi}\times\exp(E^0/T)) \qquad \text{For } T<T_c \tag{8.11}$$

where $C=C_{semi}/C_{in}$ and $E^0=E/k$. Choosing the activation energy term $E^0=100$, and $C=C_{semi}/C_{in}=88$, the calculated contact resistivity and its temperature dependence for this model is shown in Fig.8.9 in comparison with the experimental data, and it shows to fit approximately the trend of typical experimental results.

8.3.4. Model for contacts with resistivities $10^{-2}>Rc>10^{-3}\ \Omega cm^2$

For contact resistances in the range $10^{-2}>Rc>10^{-3}\Omega cm^2$, the contacts have semiconducting behaviour above and below Tc (Fig.8.10).

Let us assume a continuous thin layer of impurities is present at the interface and acts as semiconductor, which will add in series to the resistance of the interfacial superconductor layer. The model for this particular contact can be represented as:

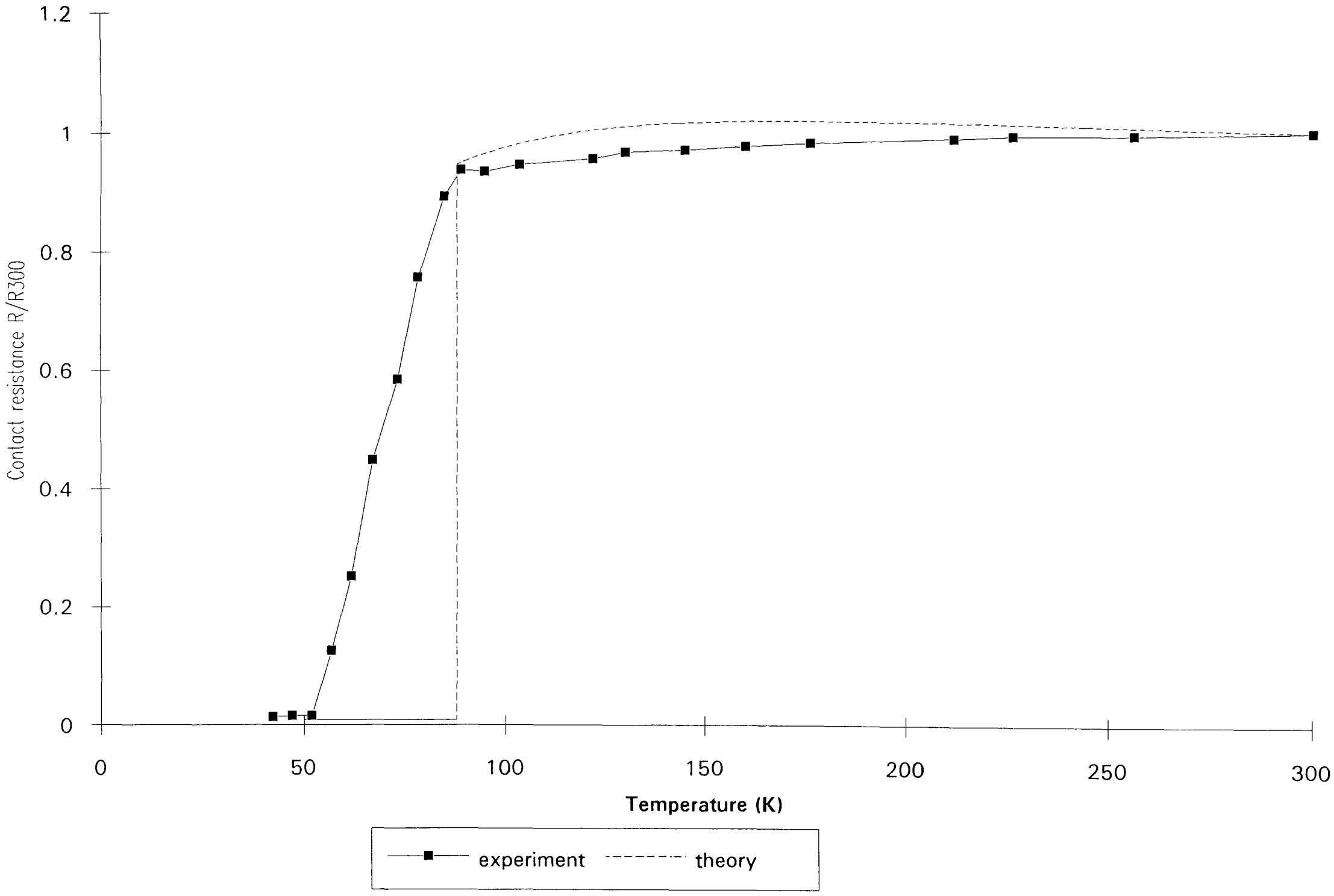

Figure 8.9 : Model for contacts with resistivities (10-5 - 10-6 Ohmcm2)

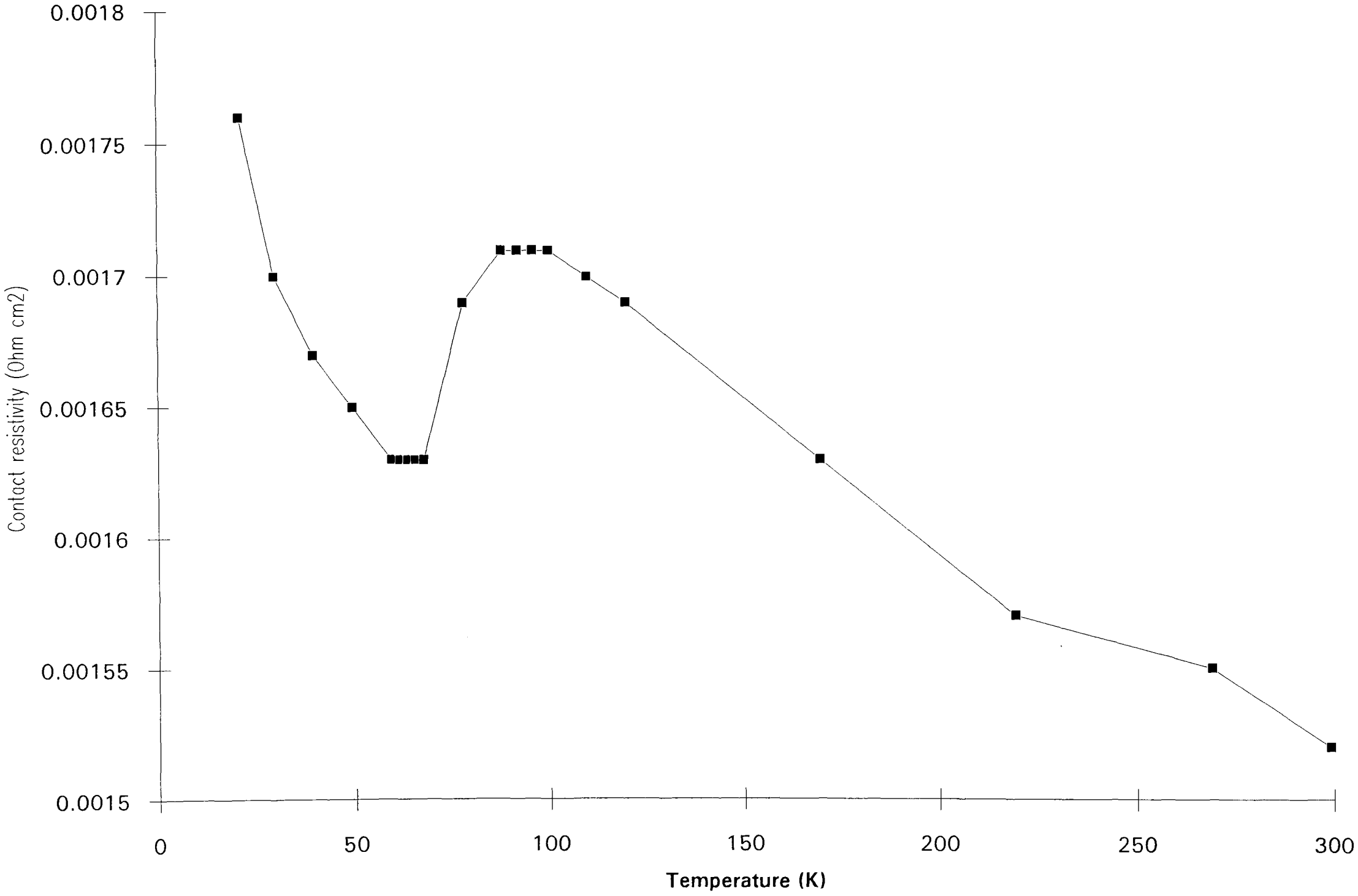

Figure 8.10: Silver contact without annealing (identical to Fig. 6.7)

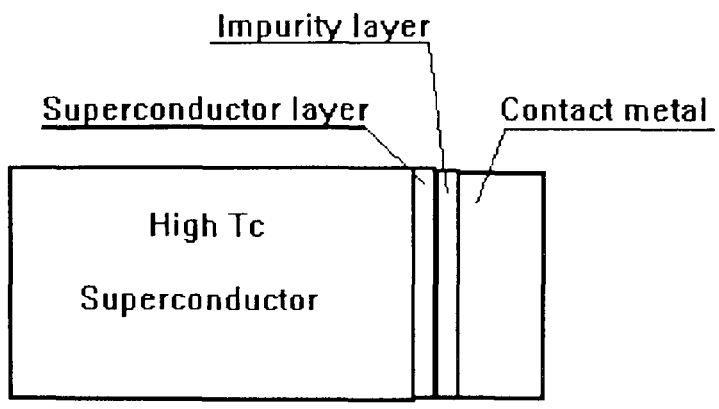

Fig. 8.11: A schematic diagram for contacts in the range $10^{-2} > Rc > 10^{-3} \Omega\ cm^2$

So the contact resistance Rc is the sum of:

$$Rc = R_{in} + R_i + R_{im} + R_m \qquad (8.12)$$

Like the noble metal contact model, the resistance of the interfacial superconductor R_{in} and resistance of the contact metal R_m can be written as equations 8.3 and 8.4, and the interfacial resistance R_i is regarded as constant.

$$R_m = r_m T \qquad (8.13)$$

R_{in} is assumed to be $r_{in} = 100 r_m$.

For the impurity layer, as it is not superconducting and not metallic, the thin layer may regard as a semiconductor layer.

R_{im} is assumed to obey the following relation:

$$R_{im} = r_{im} \exp(E/KT) \qquad (8.14)$$

where r_{im} is a constant and E is the activation energy.

So equation 8.12 can be written as:

$$R_c = r_{im}\exp(E/kT) + r_{in}T + r_m T$$

$$= r_{im}\exp(E/kT) + 101 T r_m \qquad \text{For } T > Tc \qquad (8.15)$$

$$R_c = r_{im}\exp(E/kT) + r_{in}T_c\exp(a(T-Tc)) + T(r_m) \qquad \text{For } T < Tc \qquad (8.16)$$

Models for Fig. 8.10 are shown in Fig. 8.12, with E^0 = 50 and 100

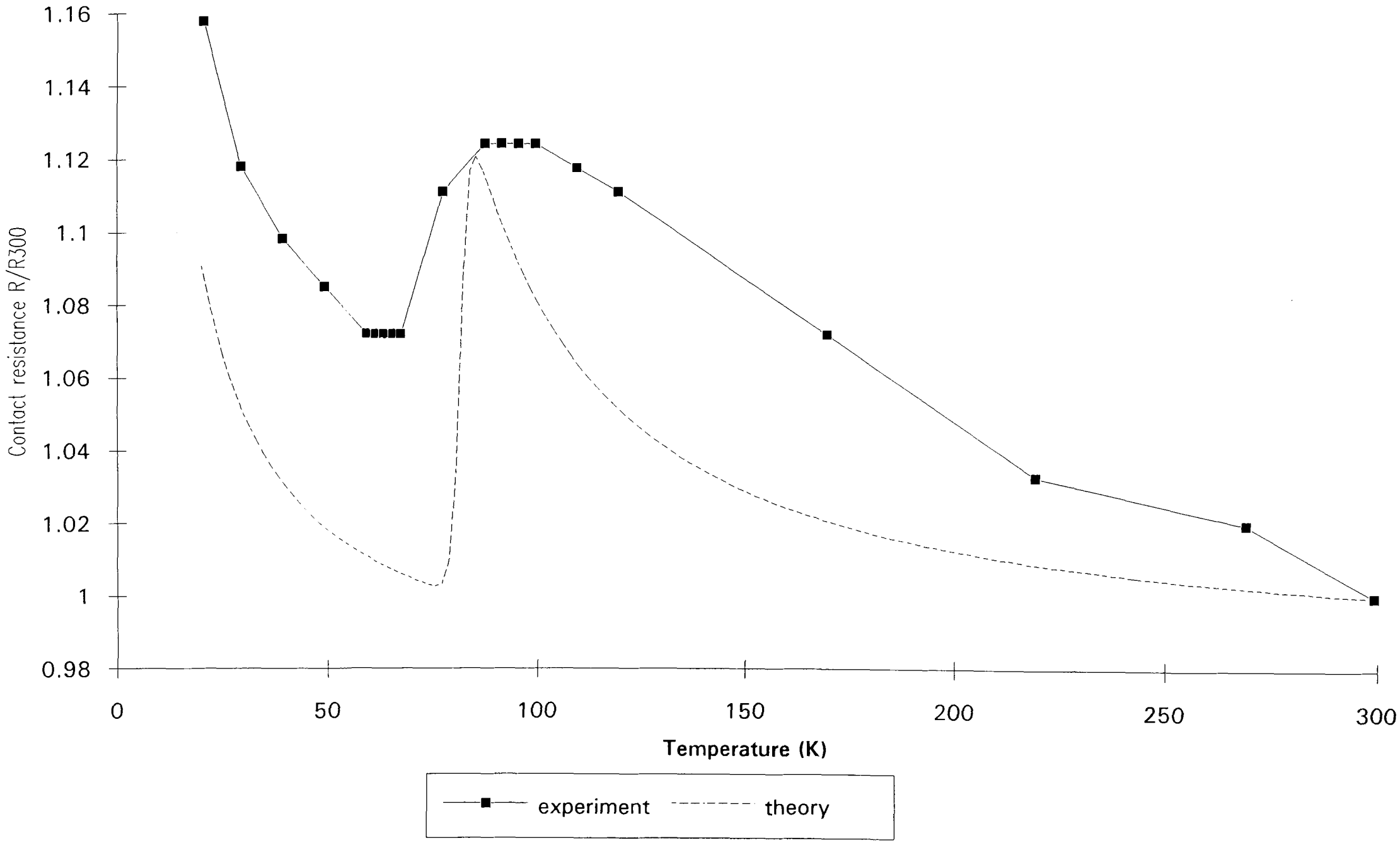

Figure 8.12: Model for contacts with resistivities 10-2 -10-3 Ohmcm2)

respectively. The results show that the model can match the data from contacts in the resistivity range $10^{-2} > Rc > 10^{-3}$ Ωcm^2 reasonably well.

However, it cannot be used to fit the Ti/Au contact resistance measurement shown in Fig.8.13 (identical to Fig.6.18).

8.3.5. Model for contacts with resistivity between 10^{-3} - 10^{-4} Ωcm^2

By examining carefully the microstructure of the contact interface of the titanium contact sample, the SEM image shows that the interface is not straight at high magnification (Fig. 8.14) due to the porous nature of the superconductor oxide. The multilayer contacts may also inherit this characteristic, and interdiffusion also encourages the contact material to fill the pores in the superconductor. So the impurities, oxygen deficient interfacial 123 phase and unaffected superconductor may form a parallel circuit at the contact interface with a very thin oxidized TiO_2 layer in series of the circuit which is due to the incomplete intermixing of the noble metals and TiO_2.

The model is shown in following diagram:

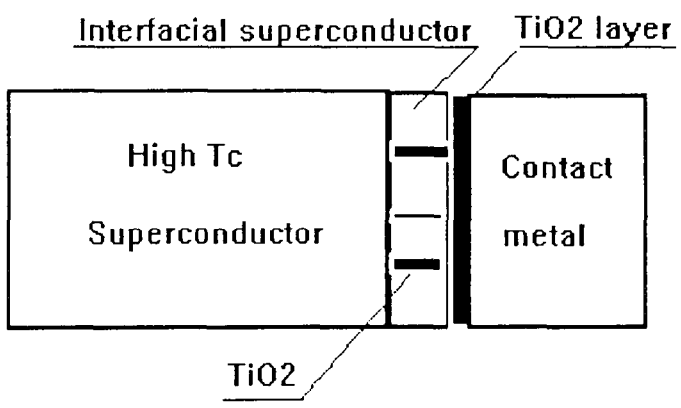

Figure 8.15: Schematic diagram for contact made with Ag/Ti

where the contact resistance is the sum of the parallel-circuits with a semiconductor in series :

For $T > Tc$:

$$R_c = C_{TiO2} \times T \times \exp(E^0/T)/(T + C \times \exp(E^0/T)) + C'_{TiO2} \times \exp(E'/T) \qquad (8.19)$$

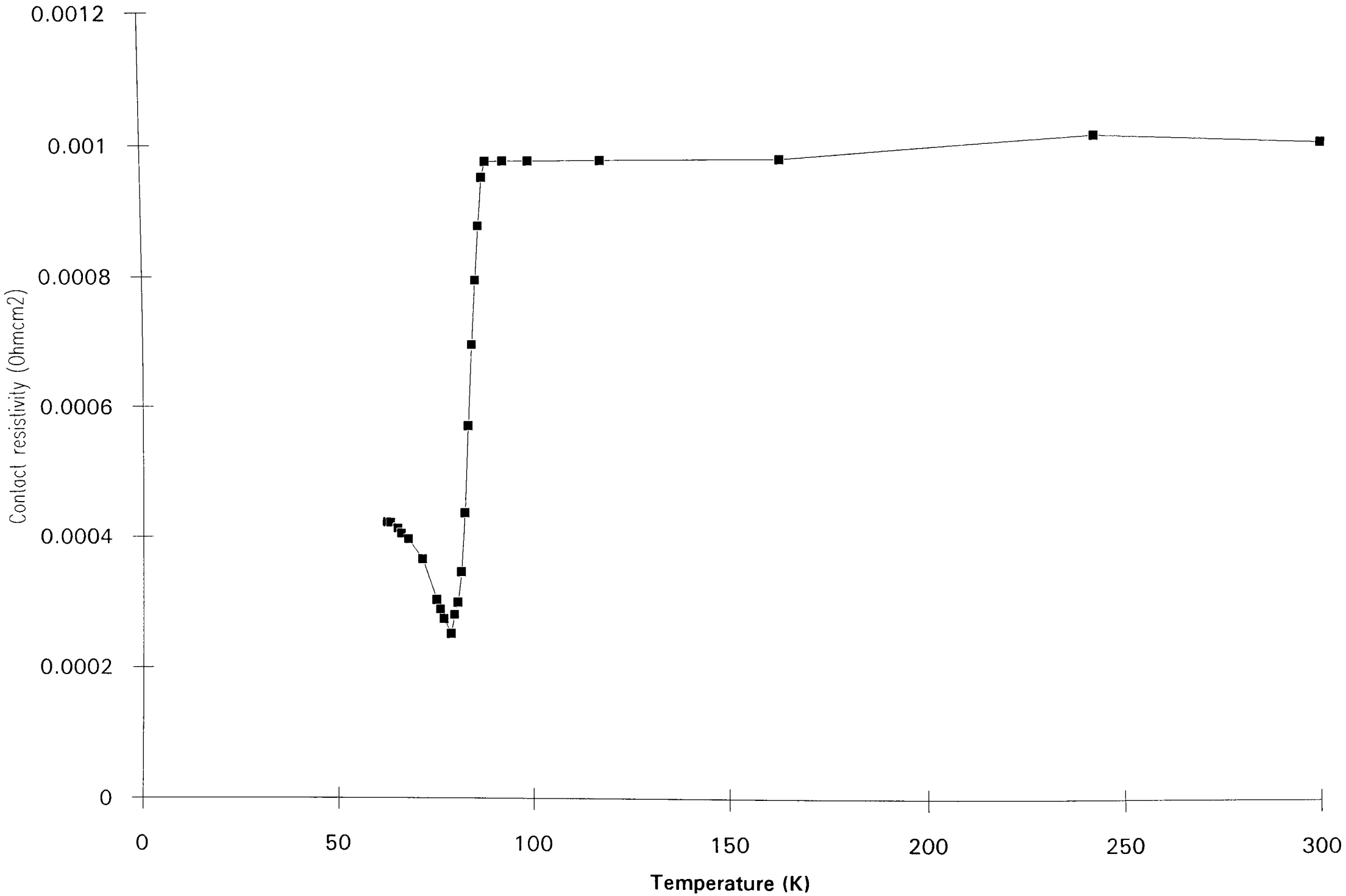

Figure 8.13: Au/Ti contact resistivity (identical to Fig. 6.18)

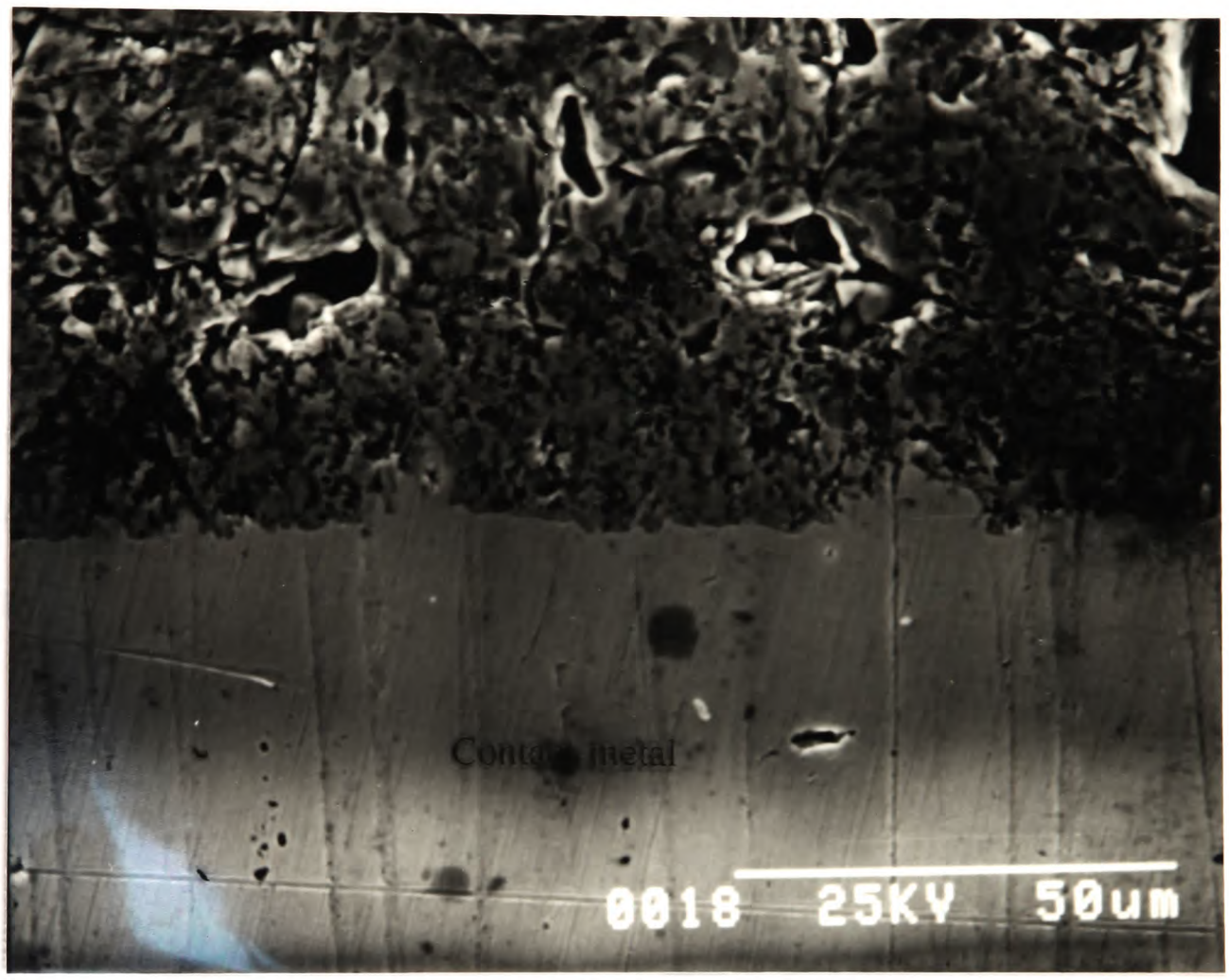

Figure 8.14: Contact interface

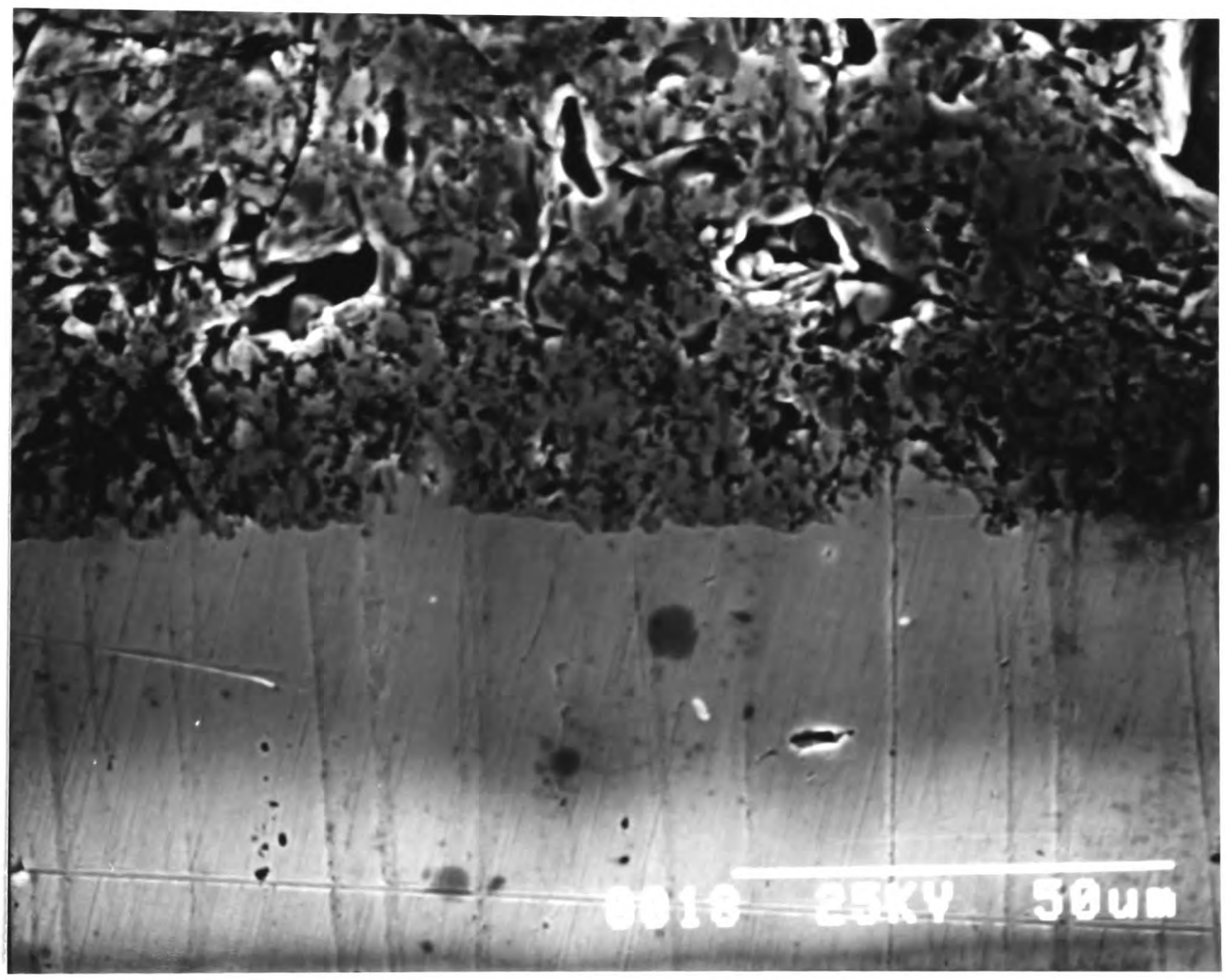

Figure 8.14: Contact interface

and

For $T < T_c$:

$$R_c = C_{TiO2} \times Tc \times \exp(a \times (T-T_c)) \times \exp(E^0/T)/(Tc \times \exp(a \times (T-Tc)) + C \times \exp(E^0/T)) + C'_{TiO2} \times \exp(E'/T) \quad (8.20)$$

where C_{TiO2}, a, C ($=C_{TiO2}/C_{in}$), C', E^0, E' are constants.

The calculated result of the model to simulate Fig. 8.13 shown in Fig. 8.16 with C= 80, E^0=38 and E'=10. The result shows that this model can be used to fit the Ag/Ti contact with resistivity in the range 10^{-3} - $10^{-4}\Omega cm^2$.

8.3.6 Model for Pd contact with strange behaviour

As we have seen in Fig.6.21 and Fig.6.22, SEM and electron microprobe analyses show that the Pd has reacted with $YBa_2Cu_3O_{7-x}$ and formed isolated Pd-rich phases scattered around the interfacial area. This observation has been used to model the contact resistivity behaviour of these Pd contacts (Fig.8.17, Fig.8.18). The model is set up as follow:

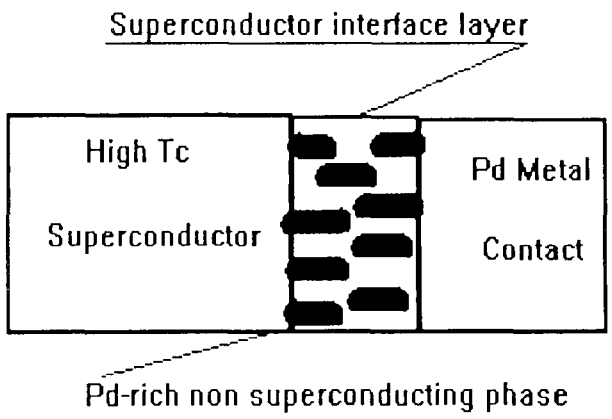

Fig.8.19: Schematic diagram of Pd contact

The contact resistance model is set up on the assumption that the scattered Pd reaction products are in parallel circuits with the superconducting interfacial layer. Assuming that the interfacial layer contains two such parallel circuits in series, the contact resistance is a sums of :

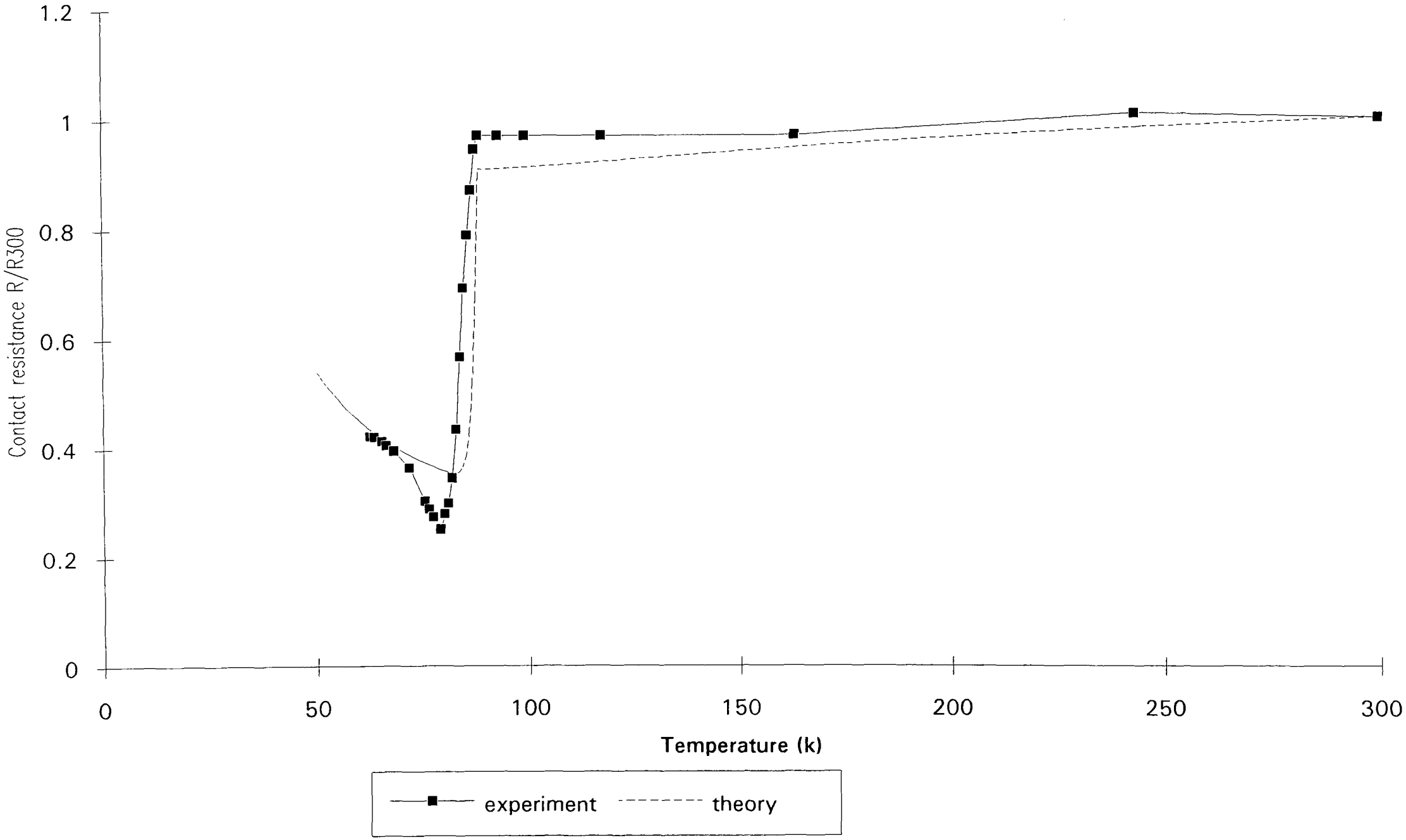

Figure 8.16: Model for Ti/Au contact

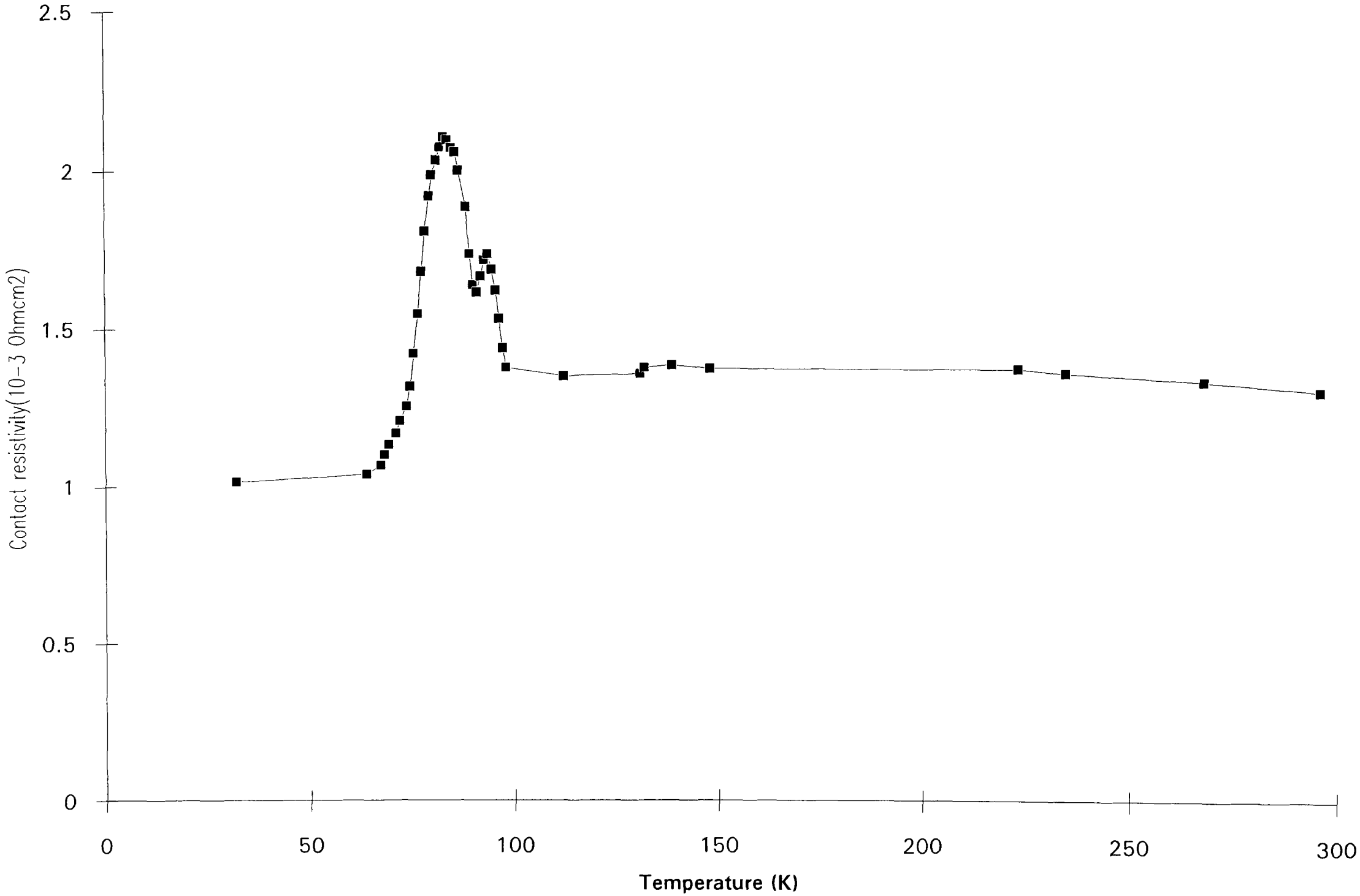

Figure 8.17: Pd contact resistivity

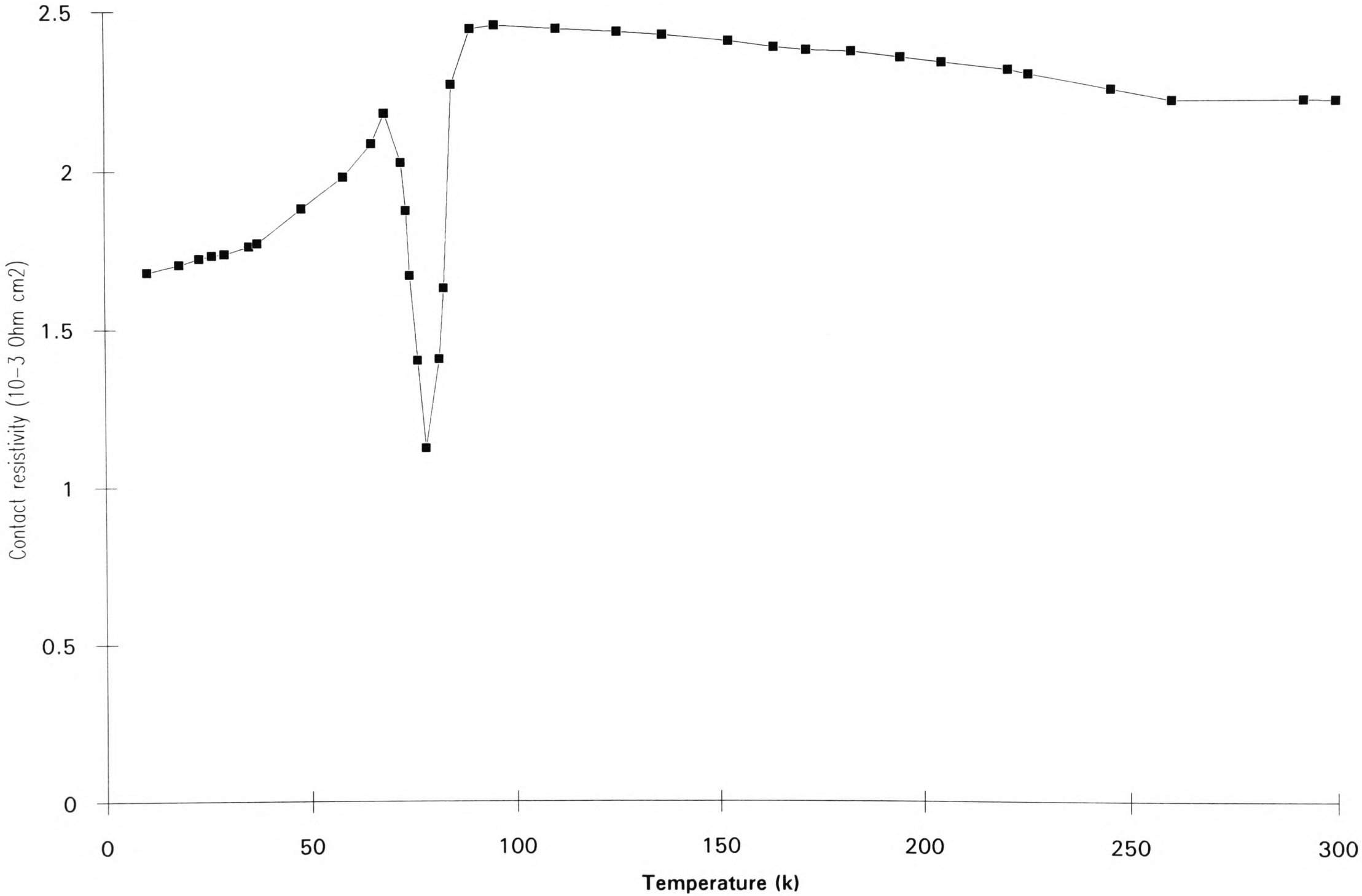

Figure 8.18: Pd contact resistivity

For $T > Tc$:

$$R_c = C_{semi} \times T \times \exp(E^0/T)/(T + C \times \exp(E^0/T)) + C'_{semi} \times T \times \exp(E'/T)/(T + C' \times \exp(E'/T)) \quad (8.21)$$

and for $T < Tc$:

$$R_c = C_{semi} \times Tc \times \exp(a \times (T-Tc)) \times \exp(E^0/T)/(Tc \times \exp(a \times (T-Tc)) + C_{semi} \times \exp(E^0/T)) + C'_{semi} \times Tc \times \exp(a \times (T-Tc)) \times \exp(E'/T)/(Tc \times \exp(a \times (T-Tc)) + C'_{semi} \times \exp(E'/T)) \quad (8.22)$$

where C_{semi}, a, C'_{semi}, and C are constants. E^o and E' are the activation energy terms for charge transport for the two different semiconductors.

The results of models to simulate the cases in Fig.8.17 and Fig.8.18 are shown in Fig. 8.20 and Fig.8.21 in comparison with experimental data, with $E^0 = 200$, $E' = 300$ and $E^0 = 50$, and $E' = 100$ respectively.

The calculated result shows that they fit the experimental result at least in the overall shape of the curves.

8.4. Discussion:

Measurements of the temperature dependence of contact resistance can reveal contact properties which contact resistivity measurements at only one temperature may miss. As a result models for contact behaviour can be set up taking into account results from analysis of interface reactions. Good contacts display a clean interface and the contact resistance behaves similarly to the pure superconductor both above and below Tc. This behaviour can be modelled by an interfacial superconductor layer with slightly modified properties; Poor contacts with resistivities over 10^{-1} Ωcm^2, do not show any resistance drop near Tc, which indicates that the semiconductor material dominates the contact resistance.

The cases in between these two extremes show a the resistance drop, but do not behave like superconductor samples. Some may show semiconductor behaviour below Tc, or both above and below Tc, and these can be modelled by assumption of thin semiconductor layer (impurities or reaction products) either in series or in parallel with

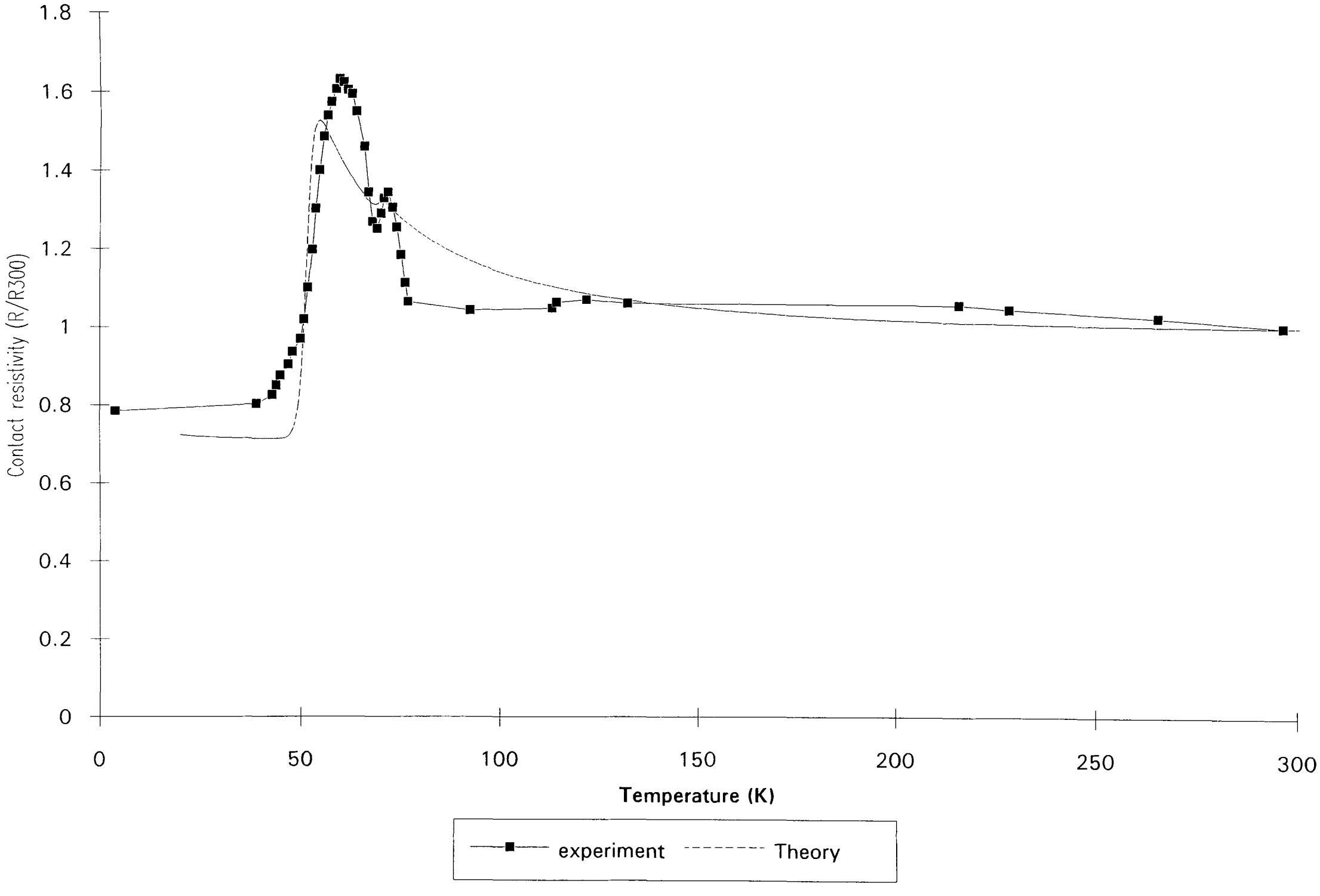

Figure 8.20: Model for Pd contact Fig. 8.17

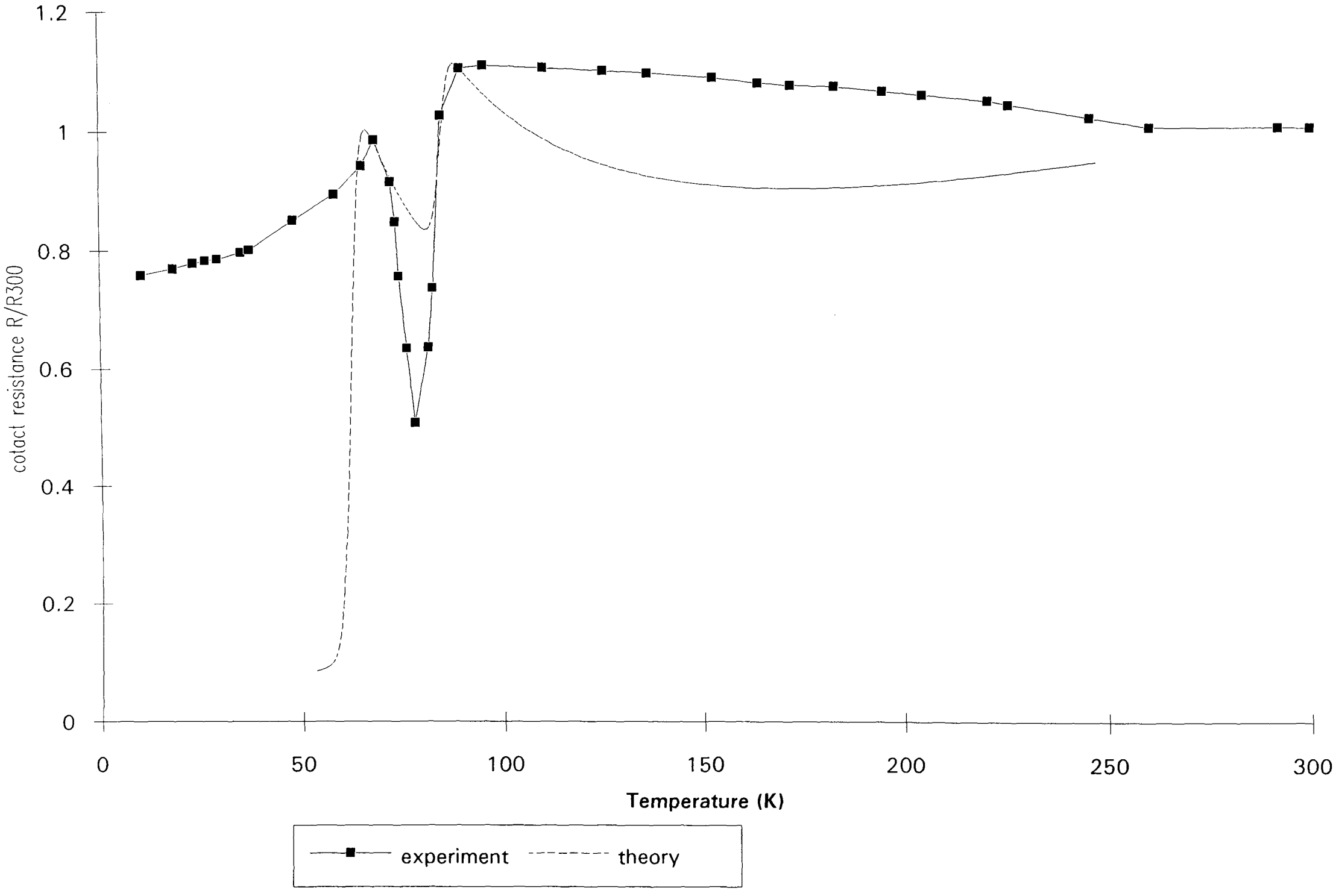

Figure 8.21: Model for Fig.8.18

the interfacial superconductor layer. The fitted values of constant C and activation energy E from the model may give some real physical information about the properties of these semiconducting layers. In the case of Fig. 8.9, the best fit with the experimental data is obtained with $E^0 = E/k = 100$ and $E = 8.6\times10^{-3}$ eV, which may indicate that the impurity is not really a genuine semiconducting material but perhaps more likely a carrier deficient metal or superconductor .

For all the cases modelled above by this method, the constants C and activation energies for conduction are listed in table 8.1.

Table 8.1

	Constant C	Activation energy E(eV)
Figure 8.9	88	8.62×10^{-3}
Figure 8.12	---	8.62×10^{-3}
Figure 8.16	80	3.275×10^{-3}
Figure 8.20	0.01, and 10^{-12}	1.7×10^{-2}, and 2.6×10^{-2}
Figure 8.21	1, and 10^{-10}	4.3×10^{-3}, and 8.6×10^{-3}

The two sets of C and E values for Fig. 8.20 and 8.21 correspond to the two parallel circuits in the model.

The activation energies are all in the range 10^{-2} - 10^{-3} eV for the semiconductor components in parallel or in series with the superconductor layer, which indicates that all the semiconductor materials which control the temperature dependence of the contact resistivity are some kind of semi-metal rather than real semiconductors (with activation energy about 1 eV). Some semiconducting or insulating material may also present at the contact interfaces with much higher resistances, and with no current passing though them. The current will all pass through the superconductor in the parallel circuit, so the insulating phases will contribute only to the resistance R_i the interfacial resistance due to the restriction of

current flow, like the case in Fig. 8.19. The reaction products may have real semiconductor or insulating character and only contribute to R_i, while the degraded superconductor which surrounds the reaction products may have semi-metal character which controls the temperature dependence of the contact resistance.

The constant C may contain useful information on the ratio of the current going through superconductor and semiconductor phases. For the case in Fig. 8.9, the current mainly passes through the superconductor, and the semiconductor has only limited effect on the contact resistance. However, in the case of Fig. 8.20 the current mainly passes through the semiconductor in the first parallel circuit, which means the semiconductor must form a nearly continuous layer.

These simple models can model most cases of the contact behaviour measured in this work, and since even the most complicated circuit at an actual interface can be simplified to a mixture of series and parallel circuits, and the more complicated resistance behaviour can be modelled by a slightly more complicated circuit.

This kind of modelling can thus provide information on the geometry of the interface reaction products and their conduction properties. This information can be usefully combined with direct observations on the structure and chemistry of the contacts to gain a fuller understanding of what controls the properties of these important interfaces.

Chapter 9

Conclusions and suggestions for further work

9.1 Conclusions

1). Methods of processing large grained textured superconductor have been successfully developed, based on a melt texturing process. Large grained textured superconductor with grain size over 10mm along the growth direction and Jc over 3600A/cm^2 (77K, 0.5 Tesla) has been produced in both one - zone and two - zone furnaces with good reproducibility.

2). Two kinds of design of reactive metal contacts have been proposed and investigated, aiming to make low resistivity contacts with strong mechanical strength. Three possible reactive contact metals have been tested for contact making, and the microstructures at the interfaces have been studied to find the relations between contact resistivity and contact processing conditions. The results can be summarized as:

Titanium metal can be used as one of the components in multilayer contacts if the resistivity is not required to be lower than $10^{-5}\Omega cm^2$. This is a promising type of contact processing technique for low resistivity and strong mechanical bonds.

Molybdenum metal is not suitable for making contacts to $YBa_2Cu_3O_{7-x}$.

Palladium metal can form strong bonds with $YBa_2Cu_3O_{7-x}$ with contact resistivities around 10^{-3}-10^{-4} Ωcm^2. The anomalous resistivity behaviour of these contacts may due to the distribution of reaction products with widely varying properties.

3). Gold and silver contact making techniques were carefully studied to find possible rugged low resistivity contacts. Gold and silver contacts give resistivities among the best reported results in the literature, and they turned out to be extremely

stable in time, could withstand repeated thermal cycling from room temperature to 10K and yield very reproducible R-T curves. Among them, silver epoxy contacts and solderable gold plate contacts are promising techniques for making strong contacts with ultra low resistivity behaviour.

4). The electrochemical titration method can be used to increase the oxygen stoichiometry of bulk textured $YBa_2Cu_3O_{7-x}$ samples. The electrochemical titration method can further oxidize melt textured thick film $YBa_2Cu_3O_{7-x}$ samples in which it may be difficult to further improve oxygen content by conventional annealing.

5). The electrochemical titration method was proved to give faster oxidation kinetics in $YBa_2Cu_3O_{7-x}$ than annealing at the same temperature and oxygen pressure.

6). The electrochemical titration method can generate very high oxygen activity at the surface of $YBa_2Cu_3O_{7-x}$ and form $YBa_2Cu_4O_8$ and $YBa_2Cu_{3.5}O_{7+x}$.

7). The solid state electrochemical cell can be used to study the thermodynamic properties of the Y-Ba-Cu-O system at high oxygen pressure by measuring the oxygen activity versus time continuously immediately after the electrochemical titration. There are three possible five-phase equilibria involved in $YBa_2Cu_3O_{7-x}$, CuO, ZrO_2, $ZrBaO_3$, $YBa_2Cu_4O_8$ and $YBa_2Cu_{3.5}O_{7+x}$ which may be responsible for the high oxygen activity observed after electrochemical titration.

8). The insufficient oxygen supply at high temperatures at the interface between gold and $YBa_2Cu_3O_{7-x}$ may be responsible for the decomposition of $YBa_2Cu_3O_{7-x}$. The electrochemical titration method can be used to make low resistivity gold contact on $YBa_2Cu_3O_{7-x}$.

9). A series of computer models were set up according to the microstructure of the contact interface to simulate the complicated contact resistivity behaviours. The nature of, and geometry of, the reaction products at the contact interfaces may be revealed by the temperature dependence of the contact resistance. This kind of modelling can thus provide information on the geometry of the interface reaction products and their conduction properties. This information can be usefully combined with direct observations on the structure and chemistry of the contacts to gain a fuller understanding of what controls the properties of these important interfaces.

9.2 Suggestions for further work

Further studies of the melt growth mechanism of the superconductor should concentrate on the continuous movement of the temperature gradient and optimization of the temperature gradient, in order to improve the grain size of the melt textured superconductor (and develop this method into single crystal processing method), and increase the continuity to make long melt textured superconductor tape.

Based on the contact interface design, rhenium contacts should be further tested, since the rhenium oxides have good electrical conduction, and with careful preparation, the rhenium contact may achieve both good electrical properties and good mechanical properties. Rhenium contacts have only been tested once without successful bonding, and probably need a higher annealing temperature in future experiments.

Electrochemical study on superconductor (thin film and bulk) samples should concentrate on both oxygen stoichiometry monitoring and thermodynamic measurement of the system. It is possible to control the oxygen activity and content not only at the contact interface, but also along the whole length of superconductor composite with one pair of electrodes.

Further study of the contact interface by electron microscopy is required for further understanding of the conduction mechanism across the metal/superconductor interface, more detailed models could be set up based on this investigation, and the ultra low resistivity contact strong mechanical properties could be designed and fabricated with a better understanding of conduction mechanism at the contact interface.

References:

Ahn B T, Lee V Y and Beyers R, 1990, Physica C **167** 529-537.

Asano T., Tran K., Byrne A.S., Rahman M.M., Yang C.Y. and Eardon J.D., 27 March 1989, Appl. Phys. Lett. **54(13)**,1275-1277

Aselage T. L. and Keefer K.D., 1988, J. Mater. Res. **3** 1279

Ashworth S.P., C Beduz, Harrison K, Scurlock R.G. and Yang Y., 1989, Cryogenics **29** 1124-1127.

Bednorz J G and Muller K A, 1986, Z. Phys. B **64** 189-192.

Bessergenev V.G., Gelfond N. V., Igumenov I.K., Ilyasov S.Sh., Kangiev R.D., Kovalevskaya Yu. A, Kravchenko V.S., Slobodyan S.A., Motorin V. I. and Shestak A.F., 1991, Supercond. Sci. Technol. **4** 273-278

Blaugher R D, 1982, Advances in Cryogenic Engineering-Materials **28** A.F. Clark and R.P. Reed, eds. New York, NY: Plenum, , pp.689-700.

Bochenek E, 1978, Thesis, University of Karlsruhe

Buckley Donald H., May/Jun 1985, J. Vac. Sci. Technol. A3(3), 762-771

Caton R, Selim R and Buoncristiani A M, 1990, J. Appl. Phys. **67(12)** 7478-7482.

Caton R., Selim R., Buoncristiani A.M., and Byvik C.E., 21 March 1988, Appl. Phys. Lett. **52(12)**, 1014-1016.

Cava R J, Batlogg B, Chen C H, Rietman E A, Zahurak S M, Werder D, 1987, Phys. Rev. **B36** 5719-5722.

Cava R.J., van Dover R.B., Batlogg B., and Rietman E.A., 1987, Phys. Rev. Lett. **58**, 408

Cava R J, Batlogg B, van Dover T B, Murphy D W, Sunshine S A, Siegrist T, Remeika J P, Reitman E A, Zahurak S and Espinosa G P, 1987, Phys. Rev. Lett. **58** 1676-1679.

Cava R J et al, 1988, Proceedings of the International Conference on High Temperature Superconductors and Materials and Mechanisms of Superconductivity, Part 1. Interlaken, Switzerland.

Champagne B., Parent L. and Moreau C., 1989, Supercond. Sci. Technol. 25-28

Chandrachood M R, Morris D E and Sinha A P B, 1990, Physica C **171** 187-193.

Chang Chin-an, 14 March 1988, Appl. Phys. Lett. **52(11)**, 924-929.

Chen L M, Barr T L, Krauss A R, Gruen D M and Gady B, 1991, J. Vac. Sci. Technol **A9 (3)** 394-400.

Chen In-Gann, Sen S., and Stefanescu D.M., 18 April 1988, Appl. Phys. Lett. **52(16)**, 1355-1357

Cheung, C.T. and Ruckenstein E., Jan/Feb 1989, J. Mater. Res., **4(1)**, 1-15.

Chu C.W., Hor P.H., Meng R.L., Gao L., Huang Z.J., and Wang Y.Q., 1987, Phys. Rev. Lett. **58**, 405

Cieplak Marta Z., Xiao Gang, Chien C.L., Stalick J.K. and Rhyne J.J., August 1990, Appl. Phys. Lett., **57(9)**, 934-936.

Collin C.A., Abell J.S. and Gilberd P.W., 1990, Journal of the less-common metals, **164&165,** 1571-1578.

David W I F, Harrison W T A, Gunn J M F, Moze O, Soper A K, Day P, Jorgensen J D, Hinks D G, Beno M A, Soderholm L, Capone II D W, Schuller I K, Segre C U, Zhang K and Grace J D, 1987, Nature **327** 310.

de Leeuw D M, Mutsaers C A H A, Langereis C, Smoorenburg H C A and Rommers P J, 1988, Physica C **152** 39.

Degterov S.A. and Voronin G.F., 1991, Physica C, **178** 213-220

Deluca J A, Garbauskas M F, Bolon R B, McMullen H G, Balz W E and Karas P L, 1991, J. Mater. Res. **6 July** 1415-1424.

Dew-Hughes D, 1988, Ceramics **December** 714-715.

Dwir B., Affronte M. and Pavuna D., 1989 Appl. Phys. Lett. **55**, 399

Einstein A., 1905, Ann. Phys. (4:Drude) **17**, 549-560

Ekin J.W., and Panson A.J., 1987, patent disclosure filed with U.S. Dept.

Ekin J.W., Panson A.J. and Blankenship B.A., 25 January 1988, Appl. Phys. Lett. **52(4)**, 331-333.

Ekin J.W., Larson T.M., Bergren N.F., Nelson A.J., Swartzlander A.B., Kazmerski L.L., Panson A.J., and Blankenship B.A., May 1988, Appl. Phys. Lett. **52**, 1819-1821, .

Ekin J.W., Braginski A.I., Panson A. J., Janocko M.A., Capone II D.W., Zaluzec N.J., Flandermeyer B., de Lima O.F., Hong M., Kwo. J., Liou S., 1987, J. Appl. Phys. **62,** 4621.

Forsyth E B, 1973, IEEE Trans. **2** 494.

Funaki K, Funaba R, Kobayashi M, Takeo M and Yamafuji K J, 1991, IEEE Trans on magnetics, **27** (2)

Frase K G and Clarke D R, 1987, Adv. Ceram. Mater. **2** 295

Frase K G, Liniger E G and Clarke D R, 1987, J. Am. Ceram. Soc., **70** (9) 204-205

Gallagher P K, 1987, Advanced Ceramic Materials, **2** (3B) 632-639

Ganapathy L., Kumar A. and Narayan J., 1989, J. Appl. Phys. **66,** 5935

Gangopadhyay, Anup K. and Mason T.O., 1991, Physca C, **178**, 64-70.

Gao Y and Merkle K L, 1990, J. Mater. Res., **5** (7) 1363-1367

Gao Y., Wagener T.J. and Weaver J.H., September 1987, Appl. Phys. Lett. **51(13)**, 1032-1034

Gavaler J R, 1973, Appl. Phys. Lett., **23** (10) 480-482

Gavaler J.R., Braginski A.I., Talvacchio J., Janocko M.A., Forrester, M.G., and Greggi J., 1988, MRS **EA-14** High Temperature Superconductors II, Capone II D.W., Butler W.H., Batlogg B., and Chu C.W., Eds. Pittsburgh, PA Mater. Res. Co., 193-196

Gazit D., Peszkin P.N., Feigelson R.S., Sun J., and Geballe T.H., 1989, Mater. Res. Bull., **24**, 467-474

Gough C, 1991, Physics World, **Dec.** 26-30

Gurvitch M. and Fiory A.T., 1987, Appl. Phys. Lett. **51**, 1027

Hagen S.J., Jing T.W., Wang Z.Z., Horvath J., and Ong N.P., 1988, Phys. Rev. B **37**, 7928

Hervieu M, Michel C and Raveau B, 1989, Journal of Less Common Metal, **150** 59

Hikata T, Ueyama M, Mukai H and Sato K, 1990, Cryogenic Engineering, **25** 191-193

Hill D.M., Gao Y., Meyer III H.M., Watener T.J., Weaver J.H., and Capone II D.W., 1987, Phys. Rev. B.36, .3979

Hill D.M., Meyer III H.M., Weaver J.H., Capone II D.W., Flandermeyer B.K., 1988, Phys. Rev. B **37**, 511

Holland G F, Hoskins R L, Dixon M A, Vernooy P D, zur Loye H C, Brimhall G, Sullivan D, Cormia R, Zandbergen H.W, Ronsky R and Stacy A M, 1987, D.L. Nelson, M.S. Whittingham and T.F. George Eds., Washington DC., Am. Chem. Soc., 102-113

Hollin C A, Abell J S and Gilberd P W, 1990, Journal of the Less-common Metals **164 &165** 1571-1578.

Holtzberg, Kaiser D.L., Scott B.A., McGuire T.R., Jackson T.N., Kleinsasser A., and Tozer S., Chemistry of High-Temperature uperconductors, ACS Symposium series **No. 351**, edited by Nelson D.L., Whittingham M.S., and George T.F. (ACS, Washington, DC,1987), 79.

Hui Y.C., Hui P.M., Lemberger T.R., and Garland J.C., 15 May 1989, J. Appl. Phys. **65(10)**, 3968-3971

Jin S., Sherwood R.C., Tiefel T.H., Kammlott G.W., Fastnacht R.A., Davis M.E., and Zahurak S.M., 1988, Appl. Phys. Lett. **52(19)**, 1628-1630.

Jin. S., Tiefel, T.H., Sherwood, R.C. Kammlott, G.W. and Zahurak, S.M., 1987, Appl. Phys. Lett., **51**, 943

Jin S., Tiefel T.H., Sherwood R.C., van Dover R.B., Davis M.E., Kammlott G.W., and Fastnacht R.A., 1 May 1988, Physical Review B, **37(13)**, 7850-7852

Jin S., Davis M.E., Tiefel T.H., van Dover R.B., Sherwood R.C., O'Bryan H.M., Kammlott B.W., and Fastnacht R.A., 19 June 1989, Appl. Phys. Lett. **54(25)**, 2605-2607

Jing T.W., Wang Z.Z., and Ong N.P., 1989, Appl. Phys. Lett. **55(18)**, 1912-1914

Jing T.W., Wang Z.Z., and Ong N.P., 1989, Physica C **162-164** 1061- 1062

Jorgensen J.D., Beno M.A., Hinks D.G., Soderholm L., Volin K.J., Hiterman R.L., Grace J. D., and Schuller I.K., 1987, Phys. Rev. B., **36(7)**, 3608-3616

Kakabatake T. and Ishikawa M., 1988, Solid state communications, **66(4)**, 413-416

Kaldis E. and Karpinski J., 1990, Eur. J. Solid state Inorg. Chem. **27** 143.

Kamarzin A.A., Logvinenko V.A., G.Konova N., Lisoyvan V.I., Stonoga Yu.A., Blinov A.G. and Guseva A.I., 1990, Journal of Thermal analysis, **36**, 1889-1893

Kammlott G.W., Tiefel T.H., and Jin S., June 1990, Appl. Phys. Lett. **56(24)**, . 2459-2461

Kapoor Rakesh R. and Eagar T.W., 1988, personal communication.

Karpinski J and Kaldis E., 21st January 1988, Nature, **331**, 242-245.

Karpinski J., Kaldis E., Jilek E., Rusiecki S. and Bucher B., 15th December, 1988,

Nature, **336**, 660-662

Karpinski J., Rusiecki S., Kaldis E., Bucher B and Jilek E., 1989, Physica C **160** 449-457

Kase Jun-ichiro, Shimoyama Jun-ichi, Yanagisawa Eiji, Kondoh Shinji, Matsubara Toshiya, Morimoto Takeshi and Suzuki Mitsuru, February, 1990, Japanese Journal of Applied Physics, **29(2)**, L277-L279

Katz J.D., Willis J.O., Maley M.P. and Castro R.G., 1988, personal communication.

Kerbs H.U. and Wordenweber R., 1988, J. Appl. Phys., **63**, 1642-1645

Kishio K., Shiomoyana J., Hasegawa T., Kitazawa K., and Fueki K., 1987, Jpn. J.Appl. Phys., **7**, L1228-1230

Kittel K., 1976, Introduction to Solid State Physics, 5th Edition, John Wiley & Sons, New York

Komolov S.A., Shtan'ko A.V., and Shalaev M.A., August 1990, Zavodskaya Laboratoriya, **56(8)**, 47-50

Kulkarni Pramada, Mahamuni Shailaja, Chandrachood Madhavi, Mulla I.S., Nigavekar Arun S., Sinha A.P.B., and Kulkarni S.K., May 1989, Appl. Phys. Lett. **54(22)**, 2262-2264

Kusaka T., Suzuki Y., Yotsuya T., Ogawa S., Aoyama T., and Imokawa H., 1988, in proc. 5th Int. Workshop on Future Electorn Devices, edited by Miyagi-Zao 205-208

Jin. S., Tiefel, T.H., Sherwood, R.C. Kammlott, G.W. and Zahurak, S.M., 1987, Appl. Phys. Lett. **51** 943

Kussmaul A., Moodera J.S., Tedrow P.M., MARCH 1991, IEEE Transactions on

magnetics, **27(2)** 1325-1326

Lakshmikumar S.T. and Rastogi A.C., 1989, Appl. Phys. **A48** 325-329

Lee Byeong-Joo and Lee Dong Nyung, 1991, J. Am. Ceram. Soc., **74(1)**, 78-84

Leupold M.J. and Iwasa Y., 1976, Cryogenics, **16**, 215-216

Liu Y.P., Warner K., Chan C., Chen K., Markiewicz R. and Moore R.L., 1 Dec. 1989, J. Appl. Phys., **66(11)**, 5514-5517

Loehman Ronald E., Tomsia A.P., Pask J.A. and Carim Altaf H., 1990, Physica C, **170**, 1-14

Lorenz A., Bochenek E., Fischer R. and Schneider R., 1989, Journal of he Less-Common Metals, **151,** 481-486

Luderer G., Dullenkopf P., and Laukien G., Sept. 1974, Cryogenics, **14**, 518-519

Ma Q.Y., Schmidt M.T., Weinman L.S., and Yang E.S., May/Jun 1991, J. Vac. Sci. Technol. **A9 (3)** 390-393

MacManus J.L., Fray D.J. and Evetts J.E., 1989, Supercond. Sci. Technol. **1**, 291-295

MacManus Judith, 1990, PhD Thesis, University of Cambridge.

Manthiram A., Swinnea J.S., Sui A.T., Steinfink H., and Goodenough J.B., 1987, J. Am. Chem. Soc. **109**, 6667

Meyer III H.M., Hill D.M., Weaver J.H., Nelson D.L., and Goretta K.C., 12 september 1988, Appl. Phys. Lett. **53(11)**, 1004-1006

Meyer III H.M., Wagener T.J., Hill D.M., Gao Y., Krahn S.D., Weaver J.H., Flandermeyer B. and Capone II D.W., 5 October 1987, Appl. Phys. Lett. **51(14)**, 1118-1120.

Meyer III H.M., Weaver J.H., and Goretta K.C., Feb. 1990, J. Appl. Phys. **67(4)**, 1995-2002.

Mizushima K., Sagoi M., Miura T., and Yoshida J., 28 March 1988, Appl. Phys. Lett. **52 (13)**, 1101- 1102.

Moorhead A.J., Henson H.M. and Henson T.J., 1986, Materials Sci. Res., Vol.21, ceramic microstructure role of interfaces, Eds. Pask Joseph A. and Evans Anthony G., Plenium press, 949-958.

Moorhead A.J., and Santella M.L., 1988, personal communication.

Moreland Jone and Goodrich L.F., Applied superconducting conference simposium, San Francisco, California, August 21-25, 1988.

Morita M., Murakami M., Miyamoto K, Sawano K and Matsuva S, 1989, Physica C, **162-164**, 1217-1218

Morris D.E., Asmar N.G., Nickel J.H., Sid R.L., Wei J.Y.T. and Post J.E., 1989, Physica C **159** 287.

Mroczkowski R., April 6, 1989, Machine Design, 134-137

Murakami M., Morita M., Doi K., Miyamoto K., 1989, Jap. J. Appls. Phys. **28**, 1189

Murakami M., Oyama T., et al, 1990, Jap. J. Appl Phys. **29**, L1991

Murakami M., Morita M., Miyamoto K. and Matsuda S., Proc. of Osaka University International Symposium, 1988

Naito M., Hammond R.H., Oh B., Hahn M.R., Hsu J.W.P., Rosenthal P., Marshall A.F., Beasley M.R., Geballe T.H., and Kapitulnik A., 1987, J. Mater. Res. **2**, 713

Nernst W., 1888, Z Phys. Chem. **2**, 613-637

Nicholas M.G. and Crispin R.M., July 1984, personal communication.

Nisenoff, M. 1988, Cryogenics, **28**, 47

O'Bryan H.M. and Gallagher P.K., 1987, Adv. Ceram. Mat., **2**, 640-648.

O'Bryan H.M. and Gallagher P.K., Jul/Aug , 1988, J. Mater. Res. **3(4)**, 619-625.

Ohkubo Masataka, 1990, Solid State Communications, **74(8)**, 785-788

Parkin S.S., Lee V.Y., Engler E.M., Nazzal A.I., Huang T.C., Gorman G., Savoy R., and Beyers R., June 1988, Phys. Rev. Lett., **60**, 2539-2542

Peterson G.G., Weinberger B.R., Lynds L., and Krasinski H.A., Jul./Aug. 1988, J. Mater. Res. .**3(4)**, 605-609.

Phillips J.C., 1989, Physics of High Tc. superconductors, Academic press, Inc.

Plecenik A., Benacka S., Darula M., and Chromik S., 1991, Solid State Communications, **78(9)**, 809-813.

Plechacek V., Landa V., Sneider J., Trejbalova Z. and Cermak M., 1988, Physica C, **153-155**, 878

Rajan K. Govinda, Parameswaran P., Janaki J. and Radhakrishnan T.S., 1990, J.

Phys. D.: Appl. Phys., **23**, 694-697.

Ray II Roger D. and Hellstrom Eric E., July 1989, J. Appl. Phys. **66(2)**, 741-744.

Roth R.S., Davis K.L. and Dennis J.R., 1987, Advanced Ceramic materials, **2(3B)**, special Issue, 302.

Rubin H.D., Rosamilia J.M., O'bryan H.M., and Miller B., May 1989, Appl. Phys. Lett. **54(21)**, 2151- 2153.

Saha R., Babu R., Nagarajan K. and Mathews C.K., 1989, Journal of Nuclear Materials, **167**, 271-277.

Salama K., Selvamanikham V., Gao L., Sun K., 1989, Appl. Phys. Lett. **54**, 2352

Schilling O.F., Yang Y, Grovenor C R M and Beduz C, 1990, Physica C, **170**, 123

Schmitz G.J., Weiss H., Wolters Ch., 1990, J. Less common metals **164B**. 1566-1570

Sevamanikham V., Salama K., 1990, Appl. Phys. Lett. **57**, 1575

Siegrist T., Schneemeyer L.F., Waszczak J.V., Singh N.P., Opila R.L., Batlogg B., Rupp L.W., and Murphy D.W., 1987, Phys.Rev. B, **36**, 8365-8368

Sleight A.W., 16 Dec. 1988, Science, **242**, 1519-1527

Specht E.D., Sparkes C.J., Dhere A.G., Brynestad J., Carin O.B., Kroeger D.M., and Oye H.A., 1988, Phys. Rev. B., **37(13)**, 7426-7434

Sun J.Z., Webb D.J., Naito M., Cher K., Hahn M.R., Hsu J.W.P., Kent A.D., Mitzi D.B., Beasley M.R., Geballe T.H., Hammond R.H., and Kapitulnik A., 1987, Phys. Rev. Lett., **58**, 1574

Sun Yue and Yang Hongchuan, 1991, Cryogenics **31**, 760-762

Suzuki Yoshihiko, Kusaka Tadaoki, Aoyama Takahiro, Yotsuya Tsutom, and Ogawa Soichi, Feb. 1989, Appl. Phys. Lett. **54(7)**, 666-668

Suzuki Rysosuke O., Okada Satoshi, Oishi Toshi, and Ono Katsutoshi, 1990, Materials Transactions, JIM, **31(12)** 1078-1084

Suzuki Yoshihiko, Kusaka Tadaoki, Aoki Akira, Aoyama Takahiro, Yotsuya Tsutom and Ogawa Soichi, 1988, Personal communication.

Swinnea J.S. and Steinfink H., 1987, J. Mat. Res. **2**, 424

Takeuchi I., Tai J.S., Tsuge H., Matsxkura N, Miura S, Yoshitake T, Kojima Y, and Matsui S, MARCH 1991, IEEE Transactions on Magnetics, **27(2)**, 1626-1629

Tiefel T.H., Jin S., Kammlott G.W., Plewes J.T. and Fastnacht R.A., 1990, Physica C, **166**, 408-412

Torrance J.B., Engler E.M., Lee V.Y., Nazzal A.I., Tokura Y., Ramirez M.L., Vazquez J.E., Jacowitz R.D., and Jacowitz P.M., Chemistry of High-Temperature Superconductors, 1987, ACS symposium Series **No. 351**, edited by Nelson D.L., Whittingham M.S., and George T.F.(ACS, Washinton, DC), 85.

Town S.L., Mathews D.N., Cochrane J., 1990, Cryogenics **30** 427-429.

Tsai J.S., Takeuchi I., Tsuge H., Matsukura N. and Miura S., 1990, Physica B **165&166** 1627-1628

Tzeng Y., Holt A., and Ely R., 11 January 1988, Apply. Phys. Lett. **52(2)**, 155-156

Tzeng Y., May 1988, J. Electorchem. Soc., **135**, 1309-1310

van der Maas J., Gasparov V.A. and Pavuna D., August 1987, Nature, **328**, 603-604,

Varlamov Yu.D., Vratskikh V.F., Zilkin A.S. et al., March 1990, Soviet Technology Physical Letter **35(3)**, 235-237.

Varma H.K., Kumar K.P., Warrier K.G.K. and Damodaran A.D., 1990, Supercond. Sci. Technol. **3**, 73-75.

Vasquez R. P., Hunt B.D., and Foote M.C., 1988, Appl. Phys. Lett.**53**, 2692

Verkouteren Jennifer R., 1989, Materials letters, **8(1-2)**, 59-63.

Vest R.W., and Honig J.M., 1974, Electrical conductivity in ceramics and glass, New York, Taller N.W. ed., 364-384

Voronin G.F. and Degterov S.A., 1991, Physica C, **176** 387-408

Wada T., Suzuki N., Maeda A., Uchida S., Uchinoku K., and Tanaka S., 1988, Jpn. J. Appl. Phys., **27(6)**, 1031-1034.

Waldram J.R., 1989, J. Phys.: Condens. Matter. **1**, 1285

Weinberger B.R., Lynds L., Potrepka D.M., Snow D.B., Burila C.T., Eaton Jr. H.E. and Cipolli R., 1989, Physica C. **161** 91- 104.

Wieck A.D., 21 March 1988, Appl. Phys. Lett., **52(12)**, 1017-1019

Wilber W.D. and Finnegan R.D., May 1990, J. Appl. Phys. **67(9)** 5073-5075

Yan M.F., Barns R.L., O'Bryan H.M., Gallagher P.K., Sherwood R.C., and Jin S., August 1987, Appl. Phys. Lett. **51(7)**, 532-534

Ying Q.Y. and Kwok H.S., 1990, Appl. Phys. Lett. **56(15)**, 1478-1480

Zandbergen H.W., Gronsky R. and Thomas G., 1988, Phys. Status Solidia, **105**, 207-218, .

Zhanguo Fan, Chunlin Ji and Zongxian Zhao, 1990, Journal of Less-Common Metals, **161**, 49-59

APPENDIX

Properties of pyrophyllite

Property	Typical values, Old and S.I. Units
Physical	
Apparent specific gravity	2.35
Water absorption	2.5 per cent by weight
safe temperature for continuous heating	2012°F = 1100°C
Maximum working Temperature	2372°F = 1300°C
Softening temperature	2912°F = 1600°C
Linear Coefficient of Thermal Expansion	
25 to 100°C	2.9×10^{-6} per °C
25 to 600°C	3.6×10^{-6} per °C
Colour (air-fired)	Pink
Thermal conductivity	≈ 0.003 Cal/cm^2/cm/sec/°C = 1.25 W/m deg C

Chemical	
SiO_2	56.85%
TiO_2	2.11
Al_2O_3	31.40
Fe_2O_3	0.63
FeO	0.28
MgO	0.40
CaO	0.03
Na_2O	0.90
K_2O	1.12
H_2O+	6.00
H_2O-	0.24
	99.96

Mineralogical (Analysis of crude)	
pyrophyllite	56.5%
felspars	14.5
kaolinite	12.0
diaspore	10.0
quartz	5.0
rutile	2.0

In other analysed samples the diaspore and kaolinite contents were higher and the felspar content was lower.

The fired material consists mainly of amorphous dehydroxylated pyrophyllite, mullite and a small proportion of cristobalite.

Property	Typical values, Old and S.I. Units
Electrical	
Eielectric strength (step 60 cycles)	100 Volts per mil = 4 volts per micrometer
Dielectric constant	
1MC	5.3
10MC	5.3
100MC	5.2
Power Factor	Power factor tanδ
1MC	0.01 $80\text{-}200\times10^{-4}$*
10MC	0.009 $40\text{-}100\times10^{-4}$*
100MC	0.007 ———
	* *depends on firing temperature*
Loss Factor	
1MC	0.053
10MC	0.048
100MC	0.036
Te value	700°C
Volume Resistivity at	
25°C	1.0×10^{14} Ohms/cm^3
100°C	6.0×10^{11}
300°C	2.0×10^{9}
500°C	5.0×10^{6}
700°C	3.5×10^{5}
900°C	5.0×10^{4}
Mechanical	
Hardness	Moh's Scale 6
Flexural strength	10,000 lb./sq. in. - 703 Kg/cm^2
Conpressive strength	25,000 lb./sq. in. - 1758 Kg/cm^2
Tensile strength	4000-6000 lb./sq. in. - 281-422Kg/cm^2
Resistance to impact (1/4 " rod)	3.3 inch-lbs = 0.584 m/kg